UNIVERSITÀ DEGLI STUDI DI PADOVA

DIPARTIMENTO DI FISICA E ASTRONOMIA "GALILEO GALILEI"

CORSO DI DOTTORATO DI RICERCA IN ASTRONOMIA

Ciclo XXXVIII

BINARY COMPACT OBJECT POPULATIONS

Coordinator: Prof. Giovanni Carraro

Supervisor: Prof. Giuliano Iorio

Co-supervisor: Prof.ssa Michela Mapelli

Prof. Giovanni Carraro

Ph.D. candidate: Erika Korb

To the friends made along the way.

Contents

Abstract

The detection of gravitational waves (GWs) from merging binary compact objects (BCOs) by the LIGO–Virgo–KAGRA Collaboration is providing a new window to investigate the lives and deaths of massive stars and compact objects that are members of binary systems, pushing the boundary previously set by electromagnetic observations. The most updated catalog of detections (GWTC-4.0) contains more than 200 BCOs, more than doubling the sample of the previous release (GWTC-3). Despite the increasing number of observations, the interpretation of BCOs remains challenging. Many formation channels could be at work, such as isolated binary evolution or dynamical formation, and the uncertainties in stellar and binary processes currently limit our ability to interpret the population properties of GW-merging BCOs.

In this thesis, I focused on the evolution of isolated binaries. In particular, I used the population-synthesis code, `SEVN`, to explore the impact of model uncertainties on BCO formation. I devoted particular attention to exploring the impact of mass transfer uncertainties - such as its stability, its efficiency and its consequences on orbital angular momentum losses - as mass transfer processes strongly affect the pre-supernova structure of compact object progenitors (thus, their remnant mass) and the binary separation (thus, its ability to merge via GW emission within the lifetime of the Universe). Eventually, I compared the results of these studies with the observations of possible progenitors binaries hosting massive stars. In particular, I considered the possible evolution through the pure-Helium or Wolf-Rayet (WR) star phase, as mass transfer events could strip the envelope of the star donating mass, exposing the underlying core, changing the stellar density profile, and overall affecting the supernova outcome.

In the first part of this thesis, I investigated the role of Wolf–Rayet stars with a compact object companion (in particular, a black hole or a neutron star), hereafter WR–CO, as progenitors of BCOs. To constrain model uncertainties, I explored the impact of a wide space of parameters and models, including metallicity, common-envelope efficiency, core-collapse supernova, and natal kicks. I found that WR–COs are a key-progenitor configuration for BCOs because the majority of BCOs have to experience the WR–CO phase to become GW sources, regardless of the combination of models considered. Even if few WR–COs become BCOs, binaries with orbital properties similar to Cyg X-3 (the only WR–CO observed in the Milky Way) are favoured as BCO progenitors. My results quantify the importance of WR–COs as BCO progenitors, highlighting that the observation and characterization of more of these systems could be crucial to constrain our models on BCO formation.

In the second part of this thesis, I considered four models for orbital angular momentum losses in mass transfer events (isotropic winds from the donor, from the accretor, Lagrangian outflows, or circumbinary disk formation) and analyzed their impact on the formation channels and the demography of GW-merging binary black holes (BBHs). I also considered the impact of tides and stellar physics for their additional impact on the variation in the orbital separation variations and pair-instability supernovae, respectively. Accounting for the stellar physics assumed, I found that the combination of efficient orbital angular momentum losses (such as Lagrangian outflows or circumbinary disk formation) and non-conservative mass transfer on an Eddington-limited BH accretor allows BBH formation even from binary progenitors that were not completely stripped of their envelope. These systems did not require a prolonged mass transfer to shrink the orbit, thus completely removing

the hydrogen envelope. Instead, their mass transfer was interrupted by the core-collapse supernova event of the donor, that collapses into a BH while retaining a fraction of its hydrogen envelope (constituting in some cases up to $\approx 60\%$ of its total mass before the collapse). In this scenario, I find that a non-negligible fraction of BBHs ($\approx 3-11$ %) has the most massive component (primary) that is more massive than ≈ 45 $M_\odot$. This threshold generally indicates the upper-limit for BH formation in BBHs in the isolated binary evolution and roughly coincides with the beginning of the pair-instability (PI) mass gap. I always find a dearth of BHs above ≈ 45 $M_\odot$ only in the case of the least massive BHs in BBHs (secondary). My results indicate that angular momentum losses in mass transfer processes influence the maximum mass expected from primary BHs evolved in isolation and should be considered for the interpretation of the putative PI gap that could be inferred from GWTC-4.0 and future GW detections. Eventually, I also highlight the need for caution when investigating the effects of mass transfer physics with various computational approaches, because it could be correlated with the impact of stellar evolution uncertainties, an aspect generally poorly explored in population-synthesis studies.

Symbols

$M_\odot$	solar mass	1.98892×10^{30} kg
$R_\odot$	solar radius	6.957×10^{8} m
au	astronomical unit	$1.495978707 \times 10^{11}$ m
pc	parsec	$3.08567758149137 \times 10^{16}$ m
Myr	megayear	3.1536×10^{13} s
c	speed of light in vacuum	$2.99792458 \times 10^{8}\,\mathrm{m\,s^{-1}}$
G	gravitational constant	6.6743×10^{-11} $\mathrm{m^3\ kg^{-1}\ s^{-2}}$

Acronyms

BBH	Binary black hole
BH	Black hole
BHNS	Black hole - neutron star binary
BNS	Binary neutron star
CCSN	Core-collapse supernova
CE	Common envelope
CO	Compact object
GW	Gravitational wave
NS	Neutron star
PI	Pair-instability
PPI	Pulsational pair-instability
RLO	Roche lobe overflow
SMT	Stable mass transfer
WR	Wolf-Rayet star
WR-BH	Wolf-Rayet - black hole binary
WR-CO	Wolf-Rayet - compact object binary
WR-NS	Wolf-Rayet - neutron star binary

Chapter 1

Theory and observations of binary compact objects

1.1 The compact object zoo

In astrophysics, the term "compact object" is used to describe objects that are able to confine a large amount of mass (as much as the Sun 1 $M_\odot \approx 1.98892 \times 10^{33}$ g, or more) within few thousands or even tenths of kilometres (Schmitt 2010). Compact objects are generally classified as White Dwarfs (WDs), Neutron Stars (NSs) or Black Holes (BHs). They can be found in different kind of environments, from the isolated field to the centre of galaxies, and their mass spans orders of magnitude, from few to million times the mass of the Sun $\approx 1 - 10^6$ $M_\odot$, as summarized in Figure 1.1.

Compact objects up to few hundreds of solar masses could be the final remnants of stars evolved in isolation, as single objects or as part of binary systems, and they could be found in the field as well as in stellar clusters (see the reviews by Marchant & Bodensteiner 2024 and Maccarone & Knigge 2007, respectively, and references therein). Heavier compact objects are classified as Intermediate-mass BHs (IMBHs) if their mass is $\approx 100 - 10^5$ $M_\odot$ or as Super-massive BHs (SMBHs) if their mass is higher $\gtrsim 10^5$ $M_\odot$ (e.g., Greene et al. 2020 and references therein). IMBHs have been observed in the centre of globular clusters (e.g., Kızıltan et al. 2017; Häberle et al. 2024), in the centre of Galactic Nuclei (e.g., Nguyen et al. 2019) and are believed to exist also in the disk of Active Galactic Nuclei (AGNs) (e.g., McKernan et al. 2014). Formation scenarios of IMBHs include the direct collapse of stars of very massive and metal-free Population III stars (e.g., Maeder 1992; Costa et al. 2023), repeated stellar collisions (Portegies Zwart & McMillan 2002), and hierarchical mergers of BHs, either in stellar clusters (Miller & Hamilton 2002) or in the disk of AGNs (McKernan et al. 2012). In a similar fashion, IMBHs could be the seed of the SMBHs found in galactic centers (e.g., Event Horizon Telescope Collaboration et al. 2019), whose collisions with other SMBHs are believed to power quasars and play a crucial role in the evolution of galaxies (Ferrarese & Merritt 2000; Di Matteo et al. 2005).

In this thesis, we will focus on the binary compact objects (BCOs) detected to merge via gravitational-wave (GW) emission within the lifetime of the Universe ($\lesssim 14$ Gyrs), so we will use the CO acronym only to indicate NSs or BHs (The LIGO Scientific Collaboration et al. 2025b). Hereafter, we review theoretical and observational state-of-the-art knowledge of BCOs, with particular attention to the evolution in the field as isolated binaries, a channel significantly influenced by stellar physics (e.g., Marchant & Bodensteiner 2024).

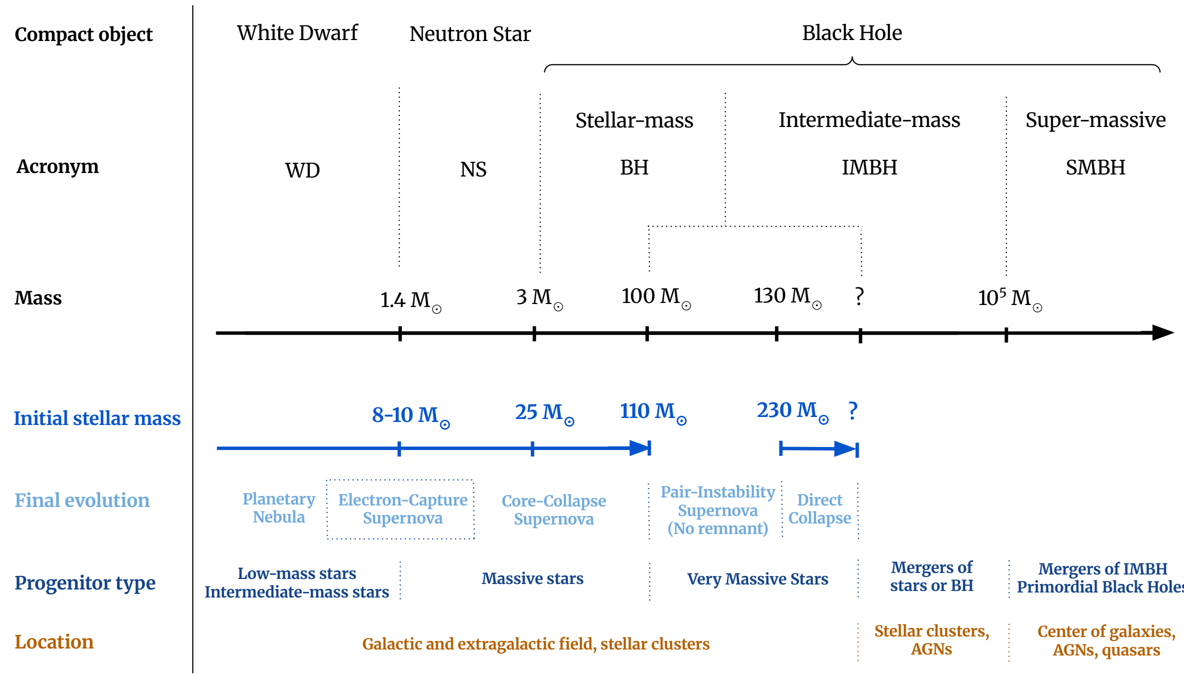

Figure 1.1: Schematic illustration of the possible classification, formation, environments, and masses of the compact objects observable across the Universe.

1.2 Single stellar evolution

1.2.1 From stars to compact objects

Low-mass and intermediate-mass stars (initial masses at the Zero Age Main Sequence, hereafter ZAMS, up to $M_{\rm ZAMS} \lesssim 2$ M$_\odot$ and $M_{\rm ZAMS} \lesssim 8-10$ M$_\odot$, respectively) will expand during their lives and eventually become Red Giants. These stars will then lose their external envelope because of pulsations and dust-driven mass loss, forming a planetary nebula and eventually leaving a degenerate core. Increasing progenitor masses allows heavier elements to ignite in the core, so the final remnants will be made of helium, carbon-oxygen or oxygen-neon, respectively known as He-WD, CO-WD, or ONe-WD. These degenerate and dense ($\rho \approx 10^4$ g cm^{-3}) cores are sustained by the electron degeneracy pressure. If the WD mass approaches the Chandrasekhar limit of ≈ 1.4 M$_\odot$ (Chandrasekhar 1931), central densities increase to the point $\rho \approx 10^9$ g cm^{-3} where electron-captures trigger a dynamical instability: an electron-capture supernova occurs and a NS is formed (Canal et al. 1992).

Massive stars (initial mass above $\gtrsim 8-10$ M$_\odot$) are expected to form an iron-rich core, undergo a core-collapse supernova (CCSN) event, and leave as remnant a NS or BH. NSs are very dense stellar objects ($\rho \approx 10^{15}$ g cm^{-3}) that are sustained by the degeneracy pressure of neutrons. Similarly to the case of WDs, NSs have maximum permitted mass that can be sustained by the degenerate matter: the Tolman-Oppenheimer-Volkoff (TOV) limit (Tolman 1939; Oppenheimer & Volkoff 1939). The maximum NS mass is approximately $M_{\rm NS,max} \approx 2.5-3$ M$_\odot$ and its precise determination is an active field of research, given its dependency on the poorly constrained equation of state of neutron stars (see Radice et al. 2018 and references therein). In a CCSN event, the core collapses into a proto-NS while the external layers are expelled by the explosion. If the CCSN is not energetic

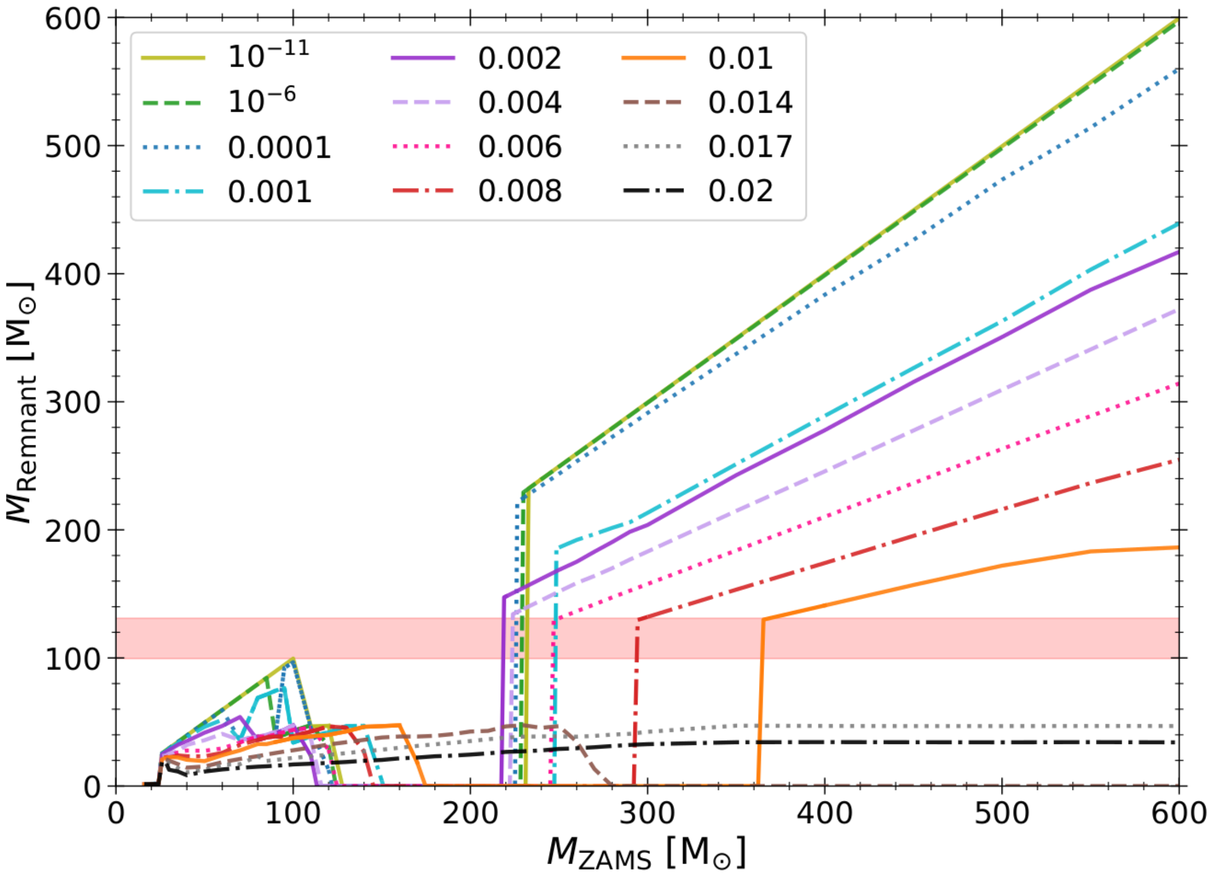

Figure 1.2: CO final masses ($M_{\rm remant}$) as a function of the initial mass of the stellar progenitor ($M_{\rm ZAMS}$). Even considering the evolution across a broad range of metallicities Z (reported in the legend), the red horizontal band shows that there is a region $M_{\rm rem} \approx 100 - 130$ M$_\odot$ where no CO can be formed by single stellar evolution because of pair-instability. This figure was produced also considering the stellar models of Figure 1.3 and is taken from Costa et al. 2025.

enough, part of the external layers will fall back to the proto-NS. It is possible that the falling back material accreted by the proto-NS increases its mass beyond the TOV limit, triggering a collapse and forming a BH. As a rule of thumb, stars with initial masses above $M_{\rm ZAMS} \gtrsim 25$ M$_\odot$ are more likely to form BHs in place of NSs because of their high binding energy (e.g., Laplace et al. 2025). However, the remnant mass is a not a linear function of the initial stellar mass, but it heavily depends on the structure of the pre-supernova progenitors (e.g., O'Connor & Ott 2011; Ertl et al. 2016; Sukhbold et al. 2016; Müller et al. 2016; Schneider et al. 2023; Maltsev et al. 2025), the explosion mechanism (Heger & Woosley 2002), and the amount of mass falling back (Fryer et al. 2012).

1.2.2 Compact object masses

Figure 1.2 shows that the CO mass is a strong function of the mass and metallicity Z of the star[1]. In a first approximation, there is a direct proportionality between the initial

[1] In astronomy, metals indicate elements heavier than He and their total mass fraction is expressed as metallicity Z.

stellar mass and the final CO mass, as heavier stars will end their lives with more mass, so they will produce heavier COs. However, stars experience many processes that can remove some mass during their lives, so the COs are generally lighter than the stellar progenitor. Among the most important processes, here we consider and discuss briefly the impact of supernovae and stellar winds.

1.2.3 Core-collapse supernovae

Massive stars evolve through a series of exothermic advanced nuclear burnings (e.g., carbon, oxygen, neon, silicon) that liberate energy in the core and, for this reason, can balance the gravity force and maintain the star's hydrostatic equilibrium. Once an iron-rich core has formed, nuclear reactions no longer release energy but instead absorb it: iron is not burned, but it accumulates. When the mass of the iron core exceeds the effective Chandrasekhar limit (Chandrasekhar 1931), electron degeneracy pressure is no longer sufficient to counteract gravity, and the core collapses into a proto-neutron star. This proto-compact object is so dense that a phase-transition occurs, producing a shock that propagates outward. While it encounters the outer infalling layers, the shock wave's energy triggers numerous nuclear reactions and produces a large amount of neutrinos. Neutrinos escape without significant interactions and dissipate the vast majority ($\approx 90-99\%$) of the the gravitational energy released during neutron star formation $\approx O(10^{53})$ erg, leaving only $\approx O(10^{51})$ erg available for conversion into kinetic and radiation energy (Burrows & Vartanyan 2021; Suzuki 2024). The evolution and the outcome of core-collapse supernovae (CCSNe) are sensitive to the details of the explosion and the microphysics considered (e.g., symmetry of the explosion or development of hydrodynamical instabilities; see Janka et al. 2012 and references therein for a review). Nevertheless, it is possible to group the fates of CCSNe into two main scenarios: successful explosions or failed explosions (Heger & Woosley 2002).

If the neutrinos carry away a sufficient amount of energy and the infalling material is strongly bound, the star will directly collapse into a BH and the explosion will fail. However, if there is some mechanism that can retain the energy of the initial shock and convert it into kinetic energy (for instance, by establishing a convective zone capable of trapping neutrinos and releasing them at a later stage), it is possible to revive the stalled shock wave and allow the supernova to proceed. In this case, the CCSN explosion is successful and the mass fallback onto the proto–neutron star is substantially reduced compared to direct collapse, making it possible to form either a neutron star or a black hole (e.g., Sukhbold et al. 2016). The structure of the pre-supernova progenitor and the details of the supernova models (for instance, the delay in the shock revival) strongly influence the explodability and final mass of the CO, constituting an active area of research (e.g., O'Connor & Ott 2011; Fryer et al. 2012; Ertl et al. 2016; Schneider et al. 2023; Maltsev et al. 2025).

1.2.4 Pair instability supernovae

Stars that develop a helium core mass above $\gtrsim 32$ M$_\odot$ have central temperatures and densities so high ($T \gtrsim 6 \times 10^8$ and $\rho \times 10^2 - 10^6$ g cm^{-3}) that they can trigger efficient pair creation, removing radiation pressure from the core and triggering a dynamical instability (Heger & Woosley 2002; Woosley 2017; Farmer et al. 2019). As long as the helium core is not too massive $\approx 32 - 64$ M$_\odot$, dynamical instability triggers core contractions and explosive ignition of oxygen in stars, that subsequently expel part of their outer layers after a series of pulses (Woosley 2017). This Pulsational Pair Instability (PPI) process removes some of the progenitor mass and determines the production of remnants that are lighter than the ones expected by CCSN alone (Mapelli et al. 2020). If pair creation occurs in heavier helium cores $\approx 64 - 135$ $M_\odot$, the outer layers have a high binding energy that prevents them from being expelled. In this case, oxygen can ignite under conditions of high temperature and pressure, leading to a runaway thermonuclear Pair Instability (PI) supernova that leaves no remnant. In even heavier helium cores $\gtrsim 135$ $M_\odot$, PI triggers a direct collapse.

The existence of PI and PPI supernovae is expected to leave a gap in the possible BH masses that could be produced by stars evolved in isolation (Spera & Mapelli 2017; Woosley 2017; Farmer et al. 2019). However, the location of the gap boundaries and the existence of the gap itself are highly sensitive to uncertainties in the stellar physics (e.g., the rate of the $^{12}C(\alpha,\gamma)^{16}O$ reaction, the amount of overshooting, the possibility that dredge-up episodes or wind mass losses reduce the size of the pre-supernova helium core, the effect of metallicity on wind mass losses (Renzo et al. 2020b; Costa et al. 2021, 2025)) and uncertainties in the details of the supernova mechanism and in the amount of hydrogen envelope falling back onto the helium core (Renzo & Smith 2024).

Over the years, many studies proposed various boundaries for the BH mass gap. Heger & Woosley (2002) studied the evolution of bare-helium cores and found that PI does not allow BHs in the $\approx 64 - 133$ $M_\odot$ range. Woosley (2017) systematically investigated the effect of PPI on bare-helium cores and showed that pulses continue until the completion of the silicon-burning evolution in hydrostatic equilibrium, extending the BH mass gap down to ≈ 52 $M_\odot$. Spera & Mapelli (2017) applied Woosley (2017) results on stellar cores to describe the final fate of a set of stellar evolution tracks developed with the `PARSEC` stellar evolution code (Bressan et al. 2012; Chen et al. 2015) for Population I and II stars ($Z \approx 10^{-2} - 10^{-4}$), suggesting that the gap exist in the $\approx 60 - 120$ $M_\odot$ range. Costa et al. (2025) extended this study to a broader range of metallicities to include the effect of Population III stars ($Z \approx 10^{-2} - 10^{-11}$), and found that the combined gap would shift to higher masses $\approx 100 - 130$ $M_\odot$ (Figure 1.2). Similarly to Woosley (2017), Farmer et al. (2019) also evolved bare-helium cores but suggested a criterion for PI determination based on the carbon-oxygen core mass, finding that this assumption shifts the lower boundary of the BH mass gap down to ≈ 45 $M_\odot$. According to Farmer et al. (2019), the ≈ 45 $M_\odot$ lower limit is robust against variations in metallicity, internal mixing and wind mass loss but it is sensitive to the $^{12}C(\alpha,\gamma)^{16}O$ reaction rate, shifting between $\approx 40 - 56$ just within 1σ uncertainty in the rate. Costa et al. (2021) accounted for the 3σ uncertainty and found that the PI gap could even disappear with enhanced overshooting.

1.2.5 Stellar winds

Massive stars $\gtrsim 8 - 10$ $M_\odot$ begin their life as hot ($T_{\rm eff} \gtrsim 12$ kK) O or B type stars (Sana et al. 2012; Shenar et al. 2022). Most of their radiation is emitted in the UV regime and it is so energetic that it ionizes the metals present in the photosphere. In the standard picture of line-driven winds (also known as CAK theory, following the work of Castor et al. 1975), ions absorb the momentum of the impinging photons and they share it via multiple scatterings with nearby nuclei and electrons: eventually, the whole gas is accelerated in the form of a wind. For higher temperatures (a property generally positively correlated with the stellar mass) and higher metallicities, more ions are produced and accelerated, so more mass will be lost from the star. For these reasons, mass-loss rates of massive stars are generally parametrized by the stellar metallicity Z, temperature, mass, and luminosity (Vink et al. 2001; Gräfener & Hamann 2008; Vink et al. 2011; Sabhahit et al. 2022).

Stellar winds progressively remove the external hydrogen layers and expose the hotter interior (effective temperatures of $T_{\rm eff} \approx 10^{4.5} - 10^5$ K (Figure 1.3) and the products of the advanced nuclear burnings (e.g., He, C, N, O). These hot and massive exposed cores could be classified as Wolf-Rayet (WR) stars if they are able to show the emission lines of these advanced nuclear burning products in their spectra (Crowther 2007). As we show in Figure 1.3, WRs are more likely to be produced at solar-like metallicity ($Z \approx Z_\odot \approx 0.014$; Caffau et al. 2011) than at lower metallicities. As metallicity decreases, winds are less powerful and stars could retain more mass, thus, forming heavier COs (Figure 1.2).

Given their stripped-star nature, WRs are often used to constrain models of stellar winds at different metallicity, in particular in the sub-solar environments of the Small and Large Magellanic Clouds (SMC and LMC, at $Z_{\rm SMC} \approx 1/5 Z_\odot \approx 0.002$ and $Z_{\rm LMC} \approx 1/3 Z_\odot \approx 0.006$, respectively). For instance, the Costa et al. 2025 stellar models show that matching the properties of the massive ($\lesssim 200$ M$_\odot$) O and B type population in the 30 Doradus region of the Tarantula Nebula (Shenar et al. 2023), inside the LMC, does not guarantee a match also for the WR stars observed in the same region. Most importantly, current models struggle to reproduce the 12 isolated WRs found in the SMC (Schootemeijer et al. 2024) because, at such low metallicities, wind mass losses are expected to be already too inefficient to produce WRs via self-stripping. Therefore, a binary interaction, such as mass transfer, is generally invoked to strip the stellar envelope. However, there is no evidence of a different binary fraction of WRs at different metallicities and the observation of isolated WRs challenges this picture (Shenar et al. 2020). Moreover, Gilkis et al. 2021 point out that stellar models generally struggle to reproduce also the dearth of observed stars with luminosity close to the Eddington limit ($L \approx L_{\rm Edd}$), where radiation pressure becomes comparable to the stellar self-gravity. Sabhahit et al. 2022 argue that the mismatch occurs because optically thick winds should be considered, especially in the evolution of Very Massive Stars (VMSs, $\gtrsim 100$ M$_\odot$) at low-metallicity (e.g., $\lesssim Z_{\rm SMC}$). Recent works in the literature (e.g., Boco et al. 2025; Shepherd et al. 2025) showed that indeed these wind models could better reproduce the observations of VMSs and WRs in the LMC and SMC, also showing that wind mass loss assumptions could have important consequences for the BH mass spectrum.

1.3 Isolated binary evolution

Observations of Main Sequence (MS) stars revealed that most stars are born with one or more companion of a similar spectral type, making single stellar evolution the exception, not the rule (Offner et al. 2023). The multiplicity order and the initial separations are strong functions of the mass of the heaviest star in the system (hereafter, the primary), of the environment density, and of the metallicity. As shown in Figure 1.4, massive O and B type stars have the higher stellar multiplicity and tightest initial separations with respect to the other stellar type. In particular, $\approx 70\%$ of massive O-type stars are born in binaries so close that they are expected to interact at least once in their lifetime (Sana et al. 2012).

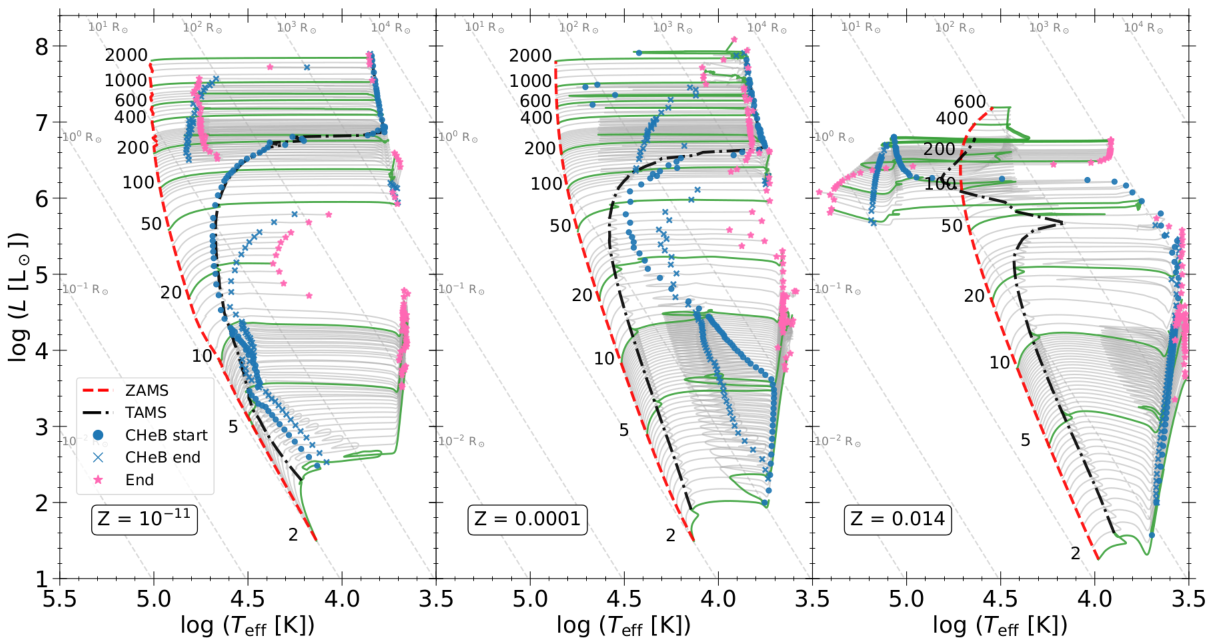

Figure 1.3: Stellar evolution models with initial mass $M_{\rm ZAMS} \geq 2$ M$_\odot$ representative of the evolution of population I stars (right), population II stars (middle), and population III stars (left). The different markers highlight the beginning of the evolution (ZAMS), end of core-hydrogen burning (TAMS), beginning and end of the core-helium burning (CheB), as well as the end of the evolution, when a CCSN occurs. Figure from Costa et al. 2025.

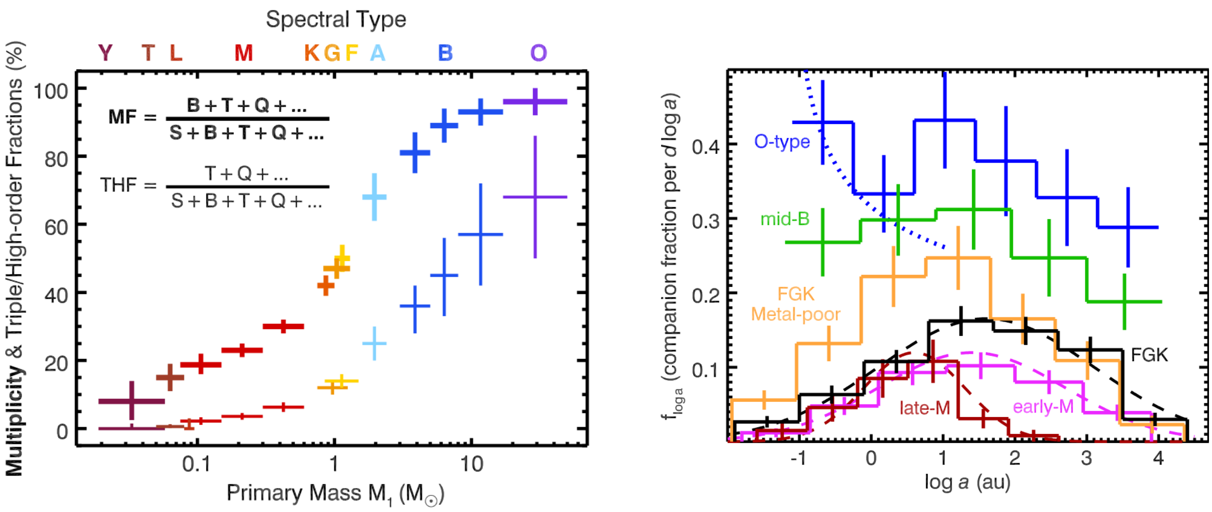

Figure 1.4: Left: Fraction of systems that are member of binary (B), triple (T), quadruple (Q) or higher multiple systems as a function of the heavier star (primary) and spectral type. Right: Distribution of the separation a of the companions in multiple systems as a function of the primary spectral type. Companions of mid-B type stars follow approximately Öpik's law (Öpik 1924), i.e. are uniform in $\log a$; O-type companions are more common in tighter binaries (dotted fit) while later-type companions (FGK, early-M, and late-M) exhibit a lognormal distribution (dashed fits). Figures from Offner et al. 2023.

1.3.1 Mass transfer

Stars can expand up to $\approx 100 - 1000\ R_\odot$ as they evolve. One of the most common causes for stellar expansion is the exhaustion of the central nuclear fuel, that drives a contraction of the core. If the core contracts during a phase of shell-burning, the envelope will rapidly expand on a thermal timescale in order to maintain thermal equilibrium (the so-called *mirror principle*). In particular, massive stars expand during the H-shell burning phase that occurs when they are transitioning from the Hertzsprung Gap (HG) phase to the Red Super Giant (RSG) phase. In this stage, the radiative envelope expands and becomes convective, while the exhausted hydrogen core contracts and heats up until it is able to ignite helium: the RSG phase begins and the expansion stops (Prialnik 2009). Because of stellar expansion, binary systems with orbital separation comparable to the stellar radius will experience a mass transfer event, one of the most important yet still poorly constrained binary processes (see e.g., Tauris et al. 2017 and Marchant & Bodensteiner 2024 and references therein).

Roche lobe overflow

In the co-rotating frame of a binary, it is possible to define the Roche lobe of a star as the potential well where the stellar material can remain bound to the star itself, as shown in Figure 1.5. Following Eggleton 1983, in a circularized and synchronized binary it is possible to define the Roche lobe radius $R_{\rm RL}$ as the radius of a sphere with volume equivalent to the one enclosed by a Roche lobe

$$R_{\rm RL} = \frac{0.49\ q^{2/3}}{0.6\ q^{2/3} + \ln\left(1 + q^{1/3}\right)}\ a, \tag{1.1}$$

where a is the semi-major axis of the system and $q = M_1/M_2$ ($q = M_2/M_1$) is the ratio between the mass of the star belonging to the lobe M_1 (M_2) and its companion M_2 (M_1).

When a star expands, it is possible that it fills its Roche lobe. Following the gravitational potential of the binary, the unbound material will be transferred to the companion through the L1 point: the system has entered a Roche lobe overflow (RLO). The stream of material could form an accretion disk around the companion, possibly heating up to emit in the X-range, thus, revealing the system as an X-ray binary (Tauris & van den Heuvel 2006).

Conservative mass-transfer

Conservative mass-transfer refers to the case where all the unbound material is channelled through L1 and is eventually accreted by the companion. As we show in Figure 1.5, if no mass is lost from the system, the orbital separation will shrink as long as the donor star M_1 is the most massive object in the system, as a consequence of angular momentum conservation. However, as mass transfer proceeds, the accreting star M_2 will become more massive, the mass ratio $q = M_1/M_2$ will reverse and the system will widen (Webbink 1985).

Non-conservative mass transfer

In a RLO, some of the transferred material could be lost in the proximity of the donor or of the accretor, for instance in the form of isotropic fast wind. Moreover, it is possible that some of the mass is lost through the outer Lagrangian point close to the donor star (L3 or

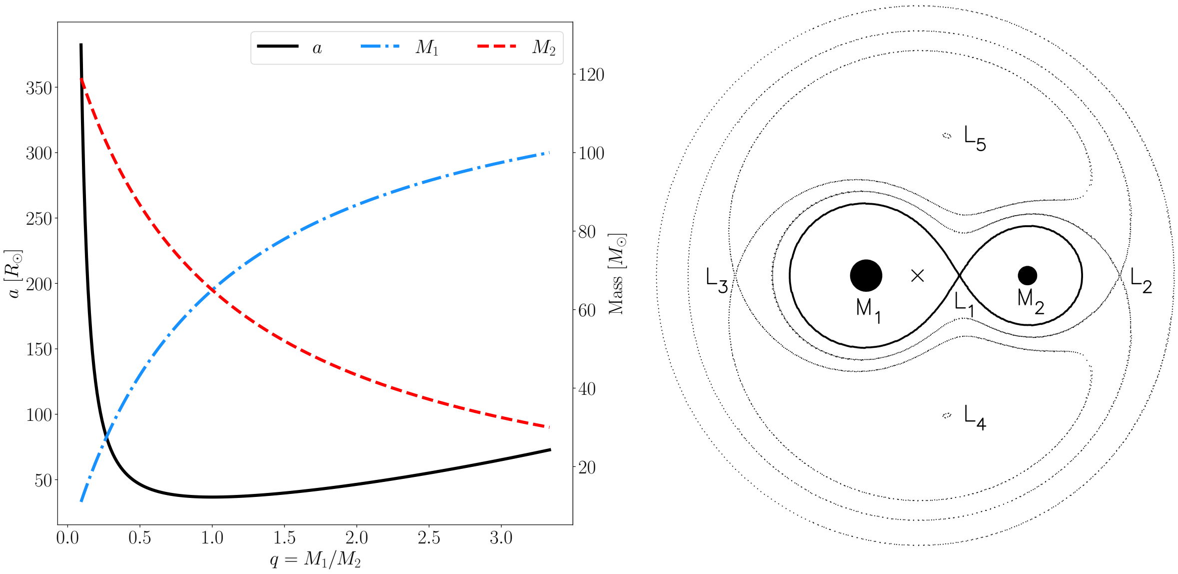

Figure 1.5: *Left:* Conservative mass transfer from M_1 to M_2 first shrinks the semi-major axis of the orbit a and then, when the secondary star becomes more massive than the primary $M_2 \geq M_1$, the orbit widens. *Right:* Orbital plane section of the equipotential curves of the Roche potential in the frame co-rotating with the binary. The Roche lobe is the black thick line containing the Lagrangian point L_1 (Tauris & van den Heuvel 2006).

L2, if the donor is the most or least massive object, respectively) or that it accumulates in a circumbinary disk. In all these cases, the mass transfer will be non-conservative and the lost material will remove a fraction of the orbital angular momentum (Jeans 1924; Ritter 1988; Kolb & Ritter 1990; Soberman et al. 1997; Pols 2008; Marchant et al. 2021). Also in this case the orbit will shrink or widen depending on the accretor-to-donor mass ratio. However, because of non-conservativeness, now the threshold for orbital widening is a function of the amount of mass lost and triggers the widening of the orbit for a wider range of mass ratios $q \gtrsim 0.79 - 1$ (see Figure A1 of van Son et al. 2020 for a detailed illustration of the functional relation). The impact of non-conservative mass transfer on the formation of BCO populations will be investigated and further discussed in Chapter 3.

1.3.2 Stability and efficiency of mass transfer

Stability and efficiency of RLO are still poorly understood and constitute an active field of research because they depend on many factors, such as the presence of a convective or radiative envelope, the size of the core, the mass transfer rate through L1 and the possibility that mass-transfer is non-conservative. All these factors determine the density profile of the star, so the timescale (dynamical, thermal or nuclear) over which it will restore its equilibrium. Furthermore, they will determine the variation of the semi-major axis, so the timescale in which the Roche lobe radius also changes (Soberman et al. 1997).

Stellar radius and Roche lobe radius. A star that loses its external layers needs to re-adjust its dimension in order to return to an equilibrium state. If the new equilibrium is achieved with a stellar radius still larger than the Roche lobe radius, the star will keep losing its outer layers in an unstable runaway that will lead the system to a Common Envelope (CE). In contrast, if the star returns to the equilibrium state inside the Roche lobe, the RLO proceeds in a stable way and the binary experiences a Stable Mass Transfer (SMT). In this case, stellar evolution may stimulate further expansion (for instance, during the HG phase or by igniting the core He-burning: the star can undergo a series of SMTs and transfer a large amount of mass.

As suggested by Webbink 1984, the (in)stability can be studied assuming that the radius is only a function of the mass $R \propto M^{\zeta}$ and, thus, comparing the logarithmic variation of the Roche lobe (ζ_L) with the one induced in the stellar radius over the dynamical[2] ($\zeta_{\rm ad}$) or thermal ($\zeta_{\rm th}$) timescale

$$\zeta_L = \frac{d\ln r_L}{d\ln M} \quad \zeta_{\rm ad} = \left(\frac{d\ln R}{d\ln M}\right)_{\rm ad} \quad \zeta_{\rm th} = \left(\frac{d\ln R}{d\ln M}\right)_{\rm th}. \tag{1.2}$$

The most rapid variation determines the dominant perturbation timescale, thus the reference mass-radius exponent $\zeta_* = \min\{\zeta_{\rm ad}, \zeta_{\rm th}\}$ that, once compared to the Roche lobe variation ζ_L, defines a Roche lobe overflow to be

$$\begin{cases} \text{stable} & \zeta_* \geq \zeta_L \\ \text{unstable} & \zeta_* \leq \zeta_L \end{cases} \tag{1.3}$$

In Equation 1.3, the orientation of inequality signs is a consequence of the negative denominators: the variation of the Roche lobe radius is referred to stars that are *losing* mass ($d\ln M \leq 0$). As a reference, the left-hand panel of Figure 1.6 shows a qualitative comparison between mass transfer episodes that are stable ($\zeta_* \geq \zeta_L$, S point), unstable on a thermal timescale but stable on the dynamical one ($\zeta_{\rm th} \leq \zeta_L \leq \zeta_{\rm ad}$, T point) or unstable on a dynamical timescale ($\zeta_{\rm ad} \leq \zeta_L$, P point).

Stellar envelope, core size, and mass ratio The convective or radiative nature of the envelope strongly affects the re-adjustment in the stellar structure after the removal of an external layer, eventually determining stability and efficiency of the RLO. Radiative envelopes have a steep density gradient that prevents the onset of convection: the pressure exerted by the outer layers is so small that, once they are removed, the star almost does not need to expand to restore the equilibrium. Thus, stars with radiative envelopes have final radii usually lower than the initial ones ($\zeta_{\rm ad} \gg 0$) and will likely undergo stable RLOs. Convective envelopes, on the contrary, have an adiabatic structure that almost restores the initial radius via adiabatic expansion ($\zeta_{\rm ad} \lesssim 0$): similar stars will likely still overfill their Roche lobe after their re-adjustment and will enter unstable RLO (Pols 2011).

Stars that have a convective envelope and a central core or that are fully convective have been historically modelled with *condensed* or *complete* polytropes[3], respectively, because of limited computational power. For instance, Hjellming & Webbink 1987 used polytropic models to study RLO instability on the dynamical timescale, finding that the core, when is present, increases the convective efficiency of the external envelope: stars lose more energy and reduce their radius as shown in the right-hand panel of Figure 1.6,

[2]The subscript "ad" of $\zeta_{\rm ad}$ indicates that dynamical perturbations act so rapidly that can be modelled as adiabatic processes.

[3]Convective envelopes, or full stars for the complete polytrope case, were modelled with a polytropic index $n = 3/2$.

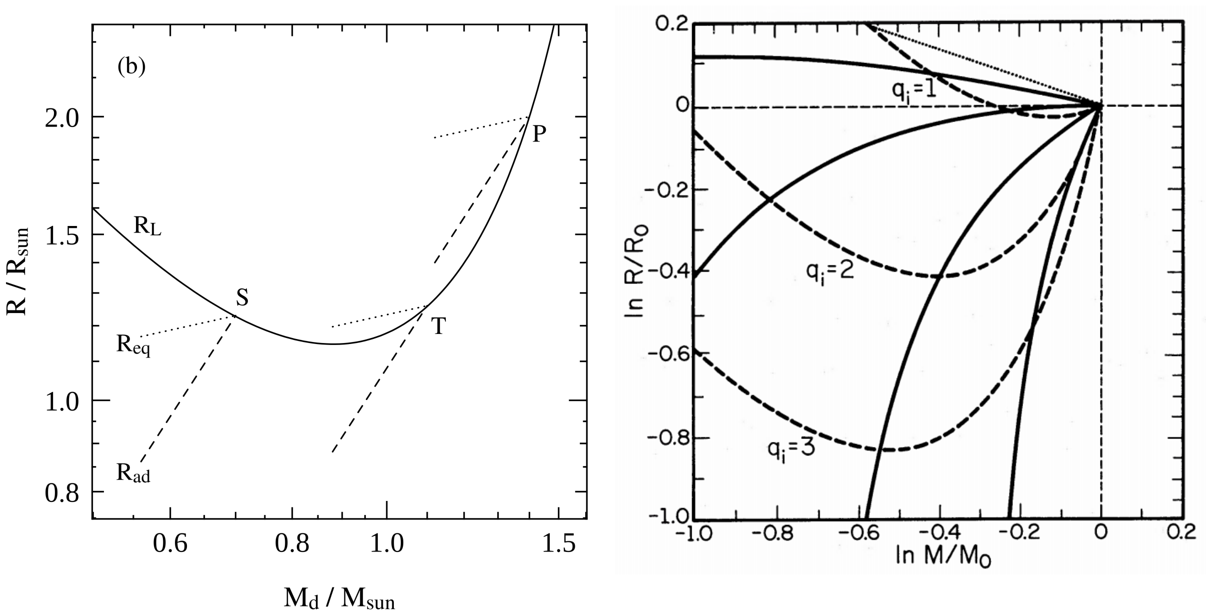

Figure 1.6: *Left:* Examples of the RLO (in)stability scenarios for a 2 $M_\odot$ binary with fixed donor mass-radius exponents ($\zeta_{\rm ad} = 1.5$ and $\zeta_{\rm th} = \zeta_{\rm eq} = 0.25$, illustrated by the dashed and dotted lines, respectively). Different donor masses determine different Roche lobe radii (solid line, Equation 1.1), thus the same adjustment to the mass loss (ζ_*) might determine a RLO stable ($\zeta_* \geq \zeta_L$, S point), stable on the dynamical timescale but unstable on the thermal one ($\zeta_{\rm th} \leq \zeta_L \leq \zeta_{\rm ad}$, T point) or unstable also on the dynamical timescale ($\zeta_{\rm ad} \leq \zeta_L$, point P) (Pols 2011). *Right:* Adiabatic variation of the stellar radius as a function of the mass lost (R_0 and M_0 are the values before mass loss). Solid lines: condensed polytropes with growing core sizes (from top to bottom $q_{\rm core}$=0.10, 0.25, 0.50, 0.75). Dotted line: complete polytrope, models a fully convective star with $n = 3/2$. Dashed lines: Roche lobe radii for different initial mass ratios (from top to bottom $q_i = M_{\rm don}/M_{\rm acc} = 1, 2, 3$). A convective star may avoid a dynamically unstable RLO if it has a prominent core $q_{\rm core} \gg$ or it has a companion with similar mass $q \sim 1$ (Hjellming & Webbink 1987).

likely avoiding an unstable RLO. The more evolved the star is, the more the core becomes important in the structure: it grows in size and mass fraction because of the advanced nuclear burning and of the removal of the external layers (caused by stellar winds and previous mass transfer episodes).

The binary mass ratio q is another factor influencing the RLO stability, since it enters the Roche lobe radius definition of Equation 1.1. As shown in the right-hand panel of Figure 1.6, a donor star M_1 much more massive than the companion M_2 ($q = M_1/M_2 \gg 1$) transfers a lot of mass and causes a rapid expansion of the companion potential well, thus shrinking its own Roche lobe and facilitating the onset of an unstable RLO. In contrast, stars with similar masses have similar Roche lobes with sizes modulated by the semi-major axis: assuming, as a reference, a conservative mass transfer as the one shown in the left-hand panel of Figure 1.5, systems with $q \sim 1$ have negligible changes in the semi-major axis extent

Many works in the literature started from the above considerations to obtain models and thresholds that could numerically determine whether or not a binary system would enter a stable or unstable mass transfer. Similar models often are too much simplified and calibrated on old stellar tracks (or even to polytropes) but provide a fast and easy-to-implement method to calculate the RLO (in)stability in population-synthesis codes. For instance, many codes - including the one adopted in this thesis, `SEVN` (Iorio et al. 2023) - derived part of their mass transfer prescriptions from the formalism suggested by Hurley et al. for the `BSE` code (Hurley et al. 2002). These codes assume a one-to-one correspondence between the burning stage, the radiative/convective nature of the envelope and the core size, starting a RLO unstable on the dynamical timescale when the mass ratio $q = M_{\rm donor}/M_{\rm accretor}$ is larger than a given threshold $q_{\rm crit}$, calibrated with stellar evolution models and function of the core size $q_{\rm core} = M_{\rm core,donor}/M_{\rm donor}$

$$q \geq q_{\rm crit}\left(q_{\rm core}\right) \tag{1.4}$$

However, more recent studies, such as the one of Klencki et al. 2020, used detailed binary simulations with the `MESA` software (Paxton et al. 2015; Paxton et al. 2019) and showed that there is not an unique correlation between the burning stage, the extent of the radiative/convective envelope, the core size and the RLO (in)stability . As shown by the works of Ge et al. 2010, 2015, 2020, 2024, the critical mass ratios $q_{\rm crit}$ have a complex relation with the density profile and the evolutionary stage of the star, that should be accounted for in population-synthesis codes.

Common envelope Stars that enter an unstable RLO, collide[4] or are part of a contact binary[5] will likely share a part or all of their envelopes (if present) and enter in a CE configuration. Friction due to stellar cores orbiting around each other in a medium denser than the interstellar one causes orbital angular momentum and energy losses: the orbit shrinks while the gas heats up and eventually is dispersed. Depending on the initial orbital energy, envelope potential energy and efficiency in the energy and angular momentum transfer, binaries can either spiral-in and merge or be able to eject the common envelope: in the latter case, only the nuclei survive and the orbit tightens.

Common envelope processes shrink efficiently the orbits and are determinant to form tight compact object binaries that can merge via emission of gravitational waves within a Hubble time (e.g., Giacobbo et al. 2018; Belczynski et al. 2020; Broekgaarden et al. 2022; Iorio et al. 2023). However, only systems with the right combination of stellar and orbital properties can survive to CE events. For instance, the orbit must be wide enough not to merge too rapidly and both stars should have a well-developed core: the latter condition prevents the core mass to be transferred into the common envelope and allows the star to survive as a self-gravitating object.

Evolution through a CE phase efficiently removes the hydrogen envelope of one or both stars. Therefore, CE events have been generally considered key-processes to form WR stars (e.g., Belczynski et al. 2010). The role of CE in WR formation will be further discussed in Chapter 2.

$\alpha\lambda$ formalism The most widely adopted description for common envelope processes is the bi-parametric one proposed by Webbink 1984. They assume that orbital energy is the only energy source to power the envelope removal and they model the energetic balance with two adimensional parameters: α and λ.

The α parameter indicates the fraction of orbital energy $E_{\rm orb}$ used to eject the envelope

[4]E.g., the stars overcome the orbital separation at periastron $R_1 + R_2 > (1 - e)\ a$ (Iorio et al. 2023).
[5]E.g., both stars overfill their Roche lobes $R_1 \geq R_{\rm RL,1}$ and $R_2 \geq R_{\rm RL,2}$ (Iorio et al. 2023).

$$\Delta E_{\rm orb} = \alpha\left(E_{\rm orb,\,f} - E_{\rm orb,\,i}\right) = \alpha\frac{G M_{\rm c,1} M_{\rm c,2}}{2}\left(\frac{1}{a_{\rm i}} - \frac{1}{a_{\rm f}}\right), \tag{1.5}$$

where $M_{\rm c,1}$ and $M_{\rm c,2}$ are the two core masses and $a_{\rm i}$ and $a_{\rm f}$ are the initial and final semi-major axis, respectively . Because of friction, the orbit shrinks, thus $\Delta E_{\rm orb} \leq 0$.

The λ parameter is related to the common envelope concentration: small values of λ indicate concentrated envelopes, more difficult to eject. In particular, λ is related to the envelope binding energy of the single stars through dimensional considerations

$$E_{\rm env} = -\frac{G}{\lambda}\left(\frac{m_{\rm env,1} M_1}{R_1} + \frac{m_{\rm env,2} M_2}{R_2}\right) \tag{1.6}$$

where R, M e $m_{\rm env}$ are respectively radius, mass and envelope mass of each star at the onset of common envelope.

Imposing that the orbital energy lost by the system equals the common envelope binding energy ($\Delta E_{\rm orb} = E_{\rm env}$), it is possible to obtain the system final semi-major axis as function of the α and λ parameters

$$\frac{1}{a_{\rm f}} = \frac{1}{\alpha\lambda}\frac{2}{M_{\rm c,1} M_{\rm c,2}}\left(\frac{m_{\rm env,1} M_1}{R_1} + \frac{m_{\rm env,2} M_2}{R_2}\right) + \frac{1}{a_{\rm i}} \tag{1.7}$$

The direct proportionality $a_{\rm f} \propto \alpha\lambda$ indicates that binaries with more chances of survival are the ones that have poorly concentrated envelopes and efficiently converted the orbital energy into heat.

Inconsistencies and improvements. Even though the $\alpha\lambda$ formalism is straightforward to implement and widely adopted in population-synthesis codes, there is general consensus in the literature that it needs to be updated with a more detailed and self-consistent treatment of stellar and binary evolution (e.g., Marchant et al. 2021; Klencki et al. 2021). Many observed systems suggest that likely $\alpha > 1$, meaning that additional forms of energy need to be considered to eject the CE (Klencki et al. 2021). Moreover, current implementations adopt λ values obtained from fits to various stellar evolution models even though a self-consistent calculation should be preferred. In particular, fits to single stellar evolution tracks do not account for changes in the binding energy due to mass transfer events and their result are sensitive to the internal energy sources considered. For instance, Marchant et al. 2021 pointed out that fits from Claeys et al. 2014, widely implemented in population-synthesis codes (including the one adopted in this thesis, `SEVN`), underestimate the binding energy of stars that frequently enter a CE, like HG stars, overestimating the number of systems that survive to it and, eventually, merge as binary black holes. Gallegos-Garcia et al. 2021 further demonstrated that, at least for H-rich donor stars, current prescriptions for entering an unstable RLO and surviving the CE may overestimate the binary black hole merger rates by a factor $\sim 5 - 500$. Gallegos-Garcia et al. 2021 compared population-synthesis and detailed simulations, finding that the population-synthesis approach favours the CE channel over the SMT one in the evolution of many systems, as shown in Figure 1.7.

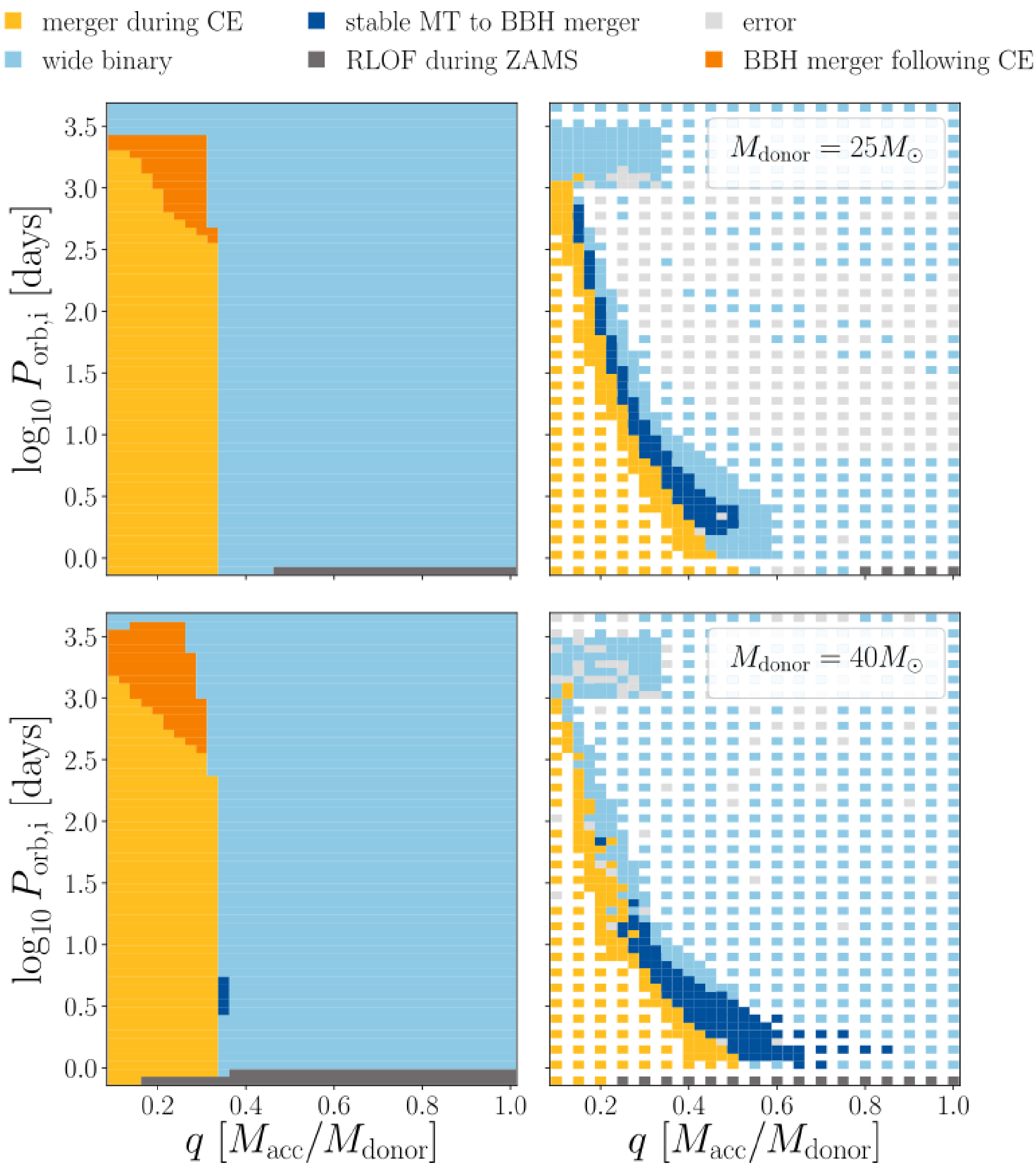

Figure 1.7: Comparison of final outcomes for the same initial binary population evolved with the `COSMIC` population-synthesis code (Breivik et al. 2020) (left) and with the `MESA` stellar evolution code, which also implements modules for binary evolution (Paxton et al. 2019) (right). Each row shows the initial period as a function of the initial mass ratio for H-rich donors of $M = 25$ M$_\odot$ (top) and $M = 40$ M$_\odot$ (bottom) at sub-solar metallicity $Z = 0.00142$. On-the-fly stellar and binary evolution carried out in `MESA` suggests that only a restricted parameter space region successfully forms merging binary black holes (BBHs), in contrast with results from population-synthesis codes. `MESA` BBHs formed mainly through SMT, whereas CE evolution dominated for `COSMIC` BBHs. Figure from Gallegos-Garcia et al. 2021.

1.3.3 Supernova kicks

After a supernova event, the resulting CO receives a natal kick formed by the combination of a Blaauw kick and a supernova kick. The first one, proposed by Blaauw in 1961 Blaauw (1961), is a $\lesssim 50$ km/s kick acting on the binary centre of mass and is caused by asymmetries in the mass lost by the system as a whole. Instead, the supernova kick is the one received directly by COs formed after successful supernova explosions and, similarly, is caused by asymmetries in the (baryonic or neutrino) mass ejection (Mandel 2016). Natal kicks could be so strong to unbind the CO from a binary. Therefore, modelling them is crucial when considering the evolution of stars and COs in binary systems. Many efforts have been put in deriving a representative distribution of compact object natal kicks from observations, but still none of the proposed models seems to offer a complete picture.

Pulsar natal kicks

Hobbs et al. 2005 measured the proper motions of 233 Galactic pulsars and then derived the velocity distribution of the 46 youngest pulsars (characteristic age < 3 Myr), assuming that it would have been representative of the pulsar birth velocities. Hobbs et al. 2005 found that the natal kick distribution of young pulsars could be modelled with a one-dimensional Maxwellian with mean at $\mu \approx 400$ km s^{-1} and root-mean-square of $\sigma = 265$ km/s. In contrast, Verbunt et al. 2017 found that pulsar velocities are best described by a bimodal Maxwellian distribution with peaks at 120 and 540 km/s. Verbunt et al. 2017 highlight that their finding does not necessary imply that pulsar velocities are indeed bimodal, but they indicate that a distribution wider than a single Maxwellian is necessary to explain their data. A bimodal distribution was indicated also by Igoshev 2020, with both Verbunt et al. 2017 and Igoshev 2020 generally favouring lower natal kick velocities with respect to the ones found in Hobbs et al. 2005. Initially, the difference between the results of Hobbs et al. 2005 and the ones of Verbunt et al. 2017 and Igoshev 2020 where attributed to a systematic effect due to the different methodology used to estimate the distance estimates of the pulsars (dispersion measure[6] and parallax, respectively). However, Disberg & Mandel 2025 found that the difference in the distributions was not due to a systematic effect in the distance measurement, but it was determined by an erroneous fit of the experimental data in Hobbs et al. 2005. Disberg & Mandel 2025 noted that Hobbs et al. 2005 likely fitted a velocity distribution $p(v)$ on logarithmically binned data, providing instead a description for the $p(log\ v)$ distribution. Disberg & Mandel 2025 included a Jacobian transformation to account for the logarithmic bin size of the same empirical transverse velocities and found that the inferred three-dimensional pulsar velocities were lower than the ones originally inferred in Hobbs et al. 2005 (Figure 2 in Disberg & Mandel 2025). Accounting for this transformation, the distribution of natal kick velocities of young pulsars ($\lesssim 10$ Myr) is lognormal and is characterized by mean $\mu = 5.60 \pm 0.12$, standard deviation $\sigma = 0.68 \pm 0.10$, and a single peak at $\sim 150 - 200$ km s^{-1}. Therefore, the median pulsar velocity estimated by Disberg & Mandel 2025 is $\approx 50\%$ lower than the one obtained by Hobbs et al. 2005. Disberg & Mandel 2025 also argue that the bimodality found by Verbunt et al. 2017 and Igoshev 2020 is not statistically significant, offering an explanation to re-coincile their results with the ones of Hobbs et al. 2005.

[6]The dispersion measure is the total column density of electrons along the line of sight $\mathrm{DM} = \int_0^D n_e(s)\, ds$ and is a standard technique to recovery the distance D of a radio pulsar from models of the electron density distribution $n_e(s)$ of free electrons in the interstellar medium.

BH natal kicks

Atri et al. 2019 studied proper motions of 16 BHs in X-ray binaries, finding that their velocity distribution is described with a Gaussian curve with mean at 107 km/s: a probability distribution function (PDF) very similar to the low-velocity peak indicated by Verbunt et al. 2017. Even if the Atri et al. 2019 study could be affected by the limited sample and the bias of considering objects that remained bound in binaries (thus, that are expected to have by default low or moderate natal kicks, in order not to unbind the system), it is reasonable to expect BHs with lower natal kicks than NSs: from a theoretical point of view, BHs are more massive and could form accreting the mass falling back in a supernova event (Fryer et al. 2012). All these factors impact the magnitude of the recoil kicks but their modelization is still debated. Therefore, parameters describing natal kick distributions of BCOs constitute some of the free parameters that it is necessary to consider in binary evolution models and in population-synthesis study (e.g., Giacobbo & Mapelli 2020).

1.4 BCOs from isolated binaries

Producing BCOs in the isolated binary evolution requires many steps, and it is not trivial that they all lead toward a successful BCO formation, as we illustrate in Figure 1.8.

1.4.1 A matter of separation

The time $t_{\rm GW}$ required to merge via GW emission is heavily dependent on the final orbital properties, in particular on the orbital separation:

$$t_{\rm GW} = \frac{5}{256}\frac{c^5}{G^3}\frac{a_{\rm orb}^4}{M_1 M_2 (M_1 + M_2)}(1 - e^2)^{3.5} \tag{1.8}$$

where c is the speed of light, G the gravitational constant, $a_{\rm orb}$ the semi-major axis, e the eccentricity, M_1 and M_2 the masses of the two objects (Peters 1964; Iorio et al. 2023).

Equation 1.8 indicates that COs of few solar masses should be distant few solar radii in order to merge via GW emission. In the previous Sections we showed that massive stars can expand up to $\approx 100 - 1000\ R_\odot$ as they evolve (Figure 1.3). Therefore, if BCO progenitors evolved in orbits so tight since the beginning, the expansion of the most massive star would determine a collision and a premature coalesce, leaving a single merger product behind. Merging binaries have been proposed to explain the existence of Blue Stragglers (Sills et al. 2002) and some supernova progenitors, such as the one of the SN 1987A (Podsiadlowski et al. 1990). However, merger products would be able to produce BCOs only if they were in a dynamically active environment or in triples, i.e. in circumstances where they could encounter another CO and merge via GW emission (Di Carlo et al. 2019; Renzo et al. 2020a; Costa et al. 2022; Ballone et al. 2023). In contrast, if the initial orbital separation is too large, the two stars will evolve as if they were in isolation. In this case, the resulting CO-CO binary will also be wide and probably will not be able to merge within < 14 Gyrs.

1.4.2 The importance of interactions

BCO formation requires a final CO-CO binary tight enough to merge within a Hubble time (Equation 1.8), but a progenitor binary wide enough to allow the expansion of the stars without premature coalescences (Figure 1.3). For this reason, BCO formation requires the intervention of mechanisms that can shrink the orbital separation up to one order of magnitude during the lifetime of the binary. These mechanisms are generally mass transfer processes, tidal interactions, and supernovae natal kicks (e.g., see Mandel & Farmer 2022, Costa et al. 2024, Marchant & Bodensteiner 2024, and references therein).

Mass transfer to shrink the orbit

As discussed in the previous sections, mass transfer processes could remain stable (SMT) or become unstable (CE) as the evolution proceeds. If the interaction remains stable, the orbital separation reduces (widens) as long as the donor star remains more (less) massive than the accretor. In a newborn binary, the most massive star of the pair will be the first one to evolve, expand and transfer mass to the companion, so, at least at the beginning, the binary starts to shrink. Depending on the initial orbital separation, mass of the donor star and mass ratio of the system, mass transfer could proceed in a stable manner or it could become unstable. For instance, if the donor star is much more massive than the companion, the donor-to-accretor mass ratio can overcome the critical threshold (Equation 1.4) to begin a CE. This possibility is even more likely if the donor star develops a convective envelope, either soon after the RLO beginning or after a while, especially if the orbit is so tight to that the star can overfill its Roche lobe for longer. If the RLO turns into a CE, the orbital separation can reduce even by one order of magnitude and the donor star loses completely its outer envelope, becoming a pure-Helium star (e.g., see Belczynski et al. 2012,Tauris et al. 2017, and references therein).

Excessive orbital reduction and Darwin instability

It is possible that mass transfer evolution does not leave a surviving system. The expulsion of the CE could consume too much orbital energy (Equation 1.7), the mass removed from the system in SMT could carry away too much orbital angular momentum (Soberman et al. 1997; Pols 2008; Willcox et al. 2023; Olejak et al. 2024; Klencki et al. 2025), or the stars could be too close and collide (Hurley et al. 2002). Moreover, as the orbit tightens, tidal forces increase and begin to transfer angular momentum between the orbit and the stars (Zahn 1977; Hut 1981). In particular, tides generally lead to orbital synchronization, but this is not always possible. For instance, if the star is spinning too slowly with respect to the orbit, the angular momentum transferred from the orbit to the star could be insufficient to spin-up the star at a rate larger than the rate with which the orbital angular velocity increases (as a consequence of the removal of orbital angular momentum, the orbit shrinks and spins up). In this case, tides drive a runaway orbital reduction, eventually leading to a premature coalescence: it is the so-called “Darwin instability” (Darwin 1880).

Natal kicks and supernovae

CCSN events could be successful explosions or failed SNe, but in all the cases they remove some of the progenitor mass (e.g., ejecting some of the outer layers or losing only neutrinos, see Fryer et al. 2012 and references therein). Due to the conservation of the stellar momentum, newborn COs will receive a recoil kick. For the conservation of the system (binary + stars) angular momentum, the kick imparted by CCSNe will modify the orbital separation. The orientation of the kick, its strength, and the location of the CCSN event (e.g., close to the periastron or apoastron) will determine the post-CCSN separation and will possibly increase the orbital eccentricity (Hurley et al. 2002). Therefore, supernova kicks act as a "random variable" in BCO formation: they can help the GW merger of a wide binary but they can also widen or even break a tight binary. Natal kicks are particularly important in the formation of BCOs that contain light COs, as for them the natal kick velocity is higher and the effects on the orbits are more significant (Giacobbo & Mapelli 2020).

A possible evolutionary pathway

In Figure 1.8 we show a possible sequence of steps that can lead to the formation of a BCO in the isolated binary evolution scenario. At the beginning, the most massive star in the binary expands and overfills it Roche lobe. The RLO could be stable or unstable, but it is nevertheless important that some mass transfer interaction occurs to begin the reduction of the orbital separation. Mass transfer strips the outer layers of the donor star (on longer or shorter timescales, depending on the SMT or CE evolution, respectively), possibly leaving a bare helium-core as progenitor of the first CO. Assuming that the first CO formation did not break or significantly widen the binary, the companion can then start a second mass transfer event when it will expand. Similar to the first RLO, also this mass transfer could be stable or unstable, possibly leading to a premature coalescence in the place of a BCO. Also in this second RLO, the donor star could be stripped of its envelope and become a pure-Helium star, before turning into a CO. If also the second CO formation does not break or significantly widen the binary, a bound system with two COs will be formed, and it will be tight enough to merge via GW emission within < 14 Gyrs.

We reported a simplified picture to highlight the key evolutionary passages that are needed (or that could prevent) the formation of a BCO. We underline that the detailed evolutionary pathways (e.g., number and type of mass transfer events, outcome configurations) heavily depend on the physical assumptions (e.g., metallicity, CE efficiency, natal kicks) as well as on the type of BCOs. For instance, the formation of BNSs is favoured by CE evolution and is sensitive to natal kick assumptions (e.g., Tauris et al. 2017; Chruslinska et al. 2018; Sgalletta et al. 2023), whereas the formation of BBHs is favoured by SMT, especially at low metallicity (e.g., Broekgaarden et al. 2022; Iorio et al. 2023; Sgalletta et al. 2025)

1.4.3 Other formation channels

In the following paragraphs, we provide a brief overview of some of the many alternative formation scenarios for BCOs. We refer to the reviews of Mandel & Farmer 2022; Costa et al. 2024; Marchant & Bodensteiner 2024 and references therein for a more detailed description.

Chemically homogenous evolution

In massive, metal-poor stars, rapid rotation can drive strong internal mixing, making the star partially or even fully mixed before hydrogen exhaustion (Eddington 1925). Rotational mixing transports to the surface the elements produced in the core, while simultaneously feeding the core with fresh hydrogen from the envelope, beyond the region reached by convection. As a result, the chemical gradient between core and envelope is smooth and

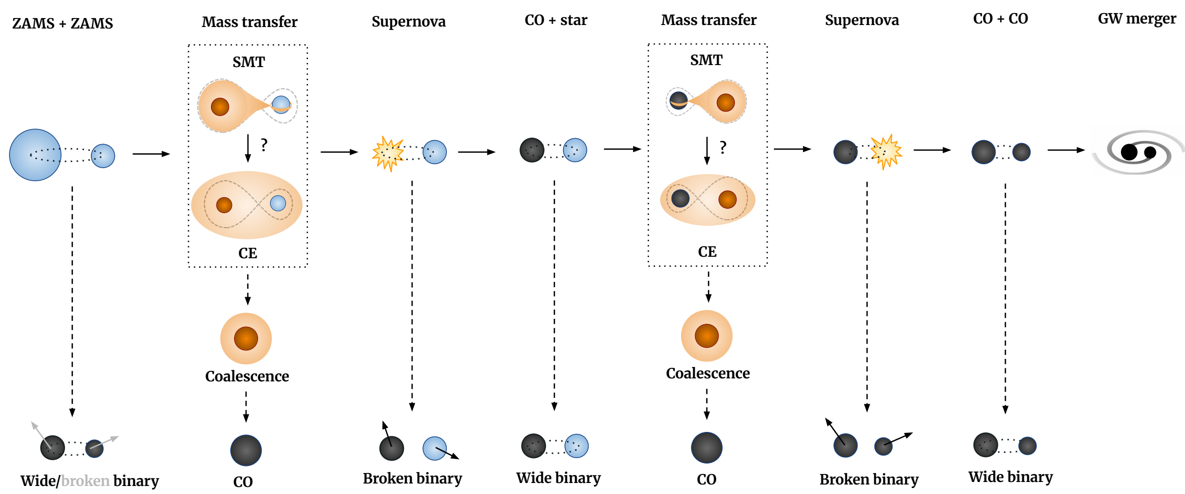

Figure 1.8: Schematic illustration of the evolutionary steps required to form a BCO in the isolated evolution scenario. Dashed arrows highlight possible alternative fates of the binaries that reached a certain evolutionary configuration, highlighting the necessity of a fine-tuned evolution to achieve the production of a GW merger. Figure inspired by Tauris et al. 2017.

the star experiences a chemically homogeneous evolution (CHE). (Maeder 1987; de Mink et al. 2009).

Stars that evolve as chemically homogeneous are more compact and expand less with respect to "standard" stars that develop a steep core-envelope separation during their lifes. As a consequence, mass transfer interactions in CHE are rare and the two stars will evolve almost in isolation. The two COs will likely have similar masses and be highly spinning, especially if the CHE is triggered by tidal interactions (e.g., de Mink & Mandel 2016; Mandel & de Mink 2016; Riley et al. 2021; Dall'Amico et al. 2025).

Dynamical channels and hierarchical mergers

As we already showed in Figure 1.4, massive stars can be born also in triple or higher multiple systems (Offner et al. 2023). This could occur not only in the field, but also in denser environments, such as open cluster, globular clusters, and young massive clusters (e.g., Rodriguez et al. 2016, 2019; Rastello et al. 2020, 2021; Antonini & Gieles 2020; Banerjee 2021; Di Carlo et al. 2021; Arca Sedda et al. 2024). In all of these cases, the evolution in a dynamically active environment will likely trigger exchanges and hierarchical mergers, eventually forming more asymmetric final masses ($q << 1$) (e.g., Rastello et al. 2021), favouring an isotropic spin orientation (e.g., Rodriguez et al. 2016) and possibly eccentric mergers (e.g., Samsing 2018). These signatures in the final BCO orbital properties could be found also in BBHs that form via hierarchical mergers in the disks of AGNs, even though the friction with the gas in the AGN disk will likely eventually re-align the spins(e.g., Samsing et al. 2022; Vaccaro et al. 2024; Delfavero et al. 2025). Eventually, dynamical captures and hierarchical mergers favour the production of BHs heavier than the ones produced by the collapse of single stars, allowing to fill the putative PI mass gap in the BH mass spectrum (e.g., Di Carlo et al. 2019) (also see Figure 1.1).

1.5 BCOs from gravitational waves

1.5.1 GWTC-4.0

With the release of fourth Gravitational-Wave Transient Catalog GWTC-4.0 (The LIGO Scientific Collaboration et al. 2025b), the sample of BCOs candidates detected by the LIGO-Virgo-Kagra (LVK) Collaboration increased to about $\approx 150-200$ systems: there are 218 astrophysical detections ($p_{\rm astro} \geq 0.5$) and 161 of them can be considered sufficiently significant for population studies ($p_{\rm astro} \geq 0.5$ and False Alarm Rate < 1 yr^{-1}).

The number of detected systems nearly doubled from the previous catalogue release GWTC-3 (Abbott et al. 2023a), also thanks to the improved sensitivity of the detectors. The noise levels of the LVK detectors[7] was reduced (Figure 1.9) and at the end of the last observing run included in GWTC-4.0 (O4a) it was possible to probe ≈ 8 times the volume of the Universe available in the first observing run (O1) (Figure 1.10), now extending also beyond redhsift $z \approx 1$ (The LIGO Scientific Collaboration et al. 2025a). In this wider volume, the last O4a run alone detected about the same number of GW events of the previous three (O1, O2, O3) combined. Moreover, O4a was able to achieve this result only observing for about $\approx 1/3$ of their cumulative observing time (Figure 1.10).

At the end of the O4a observing run (January 2024), the bulk of the observed BCOs is composed of merging binary black holes (BBHs), with 153 candidate BBHs out of 161 BCO candidates. The other candidates are 5 black hole - neutron star mergers (BHNS), 1 event that is either a BHNS or a BBH, and 2 binary neutrons star mergers (BNSs) (The LIGO Scientific Collaboration et al. 2025b). Given the much larger statistics of BBHs, in the following sections we will focus on the properties of the detected BBH population. We expect that the number of detected BCOs, thus also of BNSs and BHNSs, will further improve by orders of magnitudes with the forthcoming observing runs (O4b, O4c, O5), the sensitivity improvements in Advanced LIGO/Virgo and the construction next generation detectors, such as Cosmic Explorer and Einstein Telescope, as shown in Figure 1.11 (e.g., Broekgaarden et al. 2024; Abac et al. 2025).

1.5.2 Detectable properties

A BBH undergoing a quasi-circular inspiral is characterized by fifteen parameters[8]: eight intrinsic (the mass M_i and the three-dimensional components of the spin vectors $\vec{S}_i$ for each i-th black hole) and seven extrinsic, for the sky location and orbit orientation (right ascension α, declination δ, luminosity distance d_L, orbital inclination ι, polarization angle Φ, time of coalescence t_c and phase at the coalescence ϕ_c) (Abbott et al. 2019; The LIGO Scientific Collaboration et al. 2025d).

Individual masses

The observation of a GW signal allows to measure directly many binary parameters, but not the individual masses M_1 and M_2 of the coalescing objects. The quantities directly

[7] We refer only to LIGO-Virgo, as Kagra did not yet contribute and GEO is mainly used to constrain post-merger signals.

[8] The 16^{th} parameter, eccentricity, is currently neglected in the LVC analysis for computational reasons.

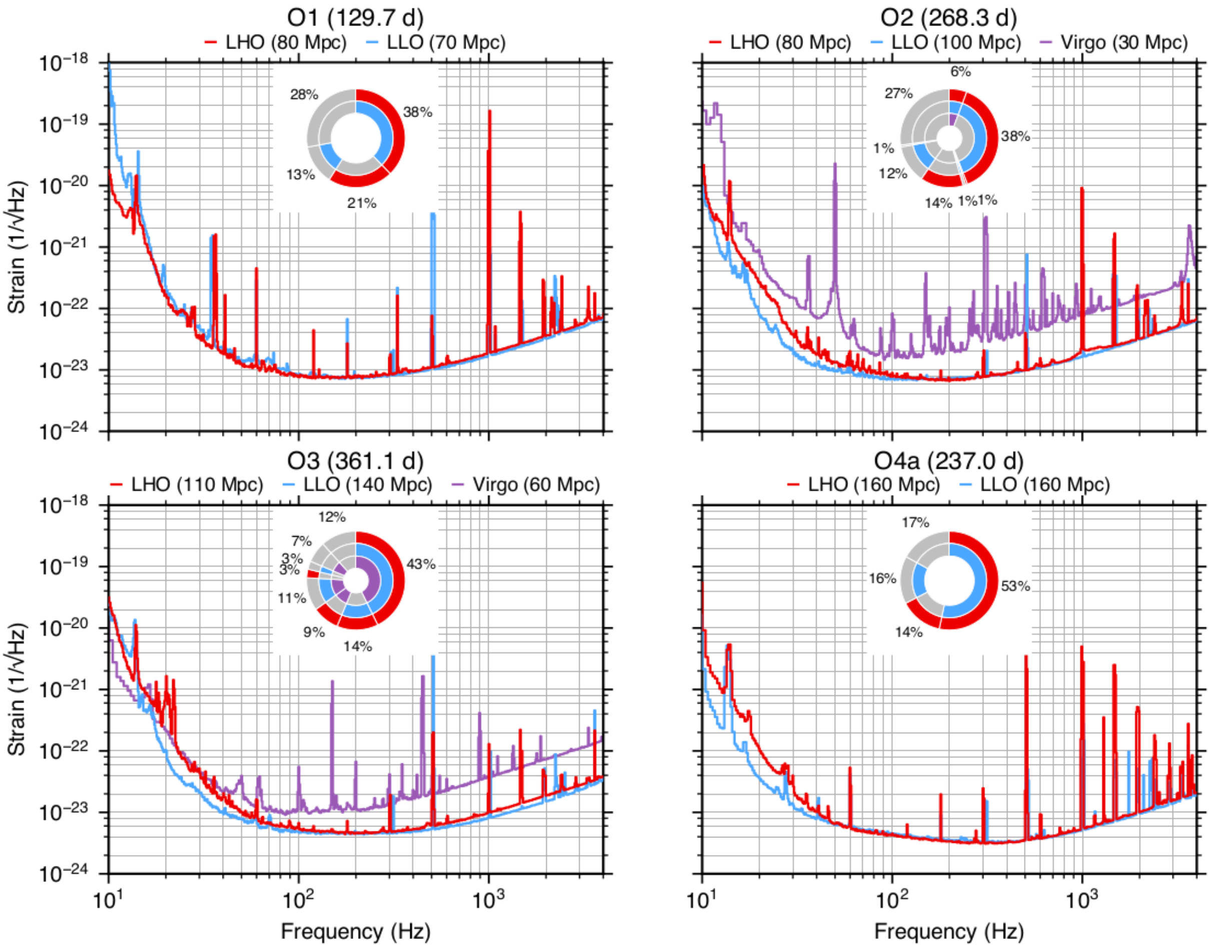

Figure 1.9: Noise amplitude spectral densities for LIGO Hanford Observatory (LHO), LIGO Livingston Observatory (LLO), and Virgo in the first four observing runs (O1, O2, O3, and O4a). For each run, the legend shows the fraction of time where each detector was operative and the estimated maximum distance for the detection of a quasi-circular BNS inspiral (component masses of 1.4 $M_\odot$; SNR $= 8$). Figure from The LIGO Scientific Collaboration et al. 2025d.

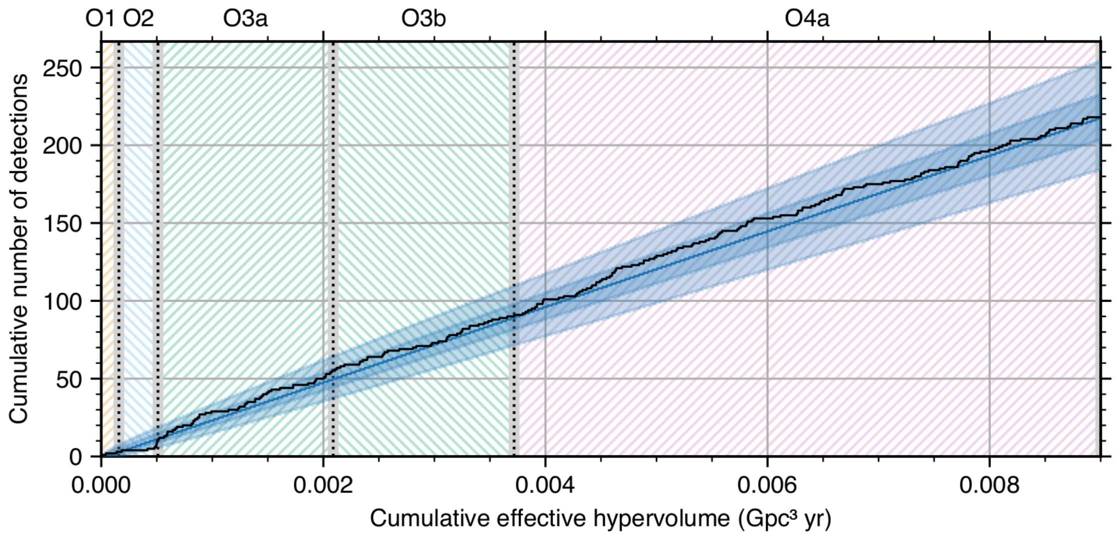

Figure 1.10: Number of BCO detectable candidates ($p_{\rm astro} \geq 0.5$) as a function of the detector network's effective surveyed hypervolume for BNSs, used as a proxy for the BCO sensitivity across the Universe. Coloured bands indicate different observing runs (O1, O2, O3a, O3b, and O4a). The cumulative number of probable candidates is indicated by the solid black line, while the blue line, dark blue band, and light blue band are, respectively, median, 50%, and 90% confidence intervals for a Poisson distribution fit to the number of candidates at the end of O4a. Figure from The LIGO Scientific Collaboration et al. 2025d.

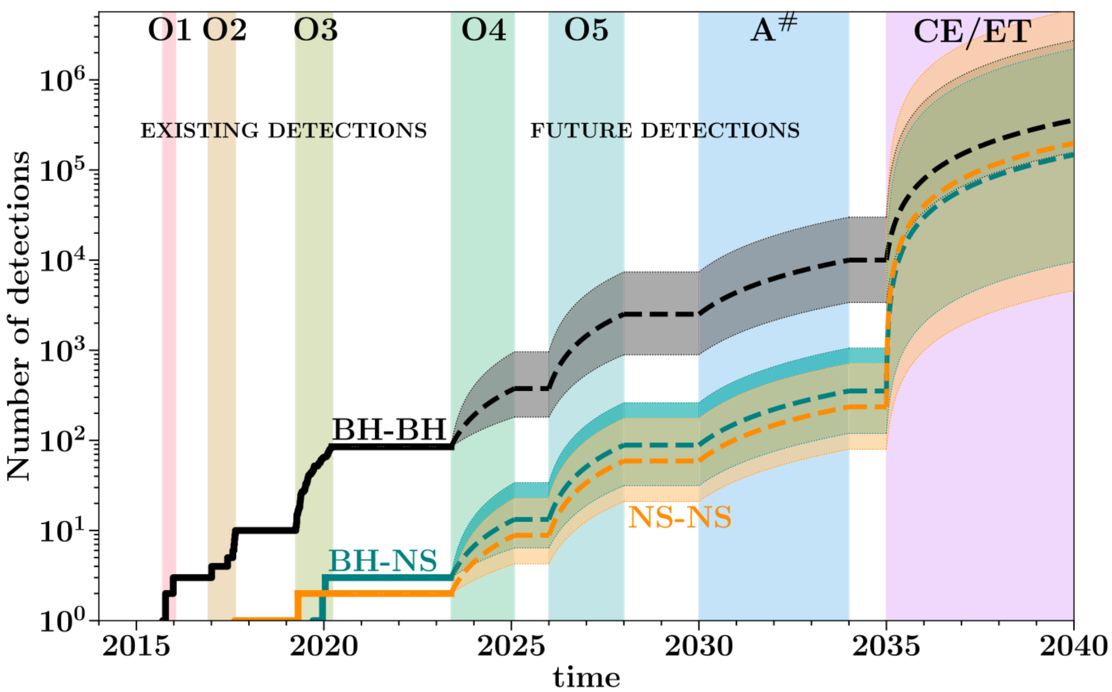

Figure 1.11: Current and future number of BCOs detected via GW emission with the current (O1,02,03,04) and future (O5) observing runs, as well as future observatories: the improved LIGO/Virgo detectors (A#), Cosmic Explorer (CE) and Einstein Telescope (ET). Figure from Broekgaarden et al. 2024

derived from the GW data are the combinations of the individual masses, namely the *total mass* of the binary $M_{\rm bin} = M_1 + M_2$ and the *chirp mass* $\mathcal{M}$, defined as

$$\mathcal{M} = \frac{(M_1\, M_2)^{3/5}}{(M_1 + M_2)^{1/5}} \tag{1.9}$$

Intuitively, chirp mass and total mass are related to the up-ward frequency variation of the signal (the "chirp") and the maximum frequency $\nu_{\rm GW,max}$ reached before the ringdown (Maggiore 2007; Spurio 2019). Assuming a circular orbit, we could describe these quantities as functions of the GW frequency $\nu_{\rm GW}$ and frequency derivative $\dot{\nu}_{\rm GW}$, as follows:

$$\mathcal{M} \approx \frac{c^3}{G} \left(\frac{5}{96}\, \pi^{-8/3}\, \nu_{\rm GW}^{-11/3}\, \dot{\nu}_{\rm GW} \right)^{3/5} \tag{1.10}$$

$$M_{\rm bin} = \frac{1}{\pi\sqrt{8}} \frac{c^3}{G\, \nu_{\rm GW,max}} \tag{1.11}$$

Spins

The three spin vectors are the most difficult parameters to infer from GW detections, because they imprint a second-order effect in the waveform and require advanced numerical relativity calculations to be correctly modelled. In place of the six spin vectors, the pipeline analysis fits six effective spin parameters that are slightly easier to obtain from the observations: the two dimensionless spin magnitudes $\chi_{\rm i}$, the two polar tilt angles $\theta_{\rm i}$, the effective spin $\chi_{\rm eff}$ and the effective precessing spin $\chi_{\rm p}$. All the values are calculated at the reference frequency of 20 Hz (Abbott et al. 2019; Abbott et al. 2023b; The LIGO Scientific Collaboration et al. 2025d).

The *dimensionless spin* $\chi_{\rm i}$ quantifies the amplitude of the spin by measuring how much the black hole is close to being a Schwarzschild, non-rotating black hole ($\chi_{\rm i} = 0$) or to a maximally-spinning Kerr black hole ($\chi_{\rm i} = 1$)

$$\chi_{\rm i} = \frac{|\vec{S}_{\rm i}|c}{GM_{\rm i}} \quad \in [0,1] \qquad\qquad i = 1, 2, \tag{1.12}$$

where $\vec{S}_{\rm i}$ is the spin vector, G the gravity constant, and c the speed of light.

The two polar angles $\theta_{\rm i}$ measure the inclination of each black hole spin with respect to the orbital angular momentum $\hat{L}_{\rm N}$ and enter in the definition of both the effective spin $\chi_{\rm eff}$ and the effective precessing spin $\chi_{\rm p}$. The *effective spin* $\chi_{\rm eff}$ measures the mass-weighted components of black hole spins that are aligned with the Newtonian orbital angular momentum $\hat{L}_{\rm N}$ (normal to the orbital plane)

$$\chi_{\rm eff} = \frac{M_1\chi_1 \cos\theta_1 + M_2\chi_2 \cos\theta_2}{M_1 + M_2}. \tag{1.13}$$

The *effective precessing spin*, which measures the dominant spin projected on the orbital plane, that eventually causes the relativistic precession of the orbital plane itself

$$\chi_{\rm p} = \max\left\{ \chi_1 \sin\theta_1,\ \left(\frac{3+4q}{4+3q}\right) q\chi_2 \sin\theta_2 \right\}, \tag{1.14}$$

where $q = M_2/M_1$ is the binary mass ratio Abbott et al. (2023b); The LIGO Scientific Collaboration et al. (2025d).

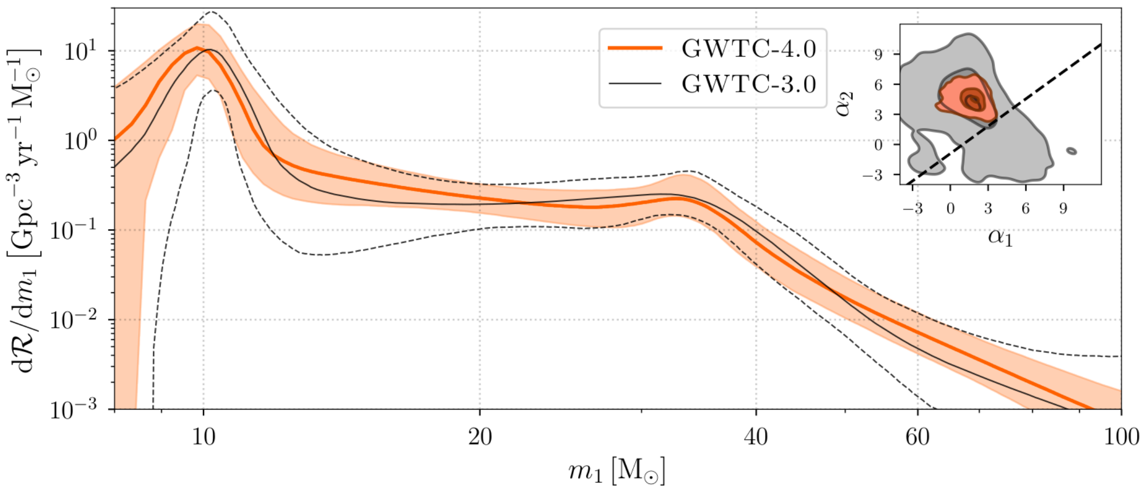

Figure 1.12: Differential merger rate as a function of the primary BH mass (evaluated at redshift $z = 0.2$). The orange shaded region shows the 90% credible interval for GWTC-4.0 and the solid orange curve shows the posterior median; black dashed curves delimit the 90% credible region for GWTC-3.0 and the solid black curve shows the posterior median. The inset shows the joint posterior of the broken power law index parameters for GWTC-3.0 (gray) and GWTC-4.0 (orange), with the contours showing the 5 th, 50 th, and 95 th percentiles. Figure from The LIGO Scientific Collaboration et al. 2025a.

1.5.3 BBH population properties from GWTC-4.0

Mass spectrum

Accounting for observational biases, detector sensitivity functions, as well as the intrinsic correlation between the individual masses (M_1 and M_2) and their observed combinations ($\mathcal{M}$ and $M_{\rm bin}$), it is possible to infer the distribution of the primary ($M_1 < M_2$) and secondary (M_2) BH masses, respectively the more massive and least massive BHs in each BBH. Since BBHs merge across cosmic time, the distributions of their properties are inferred as differential merger rates i.e. as the number of merging systems per unit of co-moving quadri-dimensional volume, evaluated at a fixed redshift (Abbott et al. 2023b; The LIGO Scientific Collaboration et al. 2025a).

Figure 1.12 shows the differential merger rate of primary BH masses inferred with data from GWTC-4.0 (The LIGO Scientific Collaboration et al. 2025a). The distribution exhibits two peaks at $\approx 10\ \mathrm{M}_\odot$ and $\approx 35\ \mathrm{M}_\odot$, as already found in GWTC-3 data. The continuum is well-described by a broken-power law that is flatter ($\alpha_1 \approx 1.7$) between $\approx 15 - 35\ \mathrm{M}_\odot$ and steeper ($\alpha_2 \approx 4.5$) beyond $\approx 35\ \mathrm{M}_\odot$. There is also a mild support for a bump at $\approx 20\ \mathrm{M}_\odot$, but more data is required to support it.

Mass ratio

Figure 1.13 shows the secondary-to-primary BH mass ratios as inferred from GWTC-4.0 data (The LIGO Scientific Collaboration et al. 2025a). The new data confirm the findings of GWTC-3, indicating that there is a preference for equal mass systems $q \approx 1$. Inference models that account for possible correlations in the source parameters suggest that the bulk of primary BHs produced at $M_1 \approx 10\ \mathrm{M}_\odot$ (Figure 1.12) could be responsible for a peak at $q \approx 0.74$ in the mass ratio distribution (blue model in Figure 1.13) and suggest

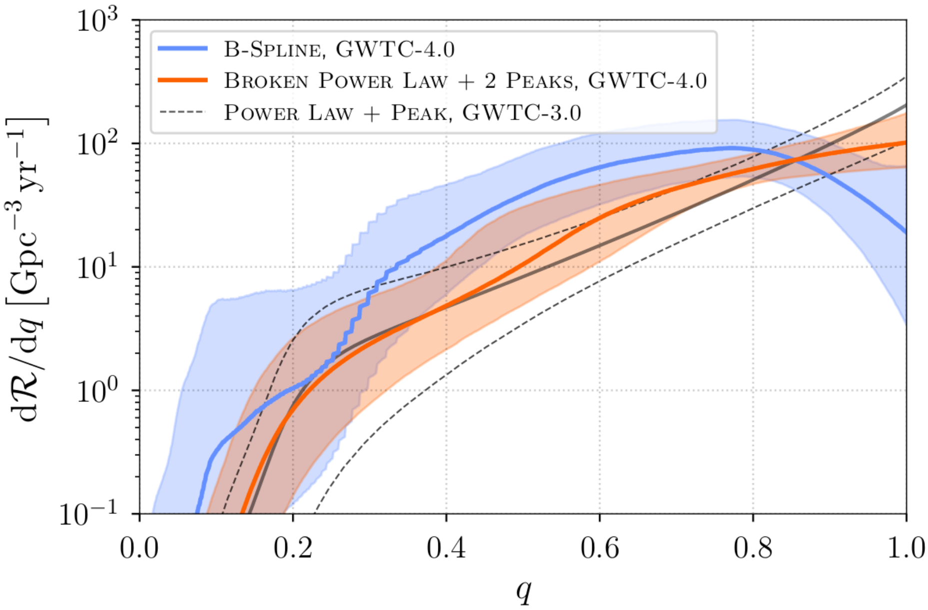

Figure 1.13: Differential merger rate as a function of the secondary-to-primary mass ratio $q = M_2/M_1$, evaluated at redshift $z = 2$. The q distribution favours BHs with similar masses $q \approx 1$ and could peak at ≈ 0.74 (be a simple power law) if correlations between the source parameters are (not) taken into account, as shown in blue (orange). For each model, median and 90% credible intervals are reported. Dashed lines show the distribution inferred from GWTC-3. Figure from (The LIGO Scientific Collaboration et al. 2025a).

that the BH primaries at $M_1 \approx 35\ \mathrm{M}_\odot$ exhibit a stronger preference for similar masses than the rest of the population. However, not accounting for the possible correlations in the source parameters allows to describe the mass ratio distribution with a simple power law of index $\beta \approx 1.2$ (orange model in Figure 1.13).

Spins

Figure 1.14 and Figure 1.15 show the inferred distributions of spin magnitudes and tilt angles for BBHs detected until the end of the O4a observing run (The LIGO Scientific Collaboration et al. 2025b). The detected BBHs exhibit a preference for low-spinning black holes $\chi \lesssim 0.3$ aligned with the orbit ($\cos\theta > 0$), although both distributions are quite broad. Separate analysis of the fastest (χ_A) and slowest (χ_B) spinning components of the binary also indicate that even the rapid-spinning components are still quite slow $\chi_A \sim 0.4$ while the slow-spinning ones are concentrated below $\chi_B \sim 0.2$. These results are in agreement with what was found already in GWTC-3.

In Figure 1.15 and Figure 1.17 we show also the inferred distribution of the effective spin parameter $\chi_{\rm eff}$ and its possible correlation with the mass ratio q. A pure isotropic spin distribution would be symmetric around $\chi_{\rm eff} = 0$ (e.g., Rodriguez et al. 2016), but Figure 1.15 shows that this is not the case for GWTC-4 data, that instead supports an asymmetric $\chi_{\rm eff}$ distribution with a skew that favours positive $\chi_{\rm eff} > 0$. The presence of this asymmetry suggests the existence of a sub-population of BBHs with aligned spins (e.g., Gerosa et al. 2018). However, the distribution extends also to negative $\chi_{\rm eff} < 0$, indicating that in some systems tilt angles could be larger than $\theta > 90°$, probably indicating a dynamical assembly (Rodriguez et al. 2019).

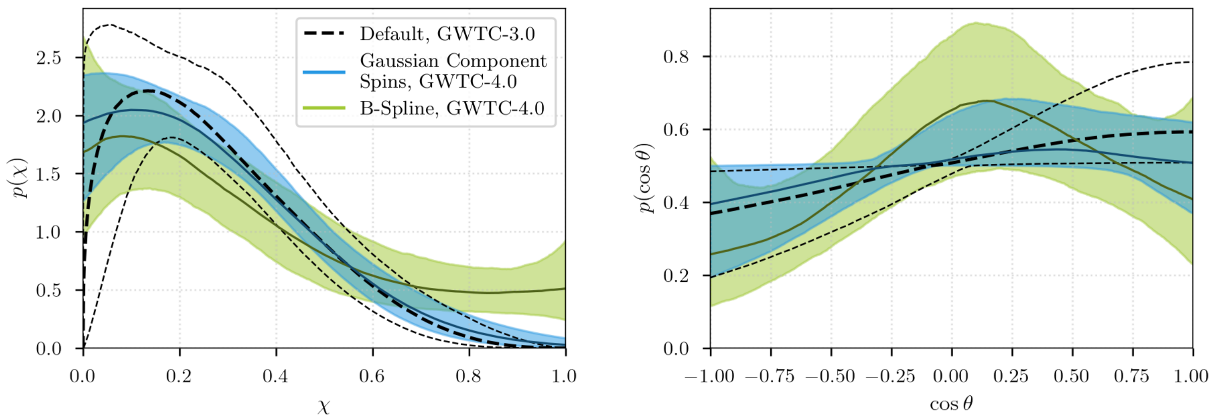

Figure 1.14: Marginal spin magnitude χ (left) and cosine tilt angle $\cos\theta$ (right) distributions inferred from GWTC4-0. Solid lines show the median distribution of possible models, with 90 % credible intervals. Dashed lines show the GWTC-3 distributions, as a comparison. For more details on the models we refer to The LIGO Scientific Collaboration et al. 2025a, from where the Figures are taken.

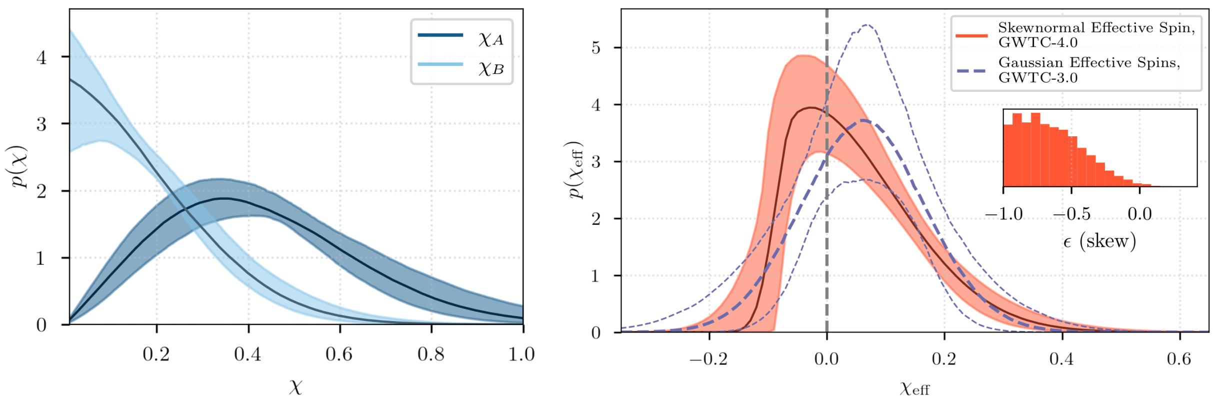

Figure 1.15: Left: inferred distribution of the larger ($\chi_{\rm A}$) and smaller ($\chi_{\rm B}$) spins in each BBH pair. Right: Inferred distributions of the effective spin parameter ($\chi_{\rm eff}$), that show a preference for a skewed $\chi_{\rm eff}$ distribution (skewness $\epsilon < 0$). Solid lines show the median distribution inferred on GWTC-4.0 data, with 90 % credible intervals. Dashed lines show the GWTC-3 distributions, as a comparison. For more details on the models we refer to The LIGO Scientific Collaboration et al. 2025a, from where the Figures are taken.

1.5.4 Astrophysical interpretation of BBH properties

The multiple-population problem

Even if the number of detections nearly doubled from GWTC-3 to GWTC-4.0, the interpretation of the BCO population properties remains challenging (The LIGO Scientific Collaboration et al. 2025a).

The main formation channels of BCOs include evolution as isolated binaries (e.g., Giacobbo & Mapelli 2018; Neijssel et al. 2019; Belczynski et al. 2020; Broekgaarden et al. 2022; Iorio et al. 2023), in dynamically active environments, such as open cluster, globular clusters, and young massive clusters (e.g., Rodriguez et al. 2016, 2019; Rastello et al. 2020, 2021; Antonini & Gieles 2020; Banerjee 2021; Di Carlo et al. 2021; Arca Sedda et al. 2024), in gas-rich environments (e.g., Samsing et al. 2022; Vaccaro et al. 2024; Delfavero et al. 2025), and their existence could be linked to primordial BHs (e.g., Papanikolaou et al. 2021). Therefore, the observed population of BCOs is likely the result of multiple sub-populations evolved through multiple channels. Ignoring some of the possible multiple origins of BCOs introduces biases in the determination of the mixing fractions of each formation channel, so there is an ongoing effort that aims at determining all the possible evolutionary channels and features of the BCO population (e.g., Zevin et al. 2021; Mapelli et al. 2022; Cheng et al. 2023).

Degenerate predictions

One of the main challenges in the interpretation of the BCO properties is the degeneracy of many BCO features with the possible formation channels and sub-populations. (Mandel & Broekgaarden 2022). For instance, the existence of the $\approx 10\ \mathrm{M}_\odot$ peak in the mass distribution of BH primaries (Figure 1.12) could be reproduced both by the isolated and by the dynamical formation scenario (Giacobbo et al. 2018; Neijssel et al. 2019; Rodriguez et al. 2019; Antonini & Gieles 2020; Banerjee 2021; Belczynski et al. 2020; van Son et al. 2022b; Mandel & Farmer 2022; Willcox et al. 2025). Similarly, both the isolated and the dynamical channels favour the formation of similar masses (e.g., Rodriguez et al. 2016; Giacobbo et al. 2018; Broekgaarden et al. 2022; Torniamenti et al. 2024), in agreement with the inferred mass ratio distributions (Figure 1.13). So far, the most promising strategies to disentangle the BCO sub-populations aim to identify over-densities, gaps, and correlations among the BCO parameter distributions (e.g., masses, mass ratios, spins) that could be unambiguously associated with a specific sub-population. As presented in the next paragraphs, these strategies are currently limited by the small size of the observed sample, by the large uncertainties in measurements and model predictions, and by choice of the prior adopted in the Bayesian inference (e.g, The LIGO Scientific Collaboration et al. 2025a; Ray & Kalogera 2025).

Characterization of the putative PI mass gap

Stellar evolution theory predicts that PI should create a gap in the BH mass distribution between $\approx 40 - 100\ \mathrm{M}_\odot$ and $\approx 120 - 130\ \mathrm{M}_\odot$ (Section 1.2.4). Although the precise boundary location is heavily dependent on the stellar physics assumptions (Woosley 2017; Spera & Mapelli 2017; Farmer et al. 2019; Renzo et al. 2020b; Costa et al. 2021; Renzo & Smith 2024; Costa et al. 2025), the identification of a PI gap in the BH mass spectrum has been extensively suggested as a possible smoking gun to disentangle BHs of stellar origin, evolved in isolated binaries, from BHs formed through hierarchical merging, that can pollute the gap (see The LIGO Scientific Collaboration et al. 2025a and references therein). However, as underlined by Ray & Kalogera 2025, the observed sample of BBHs in GWTC-4.0 is still too small and too much affected by measurement uncertainties to reliably infer the existence of a PI mass gap in the BH mass distribution.

The LIGO Scientific Collaboration et al. 2025a assumed a power-law distribution with two peaks for the primary BH mass distribution, finding that the data indicate a moderate decline beyond ≈ 35 $M_{\odot}$. Banagiri et al. 2025 suggest that the primary BH mass spectrum could be the result of three sub-populations, with one of them that is characterized by primary BHs more massive than $\gtrsim 40$ $M_{\odot}$, large spin magnitudes and mass ratios $q \approx 0.5$. Antonini et al. 2025 and Tong et al. 2025 support the existence of a PI mass gap between $\approx 45 - 120$ $M_{\odot}$ only in the secondary BH mass distribution, with evidence for a continuum up to ≈ 140 $M_{\odot}$ in the primary BH masses. Antonini et al. 2025 and Tong et al. 2025 interpret the absence (presence) of the PI gap in the primary (secondary) BH mass distribution with the presence (absence) of a sub-population of BHs formed via hierarchical mergers. In particular, the absence of secondary BHs of hierarchical origins suggests that it exists a sub-population of BBH mergers where the GW-observed coalescence occurs between a first generation (1G) secondary (i.e. a BH of stellar origin) and a second generation (2G) primary (i.e. a BH that is already the result of a previous coalescence). Antonini et al. 2025 and Tong et al. 2025 further support this conclusion with the observation of a transition in the distribution of effective spins into a uniform density function that is consistent with the properties of 1G+2G mergers found in simulations of star clusters (Rodriguez et al. 2019). Ray & Kalogera 2025 argue that the inferences of Tong et al. 2025 are biased by the choice of a prior in the secondary BH mass distribution that already enforces the existence of a gap. As shown in Figure 1.16, Ray & Kalogera 2025 demonstrate that assuming a flexible prior for the secondary BH mass distribution, that allows but does not force the existence of a gap, produces a better agreement with the GWTC-4.0 data and infers a continuous distribution similar to the one that it is possible to infer with an agnostic non-parametric model (The LIGO Scientific Collaboration et al. 2025a). Nevertheless, Ray & Kalogera 2025 still identify a moderate cut-off in the secondary BH mass distribution beyond ≈ 57 $M_{\odot}$, within measurement uncertainties, but underline that more observations are needed to confirm the existence and the location of a PI gap.

Single events in the PI mass gap

In the context of PI gap investigation, the detection of the GW231123 event seems to support the existence of a sub-population of hierarchical mergers (The LIGO Scientific Collaboration et al. 2025c). GW231123 is a BBH with a ≈ 137 $M_{\odot}$ primary and a ≈ 103 $M_{\odot}$ secondary, resulting in a merger product of ≈ 240 $M_{\odot}$, the most massive BH detected so far with GWs (The LIGO Scientific Collaboration et al. 2025a). The presence of the secondary BH in the PI gap supports the 1G+2G merger scenario, for instance, in star clusters located in metal-poor dwarf galaxies or in Milky Way-like galaxies (Paiella et al. 2025). However, Stegmann et al. 2025 suggest that a dynamical assembly in star clusters in challenging for GW231123: both components have a high spin ($\chi_{1,2} \gtrsim 0.8$), in disagreement with the expected isotropic spin distribution induced by dynamical pairings, and few percent of GW231123-like mergers could be retained in star clusters because of the strong recoil kicks. On the contrary, Gottlieb et al. 2025 use 3D general-relativistic

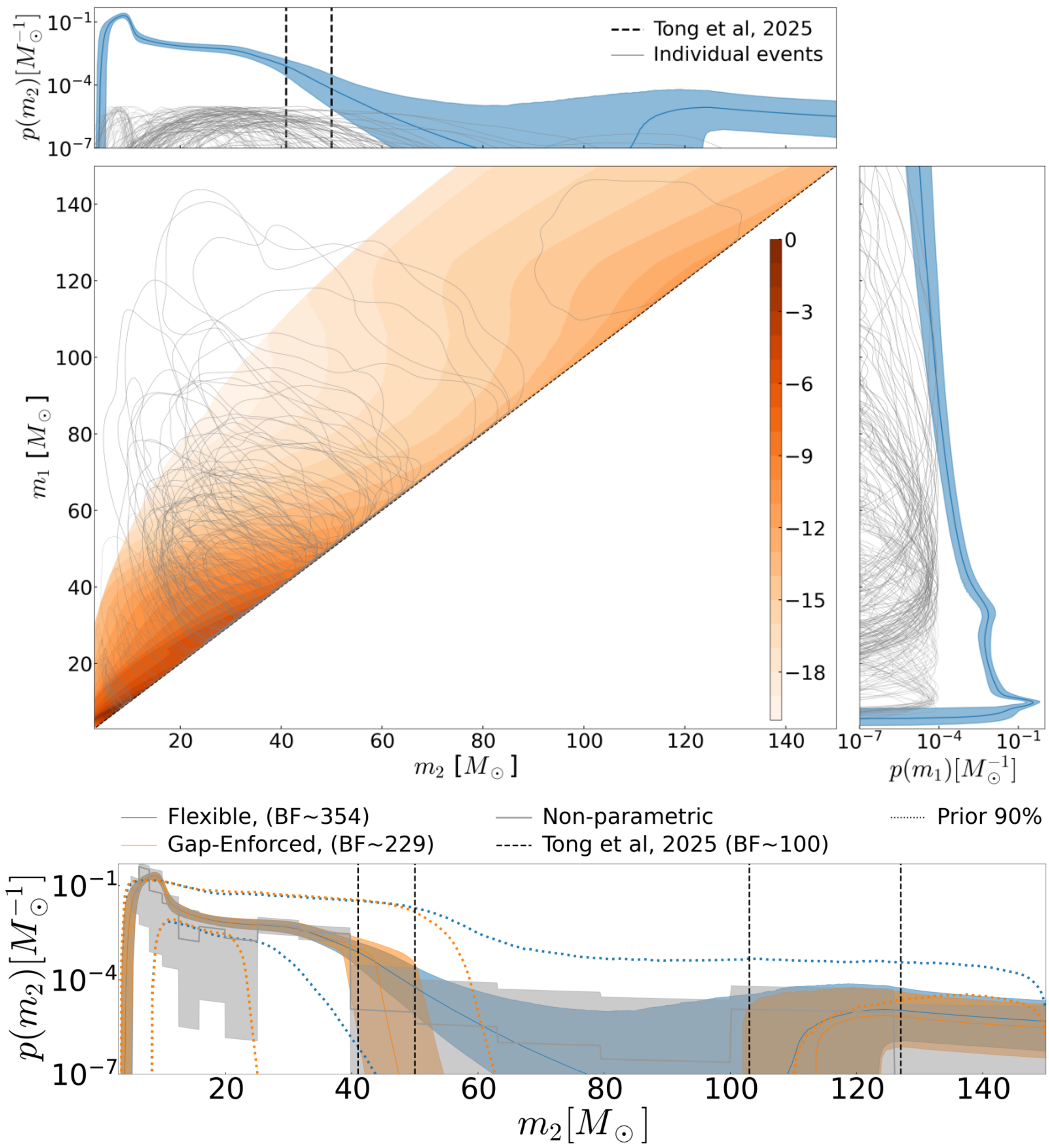

Figure 1.16: *Top*: Primary (m_1) and secondary ($m_2 < m_1$) BH mass distributions as reconstructed by Ray & Kalogera 2025 with GWTC-4.0 data. Mean prediction of the joint distribution is shown in orange while median predictions of the marginal distributions are shown with solid line in blue (along with 90% credibility intervals). Gray contours indicate individual event posteriors, with the high-mass event GW231123 (The LIGO Scientific Collaboration et al. 2025c) standing out in the upper-right corner of the two-dimensional plane. .*Bottom:* Secondary mass distributions inferred from non-parametric (The LIGO Scientific Collaboration et al. 2025a, grey), flexible (Ray & Kalogera 2025, blue), and gap-enforced (Tong et al. 2025, orange) priors, with the correspondent Bayes Factors (BF, evaluated against a single power-law model). The existence of the putative PI gap is biased by the choice of the prior: Tong et al. 2025 find a gap between $m_2 = 45^{+7}_{-6}$ and $m_2 = 116^{+13}_{-9}$ (90 % credible intervals, black dashed lines) while Ray & Kalogera 2025 find a moderate cut-off from $m_2 \approx 40$ $\mathrm{M}_\odot$, with a possible gap starting at $m_2 = 57^{+17}_{-10}$. Figures from Ray & Kalogera 2025.

magnetohydrodynamic simulations to show that the large spins and the formation of GW231123 could be explained via binary isolated evolution if the effects of magnetic fields are included in the models.

The various formation scenarios proposed for GW231123 resemble the many works in the literature that were derived from the detection of GW190521 (Abbott et al. 2020), a BBH with a ≈ 85 M$_\odot$ primary and a ≈ 66 M$_\odot$ secondary. These works showed that there were many possible channels that were capable of producing a primary BH in the PI gap, such as the dynamical one (e.g., Romero-Shaw et al. 2020), AGNs (e.g., Tagawa et al. 2021), or even by the isolated evolution scenario itself (e.g., Costa et al. 2021), if uncertainties in the ^{12}C$(\alpha,\gamma)^{16}$O reaction rate and overshooting were taken into account.

Effective spin - mass ratio putative anti-correlation

The marginal distributions of masses and mass ratios inferred so far are not sufficient to discriminate between the isolated and dynamical evolution scenarios. Therefore, joint distributions of mass and spin parameters (e.g., masses, mass ratios, spin magnitudes, and spin orientations) could also be considered to disentangle the possible BCO formation channels. However, so far model and measurement uncertainties remain large, so the detection and the interpretation of possible features in multi-dimensional distributions remains open (see The LIGO Scientific Collaboration et al. 2025a and references therein).

For instance, the existence of over-densities, gaps or anti-correlations in the effective spin-mass ratio $\chi_{\rm eff} - q$ plane could be used to confirm or rule out some models. CHE strongly supports the production of BBHs with mass ratio close to unity $q \approx 1$ and spins aligned as a result of tides (e.g., de Mink & Mandel 2016). Similarly, the isolated evolution scenario generally supports the production of similar masses and aligned spins (e.g., Banerjee & Olejak 2024). However, it is possible that the mass ratio distribution exhibits an over-density at $q \approx 0.6-0.8$ if mass-ratio-reversal processes (driven generally by SMT) occurred in the BBH formation, i.e. if the primary BH was born from the star that was initially the least massive one (Neijssel et al. 2019; van Son et al. 2022b). Moreover, if there is efficient transport of angular momentum inside the stars, it is possible that the first-born BH has a negligible spin while the secondary star, possibly a pure-Helium star, is spun-up by tides (Bavera et al. 2020; Bavera et al. 2021a; Qin et al. 2018; Qin et al. 2023). On the other hand, dynamical evolution in clusters does not exhibit a preferential orientation, predicting isotropic spins with the exception of second-generation merger productions, that are expected to have a spin magnitude of $\chi \approx 0.7$ (e.g., Rodriguez et al. 2019; Gerosa & Fishbach 2021).

GWTC-4.0 data support a mild $\chi_{\rm eff} - q$ anti-correlation, although it appears to be less evident than the anti-correlation inferred from the analysis of the GWTC-3 population (Abbott et al. 2023b; The LIGO Scientific Collaboration et al. 2025b). Moreover, Figure 1.17 shows that the inferred posteriors are broad and that the putative anti-correlation could be model-dependent. As discussed in the previous paragraphs, individual BH masses and spins are not directly measured from GW data, but are inferred from other measured quantities, such as the chirp mass (Equation 1.14) and the effective spin (Equation 1.13). Therefore, it is difficult to understand if the anti-correlation is real or if it is a consequence of the hierarchical Bayesian analysis required to extract the distributions from the observed signal, as discussed in (Callister et al. 2021; Abbott et al. 2023b; The LIGO Scientific Collaboration et al. 2025a).

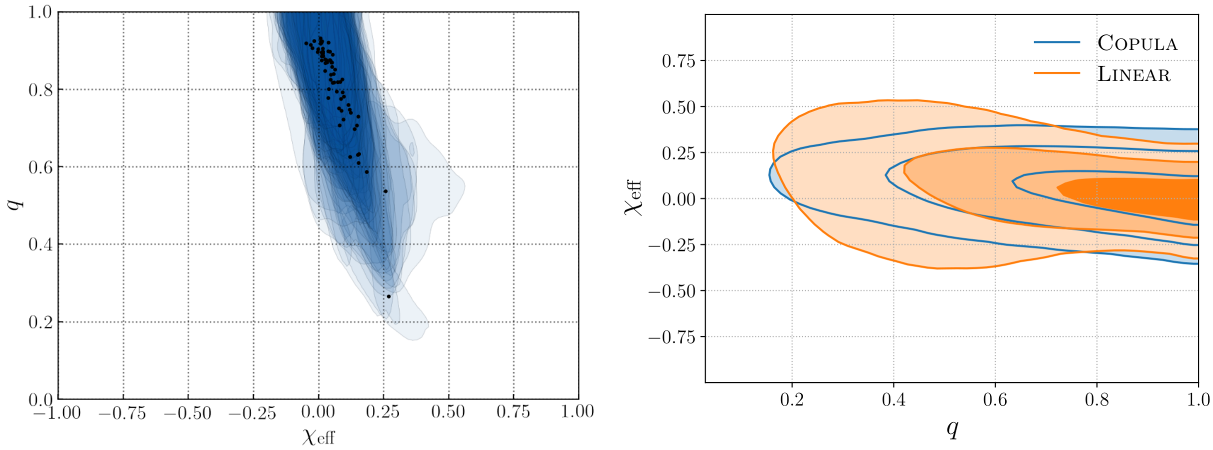

Figure 1.17: Mass-ratio q - effective spin χ_{eff} anti-correlation as inferred from GWTC-3 (left) and GWTC-4 data (right). In the GWTC-3 Figure, black points mark the median of the PDF obtained using an informed prior where mean and standard deviation of the Gaussian posterior of χ_{eff} were allowed to evolve with q. Blue shaded areas indicate the 90 % credible intervals for each median point.

1.6 Computational tools for binary evolution

1.6.1 From detailed to rapid simulations

The formation of BCOs is heavily influenced by stellar and binary physics, as discussed in the previous sections. Therefore, the correct interpretation of BCO detections requires an accurate modelling of the stellar and binary processes, that can be achieved only through numerical simulations. The available tools can range from computationally expensive and accurate hydrodynamical simulations, to detailed stellar and binary simulations, to more approximated but faster population-synthesis simulations. Each tool is designed to investigate a specific aspect of BCO formation (e.g., the detailed physical processes or the impact of systematics and uncertainties in the population predictions) and each one of them is necessary to obtain calibrations for the other tools, allowing for an overall progression in our modelling capabilities.

Hydrodynamical simulations

Multidimensional (magneto-)hydrodynamical simulations can be considered as the most accurate approach to model stellar and binary physics. However, accuracy comes at the cost of computational time. For instance, simulating just a single process, such as the merger of two NSs, can require about $\approx 10^4 - 10^5$ CPU hours with a general relativistic moving-mesh hydrodynamic simulation (Lioutas et al. 2024). Even if there are many hydrodynamical codes available in the literature - such as `AREPO` (Springel 2010), `PHANTOM` (Price et al. 2018), and `ATHENA++` (Stone et al. 2020) - their prohibitive computational cost restricts their application to the study of single processes, such as CE, mergers, or CCSNe (see Janka et al. 2012 and Röpke & De Marco 2023 for a complete review).

Detailed stellar and binary evolution codes

Simulating the evolution of a star in isolation requires the integration of the differential equations that determine the stellar structure and the nuclear burnings (Prialnik 2009). Adopting a 1D approach, stellar evolution codes such as `BEC` (Yoon et al. 2010), `FRANEC` (Chieffi & Limongi 2013; Limongi & Chieffi 2018), `GENEC` (Meynet & Maeder 1997; Eggenberger et al. 2008; Ekström et al. 2012), `MESA` (Paxton et al. 2011; Paxton et al. 2015; Paxton et al. 2019), `PARSEC` (Bressan et al. 2012; Chen et al. 2015; Nguyen et al. 2022; Costa et al. 2025), and `STARS` (Eggleton 1971; Han et al. 1994; Eldridge et al. 2008) require only few CPU hours to complete the evolution of a star (Marchant & Bodensteiner 2024).

Simultaneously simulating the full internal evolution of two stars as they interact in a binary system is more challenging and so far is permitted only by the `MESA` stellar evolution code (Paxton et al. 2015; Paxton et al. 2019). Thanks to this `MESA binary` evolution module and thanks to the fact that `MESA` is the only public-available and open-source[9] stellar evolution code, `MESA` became the state-of-the-art software for detailed binary evolution simulations. For instance, many works used `MESA` to investigate in detail the effects of stellar and binary evolution in the context of BCO formation (e.g., Qin et al. 2018, 2019; Marchant et al. 2021; Klencki et al. 2020; Klencki et al. 2021; Laplace et al. 2020; Laplace et al. 2021; Gallegos-Garcia et al. 2021; Henneco et al. 2024; Picco et al. 2024; Klencki et al. 2025; Laplace et al. 2025)

Population-synthesis codes

BCO formation is influenced by many physical processes that, in turn, are described by a large set of free parameters. Therefore, when investigating BCO formation, it is necessary to account also for the impact of the parameter space. Moreover, the characterization of the BCO population of GW mergers requires the simulation of a large ($\gtrsim 10^6$) number of binaries, since GW-merging BCOs are rare events (Broekgaarden et al. 2019). Detailed binary simulations with `MESA` can investigate in detail only a small portion of the parameter space and they would require millions of CPU hours just to simulate a single population. To overcome this limit, population-synthesis codes have been developed. Paying the price of some approximation, population-synthesis codes can simulate $\approx 10^6$ binaries just in few CPU hours (e.g., Compas et al. 2022).

Population-synthesis codes can be divided into three families: rapid, hybrid, and detailed (Breivik 2025). Most rapid codes derive their structure and formalism from `BSE` (Hurley et al. 2002), a code that implements semi-analytic prescriptions for binary processes (e.g., mass transfer and tides) and adopts the fitting formulae of Hurley et al. 2000 on the stellar tracks generated by Pols 2008 with the `STARS` stellar evolution code (Eggleton 1971; Han et al. 1994; Pols et al. 1995). Examples of rapid codes that derived their structure from `BSE` and adopt the Hurley et al. 2000 fits for single stellar evolution include `binary_c` (Izzard et al. 2004, 2018), `COMPAS` (Compas et al. 2022; Team Compas et al. 2025), `COSMIC` (Breivik et al. 2020), `MOBSE` (Giacobbo et al. 2018; Giacobbo & Mapelli 2018), `SeBa` (Portegies Zwart & Spreeuw 1996; Toonen et al. 2012), and `StarTrack` (Belczynski et al. 2008).

Rapid codes allow a wide exploration of the binary parameter space but are limited in the exploration of the stellar parameter space, as they are all bound to the same set of stellar fits. Therefore, a hybrid family of population-synthesis codes was developed.

[9] https://docs.mesastar.org/en/latest/

Hybrid codes like `ComBinE` (Kruckow et al. 2018), `METISSE` (Agrawal et al. 2020), and `SEVN` (Iorio et al. 2023) interpolate the stellar properties from sets of pre-computed stellar tracks, while they maintain most of the `BSE` framework for binary evolution. In particular, `ComBinE` interpolates stellar tracks obtained with the `BEC` stellar evolution code (Yoon et al. 2010); `METISSE` has been tested with the `MESA` tracks generated for the `MIST` isochrones (Choi et al. 2016), with `BEC` models (Yoon et al. 2010), and with the `STARS` models of Pols et al. 1998; the `SEVN` public release includes the `MESA` models of the `MIST` isochrones (Choi et al. 2016) and the tracks generated with the `PARSEC` code (Costa et al. 2025), but it has been tested also with `FRANEC` (Mapelli et al. 2020) and other customized sets of `MESA` tracks (Simonato et al. 2025; Torniamenti et al. 2025).

Both rapid and hybrid population-synthesis codes decouple the evolution of the stellar property with the evolution of the binary properties. For instance, the changes in the stellar radius and density profile generally follow the behaviour of the single stellar evolution models even during a mass transfer process. However, the size of a star, its binding energy, and its internal structure are crucial to determine binary processes like mass transfer evolution (e.g., Ge et al. 2010, 2015, 2020, 2024; Klencki et al. 2020; Klencki et al. 2021). Moreover, binary interactions can change the final size of the core and its compactness, impacting CCSN events and the final CO masses (e.g., Laplace et al. 2021; Schneider et al. 2023; Maltsev et al. 2025). To overcome this limit, detailed population-synthesis codes like `BPASS` (Eldridge et al. 2017; Byrne et al. 2022) and `POSYDON` (Fragos et al. 2023) were developed. `BPASS` adopts a custom version of the `STARS` stellar evolution code to evolve in detail a star as it interacts and evolves in a binary system. To speed up the computation, the properties of the companion star are not computed in detail but are interpolated from the Pols et al. 1998 models, also generated with a previous version of the `STARS` code. On the other hand, `POSYDON` interpolates binary and stellar properties from pre-computed sets of stars evolved in binary systems with `MESA`. This approach allows to treat self-consistently the changes in the stellar structure due to mass transfer processes but limits the parameter space exploration to the one of the pre-computed grids.

Population-synthesis codes as building blocks for N-body codes

Because of their reduced computational cost, population-synthesis codes can be coupled with N-body codes to allow accurate simulations of cluster dynamics that can account for the stellar and binary physics, eventually leading to accurate predictions also for BCOs that can be formed in clusters. For instance, `BSE` (Hurley et al. 2002) has been coupled with the direct N-body codes `NBODY6` (Aarseth 2003) and `NBODY6++GPU` (Wang et al. 2015) to produce detailed `DRAGON` (Wang et al. 2016) and `DRAGON II` (Arca Sedda et al. 2024) simulations of globular clusters (with 10^6 stars involved and up to 33% of them in binaries, as described in Arca Sedda et al. 2024). Other examples include the coupling between the `PETAR` N-body code with `BSE` (e.g., Barber & Antonini 2025; Rastello et al. 2025) or with `MOBSE` (Mestichelli 2024; Barber & Antonini 2025) as well as the coupling between the `BIFROST` N-body code (Rantala et al. 2023) with `SEVN` (Rantala et al. 2024, 2025).

1.6.2 BCO formation with the SEVN population-synthesis code

In this thesis, BCO formation will be explored in the isolated evolution scenario with the SEVN population-synthesis code (Spera et al. 2015; Spera & Mapelli 2017; Spera et al. 2019; Iorio et al. 2023). In this Section, we will briefly present its main features and use it as case study to illustrate the importance of considering model uncertainties in BCO formation.

Structure of a hybrid code

SEVN (acronym for *Stellar EVolution for N-body simulations*) is an open-source[10] population-synthesis code written in C++. It can be considered a "hybrid" population-synthesis codes because it interpolates the stellar properties from pre-computed sets of stellar tracks but it follows the framework of BSE to implement semi-analytic prescriptions for binary processes (e.g. mass transfer and tides). The interpolation of stellar tables allows SEVN to be flexible and easy to update with the latest stellar evolution results: when new stellar evolution models are available, they can be directly implemented as interpolating tables without the need to fit the new properties, as it was done for instance by Hurley et al. 2000 with the Pols et al. 1998 tracks in order to implement them in BSE (Hurley et al. 2002). Stellar evolution is interpolated from the ZAMS to the end of the carbon burning phase. Then, the final core properties (helium or carbon-oxygen, depending on the prescriptions) is used to estimate the final fate of the star and the CO mass, following the framework of BSE-like codes.

The stellar interpolator

The interpolation method of stellar tracks exploits one of the main results from stellar evolution theory: stellar properties are mainly determined by their mass M and metallicity Z (Prialnik 2009). Therefore, as a first step, each evolutionary track can be identified its correspondent mass and metallicity at the ZAMS ($M_{\rm ZAMS}, Z_{\rm ZAMS}$) and can be represented as grid node in a (M, Z) plane. When SEVN needs to evolve a star with intermediate properties with respect to the provided tracks, the code will interpolate the stellar properties as a weighted average of the properties of the closest four tracks in the (M, Z) plane. This interpolation process is iterated as the star evolves and it is illustrated in Figure 1.18.

When interpolating stellar properties, SEVN ensures to use the properties of the closest interpolating tracks that best match the evolutionary stage of the star. SEVN distinguishes eight physically-motivated evolutionary phases: pre-MS (before core-hydrogen burning), MS (ongoing core-hydrogen burning), Terminal-age MS (TAMS; growth of a He-core with mass > 0), shell-hydrogen burning (end of core-hydrogen burning), core-helium burning (CHeB), Terminal-age CHeB (growth of a CO-core with mass > 0), shell-helium burning (end of core-helium burning), and remnant formation. The phase information is one of SEVN-specific informations that are included in the stellar tables by the TRACKCRUNCHER code[11], the custom software that it is used to re-map raw stellar tracks in the format needed for the interpolation. SEVN uses the phase information to calculate the percentage of life that a star currently has in that phase, using this parameter to match the track properties

[10] https://sevncodes.gitlab.io/sevn/
[11] https://gitlab.com/sevncodes/trackcruncher

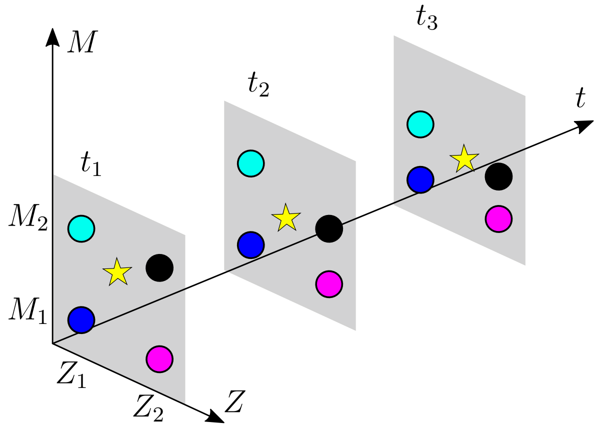

Figure 1.18: Schematic representation in the mass-metallicity-time space (M, Z, t) of the stellar interpolation scheme implemented in SEVN (Iorio et al. 2023). The properties (e.g. mass, radius, luminosity, etc.) of the desired input star (yellow star) are interpolated as weighted mean from the properties of the four closest pre-computed evolutionary tracks (circled dots). For didactic purposes, stars on the top (cyan and black circles) are assumed to be more massive and to lose mass more rapidly than stars on the bottom (blue and pink circles), with the more massive and metallic one (black circle) having the higher mass loss rate.

(the scheme is adapted from Spera et al. 2019). For more details on the interpolation method and on the definitions of the phases, we refer to Section 2.1.3 of Iorio et al. 2023.

The PARSEC set of tables

The SEVN public release includes two main families of stellar tracks[12]: the ones derived from the MIST isochrones, calculated with MESA, (Choi et al. 2016) and the ones calculated with the PARSEC code (Costa et al. 2025). Hereafter, we will focus on the PARSEC set of tables, as they are the default ones in SEVN and the fiducial ones in this thesis.

The PARSEC tracks available in SEVN are non-rotating stars that were developed specifically to study popI and popII massive stars between $2\ \mathrm{M}_\odot \leq \mathrm{M}_{\mathrm{ZAMS}} \leq 600\ \mathrm{M}_\odot$, for metallicities in the $10^{-4} \leq Z_{\mathrm{ZAMS}} \leq 4 \times 10^{-2}$ range, and popIII stars up to $M_{\mathrm{ZAMS}} = 2000\ \mathrm{M}_\odot$ for $Z \leq 10^{-4}$. As shown in the left-hand panel of Figure 1.19, the properties of these PARSEC tracks are in excellent agreement with the massive stars observed in the Tarantula Nebula (Schneider et al. 2018; Brands et al. 2022). We refer to Iorio et al. 2023; Costa et al. 2023, 2025 for a complete description of the input physics and we recall hereafter only the main assumptions that can determine the most macroscopic differences with respect to other sets of stellar tracks available in the literature, for which we report an example in the right-hand side of Figure 1.19.

Convection and overshooting

Convective energy transport in PARSEC is described with the Mixing-Length-Theory (MLT) developed by Böhm-Vitense 1958 and the tracks considered here have a mixing-length parameter of $\alpha = 1.74$, following a solar calibration (Bressan et al. 2012). Development of convective instability is determined through the Schwarzschild criterion (Schwarzschild

[12] https://gitlab.com/sevncodes/sevn/-/tree/SEVN/tables?ref_type=heads

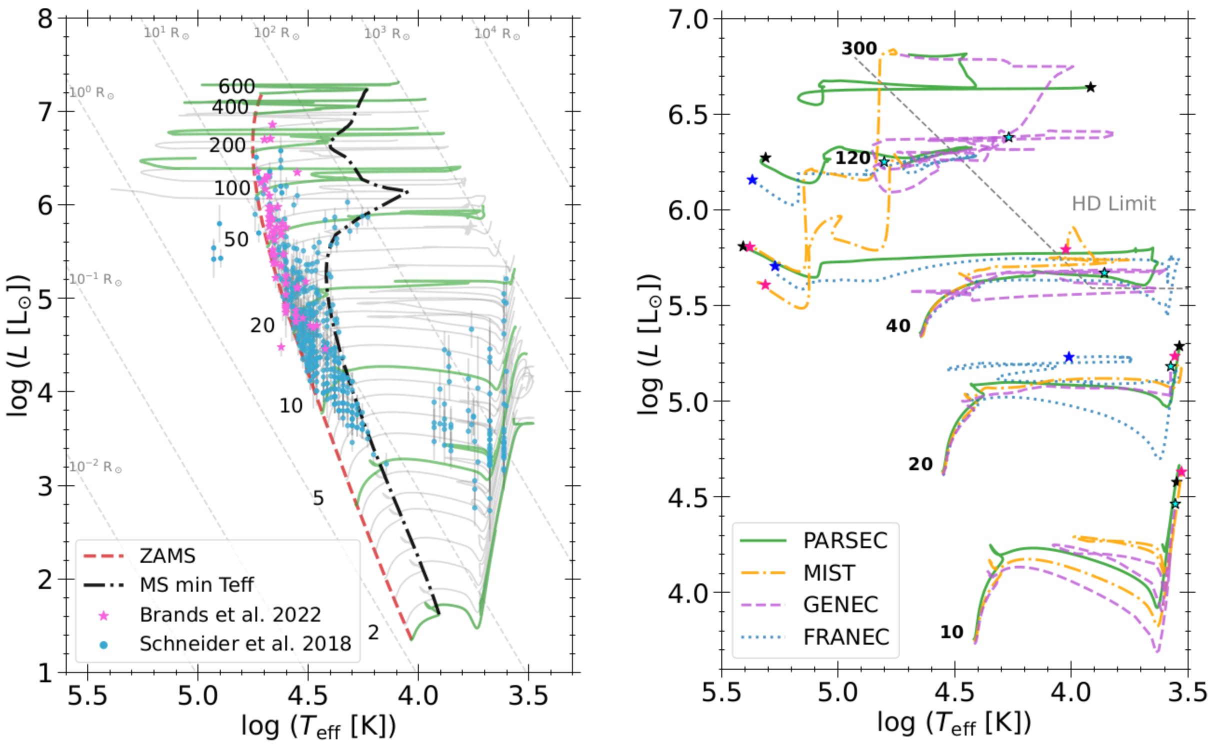

Figure 1.19: *Left*: Comparison between the massive stars of the Tarantula Nebula (Schneider et al. 2018; Brands et al. 2022) and the set with $Z = 0.006$ of `PARSEC` tracks (Costa et al. 2025) that were used to derive the interpolating tables for `SEVN` (Iorio et al. 2023). The dashed red and dash-dotted black lines indicate the ZAMS and TAMS, respectively. *Right*: Example of the impact of different overshooting and wind prescriptions at solar metallicity among the fiducial non-rotating stellar tracks developed with `PARSEC`, (Costa et al. 2025), `MESA` (`MIST` isochrones; Choi et al. 2016), `GENEC` (Ekström et al. 2012), and `FRANEC` (Chieffi & Limongi 2013). More details on the different assumptions in Costa et al. 2025, where the Figures are taken from.

1958). Core overshooting is described with the penetrative overshooting formalism described in Bressan et al. 1981 and assumes an overshooting parameter of $\lambda_{\rm ov} = 0.5$ that corresponds to a core overshooting length of $l_{\rm ov} \approx 0.5\ \lambda_{\rm ov} H_{\rm p} \approx 0.25\ H_{\rm p}$, in units of pressure scale height $H_{\rm p}$. In terms of exponential decay overshooting (Herwig et al. 1997), the formalism adopted for instance in `MESA` (Paxton et al. 2019), this is equivalent to the choice of $f_{\rm ov} = 0.025$. These `PARSEC` models consider also a step overshooting region that extends by $\Lambda_{\rm env} = 0.7\ H_{\rm p}$ from the base of the convective envelope. Eventually, these `PARSEC` models address also problem of density inversion that could occur in the low-density envelope of massive RSGs, that can develop when the local luminosity of the layer becomes higher than the Eddington luminosity. Density inversions can an increase the super-adiabaticity of the region and lead to numerical instabilities, that can prevent the convergence of the models. To prevent this issue, in these regions super-adiabaticity is reduced through an artificial limitation of the real temperature gradient, in a fashion qualitatively similar to the `MLT++` approach of `MESA` (Paxton et al. 2013). This assumption de-facto corresponds to a more efficient convection and can determine smaller radii and higher effective temperatures with respect to other stellar models that allow for density inversions, as in the case of a previous versions of the `PARSEC` code (Chen et al. 2015).

Stellar winds

Stellar winds for intermediate-mass stars follow Reimers 1975 ($\eta_R = 0.2$, as in Nguyen et al. 2022) for the Red Giant Branch (RGB) and CHeB phases; afterwards, in the Asyptotic Giant Branch (AGB) wind mass losses follow the two-stage process described in Marigo et al. 2020 and Pastorelli et al. 2020, as implemented in Addari et al. 2024. Stellar winds in hot massive stars (effective temperature $T_{\rm eff} \geq 10^4$ K) follow Vink et al. 2001 and take into account the dependence on the Eddington ratio for the most luminous stars, as indicated in Gräfener & Hamann 2008 and Vink et al. 2011. In cold massive stars, for instance in RSGs, wind mass losses follow de Jager et al. 1988 but adopt the same metallicity scaling of Vink et al. 2001.

Pure-Helium tables and WR stars

In the Costa et al. 2025 `PARSEC` set of tracks, a WR star is defined as a star with hydrogen surface abundance $X < 10^{-3}$ and effective temperature $\log T_{\rm eff} \geq 4$. When this condition is met, wind mass losses follow the WR winds of Sander et al. 2019, derived from observations on Galactic WC and WO stars. The `PARSEC` implementations of these winds follows Costa et al. 2021 and accounts for the dependence on the iron mass fraction in WN and WC stars, following a calibration on fits of WN and WC models calculated by Vink 2015. However, we highlight that the `SEVN` definition of WR star may not coincide with the one adopted in `PARSEC`. Even if `SEVN` does have the information on the surface abundances from `PARSEC` look-up tables, those values are not representatives of stars that underwent chemical mixing as a consequence, for instance, of mass transfer processes. Therefore, in `SEVN` WRs are more often defined through a mass criterion on the He-core mass (e.g., $M_{\rm He-core} \geq 97.9\ M_{\rm star}$) and are generally evolved as pure-Helium stars. `SEVN` has an ad-hoc table of pure-Helium stars that can be interpolated when the custom WR condition is met. This table of pure-Helium stars was also developed by Costa et al. 2025 and maintained the same `PARSEC` setup, except for two aspects. The first difference is about the construction of these pure-Helium tracks: these models were initialized accreting mass on a 0.36 $\rm M_\odot$ He core (up to a maximum of 350 $\rm M_\odot$) that was obtained by removing the H-rich envelope from the progenitor star when it started the He-core burning phase. The second difference is about stellar winds: these pure-Helium models implement the WR winds of Nugis & Lamers 2000. As pointed out by Higgins et al. 2021, the empirical winds Nugis & Lamers 2000 are more aggressive, probably too aggressive, than the ones of Sander et al. 2019 because their general implementation in the literature does not strongly scale with the metallicity. Sander et al. 2022 argued that the unrealistically high mass-loss rates of Nugis & Lamers 2000 are due to an overestimation of the contribution of carbon and oxygen. Moreover, Sander et al. 2022 noted that metal-rich WR stars (down to 0.1 $Z_\odot$) evolved with Nugis & Lamers 2000 had winds so strong that they ended almost with the same masses, regardless of the metallicity. In Figure 1.20 we show an example of selected pure-Helium tracks, that can be compared with the H-rich “standard” `PARSEC` tracks reported in Figure 1.3.

Stellar evolution in `SEVN` and `BSE`

Figure 1.21 shows the differences between the stellar evolution properties that are derived from the `PARSEC` tracks implemented in the `SEVN` (Iorio et al. 2023; Costa et al. 2025) and the Hurley et al. 2000 fits to the Pols et al. 1998 `STARS` tracks, generally adopted as fiducial stellar prescriptions in BSE (Hurley et al. 2002) and BSE-like codes (for instance, hereafter they are considered via the MOBSE code developed by Giacobbo et al. 2018). The Pols et al. 1998 models where evolved with masses ranging between $0.1\ \mathrm{M_\odot} \leq \mathrm{M_{ZAMS}} \leq 50\ \mathrm{M_\odot}$ and metallicities between $10^{-4} \leq Z \leq 3 \times 10^{-2}$. They were optimized to study low-mass phenomena and they show the largest differences with the PARSEC tracks in two areas. The first one is the behaviour at large masses $\gtrsim 50\ \mathrm{M_\odot}$, where extrapolation from the Pols et al. 1998 simulated range significantly deviates from the expected PARSEC models, indicating that the Pols et al. 1998 models are not optimal for massive studies in this range. The second difference arises in the size and in the timing of the stellar expansion. For instance, at $Z = 0.02$ a NS progenitor of $M_{\mathrm{ZAMS}} = 14\ \mathrm{M_\odot}$ ignites helium in its core as hot blue super giant (BSG, $\log T_{\mathrm{eff}} \approx 4 - 4.5$ K) or cold RSG ($\log T_{\mathrm{eff}} \approx 3.5$ K) if the Hurley et al. 2000 or Costa et al. 2025 models are considered, respectively. According to the Hurley et al. 2000 fits, this progenitor star will likely expand sufficiently to interact in a mass transfer process only after the ignition of core-He burning. Following the PARSEC models, this interaction would occur before the core-He burning phase. Since mass transfer stability and efficiency is heavily dependent on the evolutionary stage of the interacting star (e.g., Hurley et al. 2002; Klencki et al. 2020; Ge et al. 2024), the choice of the stellar evolution prescriptions has a significant impact on the further evolution of stars in binaries.

Parameter space exploration with SEVN: impact of stellar and binary assumptions

Figure 1.22 shows that stellar evolution assumptions do not have an impact per-se on the formation efficiency η_{f} of BCOs, but they do impact the formation efficiencies η of the ones that are able to merge via GW emission within < 14 Gyrs from the beginning of the ZAMS-ZAMS configuration (hereafter, delay time). For instance, the comparison between the BCO efficiencies found with SEVN+PARSEC (Iorio et al. 2023) and MOBSE+Hurley et al. 2000 fits (Giacobbo & Mapelli 2020) highlights that BBH formation could be larger by one or two order of magnitudes in metallic environments $Z \gtrsim 2 \times 10^{-3}$ as an effect of stellar evolution alone[13]. The effect of stellar evolution in the formation efficiency of BCO mergers is metallicity-dependent and gets convoluted with the effects of the assumptions on the binary physics. Accounting for the delay times and the Star Formation Rate (SFR) across the cosmic time, it is possible to reconstruct the correspondent predicted merger rate density for BCO mergers and compare it with the rate inferred by GW observations (e.g., Santoliquido et al. 2021). In Figure 1.23 we show an example of the merger rate densities that can be obtained with SEVN under different binary model assumptions. This type of comparison has been extensively carried out for many binary and SFR uncertainties, for instance by Broekgaarden et al. 2022 as well as with many different formation channels, as summarized by Mandel & Broekgaarden 2022. All these works together showed so far that currently there is a large degeneracy between the model predictions. Current constraints from GW observations still allow many possible incompatible predictions and it is likely that they stem from stellar and binary evolution uncertainties (e.g., Sgalletta et al. 2025). Therefore, also for this reason, while we wait for more observed GW data by current and future GW detectors, it is important to refine model predictions and be sure to consider also the impact of stellar evolution uncertainties.

[13]The Giacobbo & Mapelli 2020 model considered here is the Ej1, with CE efficiency $\alpha_{\mathrm{CE}} = 5$, and has the same binary assumptions of the fiducial one considered by (Iorio et al. 2023).

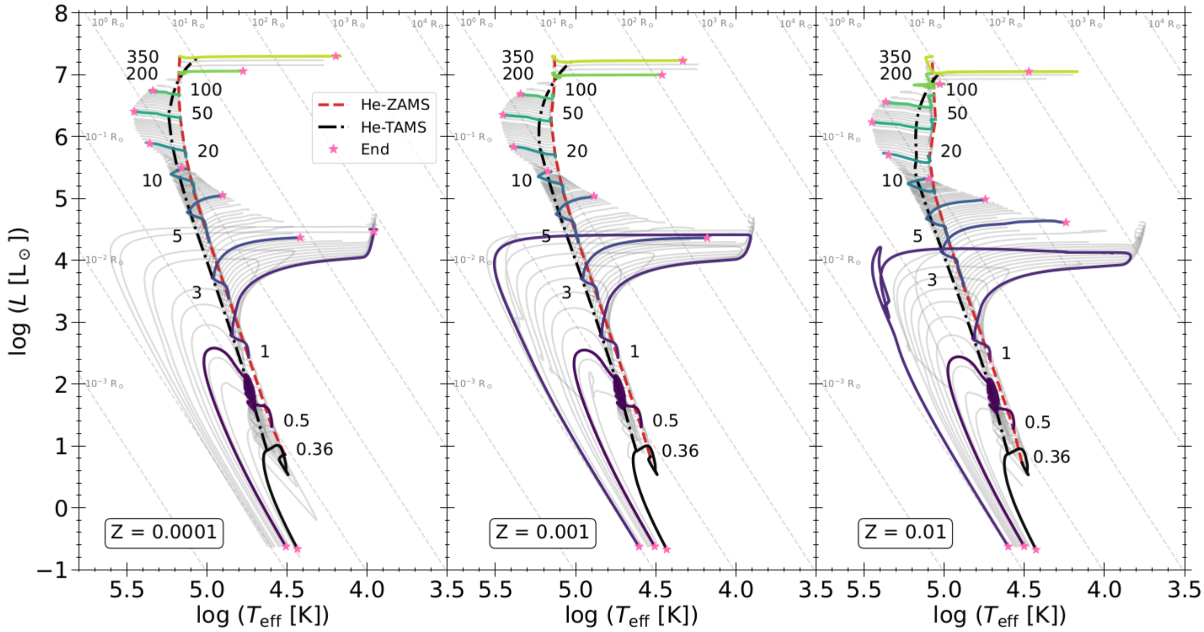

Figure 1.20: Example of the pure-Helium tracks developed with `PARSEC` (Costa et al. 2025), and available as interpolating tracks in `SEVN` (Iorio et al. 2023), for $Z = 0.0001$ (left), $Z = 0.001$ (centre), and $Z = 0.01$ (right). Dashed red and dash-dotted black lines indicate the beginning and end of the He-MS. Pink stars indicate the final location for the few highlighted masses. Pure-Helium stars follow a hotter evolutionary path with respect to the H-rich `PARSEC` tracks showed in Figure 1.3. Figure from Costa et al. 2025.

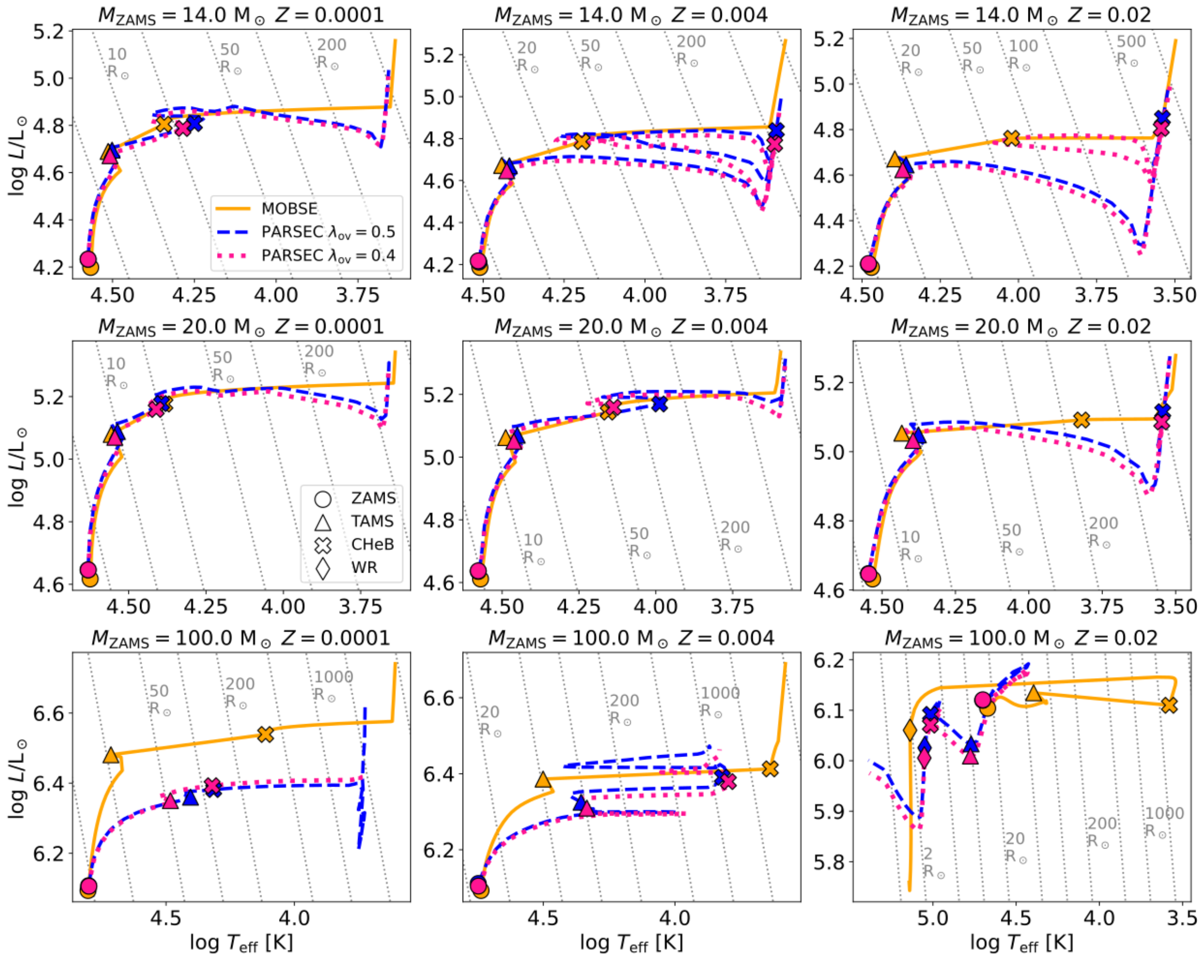

Figure 1.21: Comparison between the fiducial stellar tracks of PARSEC interpolated in SEVN ($\lambda_{ov} = 0.5$, blue dashed lines) and the Pols et al. 1998 STARS models fitted by Hurley et al. 2000 and implemented in MOBSE (Giacobbo et al. 2018) (solid yellow line), a code derived from BSE (Hurley et al. 2002). Different initial masses and metallicities are shown, as well as an additional comparison with a set of PARSEC tracks with the same assumptions of the fiducial ones but a different overshooting parameter ($\lambda_{ov} = 0.4$, dotted red lines). Hurley et al. 2000 fits show the largest discrepancies with PARSEC interpolated models at large masses ($\gtrsim 50$ M$_\odot$, where Pols et al. 1998 are extrapolated) and in the timing and size of the star in the expansion phase towards the BSG or RSG phase, one of the most sensible moments for mass transfer processes. The evolution is carried out from the ZAMS to the end of the carbon burning phase. When a WR is formed (diamond symbol), stellar properties of PARSEC stars are interpolated by SEVN from pure-Helium tracks. Figure taken from Iorio et al. 2023.

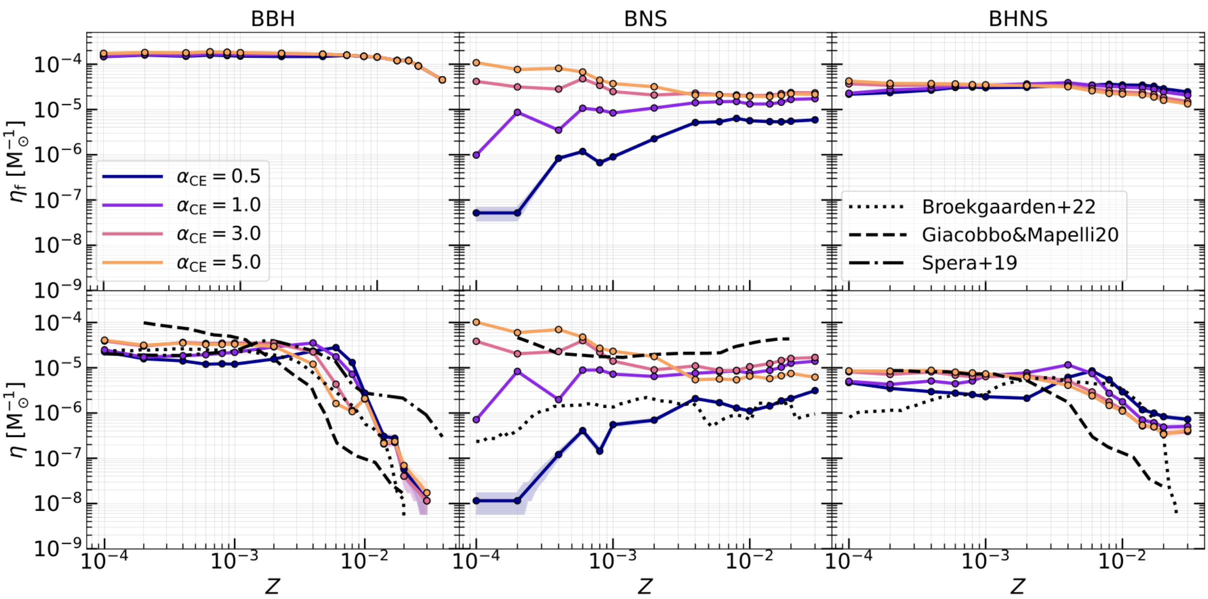

Figure 1.22: Formation (η_f) and merger (η) efficiencies (i.e. number of binaries of interest over the mass of the population) of BCOs simulated with the fiducial `SEVN` model considered in Iorio et al. 2023, for different CE efficiencies α_{CE} (Section 3.2). The differences between the $\alpha_{CE} = 5$ `SEVN` model and the Giacobbo & Mapelli 2020 one (`MOBSE`, dashed line) is determined only by the different assumptions on the stellar physics, respectively the stellar models of `PARSEC` (Costa et al. 2025) or the Hurley et al. 2000 fits (as implemented in `MOBSE`). By comparison, efficiencies obtained with the fiducial `COMPAS` setup of (Broekgaarden et al. 2022) and with a previous version of `SEVN` (Spera et al. 2019; also implementing a previous version of the `PARSEC` tracks, presented in Chen et al. 2015). Figure taken from Iorio et al. 2023.

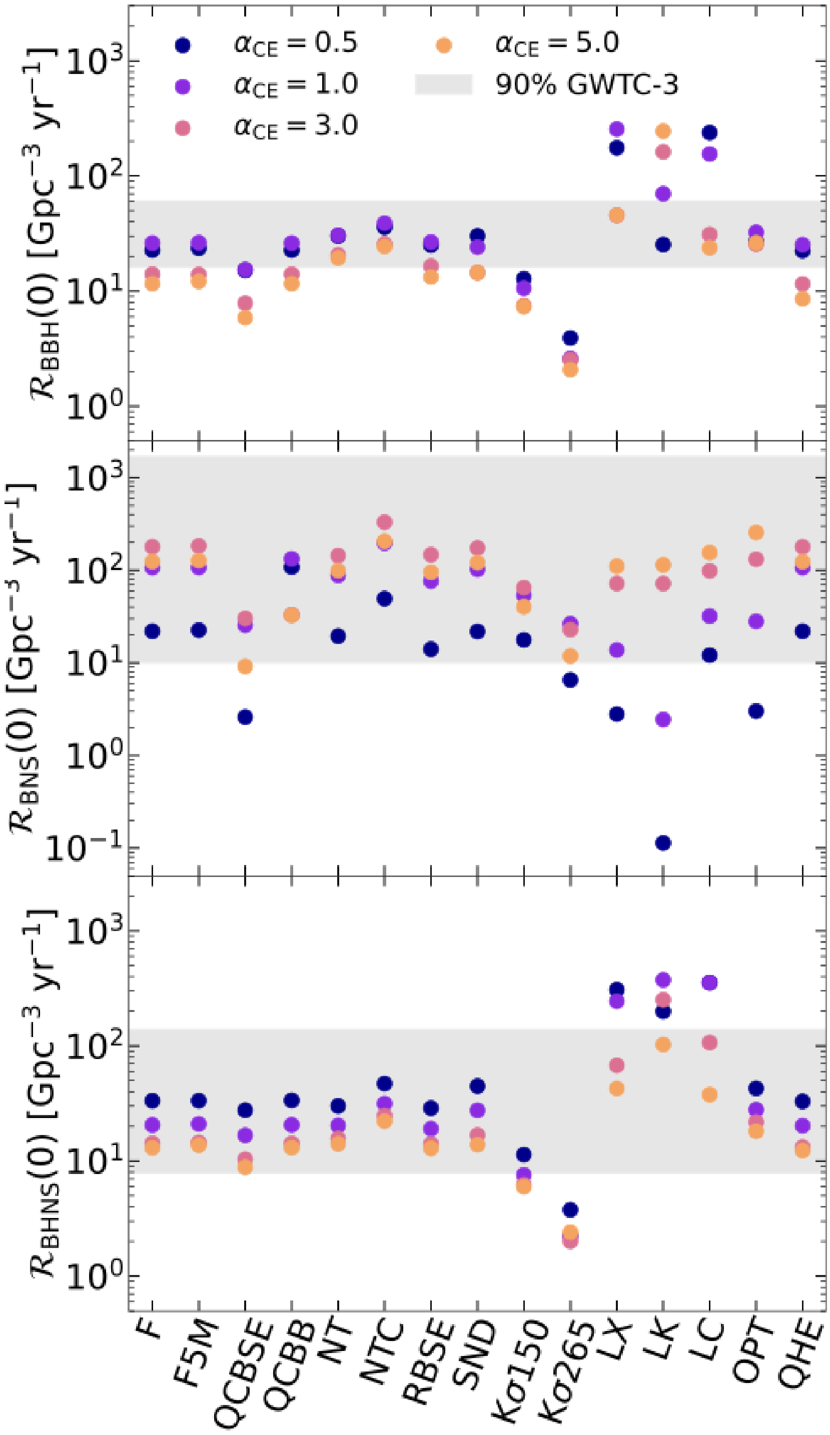

Figure 1.23: Merger rates predicted in the local universe (redshift $z = 0$) for various combinations of binary models explored with `SEVN`, compared against the constraints inferred from GW detections (GWTC-3; Abbott et al. 2023a). The "F" model refers to the fiducial one of Iorio et al. 2023 and was calculated accounting for the merger efficiencies η showed in Figure 1.22. We refer to Iorio et al. 2023 for more details on the physics assumed in each set. Figure taken from (Abbott et al. 2023a).

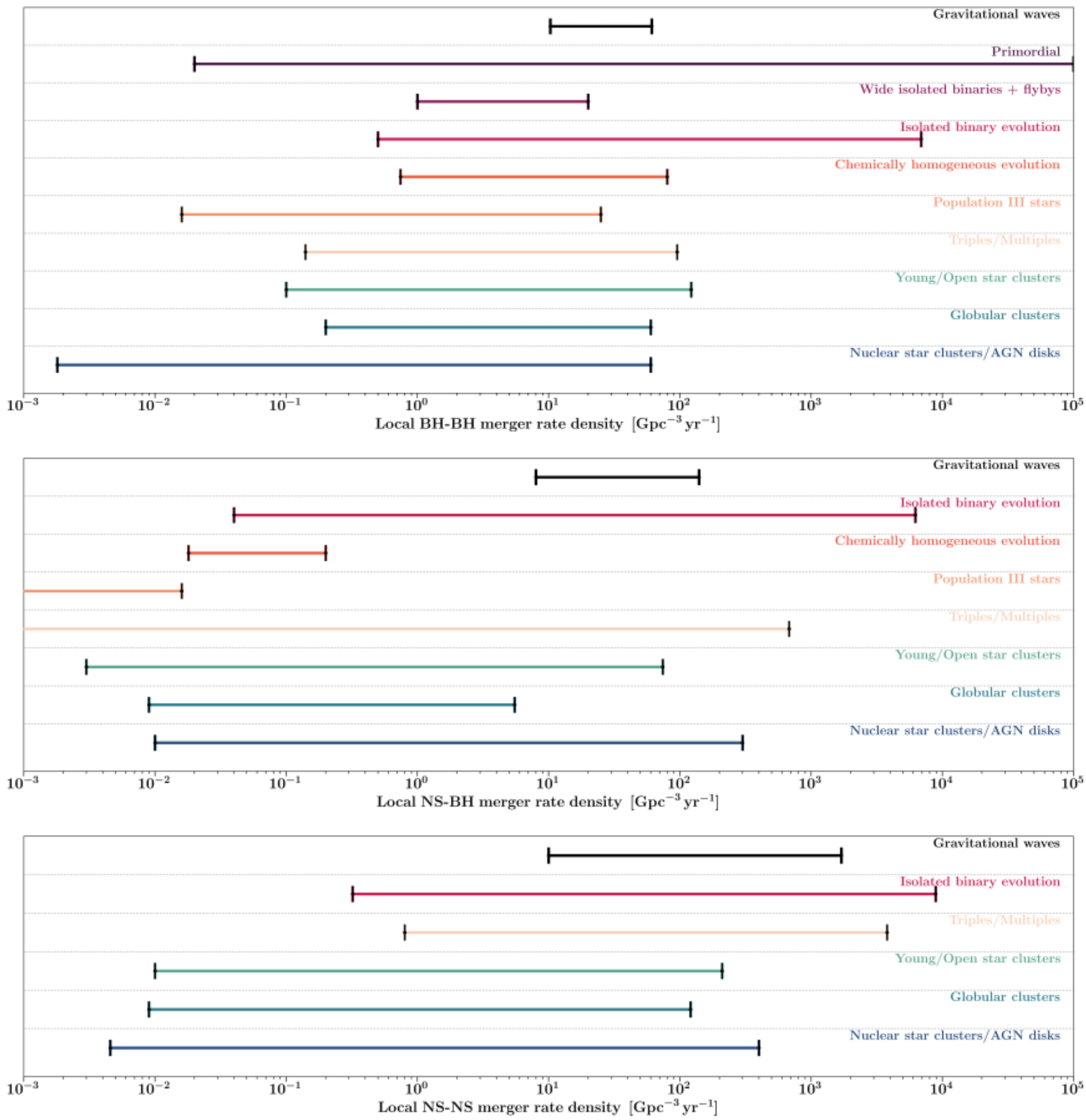

Figure 1.24: Comparison between the local merger rate inferred from GW detections (GWTC-3; Abbott et al. 2023a) and the predictions for BBHs, BHNSs, and BNSs that evolved in different astrophysical environments. Figure taken from Breivik 2025, that summarized the extended review carried out by Mandel & Broekgaarden 2022.

Chapter 2

Wolf-Rayet - compact object binaries as key binary compact object progenitors

Based on:
Korb E., Mapelli M., Iorio G., Costa G., Dall'Amico M.
"Wolf-Rayet–compact object binaries as progenitors of binary compact objects",
2025, A&A 695, A199

Abstract

Binaries with a WR star and a compact object (WR–COs), either a BH or a NS, have been proposed as possible progenitors for the BCO mergers observed with GW detectors. In this work, we use the open source population synthesis code `SEVN` to investigate the role of WR–COs as BCO progenitors. We consider an initial population of 5×10^6 binaries and evolve it across 96 combinations of metallicities, common envelope efficiencies, core-collapse supernova models, and natal kick distributions. We find that WR–COs are the progenitors of most BCOs, especially at high and intermediate metallicity. At $Z = 0.02$, 0.014, and 0.0014, more than $\gtrsim 99\%$ of all BCOs in our simulations evolved as WR–COs. At $Z = 0.00014$, inefficient binary stripping reduces the fraction of BCOs with WR–CO progenitors to $\approx 83 - 95\%$. Despite their key role in BCO production, only $\approx 5 - 30\%$ of WR–COs end their life as BCOs. We find that Cyg X-3, the only WR–CO candidate observed in the Milky Way, is a promising BCO progenitor, especially if it hosts a BH. In our simulations, about $70 - 100\%$ of the Cyg X-3-like systems in the WR–BH configuration (BH mass ≤ 10 $M_\odot$) are BCO progenitors, in agreement with the literature. Future observations of WR–COs similar to Cyg X-3 may be the Rosetta stone to interpret the formation of BCOs.

Keywords: Wolf-Rayet star – black hole – neutron star – gravitational waves – binary evolution – population-synthesis

2.1 Introduction

Wolf-Rayet star–compact object (WR–CO) binaries where a WR star orbits around a BH or a NS are regarded promising progenitor candidates for BCOs that can merge via GW emission within a Hubble time (Belczynski et al. 2012). Indeed, tight WR–CO binaries already host a CO, the WR can end its life as an NS or BH (Limongi & Chieffi 2010; Chen et al. 2015), and the presence of a stripped star (the WR) suggests that likely these systems interacted via at least one mass transfer episode - as expected for BNSs, BHNSs, and BBHs progenitors (see, e.g., Bethe & Brown 1998; Belczynski et al. 2008; Dominik et al. 2012a; Giacobbo & Mapelli 2018; Vigna-Gómez et al. 2020; Belczynski et al. 2020; Bavera et al. 2021; Santoliquido et al. 2021; Broekgaarden et al. 2022; Iorio et al. 2023; Boesky et al. 2024).

Mass transfer episodes can partially or totally remove the external layers of a star, producing a binary stripped star with a modified internal structure and evolution (e.g., Laplace et al. 2020; Laplace et al. 2021, 2025; Schneider et al. 2021, 2023). Stripped stars can form via binary stripping but also via self-stripping, if they have strong stellar winds (typical mass loss rates of WRs are up to $\dot{M} \approx 10^{-4}$ $M_\odot$; see, e.g., Sen et al. 2021; Sabhahit et al. 2022; Sander et al. 2023; Götberg et al. 2023) or are fast rotators (e.g.,with angular velocity that is more than $\gtrsim 60\%$ of the critical one, as in Boco et al. 2025). Regardless of the stripping process, stripped stars can be visible as WRs if they are sufficiently hot (temperature at the sonic point $\gtrsim 40 \times 10^3$ K; Nugis & Lamers 2002; Gräfener & Vink 2013; Gräfener et al. 2017), luminous ($L \gtrsim 10^5$ $L_\odot$ at solar metallicity; Shenar et al. 2020), and exhibit emission line-dominated spectra (e.g., helium, carbon, nitrogen lines; see the review by Crowther 2007). Observations in the Milky Way (MW), Small Magellanic Cloud, and Large Magellanic Cloud (Van Der Hucht 2001; Bartzakos et al. 2001; Foellmi et al. 2003a,b; Schnurr et al. 2008) indicate that binary stripping is a common formation channel for WRs (binary fractions $\gtrsim 40\%$), but it does not become dominant at decreasing metallicity, where stellar winds are weaker. Shenar et al. 2020 argue that the WR binary formation channel has a non-trivial dependence on metallicity and is heavily affected by WR spectral definitions and wind models.

WR–CO systems are one of the possible electromagnetic progenitors of BCOs. So far, seven WR–CO candidates have been observed (see Esposito et al. 2015 and references therein), but their characterization is challenging. The strong WR winds prevent a precise dynamical CO mass measurement, leaving uncertainties on the BH or NS nature. Uncertainties in the CO nature also affect the only WR–CO candidate known in the MW: Cyg X-3 (e.g., Zdziarski et al. 2013; Laycock et al. 2015; Koljonen & Maccarone 2017; Binder et al. 2021). Belczynski et al. 2013 showed that observational and theoretical uncertainties, such as models of core-collapse supernovae (CCSNe) and wind mass loss, significantly affect the possible fates of WR–COs similar to Cyg X-3 and should be taken into account in evolutionary studies.

In this work, we investigate the role of binaries hosting a WR and a CO as BCO progenitors in the isolated evolution scenario. We used the population-synthesis code `SEVN` (Iorio et al. 2023) to simulate the evolution of a binary population similar to the MW one under different conditions. We probed a large parameter space to characterize BCO formation and bracket uncertainties in theoretical models. Key parameters for modeling evolutionary processes, such as mass transfer and CCSNe, are still poorly constrained, and their impact on the demography of BCOs is large (see the reviews by Mapelli 2021 and Mandel & Broekgaarden 2022, and references therein). Here, we systematically explore the role of stellar metallicity, CE ejection efficiency, CCSN physics, and natal kicks. We also discuss the impact of uncertainties in mass transfer physics on the WR–CO and BCO formation channels. Eventually, we consider the implications for BH spins in the case of tidal spin-up.

This Chapter is organized as follows. In Section 2.2 we describe the features of `SEVN` relevant to this work and the assumptions on the parameter space. In Section 2.3 we present the results of our simulations and a comparison with Cyg X-3. In Section 2.4 we discuss the impact of mass transfer assumptions, BH tidal spin-up, and other aspects of our parameter-space exploration. In Section 2.5 we summarize our results.

2.2 Methods

2.2.1 The `SEVN` code

We performed our simulations using the `SEVN` population-synthesis code (Spera et al. 2015; Spera & Mapelli 2017; Spera et al. 2019; Mapelli et al. 2020; Iorio et al. 2023). `SEVN` interpolates stellar properties from a grid of pre-computed stellar tracks and implements binary evolution processes through analytic and semi-analytic models. We report hereafter only the assumptions most relevant for this Chapter; we refer to Iorio et al. 2023 and to Section 1.6.2 for a more detailed discussion about `SEVN`.

2.2.2 WR definition

WR stars: an observational definition

Ever since their discovery, WR stars are a class of stellar objects characterized by the presence of strong emission lines in their spectra (Wolf & Rayet 1867). Stellar spectra usually exhibit a continuum with narrow absorption lines because the hot radiation coming from the interior is absorbed by atoms and molecules in a cooler stellar photosphere ($T_{\rm eff} \lesssim 60$ kK in the hotter O-type stars). However, WR stars have a much hotter photosphere ($T_{\rm eff} \sim 60-100$ kK) and host many heavy elements (like He, N, C or O), often in an ionized state. Therefore, atoms and ions in the photosphere strongly interact with the energetic photons coming from the interior, producing recombination and fluorescence emission lines (visible in the UV, optical and near-IR bands) while efficiently absorbing the momentum of photons via multiple-scatterings. The net effect is the production of a very dense and strong wind ($\dot{M} \sim 10^{-4} - 10^{-5}$ M$_\odot$ yr^{-1}) with broad emission lines of elements and ions usually absent in other stellar spectra (for more details we refer to Smith et al. 1996 and references therein).

Given their peculiar nature, WR stars are objects commonly defined based on their surface abundance and spectral characteristics. For instance, WR are generally distinguished into three sub-types: WN (strong lines of helium and nitrogen), WC (strong lines of helium, carbon and less prominent lines of oxygen) and WO (strong lines of oxygen and less prominent lines of helium and carbon). In particular, WN stars can be further divided into two subfamilies on the basis of their surface hydrogen abundance X: WNL (late) if $X \gtrsim 0.5$ or WNE (early) if $X \lesssim 0.5$ (see Crowther 2007 for a complete discussion). If spectra are not available, WR stars can be roughly defined as very hot and luminous stars with optically thick winds. There is not a standard classification of WR stars based on these parameters, but as an order of magnitude it is possible to consider a star as a WR if its effective temperature is above $\log(T_{\rm eff}/{\rm K}) \gtrsim 4$ (Eldridge et al. 2008), its luminosity is above $\log(L/\,{\rm L}_\odot) \gtrsim 4.9$ (Shenar et al. 2020), and its winds are optically thick (optical depth $\tau > 1$), as assumed for instance in Dall'Amico et al. 2025.

Shenar 2024 point out that the sole adoption of temperature and luminosity thresholds for WR classification can reveal two distinctive types of WR stars. The first type corresponds to the "classical" WR stars (hereafter, cWRs) that are burning helium in their cores, were partially or completely stripped of their H-rich envelope, and have a mass between $8 \ \mathrm{M}_\odot \lesssim \mathrm{M}_\mathrm{WR} \lesssim 20 \ \mathrm{M}_\odot$. About $\approx 90\%$ of WR stars are expected to be cWRs. The second type of WRs are MS-WRs, namely MS stars that are so massive $\gtrsim 80 - 100 \ \mathrm{M}_\odot$ that they are already as hot and luminous as a WR (de Koter et al. 1997). These MS-WRs appear as H-rich WR stars and are expected to constitute $\approx 10\%$ of the WR population. So far, observations of MS-WRs in binary systems of the Tarantula Nebula revealed that they can have masses of $\approx 100 - 150 \ \mathrm{M}_\odot$ (e.g., Shenar et al. 2021; Bestenlehner et al. 2022).

WR stars: a mass-based definition for `SEVN`

`SEVN` does not model the spectral emission of stars directly and does not follow the evolution of the surface chemical composition that could occur, for instance, after mass transfer events. Therefore, in this work we do not use a spectrum-based definition for WRs but we approximate it with a mass-based definition that follows the properties of the WN sub-type at Galactic metallicity and the WR spectral models elaborated with the `PoWR` code (Hamann & Gräfener 2004; Hainich et al. 2014). In particular, we assume that a WR star is a helium star: a core-He or shell-He burning star with helium core mass constituting most of its stellar mass ($M_\text{He-core} \geq 97.9\% \ M_\text{star}$). From an observational point of view, helium stars are stripped-stars that may or may not already exhibit the spectral features of WRs (Shenar et al. 2020). Therefore, adopting this definition we pose an upper limit on the number of cWRs predicted by our simulations. On the other hand, we acknowledge that this definition assumes that WRs have a negligible residual hydrogen envelope, thus, it does not include massive H-rich MS-WRs. However, as discussed in the previous paragraph, most ($\approx 90\%$) WRs are believed to be cWRs, so we expect that the underestimation of the MS-WR contribution will not significantly affect our results.

2.2.3 Stellar tracks

We interpolate stellar properties from two sets of tracks: H-rich stars and pure-Helium stars. These tracks were calculated with the `PARSEC` stellar evolution code (Bressan et al. 2012; Chen et al. 2015; Costa et al. 2019; Nguyen et al. 2022; Costa et al. 2025), with the version described in Costa et al. 2025.

H-rich stars evolved from the pre-main sequence (pre-MS) to the end of the carbon burning phase. In such models, the mass-loss rate of hot massive stars depends on both stellar metallicity and the Eddington ratio (Vink et al. 2000, 2001; Gräfener & Hamann 2008; Vink et al. 2011). Specifically, WR winds follow the prescriptions presented by Sander et al. (2019), with the additional dependence on metallicity adopted by Costa et al. (2021). In this work, we consider the fiducial set of `PARSEC` tracks for `SEVN`, namely, the set calculated with convective overshooting parameter $\lambda_\text{ov} = 0.5$ (Iorio et al. 2023).

Pure-Helium stars evolved from a He-ZAMS to the end of the carbon burning phase. He-ZAMS stars are initialized accreting mass on a $0.36 \ \mathrm{M}_\odot$ He core, obtained by removing the H-rich envelope from the progenitor star when it started the He-core burning phase. The initial metallicity (Z) determines the initial helium mass fraction ($Y = 1 - Z$) of stars in the He-ZAMS. Winds of pure-Helium stars follow Nugis & Lamers 2000. In this work, we used this set of pure-Helium tracks to interpolate the properties of the He-stars that we used as a proxy for WRs. For more details on the `PARSEC` tracks adopted in this work, we refer to Costa et al. 2025 and Iorio et al. 2023.

2.2.4 CCSN models

In this work, we tested three CCSN models for CO formation: the rapid and delayed ones proposed by Fryer et al. (2012) and a compactness-based model that uses a compactness parameter (e.g., O'Connor & Ott 2011), as done in Mapelli et al. 2020. The three models calculate the remnant mass as a function of the carbon-oxygen core mass at the end of the carbon burning phase ($M_{\text{CO-core}}$).

Regardless of the CCSN model, in this work, we used the fiducial `SEVN` classification for COs (Iorio et al. 2023): we considered a remnant a BH if its mass is $M_{\text{rem}} \geq 3\ \text{M}_\odot$, and an NS otherwise.

Rapid and delayed CCSN models

The rapid and delayed models assume that the shock is revived by the energy accumulated by neutrinos in a convective region between the infalling external layers and the surface of the proto-NS. Fryer et al. (2012) distinguish rapid or delayed explosions considering shocks revived < 250 ms or > 500 ms after the core bounce, respectively. In both models, the remnant mass M_{rem} is expressed as

$$M_{\text{rem}} = M_{\text{proto}} + f_{\text{fb}}\ (M_{\text{star}} - M_{\text{proto}}), \tag{2.1}$$

where f_{fb} (fallback parameter) is the fraction of stellar mass M_{star} that falls back to the proto-compact object (M_{proto}). Both f_{fb} and M_{proto} are functions of $M_{\text{CO-core}}$. The heaviest stars ($M_{\text{CO-core}} \geq 11\ \text{M}_\odot$) always undergo a direct collapse, accreting all the ejected material ($f_{\text{fb}} = 1$) and forming a BH.

Compactness-based CCSN model

The compactness-based CCSN model tested in this work uses the compactness parameter $\xi_{2.5}$ (O'Connor & Ott 2011) as a proxy for the explodability of stellar cores. The parameter $\xi_{2.5}$ is defined as the ratio between a reference mass (2.5 $\text{M}_\odot$ here) and the radius that encloses such a mass at the beginning of the core-collapse. In `SEVN`, we calculate $\xi_{2.5}$ following the fit derived by Mapelli et al. 2020 on non-rotating stellar tracks generated with the `FRANEC` code (Limongi & Chieffi 2018):

$$\xi_{2.5} = \frac{M = 2.5\ \text{M}_\odot /\ \text{M}_\odot}{R(M = 2.5\,\text{M}_\odot)\ /1000\ \text{km}} = 0.55 - 1.1 \left(\frac{M_{\text{CO-core}}}{1\ \text{M}_\odot} \right)^{-1.0} . \tag{2.2}$$

Several studies suggest that there is a complex relation between the compactness parameter and the carbon-oxygen core mass (e.g., Sukhbold et al. 2018; Patton & Sukhbold 2020; Chieffi & Limongi 2020; Schneider et al. 2021, 2023). In this work, we followed the approach of Mapelli et al. 2020, based on the results of Limongi & Chieffi 2018, and considered a monotonic relation.

Here, we assumed that if $\xi_{2.5} \leq 0.35$ ($M_{\text{CO-core}} \leq 5.5\ \text{M}_\odot$), the CCSN is successful and produces an NS. The NS mass was drawn from a Gaussian distribution centered at 1.33 $\text{M}_\odot$, with a standard deviation of 0.09 $\text{M}_\odot$ and the minimum NS mass set at 1.1 $\text{M}_\odot$, in agreement with the NS observations in binaries (Özel & Freire 2016). If $\xi_{2.5} > 0.35$, the star collapses directly to a BH, with mass M_{BH},

$$M_{\text{BH}} = M_{\text{He}} + f_{\text{H}}\ (M_{\text{star}} - M_{\text{He}}), \tag{2.3}$$

where $M_{\rm He}$ is the He-core mass at the ignition of carbon burning and $f_{\rm H}$ is the fraction of the residual hydrogen-rich envelope that collapses to a BH. The amount of $f_{\rm H}$ is substantially unconstrained. The work of Fernández et al. (2018) shows that it depends on the binding energy of the envelope at the onset of core collapse. Hence, our choice of $f_{\rm H} = 0.9$ should be regarded as a crude approximation that accounts for the possibility that some (10%) of the infalling material is not accreted even in the case of direct collapse, for instance because small shocks triggered by neutrinos helped to unbind the envelope (Renzo et al. 2020a; Costa et al. 2022, e.g.,).

2.2.5 Natal kicks

Observations of CO proper motions indicate that COs receive a kick at their birth (Hobbs et al. 2005; Verbunt et al. 2017; Atri et al. 2019; Igoshev 2020; Disberg & Mandel 2025). Moreover, the binary itself will receive a recoil kick in the center of mass when some mass leaves the system (Blaauw kick, Blaauw 1961). `SEVN` includes both Blaauw and supernova kicks in its natal kick calculation. Hereafter, we will present the supernova kick models that we adopted in this thesis and that were derived from the *hobbs pure*, *hobbs*, and *unified* options available in `SEVN` (Iorio et al. 2023).

We tested four models for the magnitude of the kicks. We followed the observations of Hobbs et al. 2005 on pulsar and of Atri et al. 2019 on BHs. Moreover, we accounted for the Fryer et al. 2012 and Giacobbo & Mapelli 2020 description of fallback and angular momentum conservation, respectively. We refer to the corresponding models with the acronyms M265, M70, Mfb, and G20.

Hobbs et al. (2005) fitted the proper motions of young pulsars in the MW with a Maxwellian function with root-mean-square (rms) velocity $\sigma = 265$ km s^{-1}. Atri et al. (2019) measured the proper motions of BHs in X-ray binaries and fitted their velocity distribution with a Maxwellian with a mean of 107 ± 16 km s^{-1}, corresponding to a rms of $\sigma = 70$ km s^{-1}. Since both Hobbs et al. 2005 and Atri et al. 2019 use single Maxwellians, in both the M265 and M70 models we assign kick magnitudes drawing random numbers from a Maxwellian distribution, adopting a rms of $\sigma = 265$ km s^{-1} and $\sigma = 70$ km s^{-1}, respectively. We highlight that, as noted by Disberg & Mandel 2025, the distribution found by Hobbs et al. 2005 is likely over-estimating by $\sim 50\%$ the pulsar natal kick velocities. However, since the Hobbs et al. 2005 model has been extensively tested in population-synthesis studies and serves as a reference model for other natal kick models (e.g., Fryer et al. 2012; Giacobbo & Mapelli 2020; Mandel & Broekgaarden 2022), we included it in this study in order to facilitate the comparison with other works in the literature and to provide an upper limit to the effects of strong natal kicks.

Fryer et al. (2012) assumed that the kick is distributed according to a Maxwellian function with $\sigma = 265$ km s^{-1}, modulated by the fraction $f_{\rm fb,CCSN}$ of mass that falls back onto the proto-NS:

$$v_{\rm kick} = f_{\sigma=265}\,(1 - f_{\rm fb,CCSN}), \tag{2.4}$$

where f_σ is a random number extracted from the Maxwellian curve. In our simulations with the Mfb model, we choose $f_{\rm fb,CCSN}$ consistently with the CCSN model (see Appendix 2.6.1).

In the G20 model, we followed Giacobbo & Mapelli 2020 and re-scaled the kicks drawn from the M265 model:

$$v_{\rm kick} = f_{\sigma=265} \frac{\langle M_{\rm NS} \rangle}{M_{\rm rem}} \frac{M_{\rm NS}}{\langle M_{\rm ej} \rangle}, \tag{2.5}$$

where $\langle M_{\rm NS} \rangle$ and $\langle M_{\rm ej} \rangle$ are, respectively, the average NS mass and ejecta mass (their values are sensitive to the single stellar evolution and CCSN model assumed).

2.2.6 Binary evolution and mass transfer

Binary evolution processes - such as mass transfer, collisions, and tides - are modeled in `SEVN` following Hurley et al. 2002, with a few differences thoroughly described by Iorio et al. 2023. Hereafter, we summarize the assumptions for mass transfer processes.

A star expanding beyond its Roche lobe donates its mass to the companion in a RLO process. We assume that mass transfer is not-conservative and that half of the transferred mass is not accreted by the companion. The non-accreted mass is re-emitted in the form of isotropic wind from the vicinity of the accretor, removing a fraction of the orbital angular momentum (Soberman et al. 1997).

As in Hurley et al. 2002, we determine RLO stability by computing the donor-to-accretor mass ratio $q = M_{\rm d}/M_{\rm a}$ and comparing it with a set of critical thresholds $q_{\rm c}$. If $q > q_{\rm c}$, mass transfer becomes unstable and we either assume that the two stars merge directly (e.g., if they both fill their Roche lobe), or we start a phase of CE. For a donor star in the MS or HG phase, we assume $q_{\rm c} = \infty$, since such stars have radiative envelopes, which are less likely to develop unstable mass transfer (Ge et al. 2010, 2015). We adopt the same $q_{\rm c}$ values as Hurley et al. 2002 for stars in more advanced burning stages. We follow their fit on models of condensed polytropes (Hjellming & Webbink 1987) for giant stars with deep convective envelopes; we set $q_{\rm c} = 3.0$ for core-Helium burning stars (both H-rich and pure-Helium ones), and we use $q_{\rm c} = 0.784$ for pure-Helium stars with active He-shell burning.

We describe the orbital changes due to CE with the usual two parameters $\alpha_{\rm CE}$ and $\lambda_{\rm CE}$ (Webbink 1984). Here, the parameter $\alpha_{\rm CE}$ is the fraction of the orbital energy that is transferred to the envelope, while $\lambda_{\rm CE}$ describes the concentration of the donor's profile. For H-rich stars, we use the fits to $\lambda_{\rm CE}$ proposed by Claeys et al. 2014, while for pure-Helium stars we assume $\lambda_{\rm CE} = 0.5$ (Iorio et al. 2023). According to the original formalism (Webbink 1984), the envelope is ejected when the orbital energy lost by the binary is equal to the envelope binding energy. Thus, $\alpha_{\rm CE}$ cannot be greater than one. However, orbital energy is not the only source of energy that can be used to eject the CE. Efficient recombination of H and He inside the envelope reduces its binding energy, facilitating its removal. This and other additional sources of energy should be taken into account when modeling CE evolution (e.g., Paczyński & Ziółkowski 1968; Han et al. 1994, 1995; Ivanova et al. 2013; Klencki et al. 2021; Röpke & De Marco 2023). Thus, in this work, we also explored values of $\alpha_{\rm CE} > 1$.

2.2.7 Simulations and parameter space

We wanted to characterize the impact of different physical assumptions on the formation and fate of WR–COs. Thus, we fixed our initial binary population and evolved it across 96 combinations of parameters and models. We generated a population of 5×10^6 massive binary stars with initial mass, mass ratio, orbital period, and eccentricity drawn from

Table 2.1: Explored combinations of CCSN and natal kick models.

CCSN \ Kick	M265	M70	Mfb	G20
Delayed	dM265	dM70	dMfb	dG20
Rapid	rM265	rM70	rMfb	rG20
Compactness	cM265	cM70	cMfb	cG20

observationally motivated distributions (Kroupa 2001; Sana et al. 2012; Moe & Di Stefano 2017), as described in Appendix 2.6.2.

We chose four possible values for the metallicity ($Z = 0.02$, 0.014, 0.0014, 0.00014) and two possible values for the fraction $\alpha_{\rm CE}$ of the orbital energy required to eject the CE ($\alpha_{\rm CE} = 1$, 3). For each $(Z, \alpha_{\rm CE})$ pair, we explored twelve combinations of CCSN and natal kick models: the rapid, delayed, and compactness-based CCSN models, and the M265, M70, Mfb, and G20 natal kick models. In Table 2.1 we summarize these combinations and we report the correspondent acronyms.

2.3 Results

2.3.1 Most BCOs form from WR–CO systems

For every combination of natal kick, CCSN model, metallicity, and CE efficiency explored in this work (Table 2.1), we find that most BNSs ($\gtrsim 99\%$), BHNSs ($\gtrsim 93\%$), and BBHs ($\gtrsim 79\%$) evolved as WR–BHs or WR–NSs before becoming BCOs (Figure 2.1). In each set, more than $\gtrsim 83\%$ of the total BCO population had a WR–CO progenitor.

Metallicity (Z) and CE efficiency ($\alpha_{\rm CE}$) are the quantities that influence more the fraction $f_{\rm from}$ of BCOs with a WR–CO progenitor. Here, we calculated $f_{\rm from}$ as the ratio between the number of BCOs with a WR–CO progenitor (WR–BH or WR–NS) and the total number of BCOs (BBHs, BHNSs or BNSs) in each set. If we fix a pair of $(Z, \alpha_{\rm CE})$ values and consider the distribution of $f_{\rm from}$ across the explored combinations of CCSN and natal kick models, we find that nearly every ($\gtrsim 99\%$) BCO at $Z \geq 0.0014$ evolved through the WR–CO configuration. At $Z = 0.00014$, only $\approx 83 - 95\%$ of BCOs followed this formation scenario (the range indicates values within the 68% credible intervals, Figure 2.2). The decrease of the fraction of BCOs with a WR–CO progenitor at low Z is determined by inefficient stripping of the WR and by the combined effect of CCSN and natal kicks models.

BHNS progenitors

For all the metallicities explored in this work, we find that BHNSs generally form a BH as first CO (Figure 2.1). Evolution through the WR–BH configuration is increasingly favoured for BHNSs at lower metallicities, becoming the dominant ($\gtrsim 95\%$) formation channel at $Z = 0.00014$. For decreasing metallicities, stellar winds are weaker and stars are able to retain more mass (Vink et al. 2011). At $Z = 0.00014$, BH production is favoured while NSs require one or more CE events to be produced. Assuming a low CE efficiency ($\alpha_{\rm CE} = 1$) completely suppresses the WR–NS channel for BHNSs at $Z = 0.00014$.

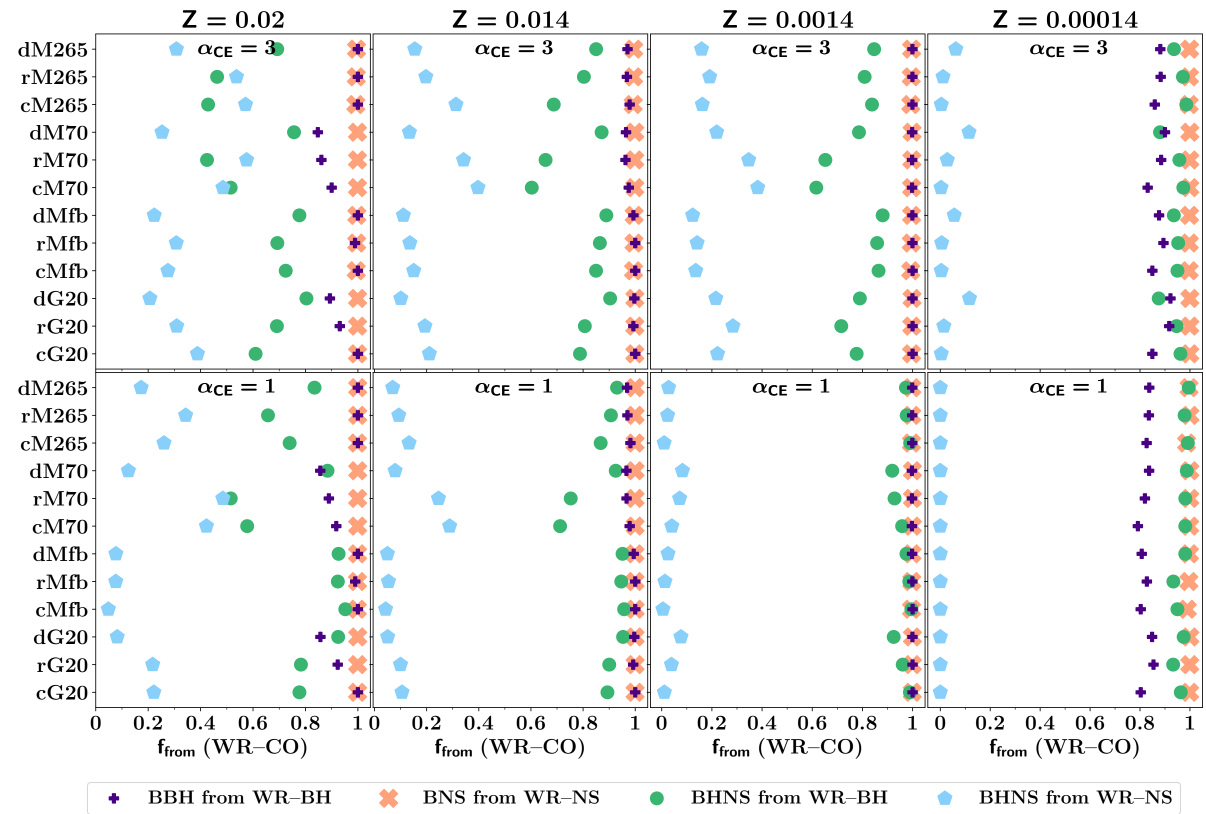

Figure 2.1: Fraction f_{from} of BCOs with WR–CO progenitors for all the metallicities (columns), α_{CE} efficiencies (rows), and combinations of CCSN and natal kick models tested in this work (horizontal entries, see Table 2.1). We distinguish BCOs into BBHs, BNSs and BHNSs; WR–CO progenitors into systems with a WR star and a BH or NS.

Remnant masses, thus their BH or NS nature, are sensitive to the model of CCSN adopted. Assuming different natal kick models influences the natal kick magnitudes and the possibility that a binary is able to survive or merge via GW emission (Figure 2.3). Thus, the abundance of the WR–BH channel over the WR–NS one is sensitive to different combinations of CCSN and natal kick models. For each pair of $(Z, \alpha_{\mathrm{CE}})$, we find variations up to 40% in the fraction of BHNSs that evolved as WR–BHs in place of WR–NSs. These variations are larger at solar metallicity ($Z = 0.02, 0.014$).

"Missing" WR–BHs

For each pair of $(Z, \alpha_{\mathrm{CE}})$, binary evolution is determined by the initial orbital properties only until the formation of the first CO. CCSNe impart a natal kick on the newly born CO, modifying the post-CCSN orbital properties, the following evolution of the system, and the possibility that it becomes a BCO and merges within a Hubble time (Peters 1964). As shown in Figure 2.1, the influence of CCSN and natal kicks is usually negligible ($\Delta f_{\mathrm{from}} \lesssim 0.01$), except for BHNSs and BBHs at $Z = 0.00014$, and BBHs at solar metallicity $Z = 0.02, 0.014$ (variations can be up to $\Delta f_{\mathrm{from}} \lesssim 0.15$). These systems can avoid the WR–CO configuration but still produce BCOs.

Weak stellar winds disfavour the production of WRs via self-stripping, especially at the lowest metallicity explored in this work: $Z = 0.00014$. In our simulations, most

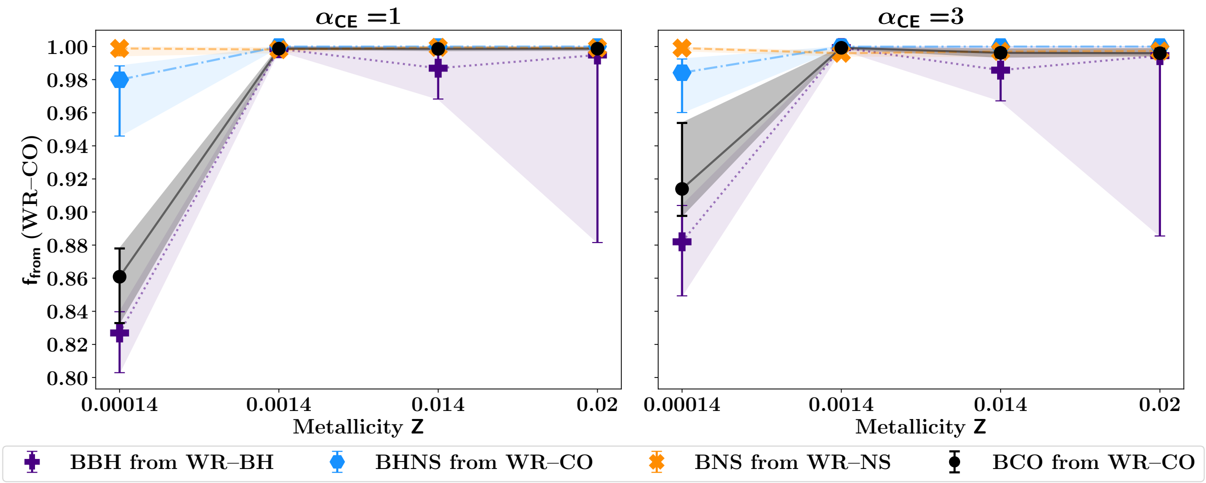

Figure 2.2: Median fractions f_{from} of BCOs with WR–CO progenitors as a function of metallicity Z and common envelope efficiency α_{CE}. Left (Right) plot shows the $\alpha_{\text{CE}} = 1$ ($\alpha_{\text{CE}} = 3$) case. We distinguish fractions f_{from} of BBHs evolved as WR–BHs (purple dotted lines, plus sign markers), BNSs evolved as WR–NSs (orange dashed lines, cross sign markers), BHNSs evolved as either WR–NSs or WR–BHs (blue dash-dotted lines, hexagon markers). We also show the fraction of all BCOs with a WR–CO progenitor (black lines, round markers). For each (Z, α_{CE}) pair and BCO type, we consider the distribution of the 12 f_{from} fractions of the correspondent simulated sets (combinations of CCSN and natal kick models, see Table 2.1), and we show their median values (scatter points) and 68% credible intervals (error bars).

($\approx 60 - 80\%$) BCOs are BBHs at sub-solar metallicity ($Z = 0.0014, 0.00014$). Thus, the lower fraction of BCOs with WR–CO progenitors at $Z = 0.00014$ is determined by the lower fraction of BBHs with WR–BH progenitors.

Binary black holes can form without passing through a WR–BH phase if they experience the second CCSN event while the non-degenerate star is still transferring mass to its BH companion. At low metallicity, if the mass transfer stops before the donor's envelope is completely stripped, the donor star cannot become a WR and the system becomes a BBH avoiding the BH-WR stage. We find that these "missed WRs" still retain a hydrogen-envelope at the end of their life. Residual envelope masses range from $\approx 50\%$ to almost $\approx 2\%$ of the total stellar mass, indicating that the most stripped stars were almost WRs according to the definition adopted in this work (He-core mass $M_{\text{He-core}} \geq 97.9\%\ M_{\text{star}}$, Section 2.2.2).

2.3.2 Formation channels of BCOs from WR–CO systems

When present, the WR–CO configuration always constitutes the last evolutionary stage before BCO formation. Figure 2.4 shows the formation channels of BCOs with WR–CO progenitors for the $\alpha_{\text{CE}} = 3$ case (the $\alpha_{\text{CE}} = 1$ case is shown in the Appendix 2.7.1). We distinguish four channels according to the type of mass transfer events occurring prior to the WR–CO formation: evolution through stable mass transfer only, CE phases only, at least one stable mass transfer and one CE event, no mass transfer at all.

Every family of WR–COs to BCOs (WR–BHs to BBHs, WR–BHs to BHNSs, WR–NSs to BHNSs, and WR–NSs to BNSs) exhibits a preferential formation pathway for a fixed

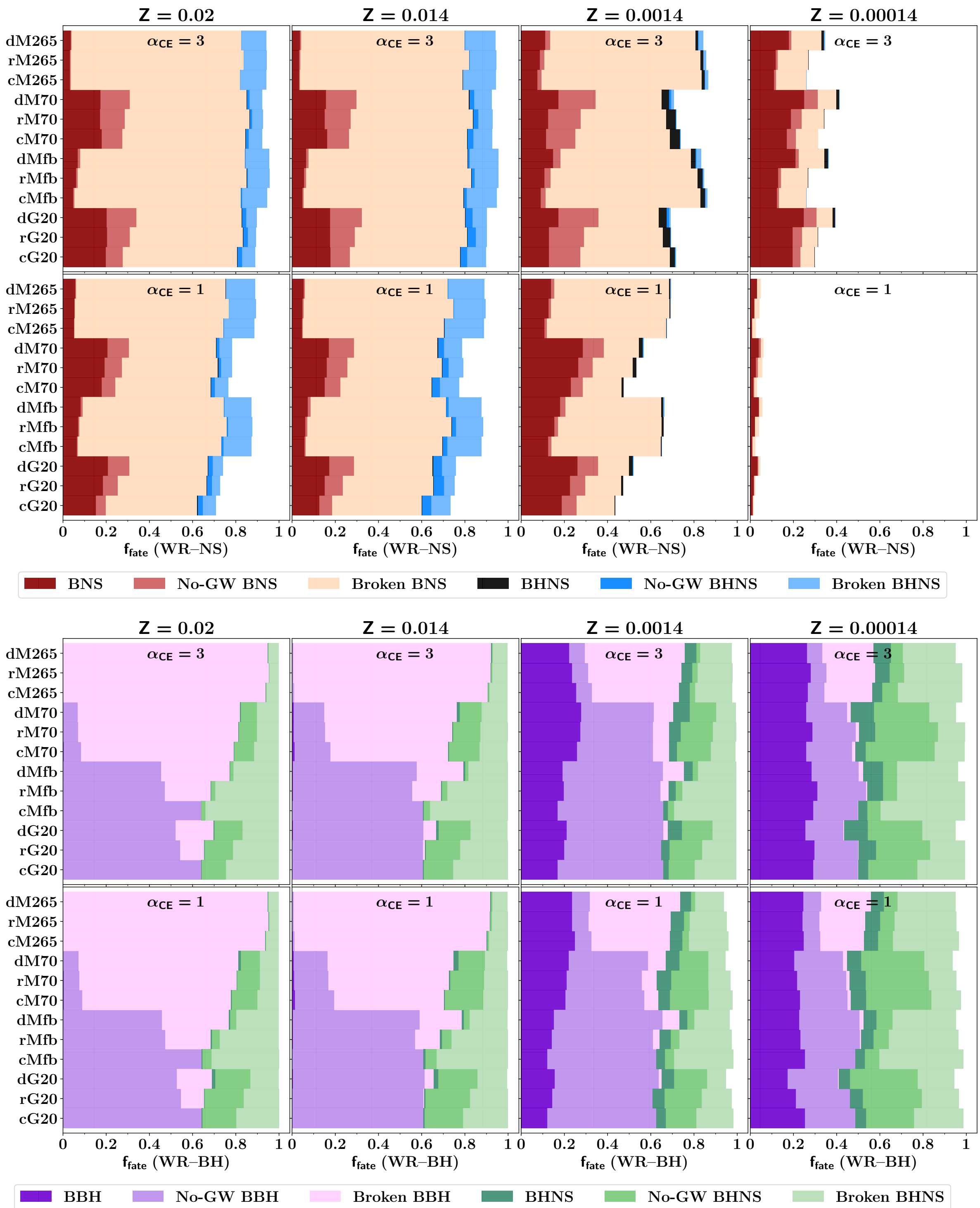

Figure 2.3: Upper (lower) panels: Fraction $f_{\rm fate}$ of WR–NSs (WR–BHs) producing a BCO (darkest shades), a bound but not merging BCO (intermediate shades), or resulting in binary ionization (lightest shades). The remaining fraction of WR–NSs (WR–BHs) merges after a collision or a CE episode (not plotted). Each set of panels shows the same fraction $f_{\rm fate}$ for all the metallicities (columns), $\alpha_{\rm CE}$ (rows), and combinations of CCSN and natal kick models (horizontal entries; see Table 2.1).

metallicity (Figure 2.4). CCSNe, natal kick assumptions, and CE efficiency $\alpha_{\rm CE}$ do not impact the relative fraction of possible formation channels as much as metallicity does. Thus, in Figure 2.5 we considered the fiducial sets (simulated with delayed CCSN, G20 natal kick models, and $\alpha_{\rm CE} = 3$) to illustrate the main features of the formation channels for these WR–COs at solar ($Z = 0.02$) and sub-solar ($Z = 0.00014$) metallicity.

WR–COs that are BCO progenitors generally form after one or more mass transfer episodes. Stable mass transfer episodes or CE events favour the stripping of the WR star and can reduce the orbital separation, facilitating the production of both a WR–CO binary and a system that merges via GW emission within a Hubble time. Only a few ($\lesssim 8\%$) BBH progenitors at solar metallicity form without exchanging mass. This sub-population of non-interacting binaries has wide orbits ($a \gtrsim 10^2 \ \ R_\odot$) and is able to merge only if the natal kick induced by the second CCSN boosts the eccentricity significantly ($e \gtrsim 0.9$). Such *lucky kicks* are more frequent for the M70 and G20 natal kick models at $Z = 0.02$.

The stability and duration of the mass transfer phases depend on several factors (e.g., donor mass, mass ratio, stellar radius, stellar phase, and orbital separation) and are influenced by metallicity (e.g., Ge et al. 2024). Thus, as shown in Figure 2.5, there are many possible formation pathways for WR–COs, with large variability in the number and type of stable mass transfer or CE episodes required. However, we can distinguish two main scenarios, corresponding to WR–COs that are produced in a "direct" or "indirect" way.

In the "direct" scenario, both stars have a similar ZAMS mass ($M_{2,\rm ZAMS} \gtrsim 0.9\ M_{1,\rm ZAMS}$). The primary star initiates a CE event (eventually after other mass transfer episodes) when it is already burning helium in its core, whereas the secondary is either close to ignite it (end of the red giant branch phase) or is also already burning it. If the CE is successfully ejected, the post-CE configuration consists of two helium cores orbiting about each other: a WR–WR binary has formed. Since the two progenitor stars were already close to the end of their lives, shortly after the end of the CE ($\lesssim 3 \times 10^5$ yr) the initially more massive star (primary at ZAMS) becomes a CO, forming a WR–CO. If the post-CE orbit is tight enough ($a \lesssim 3 - 4\,\rm R_\odot$), the most massive WR can overfill its Roche lobe and initiate additional short ($\lesssim 5 \times 10^4$ yr) stable mass transfer events before the first CO formation.

In the "indirect" scenario, the WR–CO does not evolve through the WR–WR configuration. The primary star can still experience one or more mass transfer phases as donor star, but at the time of the first CO formation, the secondary companion is not yet a WR. Thus, in this scenario, the secondary star can donate mass to the CO before entering the WR–CO configuration. This scenario is the most common one to produce WR–COs and generally requires the WR progenitor to start a CE episode, in particular at sub-solar metallicity (Figure 2.5).

Once the WR–CO phase is reached, binaries might undergo wind-fed accretion, but they will not experience other mass transfer events to produce BCOs. RLO and CE episodes after the WR–CO phase are common only among WR–COs with light COs, namely WR–NSs or WR–BHs with light BHs, as are the ones produced with the delayed CCSN model ($\sim 3 - 6\ \rm M_\odot$). Light compact remnants imply long timescales to merge via GW emission (Peters 1964). Thus, to produce a BCO able to merge within a Hubble time, the orbit often has to shrink via mass transfer events: a stable mass transfer phase is generally sufficient for WR–BHs hosting heavier BHs ($\gtrsim 6\ \rm M_\odot$), especially at lower metallicities (Figure 2.4), while a CE is preferred if an NS is involved.

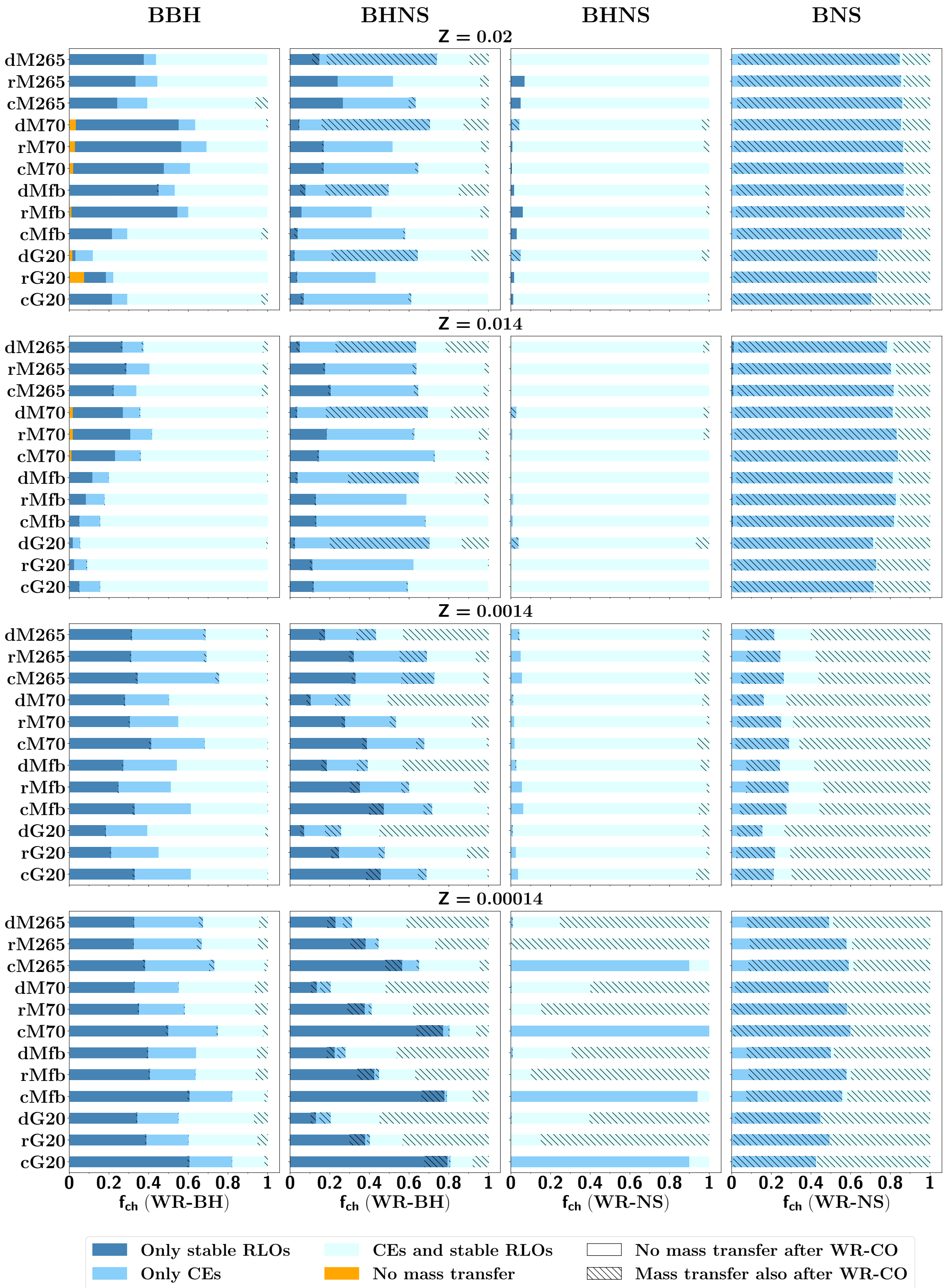

Figure 2.4: Fraction of BCOs with WR–CO progenitors evolved through different formation channels for different metallicities (rows) and combinations of CCSN and natal kick models explored in this work (Table 2.1). Here, we show the $\alpha_{\rm CE} = 3$ case. We distinguish four main evolutionary paths based on mass transfer events that occurred before the WR–CO formation: stable mass transfer only, CEs only, at least one stable and one unstable mass transfer, no mass transfer. Hatched bars indicate WR–CO systems that become BCOs experiencing at least one additional mass transfer event (stable or unstable RLO) after the WR–CO phase.

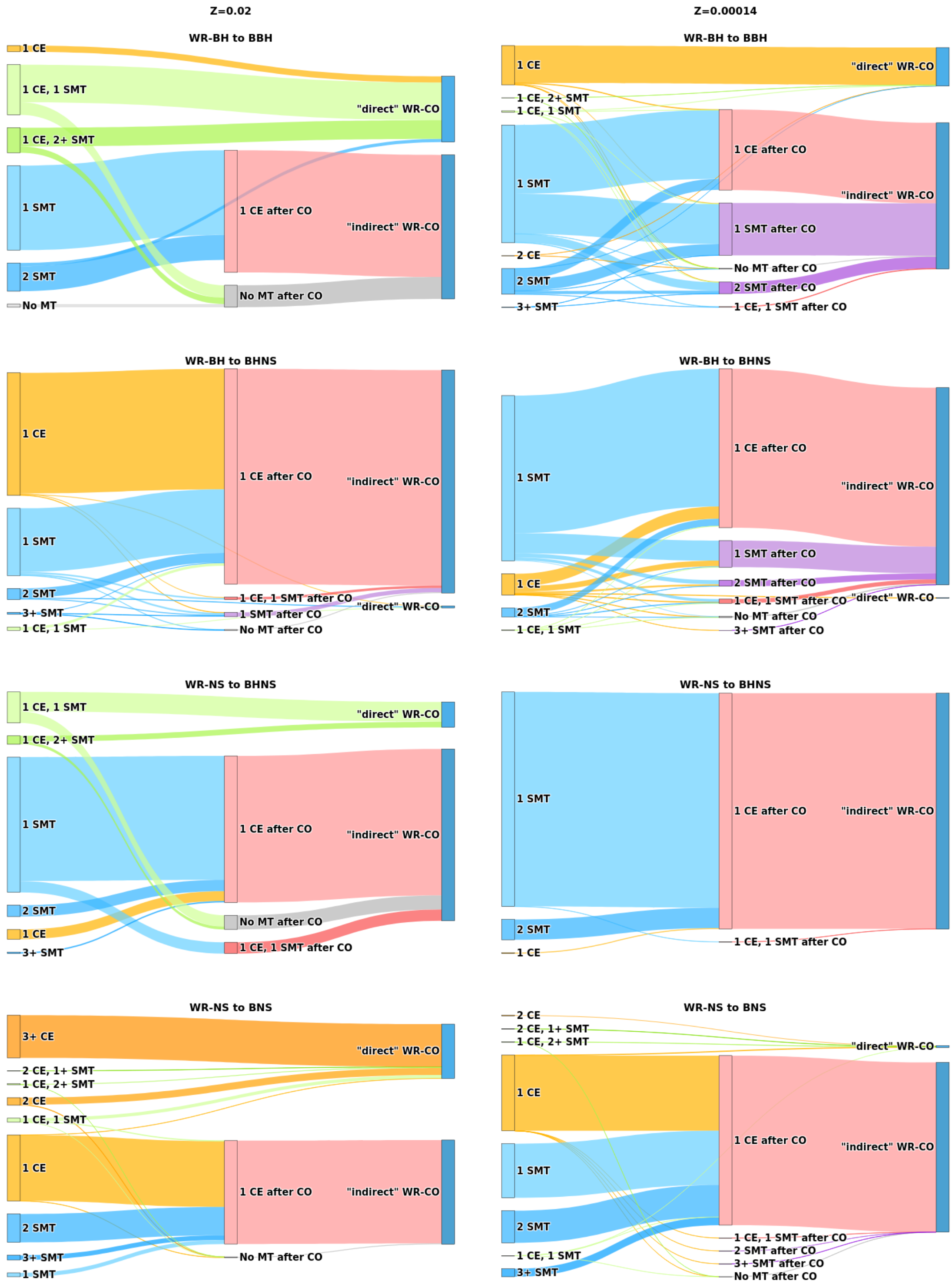

Figure 2.5: Sankey diagram illustrating formation channels of WR–COs that are also BCO progenitors. We show our fiducial sets, simulated assuming a delayed CCSN model, G20 natal kick model, and $\alpha_{\rm CE}$ =3; for solar ($Z = 0.02$, left) and sub-solar ($Z = 0.00014$, right) metallicity. We distinguish "direct" WR–COs from "indirect" WR-COs. "Direct" WR–COs are produced by a WR-WR post-CE binary; "indirect" WR-COs avoid the WR-WR evolution. Unlike "direct" WR–COs, WR progenitors in "indirect" WR–COs have the possibilty to start a stable mass transfer (indicated with SMT) or a CE phase between the first CO formation and the WR–CO phase. Few "indirect" systems avoid further mass transfer (indicated with MT) episodes.

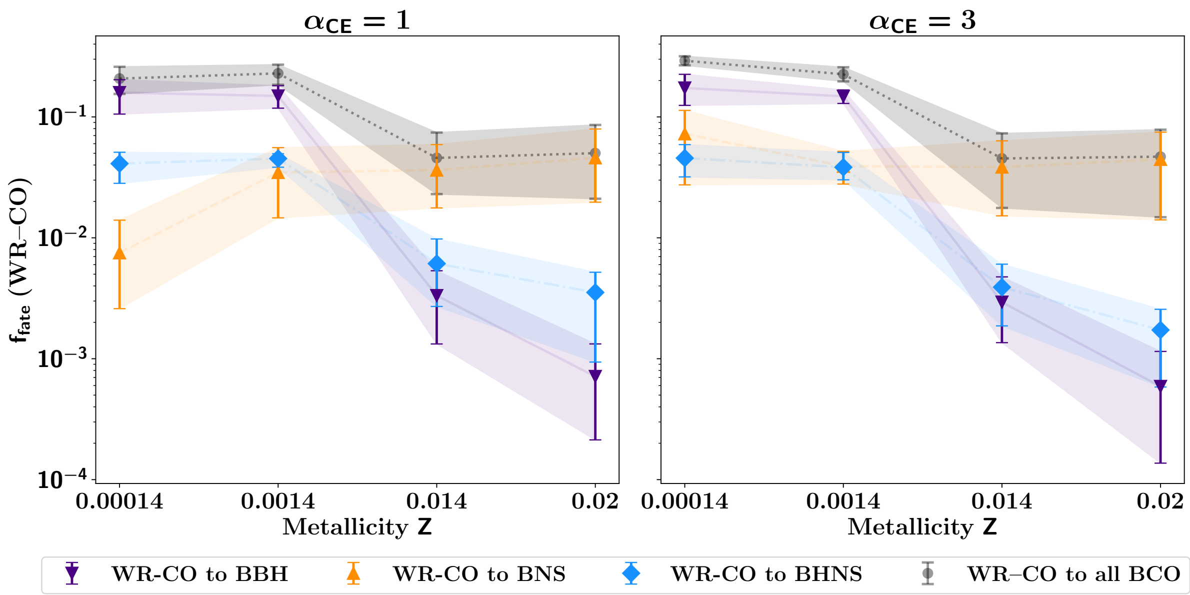

Figure 2.6: Median fraction $f_{\rm fate}$ of WR–COs that were able to produce BCOs as a function of metallicity. The left-hand (right-hand) plot refers to $\alpha_{\rm CE} = 1$ ($\alpha_{\rm CE} = 3$). In each set, we consider all WR–CO systems and we count how many of them form any type of BCOs (gray lines, circle markers), only BBHs (purple lines, lower triangle markers), only BHNSs (blue lines, diamond markers), and only BNSs (yellow lines, upper triangle markers). For each $(Z, \alpha_{\rm CE})$ pair and BCO type, we consider the distribution of the 12 $f_{\rm fate}$ fractions of the corresponding simulated sets (combinations of CCSN and natal kick models, see Table 2.1), and show their median values (scatter points) and 68% credible intervals (error bars).

2.3.3 Only a small fraction of WR–CO systems become BCOs

We showed that the vast majority of BCOs evolved via a WR–CO stage. However, only few WR–COs end their life as BCOs. At sub-solar metallicity ($Z = 0.0014$, $Z = 0.00014$), about $\approx 30\%$ of WR–CO systems produce BCOs; at solar metallicity ($Z = 0.02$, $Z = 0.014$) only $\approx 5\%$ (Figure 2.6).

WR–COs are not common: in each simulated set, we find that only $\approx 1 - 5\%$ of the initial binary population evolves as a WR–CO system. In our simulations, the relative abundance of WR–BHs (WR–NSs) in the WR–CO population is not directly correlated with the abundance of BBHs (BNSs) in the BCO population. WR–BHs always constitute $\approx 50 - 80\%$ of the WR–CO population, with a relative abundance to WR–NSs that is sensitive to the CCSN and natal kick models. In contrast, the relative abundance of BBHs in the BCO population is a strong function of metallicity. For instance, BBHs constitute the dominant BCO family at sub-solar metallicity ($\approx 60 - 80\%$) but are rare at solar metallicity ($\lesssim 10\%$). Similar arguments apply to the relative abundance of WR–NSs and BNSs, even if BNS production is also sensitive to $\alpha_{\rm CE}$.

To investigate what determines the fate of WR–COs, we considered the fraction $f_{\rm fate}$ of WR–CO systems with a specific fate. For instance, to calculate the fraction $f_{\rm fate}$ of WR–COs becoming BCOs, we consider the number of BCOs with a WR–CO progenitor (WR–BHs, WR–NSs, or WR–BH plus WR–NSs; for BBHs, BNSs or BHNSs, respectively) and divide it by the correspondent total WR–CO population (all WR–BHs, WR–NSs or WR–COs, respectively). WR–COs could have various possible fates: the system could

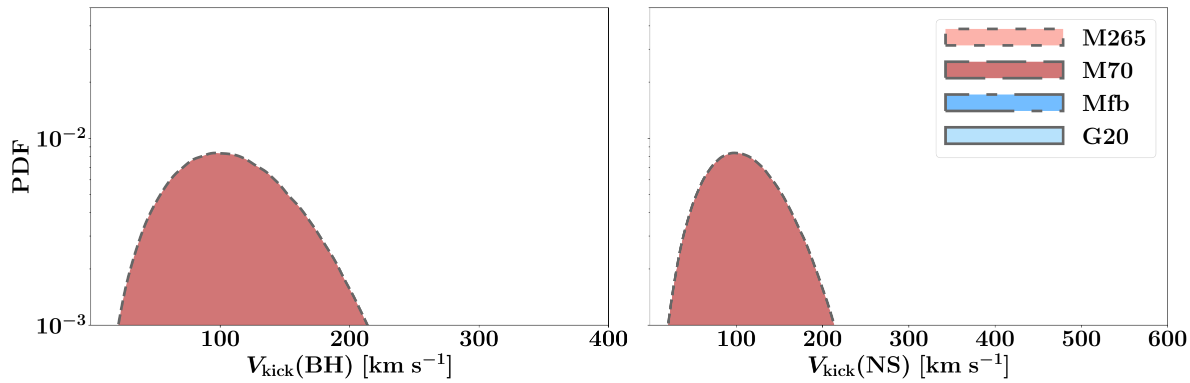

Figure 2.7: Distribution of natal kick magnitudes received by all BHs (left) and NSs (right) produced by the initial binary population at $Z = 0.02$ ($\alpha_{\rm CE} = 3$, delayed CCSN) for the four natal kick models explored in this work (Table 2.1).

prematurely coalesce (as a result of a collision or CE event); the WR could form the second CO after the binary split; the binary could be loose and not merging via GWs; the binary could be tight enough to merge via GW emission within a Hubble time. In Figure 2.3, we show the fractions $f_{\rm fate}$ calculated for WR–NSs and WR–BHs for all possible fates and throughout the parameter space explored in this work (Table 2.1). In Figure 2.6, we show median values and 68% credible intervals for the distributions of $f_{\rm fate}$ leading only to BCO production for a fixed pair of $(Z, \alpha_{\rm CE})$ values.

WR–COs and *lucky kicks*

As shown in Figure 2.3, most of the WR–NSs that are able to survive in bound orbits also have a final orbital configuration that is optimized to merge via GW emission within a Hubble time. These systems were selected by *lucky kicks*: natal kicks that are strong enough to result in highly eccentric orbits but not too strong to ionize the binary.

Figure 2.7 shows that the G20 and M70 models have natal kick magnitude distributions that peak in the optimal velocity regime of *lucky kicks* for NSs ($v \approx 100$ km s^{-1}). Since BHs are heavier than NSs, the optimal regime for *lucky kicks* of BHs is shifted to higher kick velocities ($v \approx 200$ km s^{-1}), where none of the natal kick distributions considered in this work peaks. Therefore, in our simulations, *lucky kicks* boost only the production efficiency of the lightest second-born COs, explaining the higher production efficiency of BNSs and BHNSs compared to BBHs at $Z = 0.02$ (Figure 2.6).

We highlight that selection effects due to *lucky kicks* are also responsible for the higher fraction of BBHs without a WR–BH progenitor at $Z = 0.02$ (Figure 2.1). In this case, the selection effect is relevant only for the population of the lightest BHs, especially for BHs with mass $\lesssim 6$ M$_\odot$ produced by the delayed CCSN model. For decreasing metallicity, the BH mass increases and the effect of *lucky kicks* is negligible. Nevertheless, we argue that the effects of *lucky kicks* shown here are probably under-estimated because we are assuming a post-mass transfer circular orbit and we are not accounting for the cumulative effects of mass transfer in eccentric orbits (Parkosidis et al. 2025a,b).

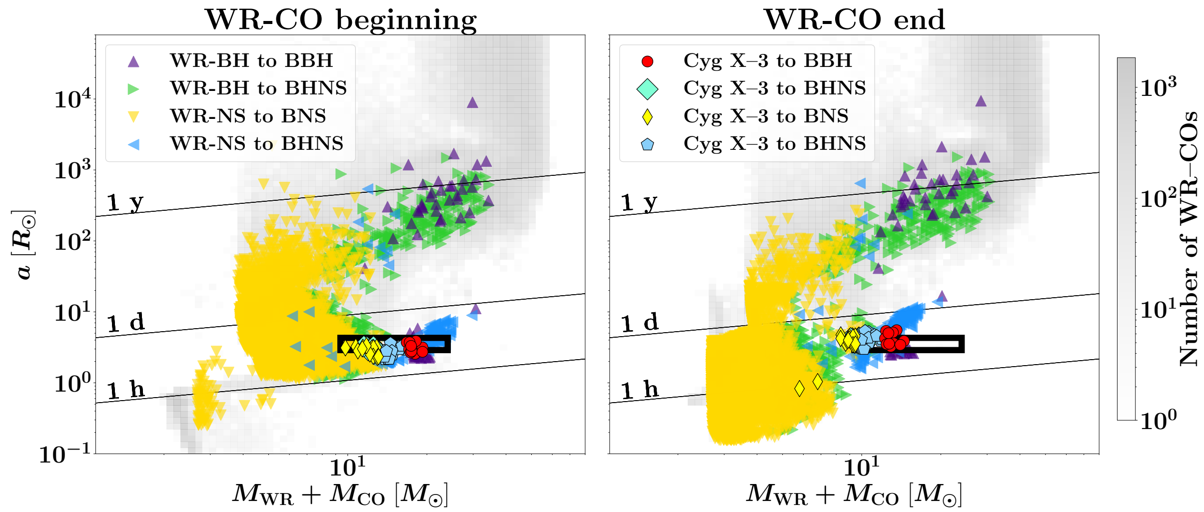

Figure 2.8: Orbital properties of WR–COs and Cyg X-3 at the beginning (left) or end (right) of the WR–CO configuration. We highlight the properties of WR–COs (triangular markers) and Cyg X-3-like binaries (non-triangular markers) that are BCO progenitors, comparing them to the properties of the whole sample of WR–CO (gray areas in the background). We distinguish binaries ending up as BBHs (purple upward triangles; red circles), as BNSs (gold downward triangles; yellow thin diamonds), or as BHNSs, either forming the BH first (green rightward triangles; thick turquoise diamonds) or the NS (blue leftward triangles; turquoise pentagons). The black rectangular box indicates the region of orbital parameters that we use to select Cyg X-3 candidates (Section 2.3.4). Black diagonal lines indicate orbital periods of 1 hour, 1 day or 1 year. Here we show the set evolved with $\alpha_{\rm CE} = 3$, $Z = 0.02$, G20 natal kick model and delayed CCSN model. In Appendix 2.7.2 we show other sets at $\alpha_{\rm CE} = 3$ and $Z = 0.02$.

WR–NSs and CE evolution

CE evolution is the most common channel to form binaries with one or two NSs (WR–NSs, BHNSs, BNSs) and is necessary to produce BNSs at every metallicity (Figure 2.4). Unstable mass transfer events may completely remove the stellar envelope and facilitate the creation of NSs. However, entering a CE phase may cause a reduction of the semi-major by $\Delta a \approx 2000\ R_\odot$ and a premature collision. This possibility is enhanced for low $\alpha_{\rm CE}$ values. The sets evolved with $\alpha_{\rm CE}$ =1 need to extract more orbital energy to expel the CE with respect to the sets evolved with $\alpha_{\rm CE}$ =3, often leaving no surviving system.

Collisions driven by CE events reduce the fraction of WR–NSs that can successfully form BHNSs or BNSs. At the lowest metallicity ($Z = 0.00014$), NSs are produced via binary stripping, and the effect of inefficient CE ejection is more evident. At $\alpha_{\rm CE}$ =1, $\gtrsim$ 90% WR–NSs coalesce prematurely, limiting the production of BNSs (Figure 2.6) and suppressing the formation of BHNSs from WR–NSs (Figure 2.1).

2.3.4 Cyg X-3: A possible BCO progenitor

Cyg X-3 is the only WR–CO candidate known in the MW (Zdziarski et al. 2013; Esposito et al. 2015; Veledina et al. 2024) and has been indicated as a possible BCO progenitor by Belczynski et al. 2013. Here, we investigate this possibility, looking for Cyg X-3–like binaries in our simulations and analysing their fates. In this work, we define a Cyg X-3-like system as a WR–CO system if its orbital properties satisfy three criteria: orbital period $P_{\rm orb} \in [4.5, 5.1]$ hrs, WR mass $M_{\rm WR} \in [8-14]$ $\rm M_\odot$, and CO mass $M_{\rm rem} \leq 10$ $\rm M_\odot$ (Singh et al. 2002; Koljonen & Maccarone 2017). We take a conservative approach on the mass and nature of the CO hosted in Cyg X-3 and allow for both the BH ($M_{\rm rem} = 3-10$ $\rm M_\odot$) and NS hypothesis ($M_{\rm rem} < 3$ $\rm M_\odot$), given the typical uncertainties in the CO mass determination of COs with WR companions (Laycock et al. 2015; Binder et al. 2021).

Cyg X-3 lies in the Galactic plane at a distance of $d_{\rm CygX-3} = 7.41 \pm 1.13$ kpc from the Sun (McCollough et al. 2016). According to the metallicity gradient of the MW derived from Gaia DR2 (Lemasle et al. 2018), Cyg X-3 is expected to have a solar-like metallicity ([Fe/H] $\approx$ -0.088). Given the uncertainties in the determination of the metallicity, we investigated both solar values considered in this work: $Z = 0.02$ and 0.014.

Cyg X-3: Optimal properties for BCO formation

We find that only $\approx 0.1-0.01\%$ of the WR–CO binaries at solar metallicity have a Cyg X-3-like configuration. The strong variability in the Cyg X-3 formation efficiency is determined by the combined action of CCSN and natal kick models, with the delayed CCSN model assumptions constituting the most favourable scenario for Cyg X-3 production, as discussed in more detail in the next paragraph. Typical WR–CO separations at solar metallicity in our simulations are of $a \gtrsim 10^2$ $\rm R_\odot$ (Figure 2.8). Such large orbital separations usually require *lucky kicks* in the second-CO formation to increase the eccentricity and allow for BCO production. In contrast, Cyg X-3 has a semi-major axis that is at least two orders of magnitude smaller ($a \approx 3-5$ $\rm R_\odot$), increasing the possibility that the system will merge via GW emission within a Hubble time. Figure 2.8 shows that Cyg X-3 occupies one of the regions of the space of orbital properties that strongly favours BCO production.

About $\approx 20-80\%$ of the Cyg X-3 candidates in our simulations are BCO progenitors. More than $\gtrsim 70\%$ ($\approx 100\%$ for some combinations of the parameter space, Figure 2.9) of the Cyg X-3-like binaries hosting a BH end their life as BCOs. Even if we consider evolution with the M265 natal kick model, which generates high-velocity kicks typical of Galactic pulsars (Hobbs et al. 2005; Disberg & Mandel 2025), we find that more than $\gtrsim 30\%$ of Cyg X-3 candidates hosting a BH become BCOs. In contrast, only $\lesssim 60\%$ of our Cyg X-3-like systems composed of a WR and an NS become BCOs, because most of the systems break during the second CCSN. Thus, we find that Cyg X-3 has a higher probability of becoming a BCO progenitor if it hosts a BH, in agreement with Belczynski et al. 2013.

Formation efficiency and evolution

Figure 2.9 shows the formation efficiency $\eta_{\rm CygX-3}$ of Cyg X-3 for all the sets evolved at solar metallicity. For each set, we calculated $\eta_{\rm CygX-3}$ as the ratio between the number of Cyg X-3 candidates and the total simulated mass, correcting for the incomplete initial mass sampling of the primary (Appendix 2.6.2) and assuming an initial binary fraction of 1 for simplicity.

The delayed CCSN model is the only CCSN model explored in this work that produces COs in the $\approx 2-6$ $\rm M_\odot$ range. Therefore, the delayed model produces more Cyg X-3-like binaries ($M_{\rm rem} \leq 10$ $\rm M_\odot$) compared to the rapid and compactness-based models. Assuming the delayed CCSN model, the Cyg X-3 formation efficiency can be up to one

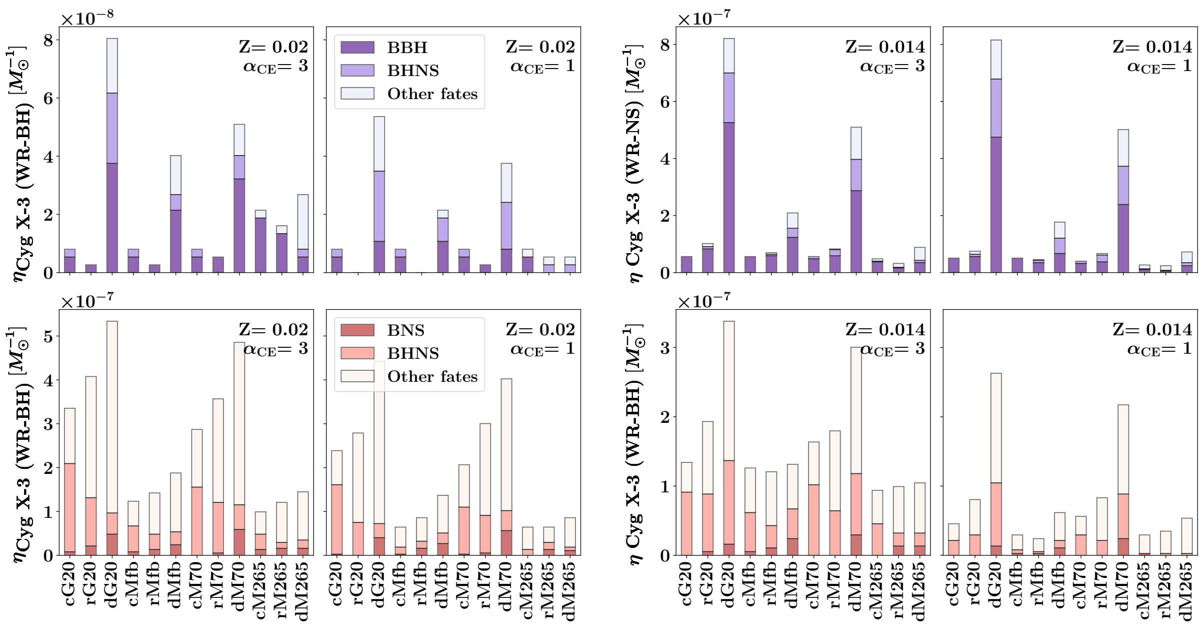

Figure 2.9: Formation efficiency of Cyg X-3 candidates (Singh et al. 2002; Koljonen & Maccarone 2017) for each set of binaries simulated at the two solar metallicity values considered in this work: $Z = 0.02$ (top) and $Z = 0.014$ (bottom). We distinguish Cyg X-3 candidates hosting a BH (upper panels) or an NS (lower panels). We highlight with darker shades the Cyg X-3 candidates that are BCO progenitors.

order of magnitude higher with respect to values obtained in other sets, reaching values of $\eta_{\rm CygX-3} \approx 5.6 \times 10^{-7}$ $M_\odot^{-1}$.

We find that Cyg X-3-like binaries evolve similarly to WR–COs at the same metallicity (Section 2.3.3). Cyg X-3 progenitors experience one or two mass-transfer events (with preference for two, one stable and one unstable), but there are no further mass transfer episodes after the system becomes a WR–CO, except for some WR–NSs. At the beginning of the Cyg X-3-like phase, the WR star does not fill more than $\lesssim 80\%$ of its Roche lobe: the binary can be wind-fed and the orbital separation can increase, as is visible in Figure 2.8. The second compact object forms after less than $\lesssim 0.15$ Myrs of evolution in the Cyg X-3 configuration.

The G20 and M70 natal kick models select a larger number of Cyg X-3 candidates, especially if they host an NS (Figure 2.9). These binaries entered in the Cyg X-3 region of the parameter space as a consequence of the natal kick. Most of these systems will break after the second CCSN or coalesce prematurely because of the additional mass transfer events that WR–NSs may experience.

2.4 Discussion

2.4.1 WR formation

In this work, WR stars can form either via self-stripping, as a result of wind mass loss, or via binary stripping, as a result of mass transfer events. WR formation via self-stripping requires powerful stellar winds. Since wind mass loss rates depend on the mass of the star and its metallicity (Vink et al. 2001; Vink et al. 2011; Nugis & Lamers 2000; Sander et al. 2023), in our simulations self-stripping can produce WRs at solar metallicity ($Z = 0.02, 0.014$) but not at sub-solar metallicity ($Z = 0.0014, 0.00014$). For instance, according to the PARSEC tracks adopted in this work, a star evolved in isolation $Z = 0.02$ becomes a WR ($M_{\text{He-core}} \geq 97.9\%\ M_{\text{star}}$) if it has an initial mass $M_{\text{ZAMS}} \gtrsim 30\ \text{M}_{\odot}$ (WR mass of $M_{\text{WR}} \approx 13\ \text{M}_{\odot}$). The same $M_{\text{ZAMS}} \approx 30\ \text{M}_{\odot}$ star, if evolved at $Z = 0.0014$, will still retain $\approx 50\%$ of its mass in its hydrogen-envelope at the end of the carbon burning phase.

We expect that changes in the input physics, in the internal mixing properties, and in the choice of the stellar evolution code adopted would modify mass losses, the internal structure, and the core growth of the star, influencing the thresholds for WR formation via single stellar evolution (e.g., Agrawal et al. 2022 and references therein). For instance, Dall'Amico et al. 2025 showed that accretion-induced chemically quasi-homogeneous evolution can enhance the formation of WR stars over red supergiants in secondary stars, increasing the fraction of binaries that can form WR–CO systems.

2.4.2 Mass transfer uncertainties

In SEVN, we use critical donor-to-accretor mass ratios $q_{\text{c}} = M_{\text{donor}}/M_{\text{accretor}}$ to determine mass transfer stability, according to the formalism adopted in BSE (Hurley et al. 2002) and other population-synthesis codes. Several works in the literature highlight that this is a simplistic approach to a complicated problem, and has to be revised. For instance, the works by Ge et al. 2010, 2015, 2020, 2024 indicate that there is no universal q_{c} threshold for a fixed evolutionary phase of the donor star; rather, their values are strongly influenced by assumptions on stellar physics, metallicity, and conservation of mass and angular momentum. Gallegos-Garcia et al. 2021 showed that setting a q_{c} threshold favors CE evolution as the dominant formation channel for BBHs, while more detailed stellar evolution calculations favour stable mass transfer evolution as the dominant channel. The work of Gallegos-Garcia et al. 2021 indicates that this approach to mass transfer processes in population synthesis codes could overestimate the merger rates of BBHs (e.g., Neijssel et al. 2019; van Son et al. 2022b; Olejak et al. 2024; Picco et al. 2024).

In this work, we did not put a q_{c} threshold for MS and HG donor stars: we assumed that they experience only stable mass transfer events, avoiding CEs. This setup corresponds to the fiducial model presented by Iorio et al. 2023. The resulting BCO formation efficiency and channels are compared with the ones obtained assuming, for instance, the q_{c} setup of Hurley et al. 2002. From Figs. 14 to 20 of Iorio et al. 2023 we can see that forcing mass transfer to be stable for MS and HG donor stars has minor effects on BBH properties, while it increases BNS merger efficiency at solar metallicity (by about one order of magnitude).

2.4.3 Spin distributions in BBHs

Spin magnitude of second-born BH

According to our models, most BBHs emerge from a WR–BH configuration. The first-born BH can be non-spinning ($\chi_{\text{BH,1}} \approx 0$) if the progenitor star loses angular momentum efficiently. In close orbits, as are the ones leading to BBHs, the BH can tidal spin up the WR star. After the CCSN, the second-born BH could be highly spinning and become the dominant contribution to the effective and precessing spin parameters ($\chi_{\rm eff}$ and $\chi_{\rm p}$) that we can measure from GW observations (Abbott et al. 2023b).

Bavera et al. 2021a used `MESA` (Paxton et al. 2015) to follow the tidal spin up in WR–BH binaries. They assumed efficient angular transport, resulting in non-spinning first-born BH. Bavera et al. 2021a derived a fitting formula to predict the dimensionless spin magnitude of the second-born BH $\chi_{\rm BH,2}$ as a function f the orbital period of the WR–BH binary $P_{\rm WR-BH}$ and the WR mass, $M_{\rm WR}$, at He or C depletion (Bavera et al. 2021b):

$$\chi_{\rm BH,2} = \begin{cases} f(P_{\rm WR-BH}, M_{\rm WR}) & P_{\rm WR-BH} \leq \ 1 \text{ day} \\ 0 & \text{otherwise} \end{cases} . \tag{2.6}$$

If we apply this relation to the population of WR–BHs in our simulations, we find a bimodal distribution for the spins of second-born BHs (Figure 2.10): they are either highly spinning ($\chi_2 \approx 1$) or no spinning ($\chi_2 \approx 0$). In the model by Bavera et al. 2021b, the spin magnitude is determined by the tidal spin-up. Thus, it is strongly influenced by the orbital period of the WR–BH system.

Figure 2.10 (left panel) shows that most WR–BHs at solar metallicity ($Z = 0.02, 0.014$) have orbital periods too large ($P_{\rm WR-BH} > 1$ day) to be spun up by tides according to Equation 2.4.3. Only BBHs produced with the G20 natal kick model (Giacobbo & Mapelli 2020), the model that generates the lowest kick magnitudes for BHs (Figure 2.7), exhibit a significant fraction of binaries with $P_{\rm WR-BH} \lesssim 1$ day.

At sub-solar metallicity ($Z = 0.0014, 0.00014$), the lower wind efficiency allows WR production only via mass transfer interactions and binary stripping. Hence, WR–BHs at these metallicities have shorter periods resulting in an efficient spin up of the WR that will produce the second-born BH.

Comparison with spins from GW observations

If one of the two BHs is not spinning ($\chi_1 \approx 0$), the effective spin parameter $\chi_{\rm eff}$ is extremely sensitive to the mass ratio $q = M_{\rm BH,L}/M_{\rm BH,H}$ of the lighter-to-heavier BH ($\rm M_{BH,H} \geq M_{BH,L}$). By construction, this[1] mass ratio is $q < 1$ and can be used to calculate $\chi_{\rm eff}$ with an explicit dependence on the possibility that the second-born BH $\rm M_{BH,2}$ is the heaviest or the lightest one:

$$\chi_{\rm eff} \approx \frac{m_2\ \chi_2\ \ \cos\theta_2}{m_1 + m_2} \approx \begin{cases} \frac{q}{1+q}\ \chi_2 \cos\theta_2 & \rm M_{BH,2} \leq M_{BH,1} \\ \frac{1}{1+q}\ \chi_2 \cos\theta_2 & \rm M_{BH,2} \geq M_{BH,1} \end{cases} . \tag{2.7}$$

GW observations suggest that most BHs have relatively low spins ($\chi \approx 0.2$) and that there might exist a $q - \chi_{\rm eff}$ correlation that favors higher $\chi_{\rm eff}$ values for more asymmetric binaries (Callister et al. 2021; Abbott et al. 2023b; The LIGO Scientific Collaboration et al. 2025a). In the case of efficient angular momentum transport and Eddington-limited accretion, the first-born BH could be non-spinning and $\chi_{\rm eff}$ would be determined mainly by the properties of the second-born BH. Assuming also spin aligned to the orbital momentum ($\cos\theta_2 = 1$), the analytical approximation of $\chi_{\rm eff}$ (Equation 2.7) indicates an intrinsic $q - \chi_{\rm eff}$ (anti-) correlation if the second-born BH the (most) least massive one. The

[1] Other mass ratio definitions could be larger than 1, for instance the donor-to-accretor mass ratio $q = M_{\rm d}/M_{\rm a}$ used to determine mass transfer stability.

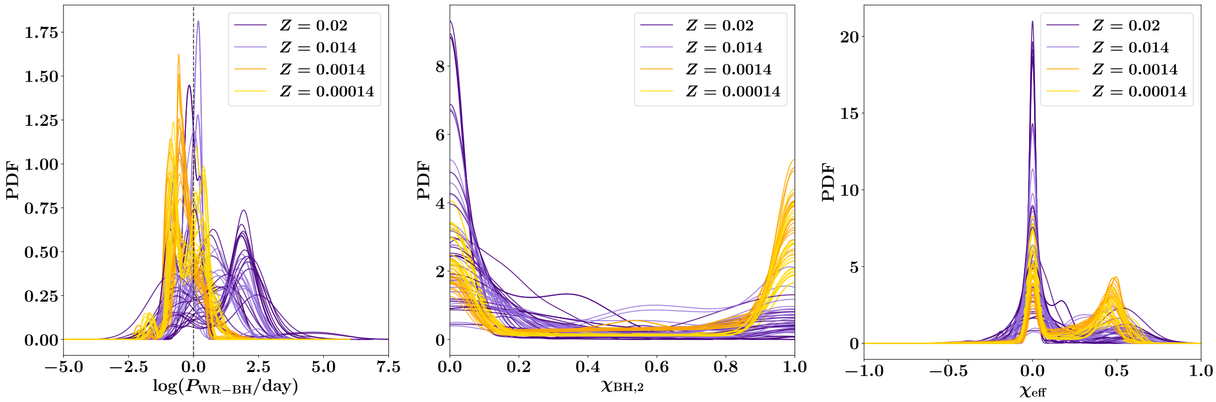

Figure 2.10: *Left:* Probability distribution function (PDF) of the orbital periods $P_{\mathrm{WR-BH}}$ at the end of the WR–BH configuration for progenitors of BBHs. The dashed line at $P_{\mathrm{WR-BH}} = 1$ day highlights the systems that are tight enough to induce efficient tidal spin-up ($P_{\mathrm{WR-BH}} \leq 1$ day) according to the model by Bavera et al. 2021b. *Center:* Probability distribution function of the dimensionless spin magnitude $\chi_{BH,2}$ of second-born BHs in WR–BHs evolving into BBHs. Spins are calculated with the model of Bavera et al. 2021b that assumes tidal spin-up in close binaries and efficient angular momentum transport. All the 96 simulated sets (Table 2.1) exhibit a bimodal distribution. *Right:* Probability distribution function of the effective spin parameter χ_{eff} obtained in all 96 sets, color-coded according to the assumed metallicity Z.

magnitude of the second-born BH spin influences the shape of the (anti-) correlation in the $q - \chi_{\mathrm{eff}}$, as we show in Figure 2.11.

In the case of maximally spinning second-born BH ($\chi_2 = 1$), the approximated formula for χ_{eff} divides the $q - \chi_{\mathrm{eff}}$ plane into three regions: an oval-shaped central region, an outer wing, and a more external one. The regions are symmetric with respect to the $\chi_{\mathrm{eff}} = 0$ centre, indicating (anti-) aligned spins for (negative) positive χ_{eff} values. In Figure 2.11 we superimpose also the properties of all the BBHs simulated in this work (96 sets, see Table 2.1) and spun up via Equation 2.4.3. We find no BBH in the more external region, thus, no systems with high $\chi_{\mathrm{eff}} \approx 1$ and similar masses ($q \approx 1$). Most of our BHs are non-spinning ($\chi_{\mathrm{eff}} = 0$) or have spin aligned with the orbital momentum ($\cos\theta_2 \approx 1$)[2]. BBHs with second-born BH that is lighter than the first-born one ($M_{\mathrm{BH,2}} = M_{\mathrm{BH,L}}$) are confined in the central oval-shaped region, with $|q| < 0.5$. BBHs with heavier second-born BHs ($M_{\mathrm{BH,2}} = M_{\mathrm{BH,H}}$) distribute both in the central oval-shaped region and in the outer wings. In this scenario, the wings centered at $|q| = 0.5$ identify a region that can be populated only by BBHs evolved through a mass-ratio-reversal evolution. The distribution of our BBHs in the $q - \chi_{\mathrm{eff}}$ plane is in agreement with other works in the literature that studied the mass-ratio-reversal scenario and considered tidal spin up (e.g., Olejak & Belczynski 2021; Broekgaarden et al. 2022; Olejak et al. 2024; Banerjee & Olejak 2024).

[2]The spin orientation $\cos(\theta_2)$ was calculated following Equation 1.16 of Mapelli 2021, assuming that only the natal kicks can change the spin orientation.

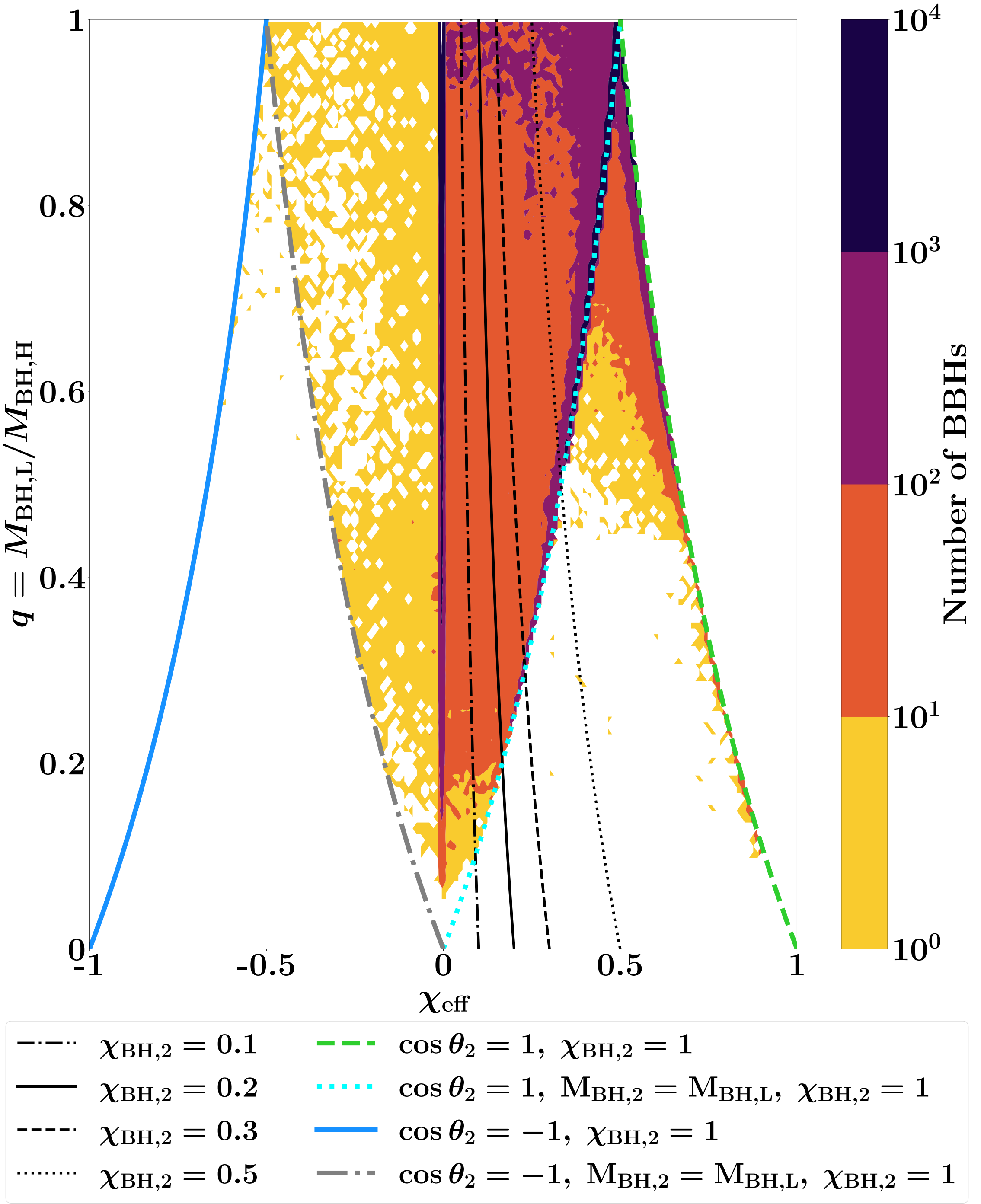

Figure 2.11: Mass ratio $q = M_{\mathrm{BH,L}}/M_{\mathrm{BH,H}}$ of the lighter-to-heavier BH and effective spin parameter χ_{eff} for all BBHs produced in the 96 sets simulated in this work (Section 2.2). Colored thick lines indicate the analytic relations (Equation 2.7) that delimit the allowed parameter space for maximally spinning ($\chi_2 = 1$) second-born BH, for spins aligned ($\cos\theta_2 = 1$) or anti-aligned ($\cos\theta_2 = -1$) with the binary orbital angular momentum. Black thin lines show the analytic relation expected for low spinning ($\chi_2 \sim 0.1 - 0.5$) and aligned ($\cos\theta_2 = 1$) second-born BH. The analytic relations assume that the second-born BH is the heaviest one ($\mathrm{M_{BH,2}} = \mathrm{M_{BH,H}}$), unless different specifications.

2.5 Summary

We investigated the role of WR–COs as the possible progenitors of BCOs. We used the population synthesis code SEVN to account for uncertainties in theoretical models, evolving the same initial binary population through 96 combinations of metallicity, CE efficiency, CCSN, and natal kick models.

We found that most ($\gtrsim 83\%$) of the simulated BCOs evolved as WR–CO systems in the considered parameter space. More than $\gtrsim 99\%$ ($\approx 83 - 95\%$) of BCOs at $Z \geq 0.0014$ ($Z = 0.00014$) have a WR–CO progenitor. The fraction of BCOs that derive from WR–CO systems is mostly affected by mass transfer (when it stops before complete envelope stripping we do not form a WR at low Z), metallicity (which influences stellar winds, thus the role of self and binary stripping in WR production), and the combined effect of natal kicks and CCSN models.

Only $\approx 1 - 5\%$ of the simulated massive binaries passes through the WR–CO phase. Despite their key role as BCO progenitors, only a small fraction of WR–COs ($\approx 5 - 30\%$, depending on the metallicity) becomes a BCO. When formed, WR–COs constitute the last evolutionary configuration prior to BCO formation. These progenitors experience all the RLOs and CE events before the WR–CO phase. Only WR–NSs require at least one additional CE event in order to produce BCOs.

We characterized the possible fate of Cyg X-3, the only Galactic WR–CO candidate, finding that it will likely evolve into a BCO if it is a WR–BH system ($\approx 70 - 100\%$). If Cyg X-3 is a WR–NS binary, the BCO fate is disfavoured ($<$ 40-60 %), in agreement with Belczynski et al. 2013. Cyg X-3 possible formation channels are representative of WR–COs at $Z = 0.02, 0.014$, suggesting that the observation and characterization of similar WR–CO systems could help us to constrain the models to interpret the BCO formation history.

Acknowledgements

EK and MM acknowledge support from the PRIN grant METE under contract No. 2020KB33TP. MM, GC, GI, and MDA acknowledge financial support from the European Research Council for the ERC Consolidator grant DEMOBLACK, under contract no. 770017. EK and MM also acknowledge financial support from the German Excellence Strategy via the Heidelberg Cluster of Excellence (EXC 2181 - 390900948) STRUCTURES. GI acknowledges financial support under the National Recovery and Resilience Plan (NRRP), Mission 4, Component 2, Investment 1.4, - Call for tender No. 3138 of 18/12/2021 of Italian Ministry of University and Research funded by the European Union – NextGenerationEU. GC acknowledges financial support from the Agence Nationale de la Recherche grant POPSYCLE number ANR-19-CE31-0022. Numerical calculations have been made possible through a CINECA-INFN (TEONGRAV) agreement, providing access to resources on Leonardo at CINECA. The authors acknowledge support by the state of Baden-Württemberg through bwHPC and the German Research Foundation (DFG) through grants INST 35/1597-1 FUGG and INST 35/1503-1 FUGG.

2.6 Appendix A: Models and assumptions

2.6.1 Fallback in the Mfb natal kick model

The Mfb natal kick model assigns the kick magnitudes drawing a random number f_σ from a Maxwellian distribution ($\sigma = 265$ km s^{-1} rms) and modulating it with the fraction $f_{\rm fb,CCSN}$ of mass falling back onto the proto-NS:

$$v_{\rm kick} = f_{\sigma=265}\,(1 - f_{\rm fb,CCSN}). \tag{2.8}$$

Here, we choose the fallback fraction $f_{\rm fb,CCSN}$ consistently with the CCSN models (Section 2.2.4).

In the rapid and delayed case, we set the fallback fraction equal to the fallback parameter $f_{\rm fb,CCSN} = f_{\rm fb}$ of (Fryer et al. 2012). In the compactness-based case, we distinguish successful and failed supernovae. For BHs formed via direct collapse, no material is ejected ($f_{\rm fb,CCSN} = 1$) and no kick is imparted. For NSs, we calculate a fallback fraction in analogy with Fryer et al. 2012: we assume that the remnant mass ($M_{\rm rem}$) is determined by the fraction $f_{\rm fb,CCSN}$ of the pre-SN mass ($M_{\rm pre-SN}$) that a proto-CO of $M_{\rm proto} = 1.1$ M$_\odot$ is able to accrete, where

$$f_{\rm fb,CCSN} = \frac{\max(M_{\rm rem} - M_{\rm proto}, 0)}{\max(\mathrm{M}_{\rm pre-SN} - \mathrm{M}_{\rm proto}, 0)}. \tag{2.9}$$

2.6.2 Initial conditions for binary population

The initial primary masses M_1 were drawn from the Kroupa 2001 initial mass function (IMF) and the initial mass ratios q from Sana et al. 2012:

$$\xi(M_1) \propto M_1^{-2.3} \qquad M_1 \in [5, 150]\ \mathrm{M}_\odot, \tag{2.10}$$

$$\xi(q) \propto q^{-0.1} \qquad q \in [0.1, 1], \tag{2.11}$$

where $q = M_2/M_1$ and $M_1 \geq M_2$. Combining $\xi(q)$ and $\xi(M_1)$, we obtained the distribution for the initial secondary masses $\xi(M_2) = \xi(M_1)\,\xi(q)$. We choose the lower cuts at $M_{1,\rm min} = 5$ M$_\odot$ and $q_{\rm min} = 0.1$ because we focus on BH and NS progenitors.

We generated a total mass of $M_{\rm IC} \approx 1.08 \times 10^7$ M$_\odot$. Accounting for incomplete mass sampling of the primary from the Kroupa IMF requires a correction factor of $f_{\rm IMF} = 0.289$, indicating a parent population of $M_{\rm tot} \approx 3.7 \times 10^8$ M$_\odot$.

We generated the initial orbital periods P from the $\mathcal{P} = \log(P/\mathrm{days})$ distribution by Sana et al. 2012:

$$\xi(\mathcal{P}) \propto \mathcal{P}^{-0.55} \qquad \mathcal{P} \in [0.30, 5.5], \tag{2.12}$$

setting $P = 2$ days as lower limit (we assumed that binaries with shorter period already circularized following Moe & Di Stefano 2017). Moe & Di Stefano 2017 showed that there is a complex correlation between the mass ratio q, period P and eccentricity e of early-type binaries. For simplicity, we assumed independent distributions for q and P and we adopted the Moe & Di Stefano 2017 prescription for e:

$$\xi(e(P)) \propto 1 - (P/\mathrm{days})^{-2/3} \qquad P \geq 2\ \mathrm{d}. \tag{2.13}$$

2.7 Appendix B: Additional plots

2.7.1 Formation channels and CE efficiency

In Figure 2.12 we show the formation channels of BCOs for $\alpha_{\rm CE}$ =1. The most notable difference with respect to the $\alpha_{\rm CE} = 3$ case (Figure 2.4, Section 2.3.2) occurs for WR–NS formation and final fate. WR–NSs require one or more CE events to form, and at least an additional one to produce a BCO. At $Z = 0.00014$, the role of CE evolution in BNS creation is enhanced at $\alpha_{\rm CE} = 1$, with $\approx 60 - 90\%$ of BNSs exchanging mass only via CE events. At these metallicity, NSs may form only after efficient envelope stripping, as it is the one induced by CE evolution. Thus, evolution through stable RLOs is disfavoured However, a low CE efficiency determines inefficient CE ejection and can induce premature coalesce of the binary members. For instance, at $Z = 0.00014$ and $\alpha_{\rm CE} = 1$ no WR–NS was able to survive the CE evolution and produce BHNSs, unlike the $\alpha_{\rm CE} = 3$ case.

2.7.2 Orbital properties of Cyg X-3

In Section 2.3.4, we showed that Cyg X-3 is a possible BCO progenitor, with formation pathways representative of WR–COs evolved at $Z = 0.02, 0.014$.

Figure 2.13 shows the orbital properties of WR–COs and Cyg X-3 in a set evolved with $\alpha_{\rm CE} = 3$, $Z = 0.02$, the G20 natal kick model and the compactness-based CCSN model. This binary population was evolved under the same assumptions of Figure 2.8, except for the CCSN model. Despite the same $\alpha_{\rm CE}$ and Z assumptions, the elevated probability of receiving a *lucky kick* through the G20 model couples with the different CCSN model (compactness-based in Figure 2.13, delayed in Figure 2.8) and determines a different distribution of WR–COs in the space of orbital parameters.

For further comparison, we show in Figure 2.14 how the occupation of space of orbital parameters changes if we assumed the kick model to be the Mfb one. In this plane, changing the initial models modifies the number of WR–COs with Cyg X-3-like properties. Nevertheless, binaries similar to Cyg X-3 remain favoured as BCO progenitors, suggesting that that further observations of WR–COs with orbital properties similar to Cyg X-3 may constrain the properties of BCO progenitors.

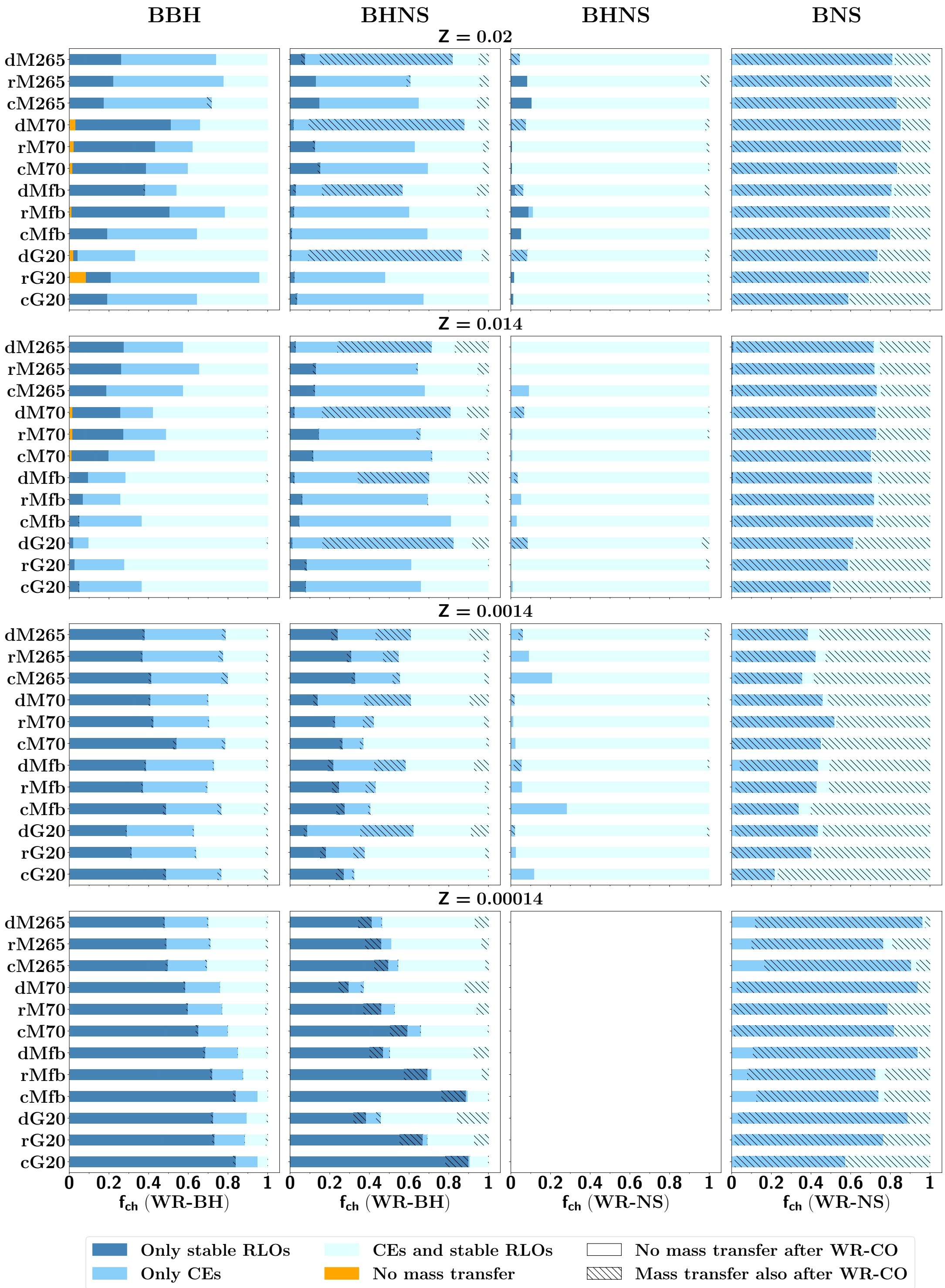

Figure 2.12: Fraction of BCOs with WR–CO progenitors evolved through different formation channels for different metallicities (rows) and combinations of CCSN and natal kick models explored in this work (Table 2.1). Here we show the $\alpha_{CE} = 1$ case. We distinguish four main evolutionary paths on the basis of mass transfer events occurred before the WR–CO formation: stable mass transfer only, CEs only, at least one stable and one unstable mass transfer, no mass transfer. Hatched bars indicate WR–CO systems that become BCOs experiencing at least one additional mass transfer event (stable or unstable RLO) after the WR–CO phase.

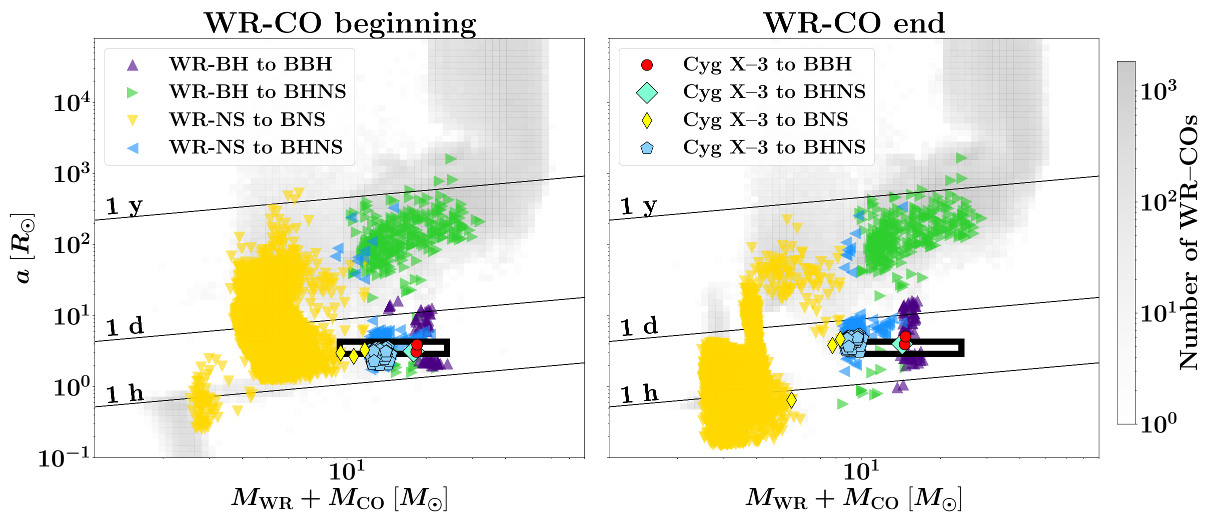

Figure 2.13: Orbital properties of WR–COs and Cyg X-3 at the beginning (left) and end (right) of the WR–CO phase. We highlight the properties of WR–COs (triangular markers) and Cyg X-3-like binaries (non-triangular markers) that are BCO progenitors, comparing them to the properties of the whole sample of WR–COs (gray areas in the background). We distinguish binaries ending up as BBHs (purple upward triangles; red circles), as BNSs (gold downward triangles; yellow thin diamonds), or as BHNSs, either forming the BH (green rightward triangles; thick turquoise diamonds) or the NS first (blue leftward triangles; turquoise pentagons). The black rectangular box indicates the region of orbital parameters that we use to select Cyg X-3 candidates (Section 2.3.4). Black diagonal lines indicate orbital periods of 1 hour, 1 day or 1 year. Here we show the set evolved with $\alpha_{\rm CE} = 3$, $Z = 0.02$, G20 natal kick model and compactness CCSN model. In Figure 2.8 we show the same set, but with the delayed CCSN model.

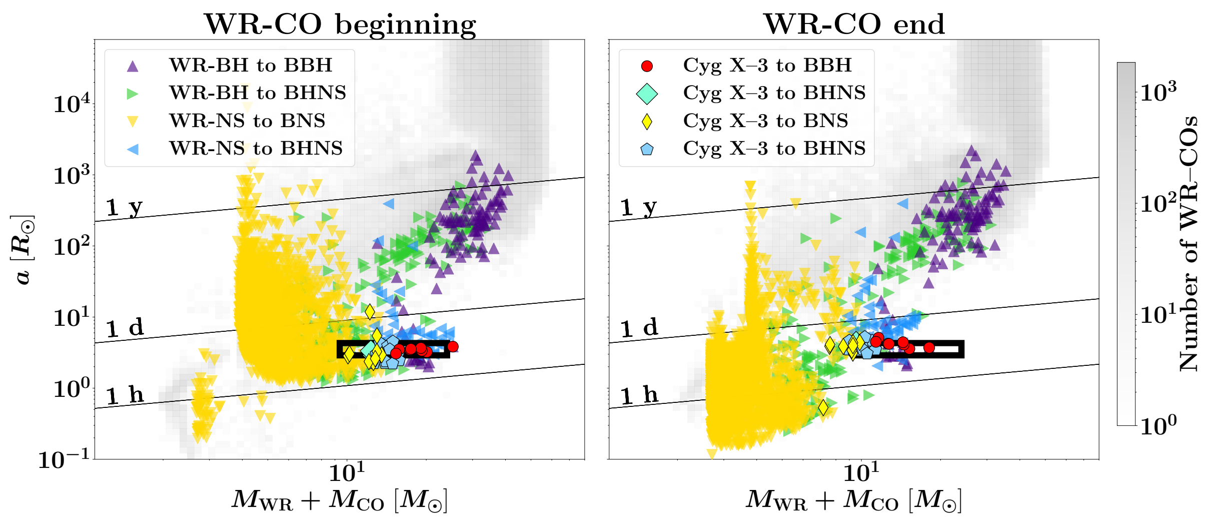

Figure 2.14: Same as Figure 2.13, but here we show the set evolved with $\alpha_{\rm CE} = 3$, $Z = 0.02$, Mfb natal kick model, and delayed CCSN model. In Figure 2.8 we show the same set, but with the G20 natal kick model.

Chapter 3

Impact of angular momentum losses on the formation of binary black hole mergers

Based on the draft of the manuscript:
Korb E., et al.
"Impact of angular momentum losses on the formation of binary black hole mergers", to be submitted to A&A.

Abstract

The release of the fourth Gravitational Wave Transient Catalog GWTC-4.0 supports the existence of a gap above $\approx 40-60\ \mathrm{M}_{\odot}$ in the mass distribution of merging BBHs. The existence of this gap is predicted by stellar evolution theory and it is attributed to the PI mechanism. However, the existence and location of the PI gap is affected by the large uncertainties in stellar physics and mass transfer processes. In this work, we considered an isolated binary evolution scenario and used the population-synthesis code `SEVN` to systematically investigate how efficient angular momentum extraction and stellar physics prescriptions can affect the properties and the formation channels of BBHs. We considered four models for orbital angular momentum losses (isotropic re-emission, Jeans mode, outflows through the outer Lagrangian point, and circumbinary disk formation) and explored also the impact of tides, in two sub-solar environments ($Z = 0.00142, 0.000142$) and considering our fiducial `PARSEC` stellar models. We find that efficient extraction of angular momentum can increase the maximum mass of the most massive BH (primary) by $\approx 10\ \mathrm{M}_{\odot}$, allowing up to $\approx 3-11\%$ of BBHs to have primary mass up to $\approx 45-78\ \mathrm{M}_{\odot}$. Instead, in our simulations the mass of the lighter BH (secondary) is always below $\leq 46\ \mathrm{M}_{\odot}$. We also find that angular momentum losses that consider Lagrangian outflows or the formation of circumbinary disks allow up to $\approx 60\%$ of BBH progenitors to maintain a hydrogen envelope at the pre-supernova stage. Moreover, BBH formation efficiencies remain broadly consistent with previous estimates. Eventually, we show that stellar evolution models strongly affect BBH masses and intermediate progenitor configurations, with an impact comparable to other uncertainties commonly explored in the literature. Our results highlight the crucial role of angular momentum losses and stellar physics in interpreting the observed BBH population.

Keywords: mass transfer – angular momentum – pair-instability supernova – binary black holes – gravitational waves

3.1 Introduction

GW observations are shedding new light on the possible final CO properties. CO masses are among the parameters better characterized from the observations and could be used to constrain current models for binary evolution (The LIGO Scientific Collaboration et al. 2025a). For instance, the detection of GW230529_181500 (Abac et al. 2024) showed the existence of a primary BH with mass between $\approx 3-5$ $M_\odot$, polluting the putative low-mass gap of COs from electromagnetic observations (e.g., Özel et al. 2010; Fryer et al. 2012). Furthermore, the observed bimodal chirp mass distribution of BBHs could be interpreted with a different pre-SN structure of progenitor stars, resulting from stars that underwent binary interactions and were stripped of their external envelopes (Schneider et al. 2021; Laplace et al. 2021; Schneider et al. 2023). Preliminary population-synthesis results on GWTC-4.0 data support this interpretation (Willcox et al. 2025).

The detection of BHs with masses between 45 $M_\odot \lesssim M_{BH} \lesssim 120$ $M_\odot$ (e.g., GW190521 and GW231123; Abbott et al. 2020 and The LIGO Scientific Collaboration et al. 2025c, respectively) showed that it is possible to populate the putative PI gap predicted by stellar evolution theory (Heger & Woosley 2002; Woosley 2017; Farmer et al. 2019). However, even though both the primary and the secondary BH mass distributions exhibit a broken power-law-like behaviour and a moderate decline after ≈ 35 $M_\odot$ and $\approx -40-60$ $M_\odot$, respectively, the current sample of ≈ 150 coalescing BBHs (GWTC-4.0, The LIGO Scientific Collaboration et al. 2025a) remains too small to identify or rule out the existence of a PI gap (The LIGO Scientific Collaboration et al. 2025a; Antonini et al. 2025; Banagiri et al. 2025; Ray & Kalogera 2025; Tong et al. 2025). Moreover, the precise boundaries and the existence of the gap itself are sensitive to the details of the nuclear reaction rates - in particular the $^{12}C(\alpha,\gamma)^{16}O$ one - internal mixing, overshooting, dredge-up episodes, and envelope fallback (e.g. Costa et al. 2021). However, even under extreme assumptions - such as super Eddington accretion, strong natal kicks or very low metallicity - it is unlikely that the BHs forming in the PI gap are produced from BBHs evolved in isolation (van Son et al. 2020; Mapelli et al. 2020; Briel et al. 2023; Iorio et al. 2023): BBHs with such heavy objects are expected to form via hierarchical mergers in dense stars clusters or in AGNs (e.g., Rodriguez et al. 2019; Mapelli et al. 2021; Delfavero et al. 2025).

The existence of BCO mergers proves that there are formation scenarios capable to bring together two COs in orbits that are only few solar radii wide, otherwise we could have not been able to see their merger within the lifetime of the Universe (Peters 1964). Stars can expand up to thousands of solar radii during their lives (e.g. Bressan et al. 2012), so the isolated formation scenario for BCOs requires some mechanisms that can shrink the orbital separation by one or two orders of magnitudes, preventing premature coalescences. In the traditional scenario, this key shrinking process is identified in unstable mass transfer events, as CE evolution is expected to produce tighter orbits than SMT events (van den Heuvel 1994; Tauris & van den Heuvel 2006; Ivanova et al. 2013).

Stability and efficiency of mass transfer processes heavily depend on the internal structure of the star and on its response to the mass lost or accreted (e.g. Webbink 1984, 1985; Hjellming & Webbink 1987; Ge et al. 2010, 2015, 2020; Klencki et al. 2020; Klencki et al. 2021). Traditionally, the impact of physical uncertainties in the BCO isolated evolution scenario has been investigated with population-synthesis studies (e.g., Giacobbo et al. 2018; Breivik et al. 2020; Belczynski et al. 2020) that relied on approximated fitting formulae to model the evolution of stars and binaries, following the formalism of Hurley et al. 2002. Detailed stellar and binary evolution models showed that this traditional approach needs to be revised, as it is probably overestimating the impact of unstable mass transfer in BCO formation (Klencki et al. 2020; Klencki et al. 2021; Marchant et al. 2021; Gallegos-Garcia et al. 2021; Bavera et al. 2021; Briel et al. 2023; Picco et al. 2024). In addition to this, the work of Willcox et al. 2023 also showed that assuming conservative or non-conservative mass transfer also significantly impacts the BCO formation channels, indicating that conservative mass transfer could underestimate the number of mergers produced by unstable mass transfer. Therefore, in the ongoing effort to investigate the role of SMT channel in the formation of BCO mergers, there is a growing interest in the effect of angular momentum losses, as the non-accreted mass can be lost from the system and carry away some orbital angular momentum, leading to an efficient orbital reduction (e.g. van Son et al. 2022b; Willcox et al. 2023; Olejak et al. 2024; Picco et al. 2024; Klencki et al. 2025).

Both detailed and rapid population synthesis codes are currently used to investigate uncertainties in BCO formation channels, but the intrinsic differences in the codes prevents a fair comparison and interpretation of the results. For instance, mass transfer prescriptions in detailed binary simulations often follow the formalism of Marchant et al. 2021 to calculate the mass transfer rate - then used to derive the threshold to transition to the CE phase (e.g., mass transfer rate $\gtrsim 1\ \mathrm{M}_\odot\ \mathrm{yr}^{-1}$) - and allows for outflows from the outer Lagrangian point accounting for the extended structure of the stellar atmosphere (e.g., Gallegos-Garcia et al. 2021, 2024; Picco et al. 2024). In contrast, population-synthesis studies generally maintain the Hurley et al. 2002 formalism to calculate the mass transfer rate, adopt a critical mass ratio to transition to the CE phase, do not account for outflows from the outer Lagrangian point, and generally assume that the non-accreted mass lost in the form of isotropic wind from the vicinity of the accretor (e.g. van Son et al. 2022b; Broekgaarden et al. 2022; Iorio et al. 2023). Furthermore, some studies used other approaches, making even harder to compare results from population synthesis and detailed codes (e.g.,Briel et al. 2023 investigated SMT and CE channels with a detailed code but assumed as CE threshold the onset of an outflow from the outer Lagrangian point). Therefore, even in studies that try to uniform the binary assumptions as much as possible in order to compare population-synthesis and detailed evolution results (e.g. Gallegos-Garcia et al. 2021; Olejak et al. 2024), the underlying stellar physics remains different, impacting on the consequent binary evolution, and complicating the interpretation of the impact of the assumed physical processes.

Iorio et al. 2023 used the population-synthesis code `SEVN` to explore the impact of stellar physics assumptions alone on population-synthesis predictions, assuming the default `BSE` formalism of Hurley et al. 2002 to investigate the BCO predictions for a wide parameter space (e.g., supernova models, parameters for the CE efficiency, critical mass ratios for the onset of the CE, metallicity) and for different sets of interpolated stellar tracks. Iorio et al. 2023 compare the BCO populations obtained with the Pols et al. 1998 tracks - initially generated with the `STARS` stellar evolution code (Eggleton 1971; Pols et al. 1995) to study stars with initial mass $\leq 50\ \mathrm{M}_\odot$ and commonly adopted in many population-synthesis studies (e.g. Belczynski et al. 2020; Breivik et al. 2020; Giacobbo et al. 2018; Gallegos-Garcia et al. 2021; Compas et al. 2022; Olejak et al. 2024) - with the BCO populations obtained with Costa et al. 2025 tracks - generated with the `PARSEC` stellar evolution code to study stars up to $\leq 350\ \mathrm{M}_\odot$. Iorio et al. 2023 showed that the effect of uncertainties in stellar evolution models alone in the BCO properties and evolution could be comparable to the effect of uncertainties due to binary processes (e.g., in CE or natal kick outcomes).

In this work, we extend the study of Iorio et al. 2023 and explore the combined effect of stellar evolution and angular momentum losses on the formation of BBHs. We systematically explore the impact of angular momentum losses on BBH populations, comparing the standard effect of isotropic re-emission with the possible emission from the donor, the outflow from the outer Lagrangian point, and the formation of a circumbinary disk. We further investigate the impact of tidal models and metallicity, since tides can drive the orbital reduction, and wind strength impacts its widening. We also test the impact of stellar evolution, since it is the first study that investigates the combined effect of the `PARSEC` stellar models with the assumptions on orbital angular momentum losses. In Section 3.2 we describe the implementation of binary orbit evolution in `SEVN` and the angular momentum loss models that we explore. In Section 3.3 we describe the simulation setup. In Section 3.4 we present our results and in Section 3.5 we discuss them, considering the impact of the assumed physics in the context of the literature. In Section 3.6 we summarize our findings.

3.2 Theoretical framework

To better understand the impact of the models for angular momentum losses that we will explore in this work, in this Section we recall the theoretical framework commonly adopted to describe the orbital changes during a mass transfer, highlighting the `SEVN` implementation of these prescriptions (Iorio et al. 2023).

3.2.1 Wind mass transfer

Bondi-Hoyle accretion

If the wind velocity is significantly larger than the orbital velocity, the orbit-averaged accretion rate $\dot{M}_\mathrm{a}$ can be estimated following Bondi & Hoyle 1944:

$$\dot{M}_\mathrm{a,Bondi} = -\frac{\alpha_\mathrm{wind}}{\sqrt{1-e^2}} \left(\frac{GM_\mathrm{a}}{V^2_\mathrm{wind}}\right)^2 \frac{\dot{M}_\mathrm{d,wind}}{2a^2_\mathrm{orb}(1+V^2_\mathrm{f})^{1.5}} \tag{3.1}$$

with

$$V^2_\mathrm{wind} = 2\beta_\mathrm{wind}\frac{GM_\mathrm{d}}{R_\mathrm{eff}} \qquad V^2_\mathrm{f} = \frac{G(M_\mathrm{d}+M_\mathrm{a})}{a_\mathrm{orb}V^2_\mathrm{wind}} \tag{3.2}$$

where V^2_wind is the wind velocity, V^2_f is the ratio between the orbital velocity and the wind velocity, $\dot{M}_\mathrm{d,wind}$ the wind mass-loss rate of the donor star, M_d the mass of the donor, M_a the mass of the accretor, a_orb the semimajor-axis of the orbit, and e its eccentricity. The mass accretion rate is regulated by the α_wind and β_wind parameters, generally assumed to take the following values $\alpha_\mathrm{wind} = 1.5$ and $\beta_\mathrm{wind} = 0.125$ after calibration of cool super-giant stars (Kučinskas 1998; Hurley et al. 2002).

Limits on the accretion rate. If the wind velocity is comparable to the orbital velocity, Equation 3.1 overestimates the mass accretion rate. So, following Hurley et al. 2002, in `SEVN` we set an upper limit to the wind mass accretion rate

$$\dot{M}_\mathrm{a,wind} = \min(\dot{M}_\mathrm{a,Bondi}, 0.8|\dot{M}_\mathrm{d,wind}|)\ . \tag{3.3}$$

If the accretor is a compact object (WD, NS, or BH), it is also possible to limit the mass accretion rate to be a fraction $\eta_{\rm Edd}$ of the Eddington limit

$$\dot{M}_{\rm Edd} = 2.08 \times 10^{-3} \eta_{\rm Edd} (1+X)^{-1} \frac{R_{\rm a}}{R_\odot} \;\; {\rm M_\odot \; yr^{-1}} \tag{3.4}$$

where $X = 0.760 - 3.0\ Z$ is the hydrogen mass fraction of the accreted material, $R_{\rm a}$ the radius of the accretor (Cameron & Mock 1967). If the accretor is a naked-Helium star or a naked-CO star, we do not accrete mass in SEVN, as the winds of these stars are expected to rapidly eject the thin layer of accreted mass (Iorio et al. 2023).

Stellar spins. As wind mass transfer proceeds, the material lost from the donor removes some of its angular momentum

$$\dot{J}_{\rm d,wind} = \frac{2}{3} \dot{M}_{\rm d,wind} R_{\rm eff}^2 \Omega_{\rm d} \tag{3.5}$$

while the accreted material brings additional angular momentum to the receiver

$$\dot{J}_{\rm a,wind} = \frac{2}{3} \dot{M}_{\rm a,wind} R_{\rm eff}^2 \Omega_{\rm a} \tag{3.6}$$

where $\dot{M}_{\rm d,wind}$ ($\dot{M}_{\rm a,wind}$) and $\Omega_{\rm d}$ ($\Omega_{\rm a}$) are the donor (accretor) wind-mass loss (accretion) rate and spin angular velocity, respectively[1]. In both Equations, $R_{\rm eff} = \min(R_{\rm d}, R_{\rm RL,d})$ is equal to the radius of the donor star $R_{\rm d}$, except during a Roche lobe overflow, where it is equal to the donor Roche lobe radius $R_{\rm RL,d}$. In SEVN we adopt this correction to account for the different effective inertia of the expanded donor star, thus, for the different amount of angular momentum transferred between the two stars (Iorio et al. 2023).

Orbital evolution via wind mass transfer

While wind-mass loss slows down the donor star (Equation 3.5) and widens the binary, wind-accretion spins-up the accretor (Equation 3.6) and returns some of the angular momentum to the orbit. As wind mass transfer proceeds, not all the donated material is generally accreted by the companion (non-conservative mass transfer). Therefore, overall wind mass transfer reduces the binary mass, widens the orbit, and circularizes it, even though the wind circularization timescale is longer than the tidal one (Hut 1981). Following Hurley et al. 2002, the evolution of the orbital semimajor axis $a_{\rm orb}$ and eccentricity e due to wind mass transfer are given by

$$\frac{\dot{a}_{\rm orb,wind}}{a_{\rm orb}} = -\frac{\dot{M}_{\rm d,wind}}{M_{\rm a}+M_{\rm d}} - \left(\frac{2-e^2}{M_{\rm a}} + \frac{1+e^2}{M_{\rm a}+M_{\rm d}} \right) \frac{\dot{M}_{\rm a,wind}}{1-e^2} \tag{3.7}$$

$$\frac{\dot{e}_{\rm wind}}{e} = -\dot{M}_{\rm a,wind} [(M_{\rm a}+M_{\rm d})^{-1} + 0.5 M_{\rm a}^{-1}] \; . \tag{3.8}$$

[1]In Equation 9 of Iorio et al. 2023, Ω_d missing because of a typo. Moreover, the $R_{\rm eff}$ specification is missing in the description, although it is present in the current version of SEVN (v. 2.14).

3.2.2 Roche lobe overflow

Mass lost in a Roche lobe overflow

Mass loss rate. Following Hurley et al. 2002, in `SEVN` we describe the donor mass loss rate accounting for its stellar structure and for the amount of Roche lobe overfilled by the stellar radius

$$\dot{M}_{\rm d,RLO} = -F(M_{\rm d}) \left(\ln \frac{R_{\rm d}}{R_{\rm RL}} \right)^3 \ \mathrm{M_\odot\ yr^{-1}} \tag{3.9}$$

where

$$F(M_{\rm d}) = 3 \times 10^6 (\min(M_{\rm d}, M_{\rm max,SMT}))^2 \times \begin{cases} \max(\frac{M_{\rm env,d}}{M_{\rm d}}, 0.01) & \text{HG donors} \\ 10^3 M_{\rm d} (\max(R_{\rm d}, 10^{-4})^{-1} & \text{WD donors} \\ 1 & \text{Other donors} \end{cases} \tag{3.10}$$

where $M_{\rm max,SMT} = 5\ \ \mathrm{M_\odot}$, as in Hurley et al. 2002. The HG and WD acronyms refer to Hertzsprung-Gap and White Dwarf donors, respectively.

Mass loss rates in a Roche lobe overflow are higher than wind mass loss rates, so they could temporarily drive the star out of the thermal or hydrostatic equilibrium. For this reason, we limit the donor mass loss rate $\dot{M}_{\rm d}$ of Equation 3.9 accounting for the timescales necessary to regain thermal or hydrostatic equilibrium. We assume that giant stars have a well-defined core/envelope structure, so their mass transfer rate is limited by the thermal rate $\dot{M}_{\rm KH} = M_{\rm d}/\tau_{\rm KH}$, where $\tau_{\rm KH}$ is the Kelvin-Helmholtz timescale, as in Equation 61 of Hurley et al. 2002. For stars that do not have a well-defined core/envelope structure, such as MS or pure-Helium stars that did not yet develop a carbon-oxygen core, we limit the mass transfer rate to the dynamical one $\dot{M}_{\rm dyn} = M_{\rm d}/\tau_{\rm dyn}$, where $\tau_{\rm dyn}$ is the timescale necessary to regain hydrostatic equilibrium, as in Equation 63 of Hurley et al. 2002.

Mass accretion rate. The companion accretes a fraction $f_{\rm MT} \in [0, 1]$ of mass lost transferred from the donor[2]. With this notation, the mass accretion rate is given by

$$\dot{M}_{\rm a} = -f_{\rm MT} \dot{M}_{\rm d} \tag{3.11}$$

and can be limited to the Eddington rate in the case of accretion onto a compact object (Equation 3.4).

Orbital evolution via Roche lobe overflow

Angular momentum conservation. In a Roche lobe overflow, the exchanges or losses of mass from the donor, accretor, and binary will modify their respective angular momenta. If we conserve the total angular momentum of the system (stellar spins and orbital angular momentum), we can describe the variation of the orbital semimajor axis as

$$\Delta a_{\rm orb,RLO} = \frac{(J_{\rm orb} + \Delta J_{\rm orb,lost} + \Delta J_{\rm orb,d} + \Delta J_{\rm orb,a})^2 (M_{\rm a} + M_{\rm d})}{G(1-e^2) M_{\rm d}^2 M_{\rm a}^2} - a_{\rm orb} \tag{3.12}$$

[2]Some works in the literature indicate this parameter as $\beta = f_{\rm MT}$, e.g., Willcox et al. 2023; Klencki et al. 2025)

where M_d is the donor mass, M_a the accretor mass, a_orb the orbital semi-major axis, e the eccentricity, G the gravitational constant, J_orb the orbital angular momentum, and $\Delta J_\mathrm{orb,lost}$, $\Delta J_\mathrm{orb,d}$, $\Delta J_\mathrm{orb,a}$ its variations due to the mass lost by the system, transferred from the donor or accreted by the companion, respectively.

Orbital angular momentum. The orbital angular momentum J_orb can be expressed as a function of the reduced mass $\mu = M_\mathrm{a} M_\mathrm{d}/(M_\mathrm{a} + M_\mathrm{d})$ and angular velocity $\Omega_\mathrm{orb} = G^{1/2}(M_\mathrm{a} + M_\mathrm{d})^{1/2} a_\mathrm{orb}^{-3/2}$, as follows:

$$J_\mathrm{orb} = \mu \; a_\mathrm{orb}^2 \sqrt{1-e^2}\,\Omega_\mathrm{orb} \tag{3.13}$$

Orbital angular momentum variations. When the donor star transfers mass to the companion, it spins down. In `SEVN`, the spin angular momentum lost by the donor is added to the orbital angular momentum

$$\Delta J_\mathrm{orb,d} = -\Delta J_\mathrm{spin,d} = -\Delta M_\mathrm{d} R_\mathrm{eff}^2 \Omega_\mathrm{spin,d} \tag{3.14}$$

accounting for the stellar angular velocity $\Omega_\mathrm{spin,d}$ and considering an effective radius for the star R_eff that is equal to the Roche lobe radius: we assume that in a Roche lobe overflow, the stellar inertia is mostly affected by the mass still within the Roche lobe radius. In Equation 3.14, the mass lost by the donor star ($\Delta M_\mathrm{d} < 0$) is the one transferred via Roche lobe overflow (Equation 3.9) within a timestep.

In a similar way, in `SEVN` we consider that the mass accreted by the companion within a timestep ($\Delta M_\mathrm{a} > 0$, from Equation 3.11) removes angular momentum from the orbit

$$\Delta J_\mathrm{orb,a} = -\Delta J_\mathrm{spin,a} = -\Delta M_\mathrm{a} \sqrt{G M_\mathrm{a} R_\mathrm{acc}} \tag{3.15}$$

where we account for the possibility that an accretion disk is formed and the mass is accreted from an accretion radius R_acc (see Section 2.3 of Iorio et al. 2023 for further details).

Eventually, the mass non accreted by the companion will be lost by the system $\Delta M_\mathrm{lost} = |\Delta M_\mathrm{d}| - |\Delta M_\mathrm{a}|$ and carry away a fraction γ of the specific orbital angular momentum. For this reason, the orbital angular momentum J_orb will reduce by a quantity

$$\Delta J_\mathrm{orb,lost} = -|\Delta M_\mathrm{lost}| \; \gamma \; a_\mathrm{orb}^2 \sqrt{1-e^2} \; \Omega_\mathrm{orb} \tag{3.16}$$

3.2.3 Models for angular momentum losses in mass transfer events

The mass not accreted during a Roche lobe overflow could be lost by the system in the form of isotropic wind from the donor or from the accretor, it could outflow from the outer Lagrangian points, or it could accumulate in a circumbinary disk. In all these cases, we can model the loss of angular momentum through the γ parameter of Equation 3.16 and include its effect in the variation of the orbit semi-major axis (Equation 3.12).

The Soberman and Pols formalisms

In the literature, the γ parametrizations are described following the approach of Soberman et al. 1997 and Pols 2008. In both formalisms, the specific angular momentum j_lost carried by the ejected mass is expressed as a fraction γ of the specific orbital angular momentum $j_{\rm orb}$:

$$j_{\rm lost} = \gamma \; j_{\rm orb} \tag{3.17}$$

However, Soberman et al. 1997 and Pols 2008 adopt two different definitions for the specific orbital angular momentum $j_{\rm orb}$, as they divide the orbital angular momentum $J_{\rm orb}$[3] by, respectively, the reduced mass μ and the binary mass $M_{\rm bin} = M_a + M_d$:

$$j_{\rm orb,Soberman} = \frac{J_{\rm orb}}{\mu} = a_{\rm orb}^2 \Omega_{\rm orb} \tag{3.18}$$

$$j_{\rm orb,Pols} = \frac{J_{\rm orb}}{M_a + M_d} = \frac{M_a M_d}{(M_a + M_d)^2} a_{\rm orb}^2 \Omega_{\rm orb} \tag{3.19}$$

These approaches lead to two different definitions for the γ parameter, that can be converted one into another accounting for the donor (M_d) and accretor (M_a) masses:

$$\gamma_{\rm Pols} = \frac{(M_a + M_d)^2}{M_a M_d} \gamma_{\rm Soberman} \tag{3.20}$$

The conversion between the Pols 2008 and the Soberman et al. 1997 approach depends on the masses of the orbiting objects, so the choice of the formalism impacts the expected dependency of the γ parameter on the mass ratio $q = M_{\rm a}/M_{\rm d}$, as shown in Figure 3.1. In Table 3.1 we report the expressions for the γ parameter of Equation 3.17 with both the Soberman et al. 1997 and Pols 2008 formalism for the mass loss scenarios considered in this work. Hereafter, we will derive and use the expressions for γ according to the Soberman et al. 1997 formalism, as it is the one used in `SEVN`:

$$\gamma_{\rm SEVN} = \gamma_{\rm Soberman} = \frac{j_{\rm lost}}{j_{\rm orb,Soberman}} = \frac{j_{\rm lost}}{a_{\rm orb}^2 \Omega_{\rm orb}}. \tag{3.21}$$

As a final remark, we highlight that the Soberman et al. 1997 and Pols 2008 formalisms just provide two different approaches to describe the same physical problem. Therefore, the results that we will find in `SEVN` will be interpretable in the Pols 2008 context once the appropriate scaling (Equation 3.20) is considered.

Isotropic losses and outflows

Under the fast wind approximation, the ejected material is faster than the orbital velocity, so further interactions with the binary can be neglected. In this scenario, the mass lost from the system carries away a specific angular momentum

$$j_{\rm lost,wind} = a_{\rm lost}^2 \Omega_{\rm lost} \tag{3.22}$$

that depends only on the distance from the binary centre of mass at the moment of the ejection $a_{\rm lost}$ and on its angular velocity $\Omega_{\rm lost}$ (Jeans 1924; Huang 1963; van den Heuvel 1994).

[3]Hereafter we will refer to the orbital angular momentum for a circular orbit because we expect that a star overfilling its Roche lobe will rapidly circularize ($e \sim 0$) (Hut 1981). Nevertheless, in `SEVN` the orbital quantities and their evolution are computed accounting for the eccentricity (Iorio et al. 2023).

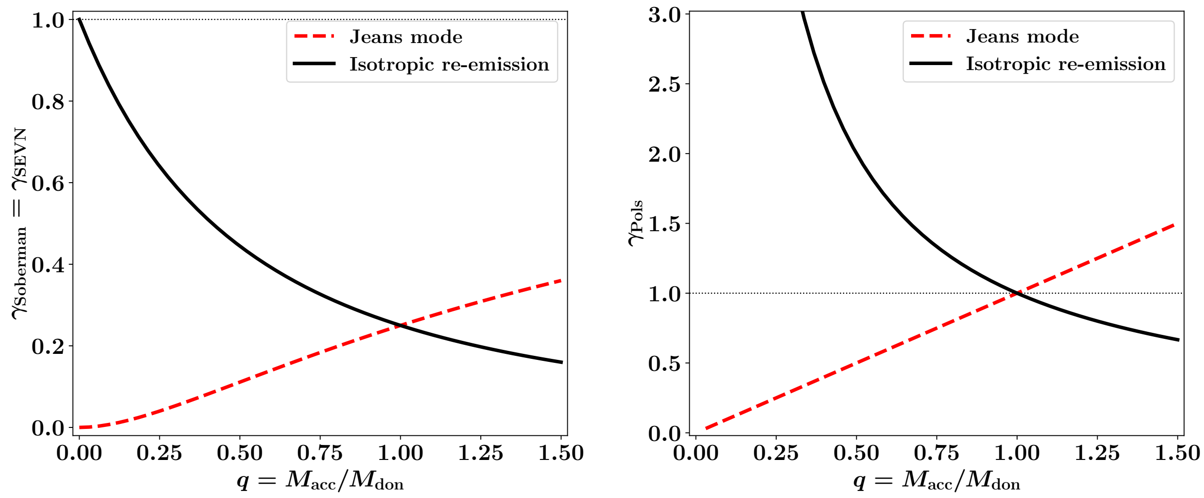

Figure 3.1: In the Soberman et al. (1997) formalism, adopted in SEVN, both the Jeans (Equation 3.24) and the isotropic re-emission (Equation 3.25) models cannot extract a specific angular momentum larger than the orbital one (γ <1). The Pols 2008 formalism has a different dependence on the component masses (Table 3.1) and a different definition of the specific orbital angular momentum (3.19), so it is possible to have $\gamma > 1$ for these models.

Assuming co-rotation at the moment of the ejection ($\Omega_{\rm lost} = \Omega_{\rm orb}$), the γ parameter of Equation 3.21 can be written as:

$$\gamma_{\rm wind} = \left(\frac{a_{\rm lost}}{a_{\rm orb}}\right)^2 \tag{3.23}$$

Jeans mode. In the Jeans mode (Jeans 1924), the mass is lost from the proximity of the donor star in the form of fast isotropic wind. The donor star has a distance $a_{\rm lost} = a_{\rm d} = a_{\rm orb} M_{\rm a}/(M_{\rm a} + M_{\rm d})$ from the binary centre of mass, so the γ parameter can be expressed as:

$$\gamma_{\rm Jeans} = \left(\frac{M_{\rm a}}{M_{\rm a} + M_{\rm d}}\right)^2 \tag{3.24}$$

Isotropic re-emission. In the isotropic re-emission model, the non-accreted mass is re-emitted from the proximity of the accretor star. If the accretor is a star, the emission occurs in the form of isotropic fast wind. Technically, the material is lost isotropically from the point of view of the star, but it is not isotropic with respect to the centre of mass of the binary: for this reason, the binary loses some orbital angular momentum. Furthermore, if the accretor is a BH, the emission could also occur via jets. In both cases, the fast wind approximation can be used to described the specific angular momentum carried away by the ejected material (Huang 1963; van den Heuvel 1994). Recalling that the accretor has a distance $a_{\rm lost} = a_{\rm a} = a_{\rm orb} M_{\rm d}/(M_{\rm a} + M_{\rm d})$ from the binary centre of mass, we obtain:

$$\gamma_{\rm iso} = \left(\frac{M_{\rm d}}{M_{\rm a} + M_{\rm d}}\right)^2 \tag{3.25}$$

γ formalism	Jeans mode	Isotropic re-emission	Lagrangian outflow	Circumbinary disk
Sobermann	$\frac{M_a^2}{(M_a+M_d)^2}$	$\frac{M_d^2}{(M_a+M_d)^2}$	$\frac{a_{\mathrm{L\ out}}^2}{a_{\mathrm{orb}}^2}$	$\sqrt{\frac{a_{\mathrm{disk}}}{a_{\mathrm{orb}}}}$
Pols	$\frac{M_a}{M_d}$	$\frac{M_d}{M_a}$	$\frac{(M_a+M_d)^2}{M_a M_d}\ \frac{a_{\mathrm{L\ out}}^2}{a_{\mathrm{orb}}^2}$	$\frac{(M_a+M_d)^2}{M_a M_d}\sqrt{\frac{a_{\mathrm{disk}}}{a_{\mathrm{orb}}}}$

Table 3.1: Expressions for the fraction γ of specific angular momentum removed from a binary by the mass ejected during a Roche lobe overflow in the form of wind nearby the donor star (Jeans mode; Equation 3.24), wind nearby the accretor star (Isotropic re-emission; Equation 3.25), outflow from the outer Lagrangian point (Equation 3.28), or circumbinary disk (Equation 3.30). We report the expressions derived in Section 3.2.2 following the Soberman et al. 1997 formalism, and their converted counterparts in the Pols 2008 formalism (Equation 3.20). We consider a donor star of mass M_d that transfers mass to an accretor of mass M_a.

Outflow through the outer Lagrangian point. In mass transfer processes, the extended stellar atmosphere of the donor can outflow through its outer Lagrangian point (L3 if $M_\mathrm{d} > M_\mathrm{a}$; L2 if $M_\mathrm{d} < M_\mathrm{a}$) or part of the transferred mass could be lost from the outer Lagrangian point of the accretor (L2 if $M_\mathrm{d} > M_\mathrm{a}$; L3 if $M_\mathrm{d} < M_\mathrm{a}$). Assuming that the ejected material has a velocity larger than the orbital velocity, Marchant et al. 2021 describe the specific angular momentum lost from the outer Lagrangian point as:

$$j_{\mathrm{lost,L\ out}} = a_{\mathrm{orb}}^2\ \Omega_{\mathrm{orb}} \left(\frac{M_\mathrm{a}}{M_\mathrm{a}+M_\mathrm{d}} - \hat{X}_{\mathrm{L\ out}}\right)^2 \tag{3.26}$$

where $\hat{X}_{\mathrm{L\ out}} = a_{\mathrm{L\ out}}/a_{\mathrm{orb}}$ indicates the distance $a_{\mathrm{L\ out}}$ of the outer Lagrangian point from the binary centre of mass[4], normalized to the orbital separation a_{orb}. Following Klencki et al. 2025, we approximate[5] Equation 3.26 to its leading order

$$j_{\mathrm{lost,L\ out}} \approx a_{\mathrm{orb}}^2\ \Omega_{\mathrm{orb}}\ \hat{X}_{\mathrm{L\ out}}^2 \tag{3.27}$$

recalling that the accretor mass is always smaller than the binary mass ($M_\mathrm{a} < M_\mathrm{a} + M_\mathrm{d}$) while the outer Lagrangian points are always larger than the orbital separation ($\hat{X}_{\mathrm{L\ out}} \approx 1 - 1.25$, with a mild dependence on the mass ratio, as described in Pennington 1985).

With this approximation, the $\gamma_{\mathrm{L\ out}}$ parameter that describes outflows through the outer Lagrangian point can be written as:

$$\gamma_{\mathrm{L\ out}} \approx \hat{X}_{\mathrm{L\ out}}^2 = \left(\frac{a_{\mathrm{L\ out}}}{a_{\mathrm{orb}}}\right)^2 \tag{3.28}$$

Comparing the definitions of γ_{wind} (Equation 3.23) and $\gamma_{\mathrm{L\ out}}$ (Equation 3.28), we can apply the same geometrical interpretation to both the specific angular momentum removed

[4]Inserting the distance of L2 or L3 in Equation 3.26 describes the respective outflows.

[5]We take as reference the definition of γ_{L2} of Equation 4 in Klencki et al. 2025. We recall that Klencki et al. 2025 follow the γ formalism of Pols 2008, so we used Eqs. 3.19 and 3.20 to retrieve the correct approximation for $j_{\mathrm{orb,L\ out}}$.

via winds and the one removed via outer Lagrangian outflows. In both cases, the amount of specific angular momentum carried away by the ejected material depends only on the location of the material at the moment of the ejection. Considering the standard case where the donor is more massive than the accretor, the outer Lagrangian point in the proximity of the accretor (L2) would be the farthest one. Marchant et al. 2021 show that, in this configuration, outflows from L2 could remove up to 47% more specific angular momentum than outflows from the proximity of the donor star (L3).

Circumbinary disk

It is possible that the mass lost from the binary is not able to exit the potential of the binary, forming a circumbinary disk. In this case, part of the specific angular momentum carried away by the lost material is returned to the orbit because of the disk-binary interactions. Only the specific angular momentum of the disk is actually removed from the binary. Considering a stable disk in a Keplerian orbit around the binary at a distance a_{disk}, we can describe the specific angular momentum of the disk as

$$j_{\mathrm{disk}} = a_{\mathrm{disk}}^2 \Omega_{\mathrm{disk}} = \sqrt{G(M_{\mathrm{d}} + M_{\mathrm{a}}) a_{\mathrm{disk}}} \tag{3.29}$$

which corresponds to

$$\gamma_{\mathrm{disk}} = \sqrt{\frac{a_{\mathrm{disk}}}{a_{\mathrm{orb}}}} \tag{3.30}$$

Circumbinary disks can be considered stable if they form beyond the outermost Lagrangian point of the binary ($a_{\mathrm{disk,min}} \geq a_{\mathrm{L\ out,max}}$). Depending on the mass ratio of the two orbiting objects, the outermost Lagrangian point of the binary could be in the $a_{\mathrm{disk,min}} = a_{\mathrm{L\ out,max}} \approx 1 - 1.25\ a_{\mathrm{orb}}$ range (Pennington 1985), corresponding to $\gamma_{\mathrm{disk,min}} \approx 1 - 1.12$ (Soberman et al. 1997).

3.3 Simulation setup

3.3.1 Parameter space exploration

Angular momentum loss models.

In this work we will explore the impact on the formation of BBHs of different prescriptions for angular momentum losses during a mass transfer. Recalling the definitions introduced in Section 3.2.2, we will conduct this study with `SEVN` exploring four possible values for the γ parameter that describes the amount of specific angular momentum removed from the orbit (Equation 3.21):

1. $\gamma = \gamma_{\mathrm{Jeans}}$. The mass is ejected in the proximity of the donor star (Jeans mode).

2. $\gamma = \gamma_{\mathrm{iso}}$. The mass is ejected in the proximity of the accretor star (isotropic re-emission model).

3. $\gamma = 1$. It can be interpreted as two limiting cases: outflow from the innermost possible outer Lagrangian point ($a_{\mathrm{L\ out,min}} = a_{\mathrm{orb}}$) or formation of an circumbinary disk at innermost possible stable orbit ($a_{\mathrm{disk}} = a_{\mathrm{orb}}$). Both interpretations can be

associated with the formation of a contact binary, although we highlight that this configuration is likely extreme: we explore it here only to bracket the uncertainty on the outflow and circumbinary disk models.

4. $\gamma = 1.5$. It can be interpreted as outflow from the outermost possible outer Lagrangian point ($a_{\mathrm{L\ out,max}} \approx 1.22\ a_{\mathrm{orb}}$) or it can be associated with the formation of a stable circumbinary disk at a distance $a_{\mathrm{disk}} = 2.25\ a_{\mathrm{orb}}$. The latter case corresponds to the fiducial stable case in Soberman et al. 1997, since this circumbinary disk is wide enough to be stable regardless on the mass ratio of the two orbiting objects ($\gamma_{\mathrm{disk,min}} \approx 1 - 1.12$).

Tides and metallicity

In environments with a small metal content, we expect that the stellar winds are less powerful, limiting the possibility that the binary widens (e.g. Vink et al. 2011). We also expect that stars remain compact, possibly delaying the onset of mass transfer episodes (e.g. Costa et al. 2023). Therefore, for each angular momentum loss assumption, we simulate the evolution of a binary population at $Z = 0.00142$ and $Z = 0.000142$, to investigate also the impact of metallicity. Furthermore, for each combination of metallicity Z and angular momentum model, we test the evolution with or without tides, as we expect that strong tidal synchronization could extract angular momentum from the orbit to spin up the star, further enhancing the orbital reduction and possibly leading to a premature coalescence (Darwin 1880).

3.3.2 Initial conditions and model variations

Simulated sets

We generate a population of 5×10^6 massive binary stars with initial mass, mass ratio, orbital period, and eccentricity drawn from observationally motivated distributions (Kroupa 2001; Sana et al. 2012; Moe & Di Stefano 2017), adopting the same methodology adopted in Korb et al. 2025 (Section 2.6.2). We evolve this same population under the 4 combinations of angular momentum losses, 2 metallicities, and 2 tidal modes explored in this work, for a total of 16 simulated sets.[6].

Hereafter, we will sometimes use verbose acronyms to indicate the sets simulated at each metallicity. We will use the -*T* (-*NT*) suffix to indicate populations simulated with tides active (disabled) and we will use the *Iso*-, *Jeans*-, *Lmin*-, *Lmax*- prefix to indicate the model for orbital angular momentum loss, respectively, isotropic re-emission (γ_{iso}, Equation 3.25), Jeans mode (γ_{Jeans}, Equation 3.24), $\gamma = 1$, and $\gamma = 1.5$ (the latter two representative respectively of the minimum or maximum possible location of the outer Lagrangian point, Equation 3.28).

Binary evolution

We set the wind accretion parameters (Equation 3.1) to their standard values of $\alpha_{\mathrm{wind}} = 1.5$ and $\beta_{\mathrm{wind}} = 0.125$, calibrated on observations of cool super-giant stars (Kučinskas 1998; Hurley et al. 2002). We assume that during a Roche lobe overflow only half of the transferred mass is accreted by the companion $f_{\mathrm{MT}} = 0.5$ (Equation 3.11) and we ensure

[6]In this work we use the main v. 2.14 version of `SEVN`, updated at the `99c2ca17` commit.

that accretion on compact objects is Eddington-limited ($\eta_{\rm Edd} = 1$ in Equation 3.4). We describe the CE evolution following the $\alpha - \lambda$ formalism (Webbink 1984), assuming that all the orbital energy is consumed to eject the CE ($\alpha_{\rm CE} = 1$) and that the envelope binding energy can be described with the $\lambda_{\rm CE}$ fits of Claeys et al. 2014. We also assume that mass transfer becomes unstable if the donor-to-accretor mass ratio overcomes a critical threshold $q_{\rm crit}$, that depends on the stellar evolutionary stage. Here, we follow the $q_{\rm crit}$ values of `STARTRACK`, as implemented in Belczynski et al. 2008, and consider $q_{\rm crit} = 3$ for all H-rich stars, $q_{\rm crit} = 1.7$ for core-helium burning pure helium stars, and $q_{\rm crit} = 3.5$ for helium-shell burning helium stars. Moreover, we allow HG stars to enter and possibly survive a CE event (the so-called "optimistic scenario"). We recall that the $q_{\rm crit}$ approach does not capture the complex dependence of mass transfer stability from the envelope structure of the donor (e.g. Ge et al. 2015, 2020; Klencki et al. 2020; Klencki et al. 2021), but we highlight that this simplified approach allows us to better identify the impact of angular momentum alone and to better compare our results with other works in the literature (e.g., Gallegos-Garcia et al. 2021). In Section 3.5.1 we will discuss variations from this fiducial model, adopting a different treatment for $q_{\rm crit}$ and $\lambda_{\rm CE}$. We will also discuss the impact of different stellar models, comparing our fiducial `PARSEC` tracks (Costa et al. 2025)[7] with the `MIST` isochrones developed by Choi et al. 2016.

Supernovae and remnants

In our simulations, all COs with final remnant mass > 3 M$_\odot$ are classified as BHs, following the fiducial setup of `SEVN` (Iorio et al. 2023). We consider the "delayed" SN model of Fryer et al. 2012, motivated by the recent observations in the putative low-mass gap (Abac et al. 2024). We rely on Mapelli et al. 2020 fits on the helium cores evolved in Woosley 2017 to model the PI mass gap. Therefore, stars that at the end of the carbon burning phase have a helium core of $32\ {\rm M}_\odot \leq {\rm M}_{\rm He,f} < 64\ {\rm M}_\odot$ enter the PPI regime, stars with helium core in the $64\ {\rm M}_\odot \leq {\rm M}_{\rm He,f} < 135\ {\rm M}_\odot$ leave no remnant (PI), and stars with heavier cores $M_{\rm He,f} \geq 135\ {\rm M}_\odot$ directly collapse into intermediate-mass BHs. In Section 3.5.4 we will discuss the impact of the PI assumption and compare our results with the model of Farmer et al. 2019, that uses the carbon-oxygen core to determine the type of instability encountered and its effects on the final BH mass (Equation A.1 in Farmer et al. 2019).

We consider only the Blaauw kick (Blaauw 1961) in the CO formation, to minimize the randomizing effect of natal kicks in the redistribution of the final BCO properties, thus on their possibility to merge within the lifetime of the Universe (< 14 Gyrs, Iorio et al. 2023). Since we are focusing on BHs formed at low metallicity, we expect that stellar winds are quenched. Therefore, BH progenitors are more likely to retain mass at the pre-supernova stage and to produce more massive BHs. Because of the linear momentum conservation, these heavier BHs are more likely to receive a low magnitude natal kick, so neglecting natal kicks in this study should not significantly affect our results (Atri et al. 2019; Giacobbo & Mapelli 2020; Korb et al. 2025).

[7] We adopt the fiducial set for `SEVN`, with $\lambda_{\rm ov} = 0.5$ overshooting parameter (Iorio et al. 2023)

3.4 Results

3.4.1 Polluting the PI mass gap

In our simulations, primary BHs can be as massive as $M_{\mathrm{BH,max,primary}} \approx 58\ \mathrm{M}_{\odot}$ ($Z = 0.000142$) while secondary BHs never exceed $M_{\mathrm{BH,max,secondary}} \leq 46\ \mathrm{M}_{\odot}$ (Figure 3.2 and Figure 3.3). These results are qualitatively in agreement with the most recent release of GW data, GWTC-4.0 (The LIGO Scientific Collaboration et al. 2025a), within model uncertainties. The current observed BBH population exhibits a declining, but non-zero, distribution of primary (secondary) BHs beyond $\gtrsim 35\ \ \mathrm{M}_{\odot}$ ($\gtrsim 40 - 60\ \ \mathrm{M}_{\odot}$). As discussed in Ray & Kalogera 2025, the sample of BBH detections is still too limited to infer the existence of a PI gap, but its presence cannot be ruled out. In this context, we show that the BH mass limit of $M_{\mathrm{BH,max}} \approx 45 - 50\ \mathrm{M}_{\odot}$, that is expected for BHs in BBHs as a consequence of PI from stars that were completely stripped of their H-envelope (Woosley 2017; Spera & Mapelli 2017; Farmer et al. 2019, 2020; Renzo et al. 2020a; Iorio et al. 2023), is sensitive to single stellar evolution and orbital angular momentum losses.

3.4.2 Stellar physics and maximum BH masses

Maximum BH mass of pure-Helium stars

In this work, we couple the `PARSEC` tracks of Costa et al. 2025 with the fits of Mapelli et al. 2020 on the Woosley 2017 PI model. With this setup, the maximum BH mass of pure-Helium stars is $M_{\mathrm{BH,max,pure-He}} = 46\ \mathrm{M}_{\odot}$, for both $Z = 0.00142$ and $Z = 0.000142$ (Figure 11 of Iorio et al. 2023). We see that the maximum BH mass from `PARSEC` pure-Helium stars alone would be in agreement with the existence of a PI mass gap above $\gtrsim 45\ \mathrm{M}_{\odot}$, as predicted by other works in the literature that also evolved bare helium cores through PPI and PI (e.g., Woosley 2017; Farmer et al. 2019). Therefore, the BHs that have higher masses than the pure-Helium star limit ($M_{\mathrm{BH}} > 46\ \mathrm{M}_{\odot}$) can only be produced by stars that retain some hydrogen envelope at the pre-supernova stage.

Maximum BH mass of H-rich stars

The onset of PPI generally determines the maximum BH mass for H-rich stars. Stellar objects with initial masses at the ZAMS of $M_{\mathrm{ZAMS}} \approx 60\ \mathrm{M}_{\odot}$ have He-core masses of $M_{\mathrm{He-core}} \approx 32\ \mathrm{M}_{\odot}$, close to the onset of PPI. At the low metallicities explored in these work, stars will retain most of their masses throughout their lives and, if they massive enough, they will directly collapse into a BH (Fryer et al. 2012): at $Z = 0.000142$ ($Z = 0.00142$), stars with initial masses of $M_{\mathrm{ZAMS}} \approx 60\ \mathrm{M}_{\odot}$ will produce BHs of $M_{\mathrm{BH}} \approx 60\ \mathrm{M}_{\odot}$ ($M_{\mathrm{BH}} \approx 55\ \mathrm{M}_{\odot}$). Heavier stars have more massive helium cores, so, they will experience PPI and produce lighter remnants: their final mass that could be as light as $M_{\mathrm{BH}} \approx 35\ \mathrm{M}_{\odot}$.

In our fiducial `PARSEC` stellar models, H-rich stars evolved in isolation are not limited to produce BHs up to $M_{\mathrm{BH,max,H-rich}} = 60\ \mathrm{M}_{\odot}$: at $Z = 0.000142$, the maximum BH mass from H-rich stars is about $\approx 90\ \mathrm{M}_{\odot}$. This heavier limit in the maximum BH mass is a consequence of the `PARSEC` stellar models interpolated here, that were computed as stellar objects with a hydrogen envelope from the ZAMS until the end of core-carbon-oxygen burning.

As discussed in Iorio et al. 2023 and Costa et al. (2025), at low metallicity ($Z \approx 0.001 - 0.0001$), the opacity increases and facilitates the creation of deep convective envelopes. As stars evolve, it is possible that this envelope extends deeply enough penetrate into the helium core, triggering a dredge-up event. Dredge-ups in the core-helium burning phase have a stabilizing effect against PPI, because they reduce the size of the helium-core. Since the impact of metallicity and dredge-up is non-linear with the initial progenitor mass, at $Z \approx 0.001 - 0.0001$ only the PARSEC stellar models with initial mass of $M_{\rm ZAMS} \approx 80 - 100$ M$_\odot$ are able to experience such dredge-up episodes during the core-He burning phase, creating BHs of $M_{\rm BH,max,H-rich} \approx 80 - 90$ M$_\odot$.

Maximum BH mass in all bound BH-BHs

The effect of single stellar evolution in the predicted BH masses of a population of binaries can be seen in the primary BH spectra of bound BH-BH binaries. Figure 3.4 shows that, in any of the simulated bound BH-BH binaries, the most massive BHs have indeed a mass below $M_{\rm BH} \lesssim 60$ M$_\odot$, but at $Z = 0.000142$ there is a tail of BHs with mass up to $\lesssim 90$ M$_\odot$.

3.4.3 Orbital angular momentum losses

BBH and bound BH-BH mass spectra.

The differences between the spectra of primary BH masses in BBHs (Figure 3.2) or in bound BH-BH binaries (Figure 3.4) are due to the effect of binary evolution, in particular mass transfer. Therefore, they will be strongly sensitive to the assumptions on the fraction γ of specific orbital angular momentum extracted by the non-accreted mass.

In the bound BH-BH population, efficient angular momentum extraction ($\gamma \geq 1$) quenches only the formation of BHs below $M_{\rm BH} \lesssim 30$ M$_\odot$. This occurs because light BHs are a common product of mass transfer interactions and Lagrangian outflows (or the formation of a circumbinary disk) can extract more angular momentum than isotropic mass losses, leading more frequently to a premature coalescence. This selection effect is less evident in the BBH population, since all BBHs had to experience at least a mass transfer event in order to merge within a Hubble time (< 14 Gyrs). In BBHs, the assumptions on γ have the largest impact on the maximum BH mass: both the primary and secondary BHs could be up to $\lesssim 10 - 15$ M$_\odot$ heavier if we assume efficient angular momentum extraction from Lagrangian outflows or circumbinary disk ($\gamma \geq 1$) in place of isotropic mass losses, either from the donor or accretor ($\gamma_{\rm iso}$ or $\gamma_{\rm Jeans}$).

Space of the initial orbital configurations

In Figure 3.5 we show that the assumption on the orbital angular momentum loss modifies the space of the initial orbital configurations of BBHs. Efficient extraction of orbital angular momentum ($\gamma \geq 1$) allows wider and heavier binaries to become BBHs, including more progenitors with initial separation beyond $a_{\rm ZAMS} \gtrsim 100$ $R_\odot$ and the heaviest stars with masses larger than $M_{1,\rm ZAMS} \gtrsim 50$ M$_\odot$. This extended space of the possible initial configurations includes also the systems that will contain a primary BH with mass larger than $\gtrsim 45$ M$_\odot$. In Figure 3.5 we see that the production of BHs beyond the $\gtrsim 45$ M$_\odot$ putative limit is indeed due to H-rich progenitor stars that are close to the onset of PPI ($M_{\rm ZAMS} \approx 60$ M$_\odot$ or the island at $M_{\rm ZAMS} \approx 80 - 90$ M$_\odot$). In some cases, such BHs could be also produced by stellar progenitors that are so heavy $M_{\rm ZAMS} \approx 150$ M$_\odot$ to avoid PPI and, instead, directly collapse.

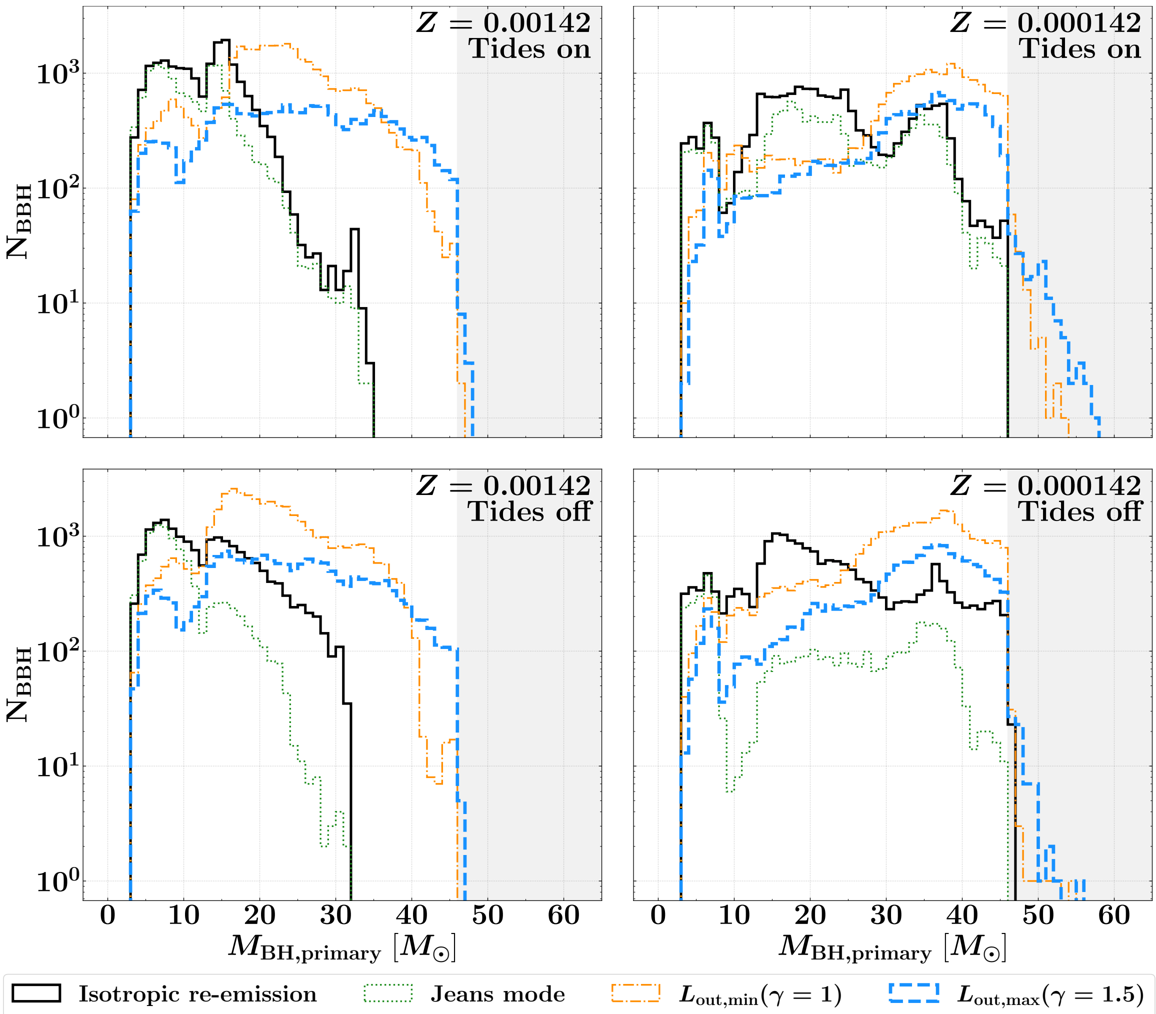

Figure 3.2: Mass distribution of the most massive BHs (primaries) in the merging BBH populations obtained for the two metallicities, tidal models, and orbital angular momentum loss models considered in this work (Section 3.3.1). Each histogram shows the number of BBHs $N_{\rm BBH}$ hosting a primary BH with mass $M_{\rm BH,primary}$ falling into a specific mass bin (all mass bins are equals, with size of $\Delta M_{\rm bin} = 1\ \ {\rm M}_{\odot}$). With the grey area we highlight the region beyond $> 46\ {\rm M}_{\odot}$ of BHs that cannot be formed by pure-Helium stars.

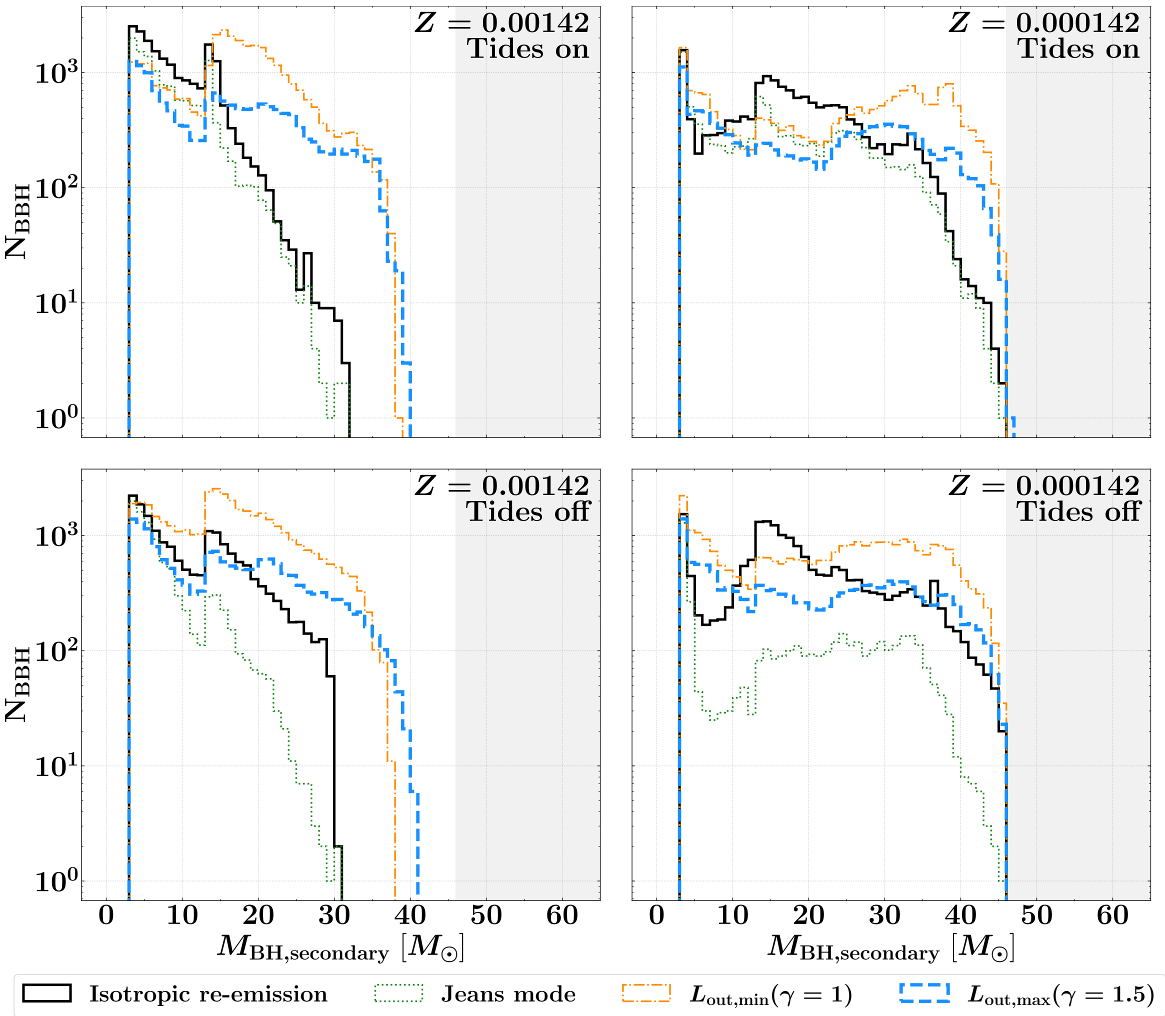

Figure 3.3: Mass distribution of the least massive BHs (secondaries) in the merging BBH populations obtained for the two metallicities, tidal models, and orbital angular momentum loss models considered in this work (Section 3.3.1). Each histogram shows the number of BBHs $N_{\rm BBH}$ hosting a secondary BH with mass $M_{\rm BH,secondary}$ falling into a specific mass bin (all mass bins are equals, with size of $\Delta M_{\rm bin} = 1\ \ {\rm M}_\odot$). With the grey area we highlight the region beyond $> 46\ {\rm M}_\odot$ of BHs that cannot be formed by pure-Helium stars.

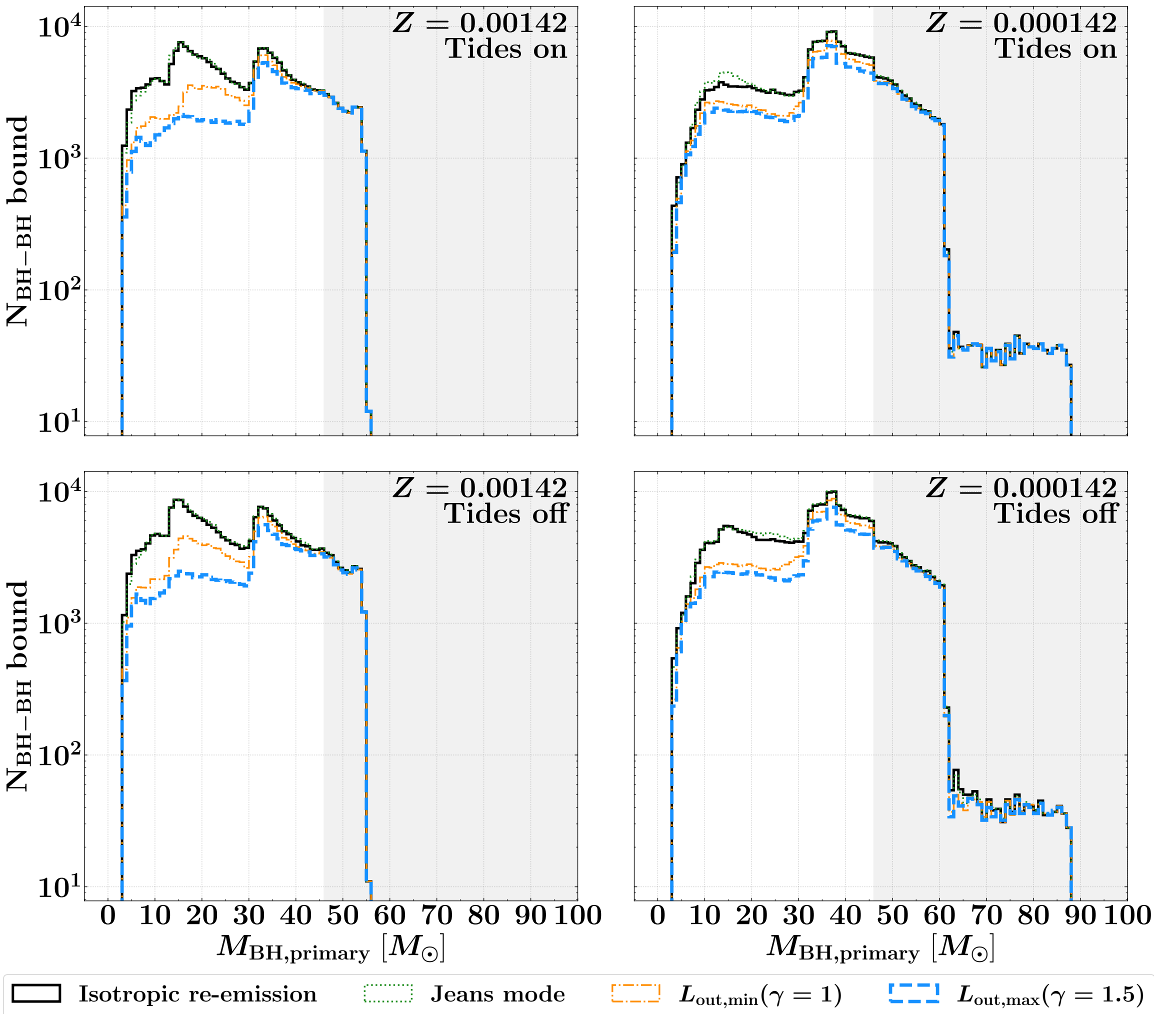

Figure 3.4: Mass distribution of the most massive BHs (primaries) in the populations of bound BH-BH systems obtained for the two metallicities, tidal models, and orbital angular momentum loss models considered in this work (Section 3.3.1). Each histogram shows the number of BH-BHs $N_{\mathrm{BH-BH}}$ hosting a primary BH with mass $M_{\mathrm{BH,primary}}$ falling into a specific mass bin (all mass bins are equals, with size of $\Delta M_{\mathrm{bin}} = 1\ \mathrm{M}_{\odot}$). With the grey area we highlight the region beyond $> 46\ \mathrm{M}_{\odot}$ of BHs that cannot be formed by pure-Helium stars.

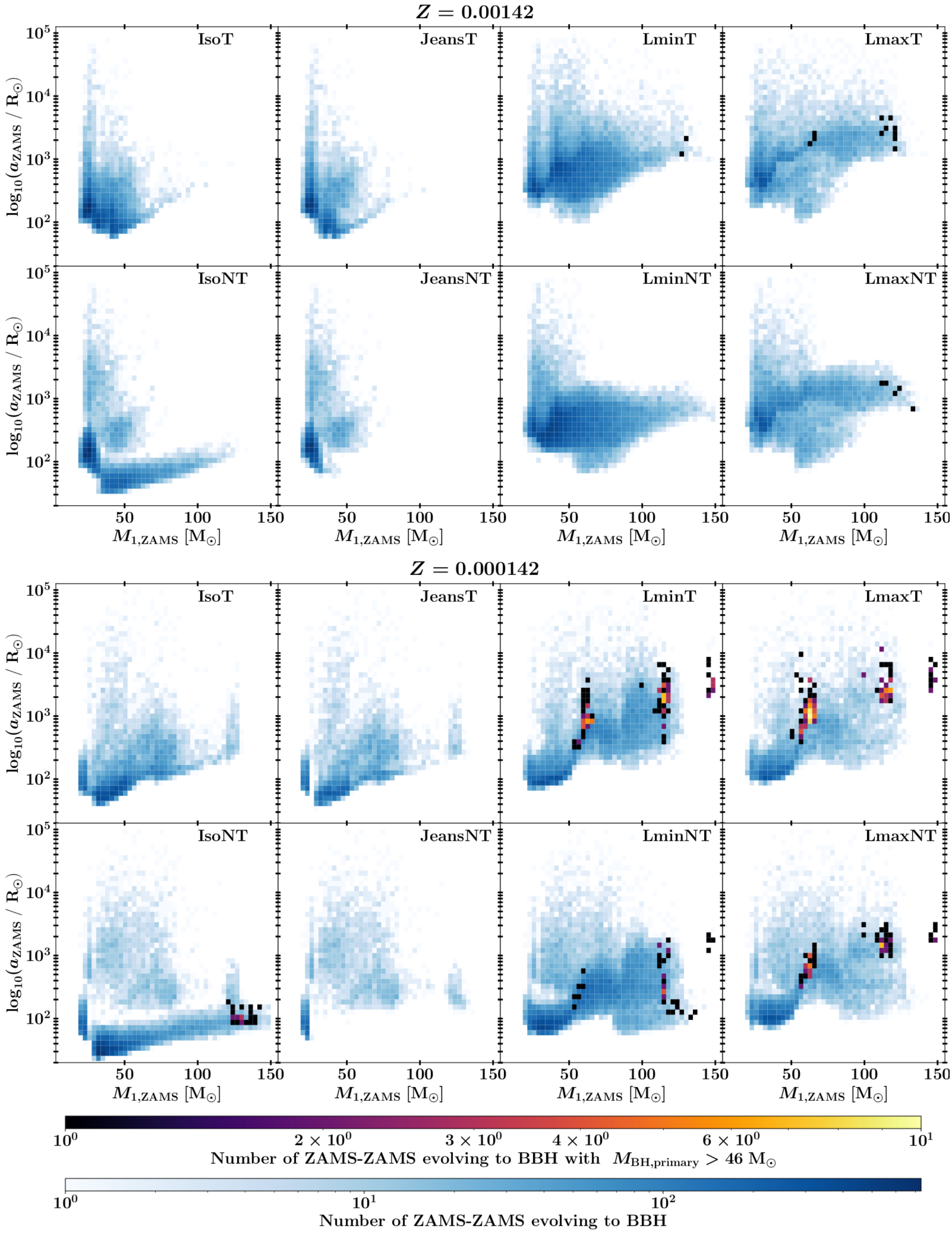

Figure 3.5: ZAMS-ZAMS orbital properties (semimajor axis $a_{\rm ZAMS}$ and heavier mass $M_{1,\rm ZAMS}$) for the BBH progenitors (blue) formed in each set considered in this work (Section 3.3.2). We highlight with the inferno colormap the progenitors of BBHs with primary BH larger than > 46 M$_\odot$, showing that they generally are formed by the heaviest initial stars and close to the onset of pair-instability (Section 3.4.2).

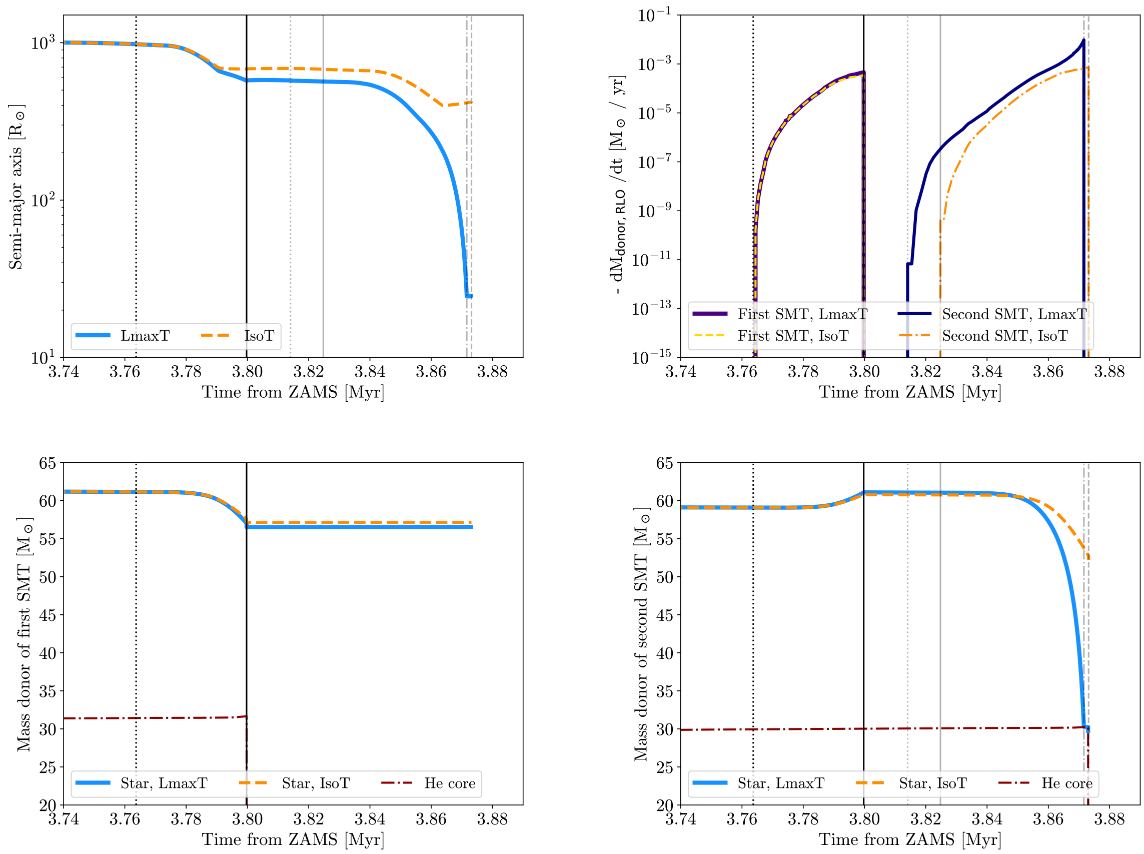

Figure 3.6: Evolution of a binary with initial separation $a_{\rm ZAMS} = 1000\ R_\odot$ and masses of $M_{1,\rm ZAMS} = 61\ \rm M_\odot$ and $M_{2,\rm ZAMS} = 59\ \rm M_\odot$, at $Z = 0.000142$ and with tides active, assuming the isotropic re-emission model from the secondary (IsoT)or the outflow from the outermost possible Lagrangian point (LmaxT). The LmaxT model will produce a merging BBHs, the IsoT will produce a wide bound BH-BH binary. We show the variation of the orbital semimajor axis (top left panel), mass of the initially most massive star (bottom left), least massive star (bottom right), and mass transfer rate during the first and second SMT events.

Isolated binary evolution of a single representative system

To better illustrate the effect of the assumption on the angular orbital momentum on the selection effects and production of BHs beyond $\gtrsim 45\ \rm M_\odot$, in Figure 3.6 we show the evolution of a representative system: a circular binary with initial separation of $a_{\rm ZAMS} = 1000\ R_\odot$ and masses of $M_{1,\rm ZAMS} = 61\ \rm M_\odot$ and $M_{2,\rm ZAMS} = 59\ \rm M_\odot$, also considering a metallicity of $Z = 0.000142$ and tides active. We focus on two assumptions for the fraction γ of specific orbital angular momentum carried away by the mass lost in a RLO event: isotropic re-emission from the secondary or outflow from the outermost possible Lagrangian point ($\gamma = 1.5$, equivalent to an outflow from $a_{\rm L,out,max} \approx 1.22\ a_{\rm orb}$ or to the formation of a stable circumbinary disk at $a_{\rm disk} \approx 2.25\ a_{\rm orb}$). By definition, Lagrangian outflows (or, equivalently, circumbinary disks) will remove a larger fraction of specific orbital angular momentum with respect to the isotropic re-emission model ($\gamma_{\rm iso} \leq 1$, as shown in Figure 3.1).

The system considered here experiences two SMT events, one before and one after the formation of the first BH. For both the assumptions on γ, the first SMT lasts for about $\approx 4 \times 10^4$ yrs and removes about ≈ 5 $\mathrm{M}_\odot$ from the donor star. Even if both assumptions remove nearly the same amount of mass from the system, the Lagrangian outflow assumption removes a larger fraction of *specific* orbital angular momentum. Therefore, the system evolved with $\gamma = 1.5$ loses more angular momentum and shrinks more than the system evolved with the isotropic re-emission model. In this example, the additional orbital reduction corresponds to about $\approx 15\%$ of the final orbital separation of the isotropic re-emission model, bringing the post-interaction orbit to ≈ 600 $R_\odot$ instead of ≈ 700 $R_\odot$.

The first SMT ended abruptly when the donor star experienced a supernova event shortly after the core-helium burning stage, given the fast evolution of such massive progenitors. Therefore, in the second SMT we deal with a MS star that donates mass to a BH. In this work we assume an Eddington-limited accretion scenario (Equation 3.4), so most of the transferred mass will not be accreted but it will be lost by the system. The second SMT is therefore expected to be more efficient in the extraction of orbital angular momentum, thus in the orbital reduction. However, in Figure 3.6 we show that this enhanced orbital variation occurs only in the Lagrangian outflow model: assuming $\gamma = 1.5$ reduces the orbital separation by more than one order of magnitude (from ≈ 600 $R_\odot$ to ≈ 25 $R_\odot$), while the isotropic re-emission model causes an orbital decrease comparable to the one in the first SMT ($\Delta a_{\mathrm{orb}} \approx 300$ $R_\odot$). The very tight (wide) orbit reached in the $\gamma = 1.5$ (isotropic re-emission) case will (not) allow the merger via GW emission within a Hubble time.

The different evolution during the second SMT is due to two concurring factors: Eddington-limited accretion and slightly different orbital separations, as a result of the first SMT. On the one hand, Eddington-limited accretion strongly enhances the amount of mass lost from the system in the second SMT, making it more impactful in the determination of the future evolution and final fate of the overall binary. On the other hand, a slightly tighter orbit determines a tighter Roche lobe radius. Therefore, the donor will overfill its Roche lobe sooner and by a larger amount, implying that the SMT will last longer and that the donor will transfer even more mass, thus, remove more orbital angular momentum[8].

As a final remark, we highlight that the most massive BH originated from the most massive progenitor: even if the first SMT reversed the mass ratio of the system during its evolution, it did not determine a mass ratio reversal also in the BH masses. This occurred because the first SMT was not able to completely strip the most massive progenitor, as the star goes supernova during the SMT itself. The progenitor has a He-core close to the ≈ 32 $\mathrm{M}_\odot$ limit to trigger PPI and the possibility that the full star collapses with all the ≈ 25 $\mathrm{M}_\odot$ masses of hydrogen envelope allows for the formation of one of the heaviest ≈ 57 $\mathrm{M}_\odot$ BHs possible (if we do not include the fates of progenitors at $M_{\mathrm{ZAMS}} \approx 90 - 100$ $\mathrm{M}_\odot$ allowed by dredge-ups at $Z \approx 0.0001$). In contrast, the strong non-conservative second SMT drove a nearly runaway orbital reduction, that completely stripped the stellar progenitor and left a bare helium core, that resulted in a BH of ≈ 30 $\mathrm{M}_\odot$.

[8]We recall that the amount of mass transferred by the donor is proportional to the ratio between the stellar radius and the Roche lobe radius $\dot{M}_{\mathrm{d}} \propto \ln(R_{\mathrm{d}}/R_{\mathrm{RL}}))^3$, see Equation 3.9

3.4.4 Stripped stars

Stripping and initial orbital configurations

In this work, we find that the existence of primary BHs in BBHs with mass above $\gtrsim 45\ \mathrm{M}_\odot$ is a consequence of BH primaries that were not completely stripped of their envelope and that were able to merge within a Hubble time if efficient orbital angular momentum extraction is at work ($\gamma \geq 1$). Figure 3.5 shows that, under these assumptions, primary BH progenitors could retain a sufficient H-envelope to pollute the $\gtrsim 45\ \mathrm{M}_\odot$ region of the primary BH mass spectrum if their progenitors have ZAMS masses of $M_{\mathrm{ZAMS}} \approx 60\ \mathrm{M}_\odot$ or $M_{\mathrm{ZAMS}} \approx 80 - 100\ \mathrm{M}_\odot$, have similar companions ($q_{\mathrm{ZAMS}} \approx 0.4 - 1$), are born in wide orbits($a_{\mathrm{ZAMS}} \approx 10^2 - 10^4\ \ R_\odot$) and symmetric binaries.

Stripping and angular momentum losses

If we extract a larger fraction of orbital angular momentum, we can reduce the orbital separation without the necessity to lose a large amount of mass. Therefore, it is possible to reach an orbital configuration that allows for the merger within a Hubble time without prolonged mass transfer events that completely strip the progenitor H-rich envelope. In the standard scenario of isotropic re-emission from the accretor, we expect that BBH progenitors have to lose all of their envelope and evolve as pure-Helium stars (e.g., Giacobbo & Mapelli 2018; Broekgaarden et al. 2022; Iorio et al. 2023). Only at the lowest metallicities, the quenched stellar winds and the more compact size of the star (Laplace et al. 2020; Costa et al. 2023) could allow the retention of a hydrogen envelope of $\lesssim 10 - 15\ \mathrm{M}_\odot$, as shown in Figure 3.7 and Figure 3.8. This metallicity effect was shown also in Korb et al. 2025 (Section 2.3.1), where at $Z = 0.000142$ up to $\lesssim 21\%$ of BBHs could avoid the evolution through the WR–BH stage, otherwise necessary. These "missed WR–BHs" experienced a late and less efficient mass transfer stripping, eventually incomplete at the time of the CCSN. Here we find that a similar effect holds in BBHs at low metallicities, but it would not produce BBHs with primary BHs above $\gtrsim 45\ \mathrm{M}_\odot$ without efficient angular momentum losses. If we enhance the extraction of orbital angular momentum - for instance assuming Lagrangian outflows or the formation of a circumbinary disk ($\gamma \geq 1$) - we find that up to $\lesssim 32\%$ of BBHs can avoid the WR–BH configuration at $Z = 0.000142$. In this scenario, BBHs progenitors can retain up to $\lesssim 60\%$ of their mass in their envelope. Since evolution through the pure-Helium stage is no more required now to form BBHs, the BH mass limit of $M_{\mathrm{BH,max,pure-He}} < 46\ \mathrm{M}_\odot$ is lifted and the collapse of the residual H-rich envelope can increase the final BH mass up to $\lesssim 60\ \mathrm{M}_\odot$, polluting the BBH mass gap. In the most optimistic case ($\gamma = 1.5$ at $Z = 0.000142$, with tides), we find that $\lesssim 1.4\%$ of the primary BH population falls in the BH mass range that cannot be populated by pure-Helium stars ($M_{\mathrm{BH,primary}} \geq 46\ \mathrm{M}_\odot$).

H-rich primary and secondary BH progenitors.

In Figure 3.7 and Figure 3.8 we show the impact of angular momentum losses in the evolution through the pure-Helium stage for the primary and secondary BH, respectively. Enhanced angular momentum losses ($\gamma \geq 1$) populate the region of the possible BH masses between the pure-Helium and the single stellar evolution predictions, with up to $\lesssim 60\%$ (e.g., in the case of $\gamma = 1.5$, tides active, and $Z = 0.000142$) of primary BH progenitors that can retain a H-envelope and BHs with up to $\lesssim 15\ \mathrm{M}_\odot$ more mass than the ones predicted

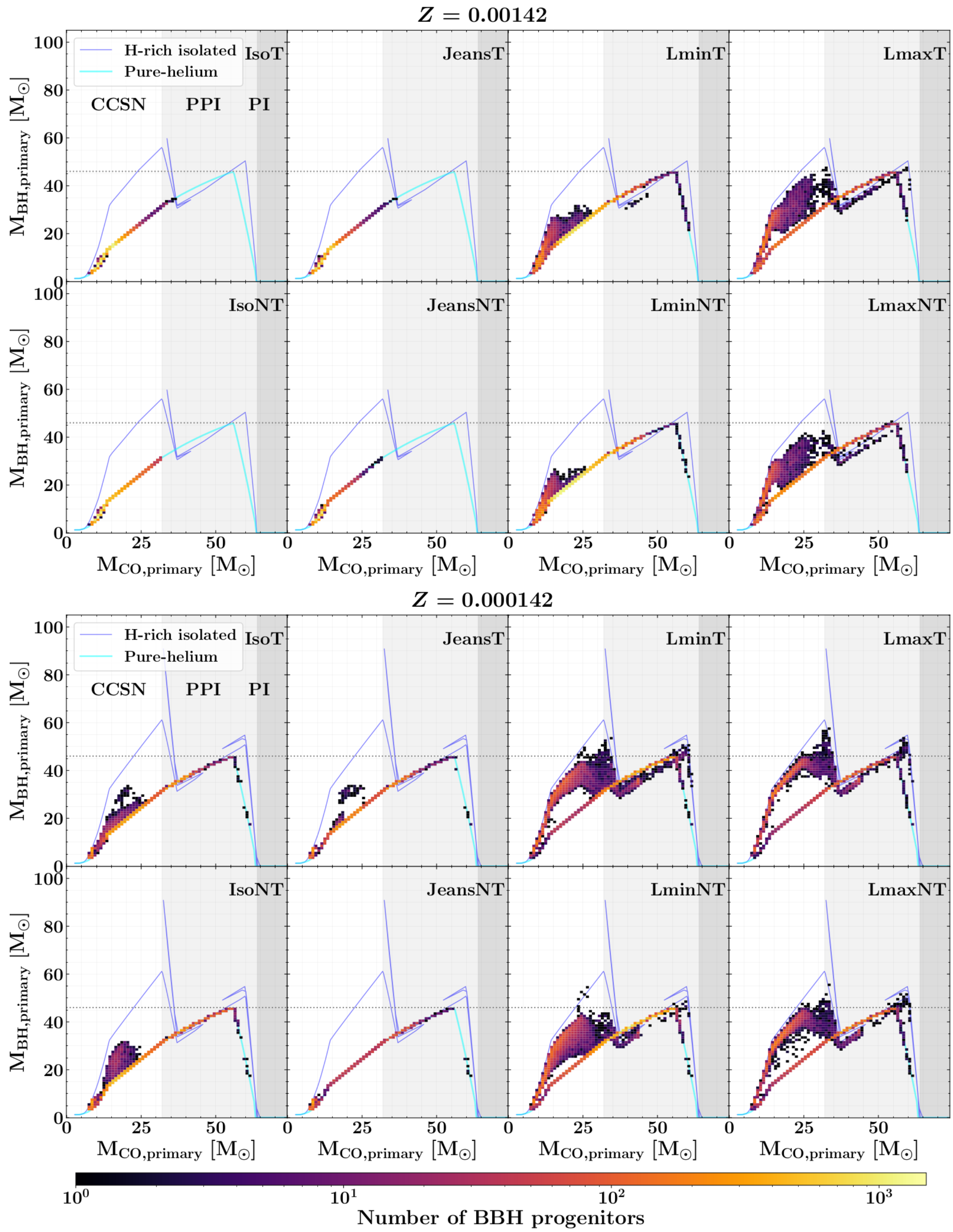

Figure 3.7: BH and helium core masses for BH primaries in our BBH populations for each simulated set (Section 3.3.2). We overplot the predictions from single stellar evolution alone, highlighting primary BHs that formed from pure-Helium stars or from stars that collapsed with a hydrogen-envelope. Vertical grey areas distinguish BHs that formed from core-collapse supernova (CCSN), pulsational pair-instability (PPI) or pair-instability (PI) supernova.

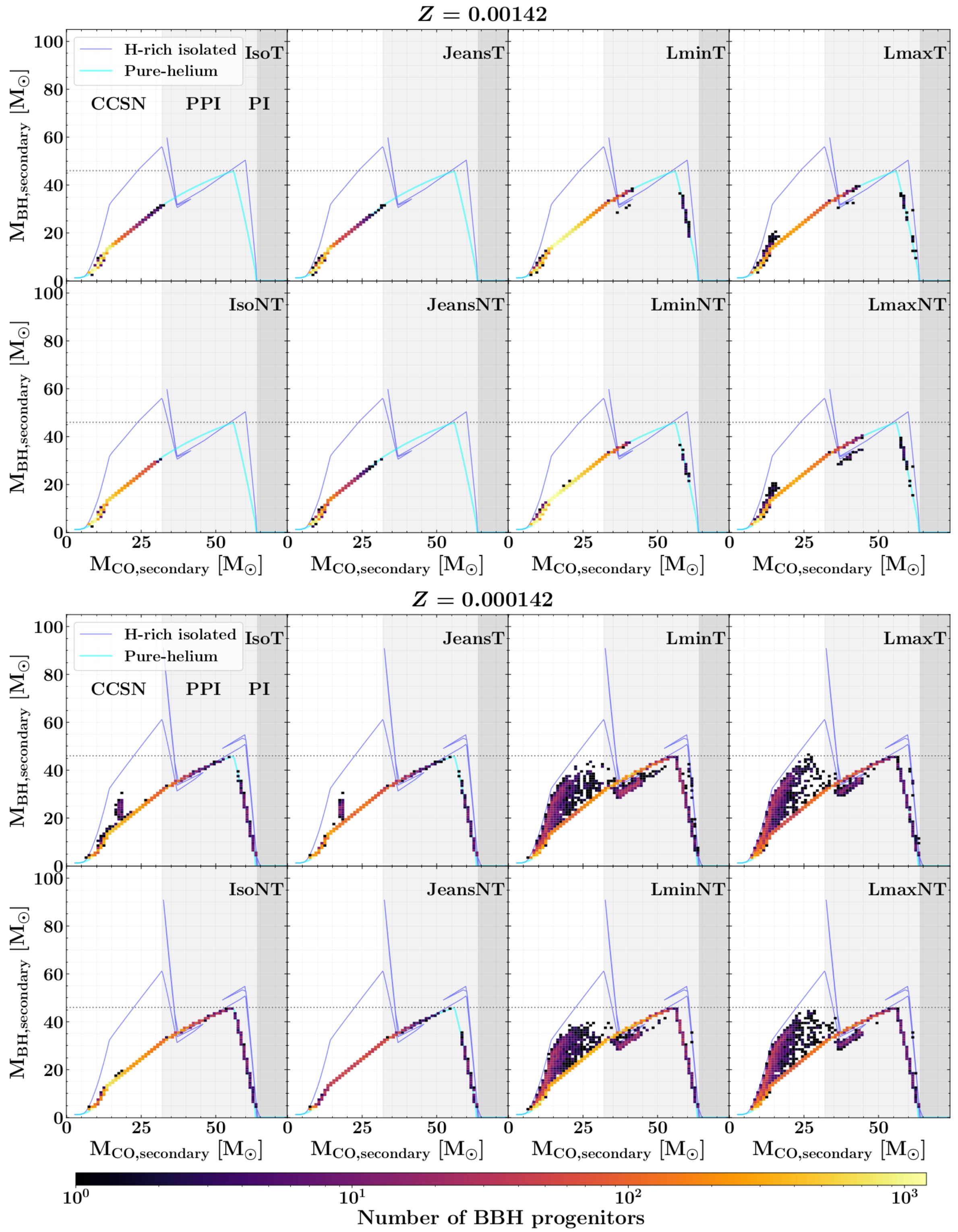

Figure 3.8: As Figure 3.7 but for BH and helium core masses of the secondary BHs. Nearly no secondary BH has a mass above the > 46 $M_\odot$ limit determined by pure-Helium stars (dotted line).

by evolution through the pure-Helium stage. In contrast, assuming isotropic mass loss from the donor (Jeans model) or the accretor (isotropic re-emission model) requires a stronger envelope stripping, generally producing pure-Helium star progenitors. With these models we expect that $\gtrsim 87\%$ of primary and $\gtrsim 99\%$ of secondary BH progenitors lose all of their H-envelope, except for a subpopulation of $\approx 15\%$ BBHs (at $Z = 0.000142$, with tides disabled) that experiences a mass ratio reversal: the mass accreted is not completely lost and the second born BH can have a progenitor that retains a H-envelope. We find that this is the most relevant case of mass ratio reversal in our simulated sets, as otherwise the primary BH is generally the first one to be formed and its progenitor star was the initially more massive one ($\approx 88 - 92\%$ of BBHs in each simulated set). This massive origin favours the retention of a larger H-envelope and the formation of a heavier BH.

Stripping determines a gap in secondary BH masses

Our results indicate that the existence of a $\gtrsim 45$ M$_\odot$ mass gap in the secondary BH mass distribution, possibly suggested by GWTC-4.0 data (see Antonini et al. 2025 and Tong et al. 2025, but also Ray & Kalogera 2025), would not be due to stellar physics nor PI alone, but it would be a natural consequence of the evolution from the least massive star (see the example reported in Figure 3.6). We find that the initially smaller He-core and H-envelope of the secondary do not grow as much as the primary ones, so even in the case of BH formation from stars retaining a H-envelope (e.g., from the ZAMS configuration or as a consequence of accretion from the primary), the final BH mass never exceeds < 46 M$_\odot$. This limit is not overcome also in the few ($\approx 10\%$) BBHs that experience a mass ratio reversal. For them, the progenitor of the secondary BH could also have been the most massive star of the ZAMS configuration, even falling in the the optimal mass range ($M_{\rm ZAMS} \approx 60$ M$_\odot$ or $M_{\rm ZAMS} \approx 80 - 100$ M$_\odot$) to produce a BH more massive than $\gtrsim 46$ M$_\odot$ by a near-single stellar evolution formation scenario. However, if these binaries have to experience a mass ratio reversal, this primary star has to transfer a sufficient amount of mass to the companion. This strong mass transfer will reduce the size of the residual H-envelope, preventing the formation of a BH as massive as the one predicted by single stellar evolution (Iorio et al. 2023; Costa et al. 2025). Therefore, in the mass ratio reversal scenario, the star initially more massive will end up producing the least massive BH in the pair, with a final mass below $\lesssim 46$ M$_\odot$.

Not all BH progenitors need to be stripped

In the standard isolated binary evolution formation scenario for BBHs, the two BH progenitors are expected to have lost all their external hydrogen envelope because of the combined action of stellar winds and mass transfer (e.g., Giacobbo & Mapelli 2018; Belczynski et al. 2020; Broekgaarden et al. 2022; Iorio et al. 2023). If BBH progenitors are pure-Helium stars, their maximum BH mass is expected to be $M_{\rm BH,max} \approx 45 - 50$ M$_\odot$ because of the onset of PPI and PI (e.g., Woosley 2017; Spera & Mapelli 2017; Farmer et al. 2019, 2020; Renzo et al. 2020b; Iorio et al. 2023). The presence of a residual H-envelope and uncertainties in the stellar physics (e.g., overshooting, dredge-ups, ^{12}C$(\alpha,\gamma)^{16}$O reaction rate) impact the size of the He-core and the final BH mass, shifting the lower boundary of the PI mass gap between $\approx 40 - 65$ M$_\odot$ or even closing the gap (e.g., Costa et al. 2021; Renzo & Smith 2024). Therefore, while the mass of single BHs may be limited at $\approx 40 - 65$ M$_\odot$ by the existence of a putative PI mass gap, it is expected that the mass of

BHs in BBHs does not overcome the $M_{\rm BH,max} \approx 45 - 50$ M$_\odot$ limit due to the evolution through pure-Helium stars.

In this work, we find that this picture could be incomplete, as the evolution through a double pure-Helium phase and the maximum BH mass for BBHs are strongly influenced by the models assumed for single stellar evolution and for angular momentum mass loss during SMT. We find that SMT may not completely strip the hydrogen-envelope of the donor star, although complete envelope-stripping still occurs in CE events. As reported in Figure 3.9, we find that the isotropic re-emission model for angular momentum mass loss, a standard assumption in many population-synthesis studies (e.g., Giacobbo & Mapelli 2018; van Son et al. 2020; Broekgaarden et al. 2022; Iorio et al. 2023) always forces the complete stripping of both BH progenitors (only at $Z = 0.000142$ less than $\lesssim 1\%$ of BBHs can avoid this evolution). Assuming the Jeans model leads to similar conclusions, but assuming an efficient angular momentum extraction ($\gamma \geq 1$) can lead to up to $\lesssim 30\%$ of BBHs to avoid double pure-Helium progenitors at $Z = 0.000142$ ($\lesssim 1\%$ at $Z = 0.00142$). The formation of circumbinary disk or an outflow from the outer Lagrangian point can shrink sufficiently (thus, allowing for a GW merger) also the orbit of systems where a supernova event prematurely terminated the SMT, determining an incomplete envelope stripping (e.g., as in the system described in Figure 3.6). We find that under these assumptions, commonly adopted in detailed binary evolution models (e.g., Marchant et al. 2021; Picco et al. 2024; Klencki et al. 2025), it is possible to form primary BHs in BBHs with mass $\gtrsim 45$ M$_\odot$.

Quantification of the pollution in the primary BH PI gap

At $Z = 0.00142$ we find nearly no BH ($\lesssim 1\%$) above 45 M$_\odot$ and $\lesssim 3\%$ ($\lesssim 5\%$) of our BBHs have a total mass larger than > 90 M$_\odot$ for the isotropic re-emission and Jeans models ($\gamma \geq 1$). However, at $Z = 0.000142$, we find that in our most optimistic (pessimistic) scenario - LmaxT (LmaxNT) setup - up to $\lesssim 3\%$ (no BH) of the BBH population have a primary BH with mass above $\gtrsim 45$ M$_\odot$ and up to $\lesssim 10\%$ ($\lesssim 8\%$) of BBHs have a total mass beyond > 90 M$_\odot$. Our results show that it is possible to pollute the $\gtrsim 45$ M$_\odot$ BBH region via the isolated binary evolution scenario if we consider progenitors at low metallicity and evolution through efficient angular momentum losses, for instance in the form of outflows from the outer Lagrangian point. These findings indicate that the hierarchical merger scenario could not be necessary to explain the whole primary BH population above $\gtrsim 45$ M$_\odot$, although it likely remains the dominant formation channel (e.g., Rodriguez et al. 2019; Antonini et al. 2025; Ray & Kalogera 2025; Tong et al. 2025).

We note that at $Z = 0.00142$, our results are similar to the ones obtained at $Z = 0.001$ by van Son et al. 2020, which found that the fraction BBHs with BH mass $\gtrsim 45$ M$_\odot$ was negligible ($\approx 2.4\%$) even assuming super-Eddington accretion. Briel et al. 2023 extended the investigation of the impact of super-Eddington accretion to also account for lower metallicities, down $Z = 10^{-5}$. They found that primary BHs above $\gtrsim 45$ M$_\odot$ were produced only at the lowest metallicities $Z \lesssim 0.006$ via a channel (SMT+SMT) that contributed only to $\approx 6\%$ of the local BBH merger rate. Briel et al. 2023 used detailed simulations and found that the tail of primary BH masses could extend up to $\lesssim 115$ M$_\odot$, a limit much higher than the one found in our simulations and in the ones by other population synthesis codes (e.g., Bavera et al. 2021; van Son et al. 2020, 2022b). Briel et al. 2023 argued that super-Eddington accretion determined a nearly-conservative mass transfer, so in their simulations the orbital reduction is a result of tides and mass transfer from very

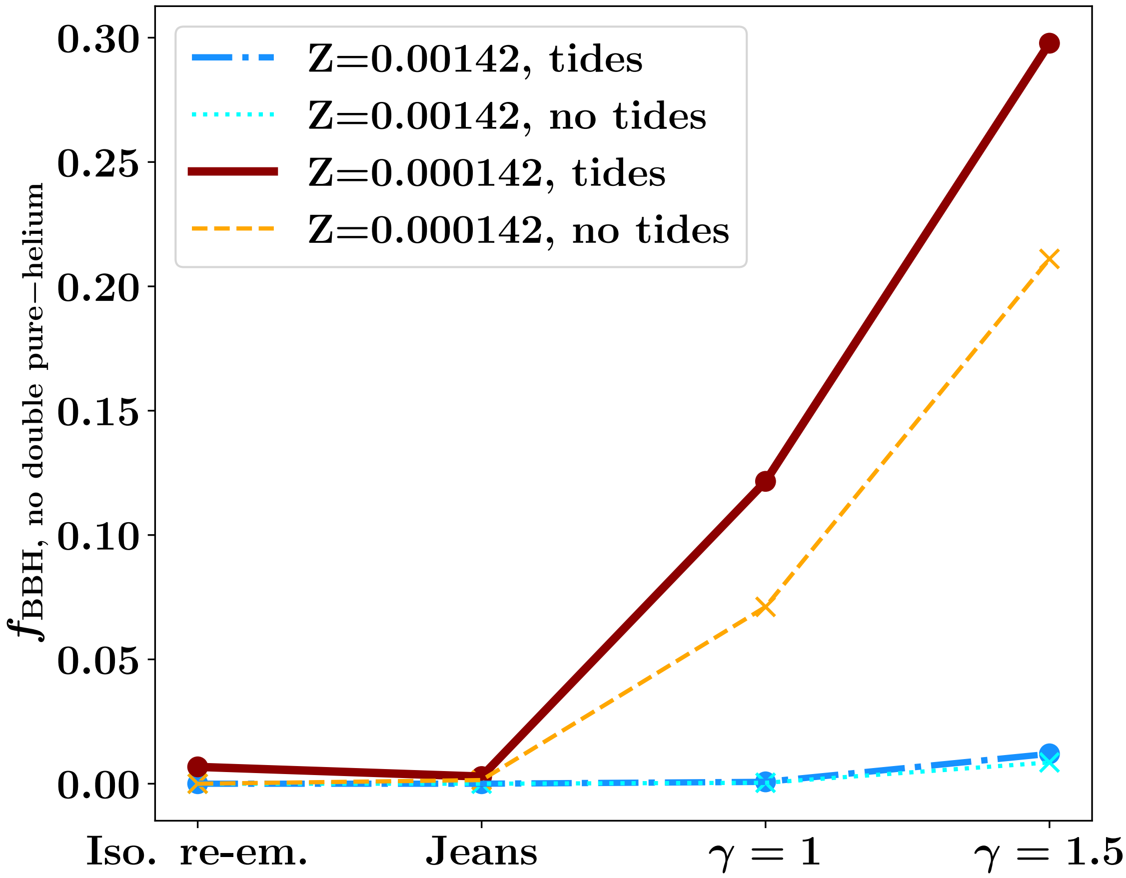

Figure 3.9: Fraction of BBHs where both progenitors were not completely stripped as pure-Helium stars, as a function of the angular momentum loss model, tidal model, and metallicity explored in this work (Section 3.3.2).

asymmetric binaries. We point out that, unlike Briel et al. 2023 and van Son et al. 2020, our systems significantly fill the $\approx 45 - 58\ \mathrm{M}_{\odot}$ region, especially at low metallicity, as a consequence of a highly non-conservative mass transfer.

3.4.5 Formation efficiency of BBHs

In Figure 3.10 we report the formation efficiencies η_{BBH} of BBHs in each simulated set,

$$\eta_{\mathrm{BBH}} = \frac{N_{\mathrm{BBH}}}{M_{\mathrm{pop}}} \tag{3.31}$$

calculated as the ratio between the number N_{BBH} of BBHs produced and the mass of the parent population M_{pop}. We correct for the incomplete mass sampling of the underlying

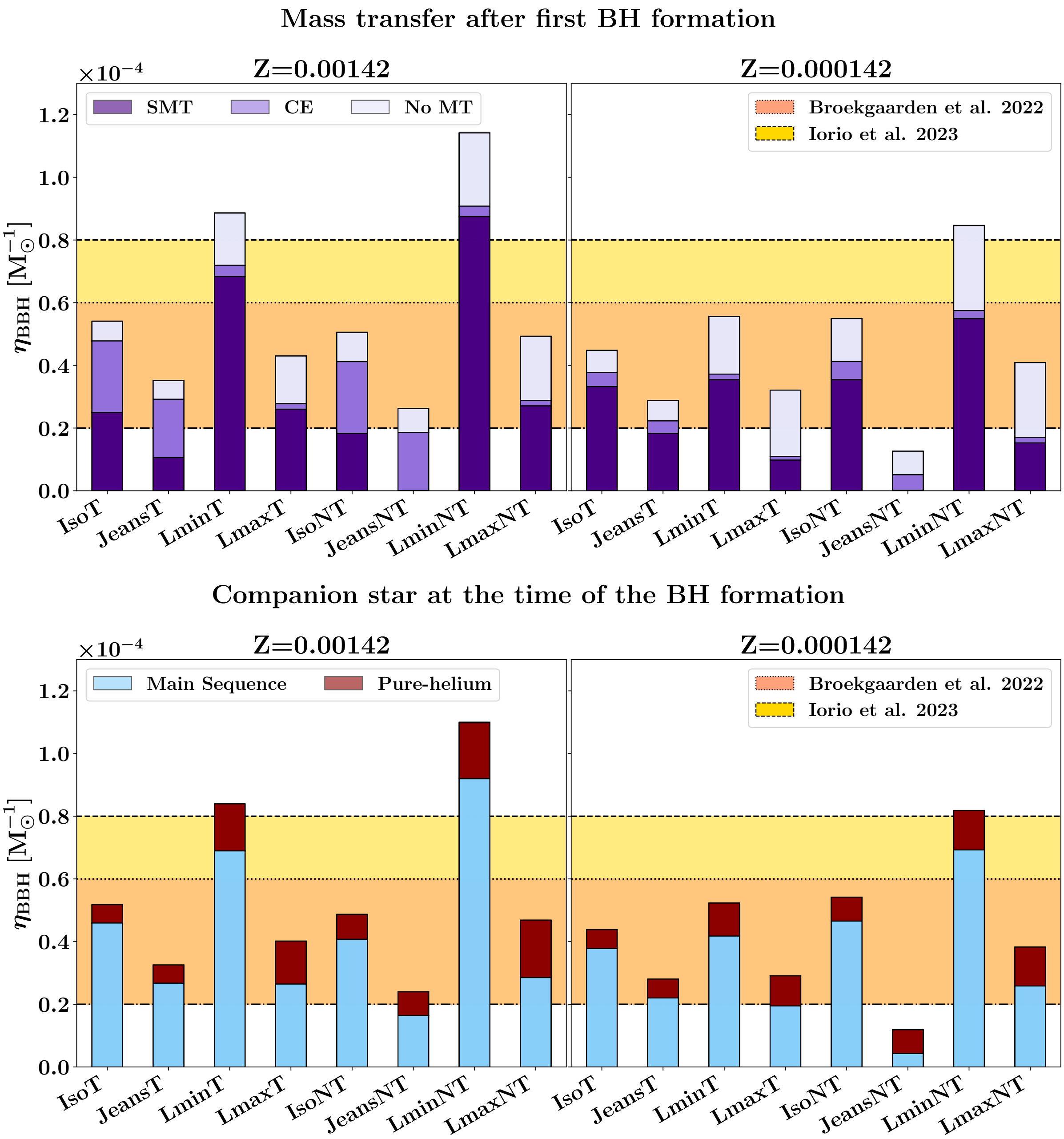

Figure 3.10: Formation efficiency of BBHs $\eta_{\rm BBH}$ for all the simulated set considered in this work (Section 3.3.2). Taking as reference time the moment of the first BH formation, we highlight with different colours the fraction of systems that will then experience a SMT, CE or no MT to produce a BBH (top panels) and the fraction of systems with a Main Sequence or pure-Helium companion (bottom panels). As a reference, we superimpose the range of formation efficiencies ($\approx 2-6\times10^{-5}$ $\mathrm{M}_\odot^{-1}$; orange patch within dotted lines) found in Broekgaarden et al. 2022 across a wide range of uncertainties, and the fiducial one ($\approx 2-8\times10^{-5}$ $\mathrm{M}_\odot^{-1}$; gold patch within dashed lines) of Iorio et al. 2023, obtained with `SEVN`. We highlight that the two ranges share a common lower limit at 2×10^{-5} with a dash-dot horizontal line. We rescaled the $\eta_{\rm BBH}$ efficiencies to consider a binary fraction equal to 1.

population[9] and assume a binary fraction of 1 for simplicity[10], so that the simulated population of 1×10^8 M$_\odot$ can be considered as representative of a parent population of $M_{\rm pop} = 3.5 \times 10^8$ M$_\odot$.

Figure 3.10 shows that the variations of angular momentum loss models, metallicity and tides explored in this work produce variations in the formation efficiency of the BBH population that are compatible with the range of uncertainties expected by the variation of other binary processes (e.g., core-collapse supernovae, WR wind efficiency, CE efficiency, mass transfer efficiency and stability), as found in Iorio et al. 2023, with `SEVN`, and in Broekgaarden et al. 2022, with another population-synthesis code (`COMPAS`, Compas et al. 2022). Both Iorio et al. 2023 and Broekgaarden et al. 2022 explored a broad range of uncertainties in binary evolution, with Broekgaarden et al. 2022 that accounted also for uncertainties in the star formation history, and found that their formation efficiencies were in agreement with the observed BBH merger rates from GWTC-3 (Abbott et al. 2023b). However, if we account for the revised lower merger rates of GWTC-4.0, we see that Broekgaarden et al. 2022 and Iorio et al. 2023 results were overestimating the merger rates of BBHs. Also for this reason, we conclude that, among the model variations explored in this work, only the overproduction of BBHs in the $\gamma = 1$ assumption is probably not realistic. This finding is in agreement with the interpretation of the $\gamma = 1$ model, that describes the extreme case of Lagrangian outflow or formation of an unstable circumbinary disk at the minimum possible distance, i.e. at the binary separation ($a_{\rm L\ out,min} = a_{\rm disk,min} = a_{\rm orb}$). Eventually, the parameter exploration conducted here confirms that, if Lagrangian outflows or circumbinary disks are at work, it is more realistic to consider Lagrangian outflows close to the maximum possible distance ($a_{\rm L\ out,max} \approx 1.22\ a_{\rm orb}$) or the formation of the circumbinary disk in a stable configuration ($a_{\rm disk} \approx 2.25\ a_{\rm orb}$), as explored in the $\gamma = 1.5$ model.

3.4.6 BBH evolution as MS-BH

At the time of the first BH formation, BBH progenitors have a companion star that is either a MS or a pure-Helium star. In most ($\approx 40-89\%$) BBH progenitors, the companion is a MS that will eventually start a mass transfer interaction($\approx 34 - 89\%$ of all BBH progenitors), as shown in Figure 3.10. If the companion is a pure-Helium, no further mass transfer events are required to produce a BBH, in agreement with Korb et al. 2025 (Section 2.3.2). The evolution through a WR–BH phase was already analysed and discussed in the previous Chapter, so hereafter we will present the final properties and the evolution of BBH systems connecting them to the intermediate MS–BH configuration.

Observed MS–BHs as possible BBH progenitors

In Figure 3.11 and Figure 3.12 we propose a qualitative comparison between our simulations and the observed periods and masses of Galactic (Cyg X-1 (Miller-Jones et al. 2021), SS 433 (Blundell et al. 2008; Hillwig & Gies 2008), HD 130298 (Mahy et al. 2022), and HD 96670 (Gomez & Grindlay 2021)) and extragalactic (M33 X-7 (Orosz et al. 2007;

[9]We limited the Kroupa 2001 IMF in the range $M_1 = [5, 150]$ M$_\odot$ and the mass ratio distribution of Sana et al. 2012 to $q = M_2/M_1 = [0.1, 1]$. Therefore, the correction factor for the IMF is $f_{\rm IMF} = 0.289$.

[10]In a more accurate rescaling, we should account for the fact that the fraction of binaries is a function of the primary mass Moe & Di Stefano 2017, so adopting the IMF of Kroupa 2001 would imply a binary fraction of 60 %.

Ramachandran et al. 2022), LMC X-1 (Orosz et al. 2009), and VFTS 243 (Shenar et al. 2022)) MS–BH systems where the MS is a O or B type star. Since many of the observed systems are Galactic, in Figure 3.13 we show a comparison with an additional set of simulations at $Z = 0.0142 \approx Z_{\odot}$.

The sample of MS-BH systems considered here includes interacting High Mass X-ray binaries (Cyg X-1, M33 X-7 and LMC X-1), with one probably surrounded by a circumbinary disk (SS 433), and detached binaries (VFTS 243, HD 130298 and HD 96670). Despite the variety of sources, we see that the MS–BH binaries observed so far have periods too short ($P_{\rm MS-BH} \lesssim 15$ days) to form a BBH under the explored assumptions.

If we assume a $\gamma \geq 1$ model for angular momentum loss, the fate of the observed sample of MS–BHs is most likely a premature coalescence. In the $\gamma < 1$ models, the $Z = 0.00142$ simulations that seem to predict a BBH fate in reality have a metallicity that is lower than the metal poor extragalactic binaries considered here ($Z \approx 0.006$, close to the one of the Large Magellanic Cloud (Ramachandran et al. 2022)): the widening action of stellar winds is suppressed and the systems appear to become BBHs, but in a more metallic environment they would widen and would not be able to merge via GW emission within a Hubble time (see Section 3.5.3).

Final orbital separations

In Figure 3.5, we showed that the minimum initial separation required to produce BBHs is $a_{\rm ZAMS,min} \gtrsim 50 \ R_{\odot}$ for nearly all the combinations of parameter tested in this work, but it can extend down to $a_{\rm ZAMS,min} \approx 20 \ R_{\odot}$ for the isotropic re-emission models. Isotropic re-emission and Jeans models favour BBH production from initial tight orbits $a_{\rm ZAMS} \lesssim 300 \ R_{\odot}$ with low mass primaries $M_{\rm ZAMS} \lesssim 50 \ \rm M_{\odot}$. Instead, Lagrangian outflows and circumbinary disk models favour wider initial orbits $a_{\rm ZAMS} \approx 10^2 - 5 \times 10^4 \ R_{\odot}$ with a wide range of possible progenitor masses, often extending up to $M_{\rm ZAMS} \lesssim 120 \ \rm M_{\odot}$. In Figure 3.11 and Figure 3.12 we show that the broader range of possible ZAMS configuration in the $\gamma \geq 1$ models broadens also the possible orbital configurations in the MS–BH phase for systems that will evolve into merging BBHs. Nevertheless, in Figure 3.14 we show that the distribution of the possible final BBH orbital separations $a_{\rm BBH}$ remains similar for the all the γ models tested in this work.

The main differences in the $a_{\rm BBH}$ distribution lays in the abundance of BBHs produced with the tightest possible orbit ($a_{\rm BBH} \approx 0.4 - 1 \ R_{\odot}$). This tight configuration has a strong and non-trivial dependence on the initial orbital configuration and on the orbital reduction, that should be strong enough to produce an orbit so tight but not too strong to determine a premature collision. If we consider only the effect of SMT evolution after the MS–BH configuration, we see that the systems that could end up with the tightest BBH orbits ($a_{\rm BBH} \approx 0.4 - 1 \ R_{\odot}$) or coalesce prematurely are the ones in the "triangular" region in the $q_{\rm MS-BH} - M_{\rm MS}$ plane (Figure 3.11), delimitated by $q_{\rm MS-BH} \lesssim 0.8$ and $M_{\rm MS} \approx 30 - 70 \ \rm M_{\odot}$ at $Z = 0.000142$; by $q_{\rm MS-BH} \lesssim 0.5$ and $M_{\rm MS} \approx 30 - 50 \ \rm M_{\odot}$ at $Z = 0.00142$. MS–BHs in this region could become BBHs if the angular momentum losses during the SMT are not too efficient, as in the case of isotropic re-emission or Jeans model. In our simulations also tides need to be active in order to produce BBHs from this region, as in our model tidal synchronization acts as an additional sink of orbital angular momentum (see Section 3.25 for a detailed discussion). In contrast, Figure 3.11 shows that Lagrangian outflows or the formation of a circumbinary disk are mechanisms that extract too much orbital angular momentum from these MS–BHs, leading to a premature coalescence. The effect of enhanced angular momentum losses ($\gamma \geq 1$) can be seen also in Figure 3.12, where MS–BH progenitors of BBHs can form only from wider periods than the ones required by the isotropic re-emission or Jeans evolution.

Delay times

We considered binary populations with a logarithmic distribution of the initial orbital periods (Sana et al. 2012) and a linear one of the masses and mass ratios (Kroupa 2001; Sana et al. 2012), therefore we had a logarithmic distribution also in the initial orbital separations $a_{\rm ZAMS}$. Here we assume that the time required to merge via GW emission is a function of the final orbital separation $t_{\rm GW} \propto a^4_{\rm BBH}$ following Peters 1964. If binary interactions are not significantly modifying the orbital configuration, the initial logarithmic distribution in orbital separations $a_{\rm ZAMS}$ is maintained also in the distribution final separations $a_{\rm BBH}$, so the number of BBHs merging via GW emission in a given bin of time should be inversely proportional to the time itself $dN/dt_{\rm GW} \propto t^{-1}_{\rm GW}$[11]. This trend would not change if we were to consider the whole delay time of a binary $t_{\rm del} = t_{\rm GW} + t_{\rm from\ ZAMS}$, i.e. the time from the ZAMS to the GW merger; a quantity that defines the formation redshift (Dominik et al. 2012b).

For BBH progenitors, stars require just few Myrs to evolve into BH and then it is possible that up to few Gyrs are required to merge via GW emission ($t_{\rm from\ ZAMS} << t_{\rm from\ GW}$), so we do not expect significant deviations from the t^{-1} trend. In Figure 3.15 we show that, indeed, the distribution of the delay times in our simulations follows the predicted $dN/dt_{\rm del} \propto t^{-1}_{\rm del}$. The only exception occurs for $t_{\rm del} \lesssim 100$ Myrs, when the time to merge becomes comparable to the one to evolve ($t_{\rm from\ ZAMS} \approx t_{\rm from\ GW}$) and the effect of binary interactions emerge, steepening the relation $dN/dt \propto t^{-1.5}$. The overabundance of BBHs with short delay times is due to an abundant sub-populations with tight orbits and light BH masses (e.g., after a CE event), with a mild presence also of with wider orbits with heavier BH masses (e.g., after a SMT event), in agreement with the standard outcomes of the isolated binary evolution scenario (Dominik et al. 2012b; van Son et al. 2022a).

At $Z = 0.000142$, assuming no-tides and isotropic re-emission, we find the strongest deviation from the $dN/dt_{\rm del} \propto t^{-1}_{\rm del}$ scenario. In particular, we find a strong bimodal distribution of the delay times, that resembles the one found in the final orbital separations (Figure 3.14) and is connected to a bimodal period distribution in the MS–BH configuration (Figure 3.12). We highlight that both the isotropic re-emission and the Jeans model, for both the metallicities considered here, show two distinct "islands" of possible MS–BH periods, if tides are active. The bimodality is determined by the existence of a fixed $q_{\rm crit}$ threshold for mass transfer stability, that forces a sharp separation in the orbital progenitors between the SMT or CE evolution after the MS–BH formation. In this context, the evolution with active tidal synchronization spreads the possible final orbital separations, diluting the bimodal distribution. If tides are disabled, BBHs are less likely to have progenitors in wide orbits ($P_{\rm MS-BH} \gtrsim 10$ days), so the contribution from the CE channel to the tightest orbits $a_{\rm BBH} \lesssim 10\ \ R_\odot$) is reduced.

[11]From the logarithmic initial distribution of Sana et al. 2012 we get $dN/da \propto 1/a$, while from Peters 1964 we get $a \propto t^{-4}$ and $da/dt \propto a^{-3}$. Adopting the chain rule, we obtain $dN/dt = dN/da\ da/dt \propto t^{-1}$.

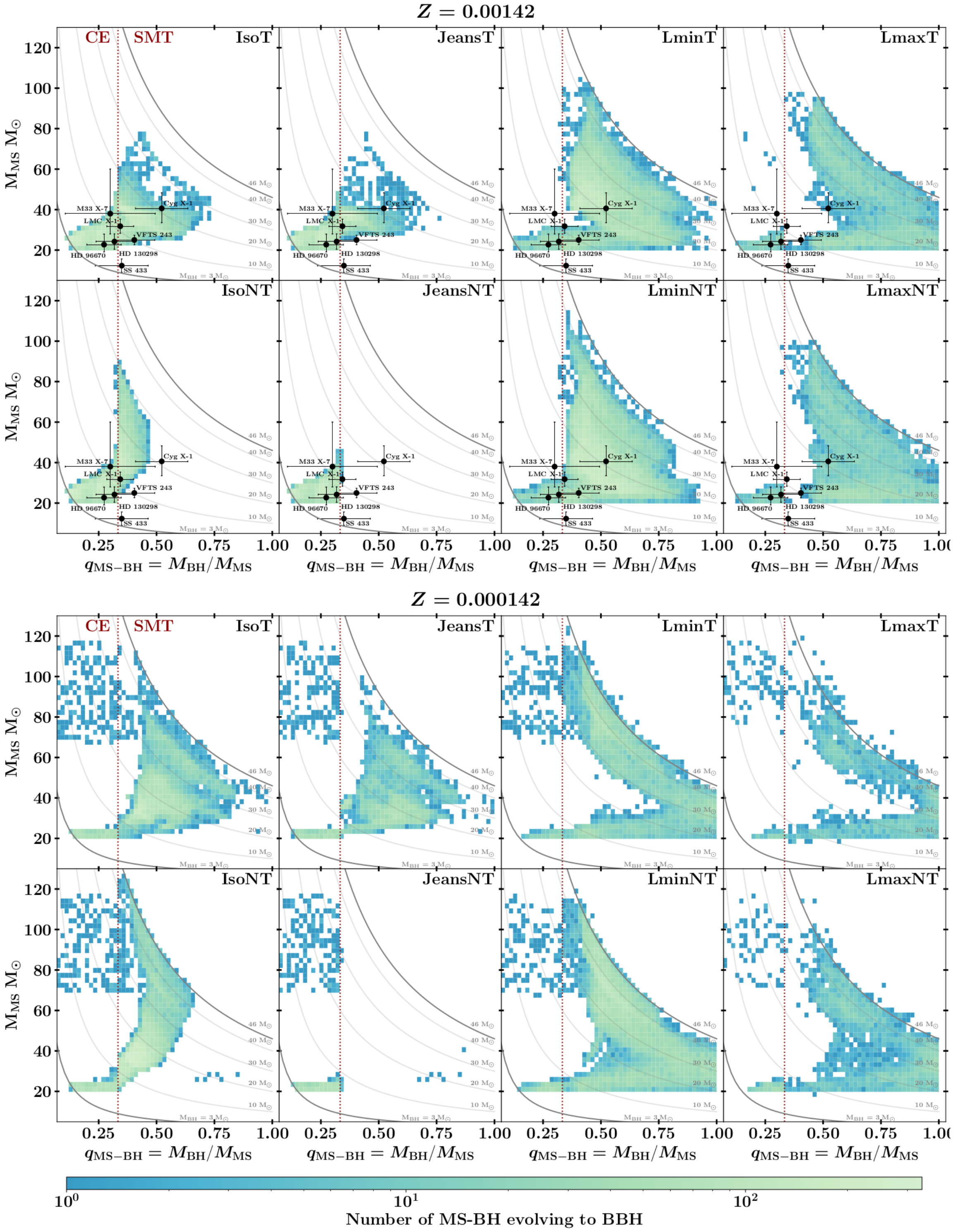

Figure 3.11: Main Sequence mass $M_{\rm MS}$ and mass ratio $q_{\rm MS-BH} = M_{\rm MS}/M_{\rm BH}$ for all the BBH progenitors that experience a MS-BH configuration. The snapshot considers the properties at the time of the BH formation, so the $q_{\rm crit} = 0.3$ threshold (Belczynski et al. 2008) to distinguish CE from SMT is indicative. For a qualitative comparison, we plot also the properties of a sample of observed MS-BH systems (see Section 3.4.6 for their references).

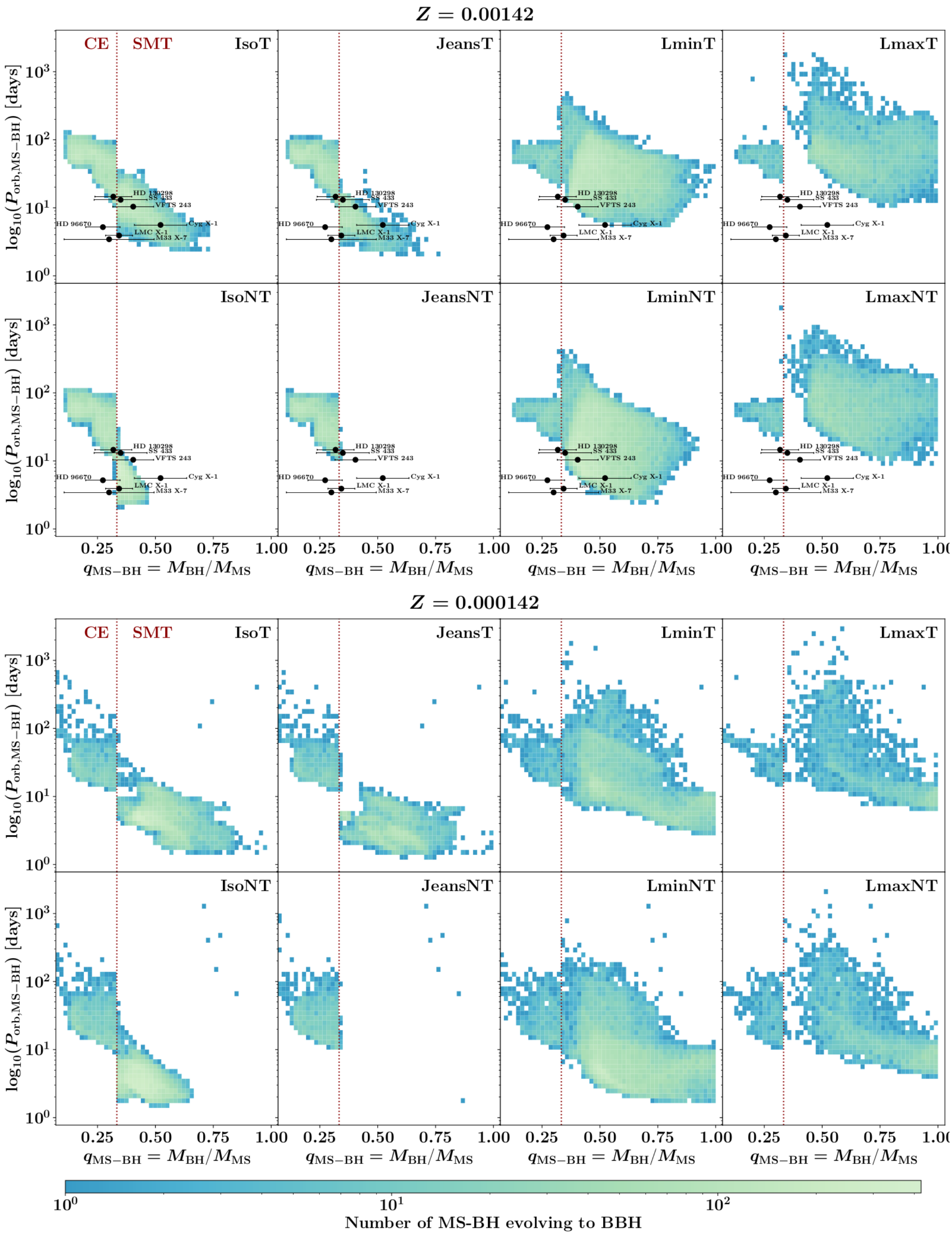

Figure 3.12: As in Figure 3.11, but here we show the orbital period $_{\rm MS-BH}$ as a function of the mass ratio $q_{\rm MS-BH} = M_{\rm MS}/M_{\rm BH}$ at the time of the BH formation.

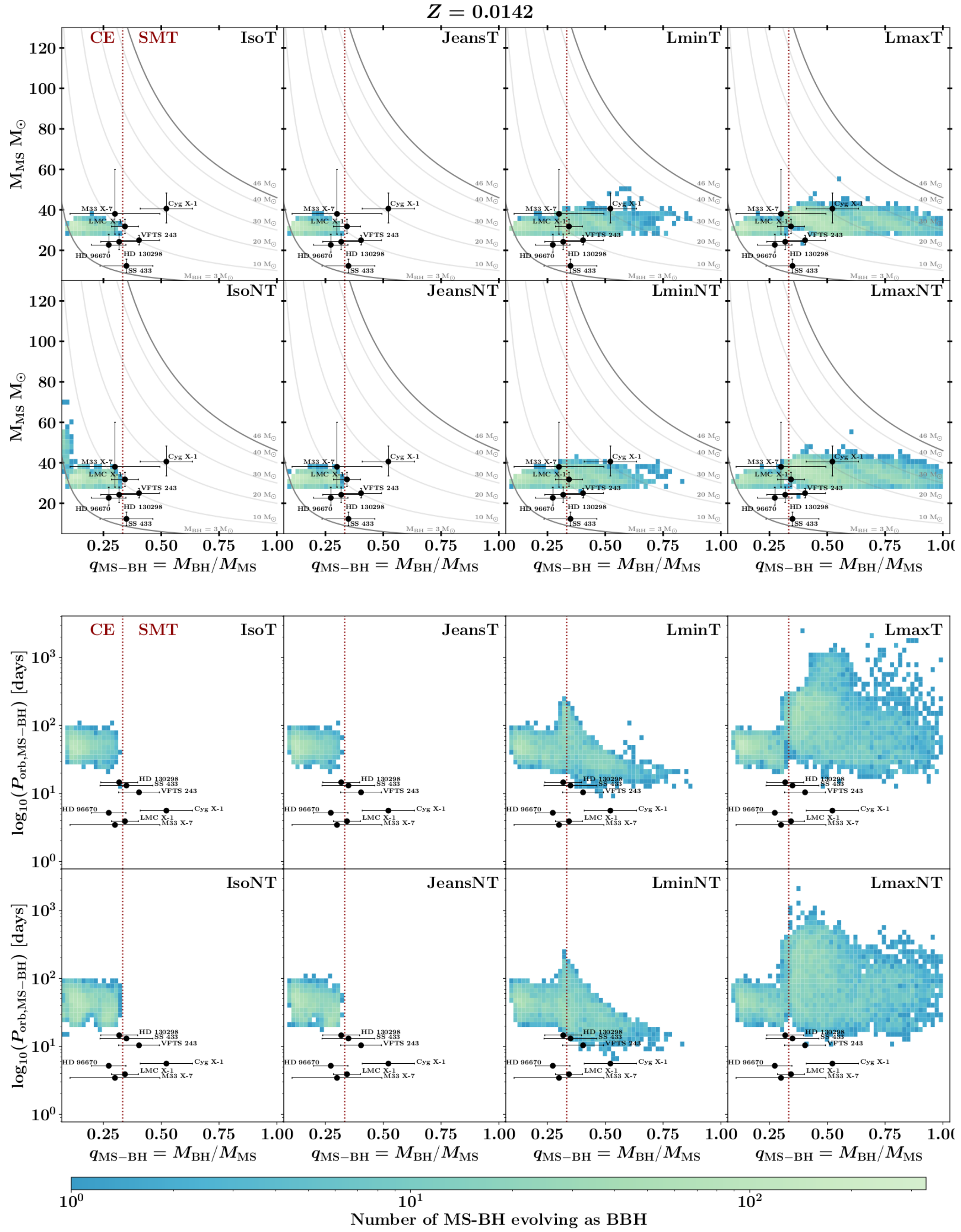

Figure 3.13: As in Figure 3.11 and Figure 3.12, but here we show the orbital period $_{\text{MS-BH}}$ and MS mass M_{MS} as a function of the mass ratio $q_{\text{MS-BH}} = M_{\text{MS}}/M_{\text{BH}}$ at the time of the BH formation for BBHs with MS–BH progenitors evolved at solar metallicity $Z = 0.0142$, to facilitate the comparison with the observed MS-BH systems in the Galaxy (Section 3.4.6).

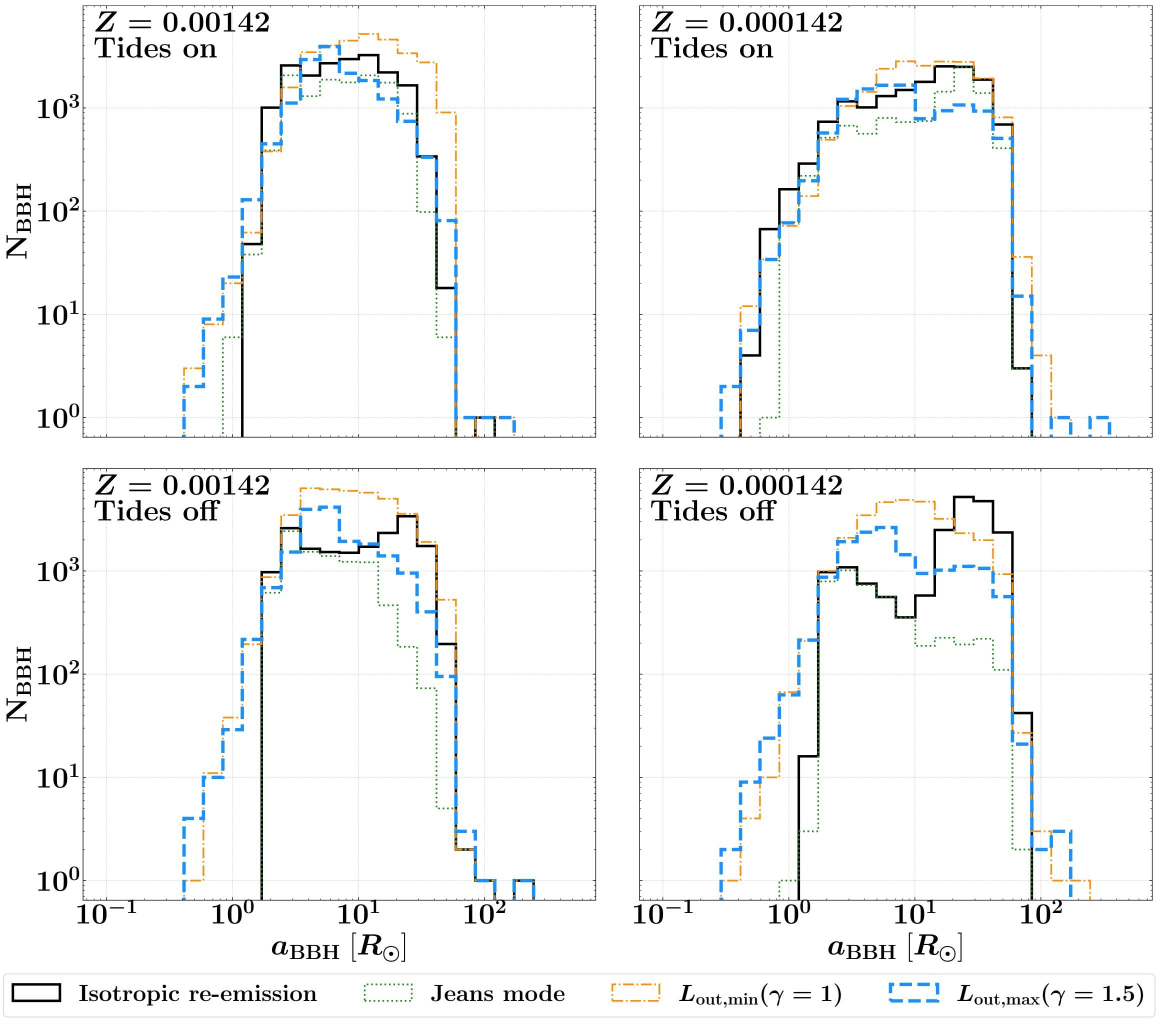

Figure 3.14: Distribution of the final semimajor axis $a_{\rm BBH}$ for all the BBHs produced in each simulated set (Section 3.3.2.

Mass ratio distribution

In Figure 3.16 we see that all the combinations of metallicity, tides and angular momentum losses favour the formation of BBHs with BHs of similar mass ($q_{\rm BBH} \approx 1$), as expected in the isolated binary evolution scenario (Giacobbo et al. 2018; Broekgaarden et al. 2022). We find that efficient angular momentum extraction ($\gamma \geq 1$) allows the creation of more BBHs with unequal masses ($q_{\rm BBH} \lesssim 0.4$). These asymmetric BBHs have light secondary BHs $M_{\rm BH,secondary}$ that evolved from light progenitors $M_{\rm ZAMS,secondary} \approx 20-30$ M$_{\odot}$. Their primary companions where either similarly massive ($M_{\rm ZAMS,primaries} \lesssim 50$ M$_{\odot}$) and born in tight orbits ($a_{\rm ZAMS} \approx 7\times10^2 - 2\times10^3$ $R_{\odot}$ at $Z = 0.000142$; $a_{\rm ZAMS} \approx 10^2 - 10^3$ $R_{\odot}$ at $Z = 0.00142$) or where very massive ($M_{\rm ZAMS,primaries} \approx 50 - 120$ M$_{\odot}$) and born in wide orbits ($a_{\rm ZAMS} \approx 2\times10^2 - 5\times10^4$ $R_{\odot}$ at $Z = 0.000142$; $a_{\rm ZAMS} \approx 10^3 - 5\times10^4$ $R_{\odot}$ at $Z = 0.00142$). In such massive systems, the primary star is able to retain enough mass to form a BH that has a mass similar to ($q_{\rm MS-BH} = M_{\rm BH}/M_{\rm MS} \approx 0.5-1$) or larger than ($q_{\rm MS-BH} \approx 1-2$) the MS companion. These systems can then become BBH mergers only under the assumption of efficient angular momentum extraction ($\gamma \geq 1$), otherwise they would remain too wide to merge via GW emission within a Hubble time.

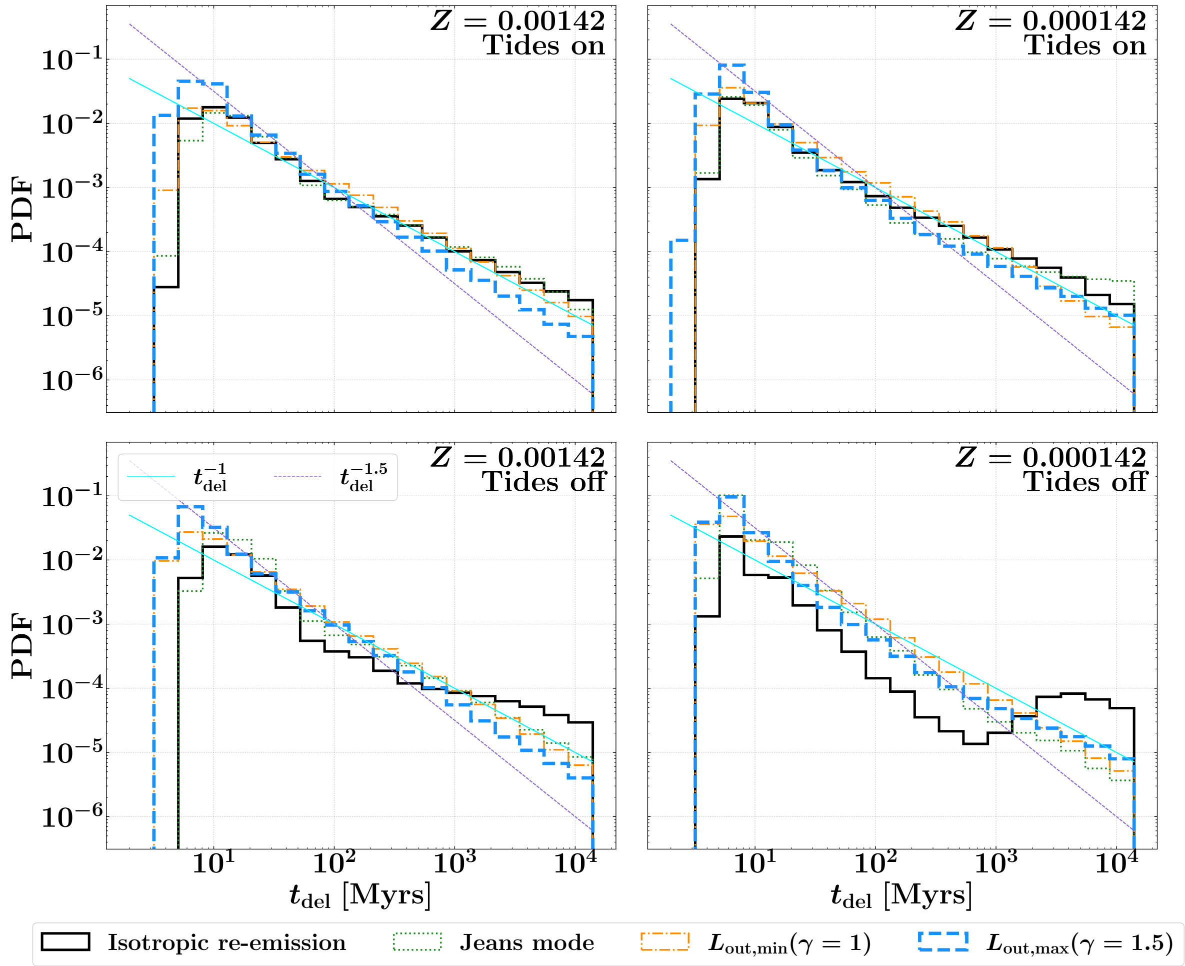

Figure 3.15: Probability density function of the delay times $t_{\rm del}$ for all the BBHs produced in each simulated set (Section 3.3.2. Diagonal lines indicate the expected t^{-1} trend and the steeper one $t^{-1.5}$ driven by binary interactions.

The $\gamma \geq 1$ models determine the formation of a bulk of BBH progenitors with a MS–BH configuration that has a MS star of $M_{\rm MS} \approx 20 - 30$ M$_\odot$ and large mass ratios $q_{\rm MS-BH} \gtrsim 0.5$, as shown in Figure 3.11 and Figure 3.12. The isotropic re-emission and Jeans models could not form a merging BBH from these systems. In particular, the $\gamma < 1$ models predict that the lightest possible BH progenitors, while still in the MS phase with $M_{\rm MS} \approx 20 - 30$ M$_\odot$, could form BBH only if it is part of asymmetric MS–BH binaries $q_{\rm MS-BH} \lesssim 0.5$, generally requiring a CE evolution to obtain a BBH orbit that is tight enough to allow the GW merger within 14 Gyrs.

3.4.7 MS-BH vs ZAMS-BH configurations

In Figure 3.6 we showed that SMT events after the first BH formation could reduce the orbital separation by more than one order of magnitude, with a larger impact on the final fate of the binary with respect to SMT events occurring prior to the BH formation. Moreover, in Figure 3.10 we showed that most BH companions are MS stars, at the time of the first BH formation. Also for these reasons, in the literature, detailed binary

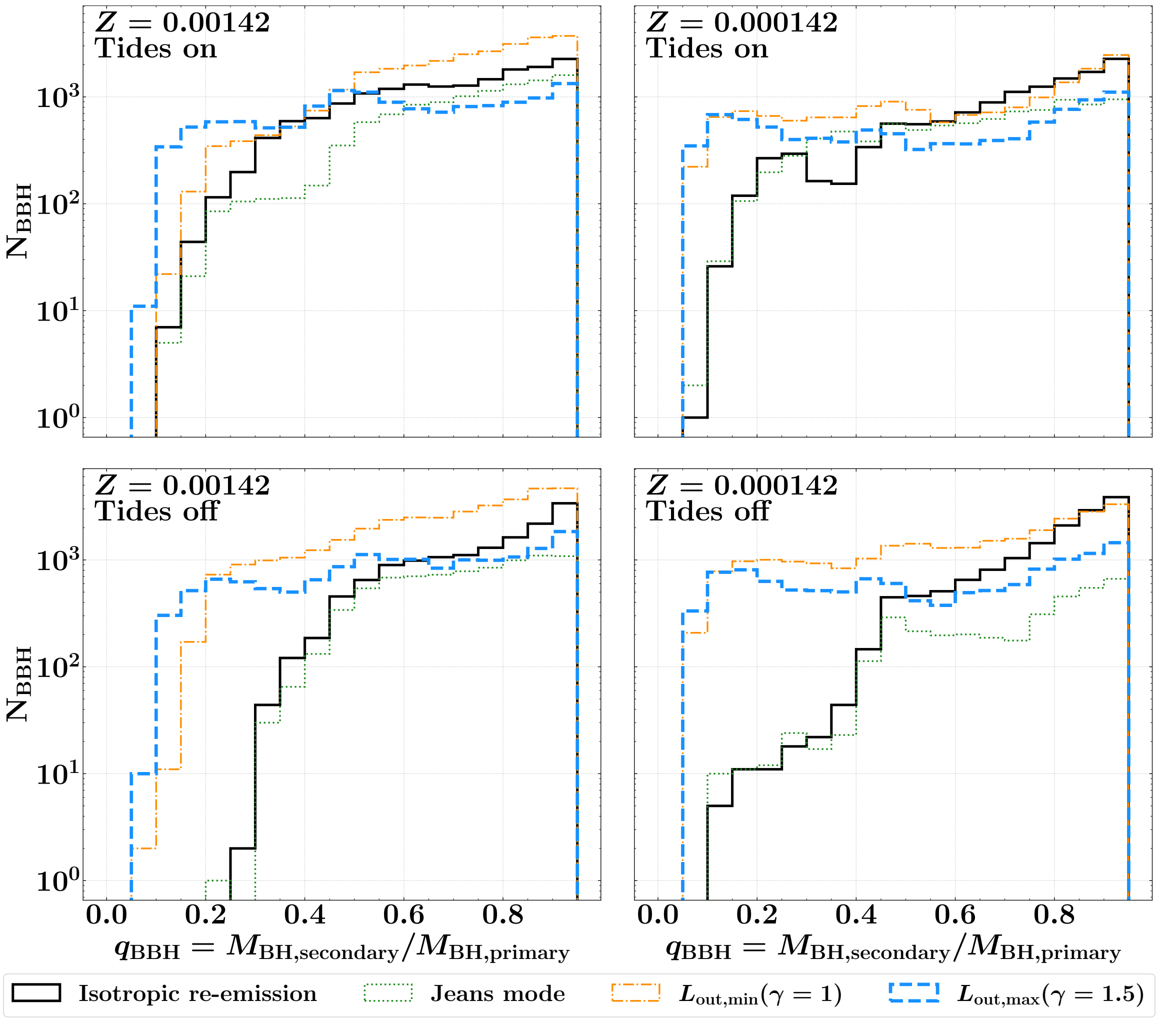

Figure 3.16: Distribution of the final mass ratios $q_{\rm BBH} = M_{\rm BH,secondary}/M_{\rm BH,primary}$ for all the BBHs produced in each simulated set (Section 3.3.2.

simulations investigate the impact of stellar and binary physics on BBH formation by analysing the evolution of MS–BH binaries through the mass transfer event that links the MS–BH configuration to the possible BBH fate (e.g., Marchant et al. 2021; Gallegos-Garcia et al. 2021; Picco et al. 2024; Klencki et al. 2025). Because of the large computational time, these studies generally select a grid of systems by fixing the BH or MS mass, often initializing the evolution from a grid of ZAMS-BH systems. In the following sections we adopt a similar approach, to compare our population-synthesis approach with the detailed one, inspired by the work of Gallegos-Garcia et al. 2021.

Evolution after the MS-BH configuration.

The formation of MS–BH binaries, regardless of their fates, is not very sensitive to metallicity, tides or angular momentum losses: the formation efficiency of MS-BHs is in the range $\eta_{\rm MS-BH} \approx 1 - 1.5 \times 10^{-3}$ $\rm M_\odot^{-1}$ for every combination of assumptions considered in this work, as shown in Figure 3.17. The stationary formation efficiency of MS–BH is partially due to the fact that many ($\approx 40 - 50\%$) MS–BHs can form in wide binaries, where no mass transfer interaction is required. Furthermore, stable or unstable mass

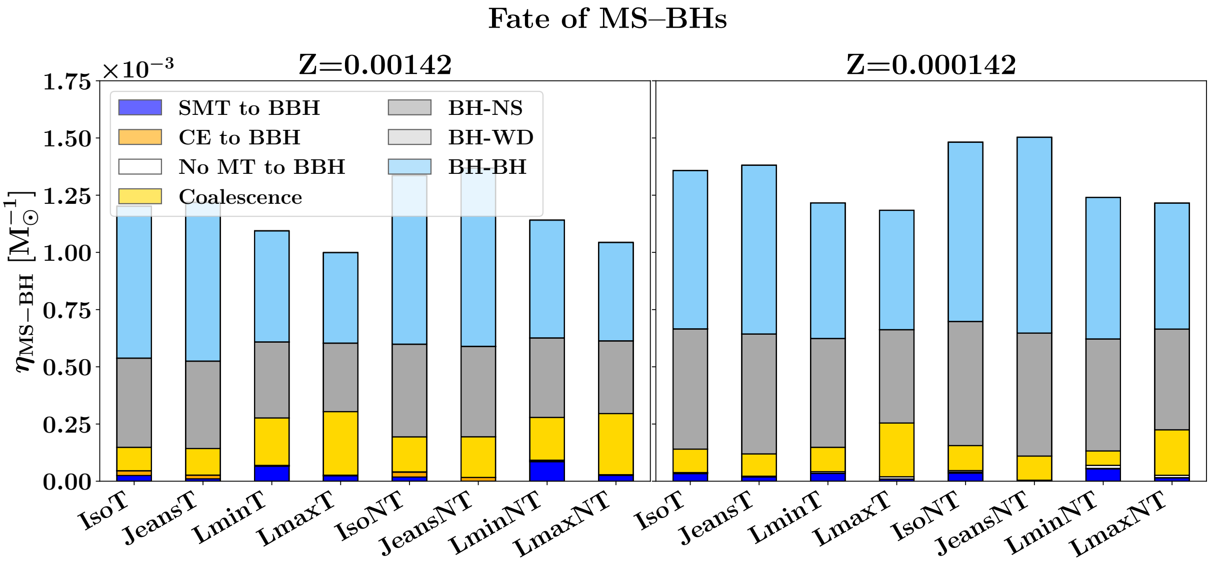

Figure 3.17: Formation efficiency $\eta_{\rm MS-BH}$ of all the MS-BH binaries formed in each set simulated in this work (Section 3.3.2). We highlight with different colors the possible evolution after the MS-BH stage: formation of BBH after a SMT (blue), CE (dark orange), no MT (white); formation of bound BH-BH (light blue), BH-NS (dark grey) or BH-WD (light grey) binaries; premature coalescence (yellow).

transfer prior to the first BH formation often leave a surviving binary, indicating that indeed mass transfer events after the first BH formation are crucial to the BBH production. In Figure 3.17 we show that most MS–BHs form two compact objects in wide or broken binaries ($\approx 40-50\%$ as BH-BHs, $\approx 30-40\%$ as BH-NSs): only few MS–BHs are able to produce BBHs ($\lesssim 7\%$, in the most optimistic - but irrealistic - case of $\gamma = 1$). We find that efficient angular momentum extraction ($\gamma \geq 1$) does not increase the production efficiency of BBHs (Figure 3.10) as much as it increases the premature coalescences, since Lagrangian outflows or the formation of circumbinary disk nearly double the coalescences with respect to the isotropic re-emission or Jeans models ($\approx 16-25\%$ with respect to $\approx 8-12\%$ of all the MS–BH possible fates, respectively).

MS-BH sub-populations with fixed MS mass.

We investigate the impact of angular momentum losses in the MS–BH fates and in BBH production by considering a sub-population of MS–BH binaries with MS star of about $M_{\rm MS} \approx 40$ M$_\odot$. Following the approach of Gallegos-Garcia et al. 2021, we select all the MS–BH systems formed with MS star in the $M_{\rm MS} = 40 \pm 2.5$ M$_\odot$ mass bin. In Figure 3.18 we show the full sub-population and in Figure 3.19 only the systems that will become BBHs. We stress that Figure 3.19 corresponds to an horizontal slice (at $M_{\rm MS} \approx 40$ M$_\odot$) of the orbital configurations showed in Figure 3.11, showing the corresponding subset of the period distributions reported in 3.12.

Comparing Figure 3.18 and 3.19 we find that, within this sub-population, BBHs are generally produced from the most common MS–BH orbital configurations, with few exceptions. For instance, in MS–BH binaries with very short orbital periods ($P \approx 2-5$ days) produced under the assumption of efficient angular momentum losses and $Z = 0.00142$, the mass transfer initiated by the MS will extract too much orbital angular momentum

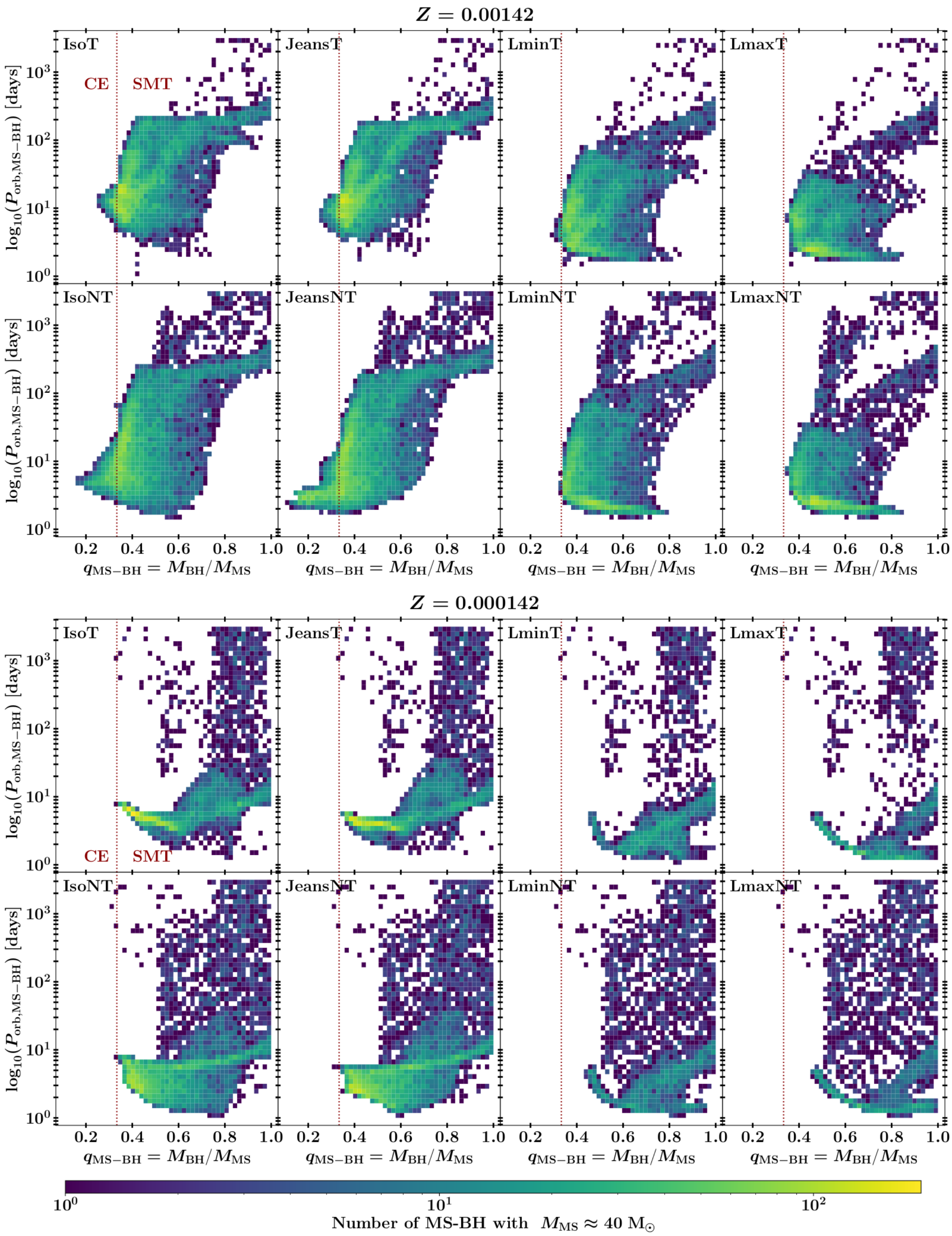

Figure 3.18: MS-BH configuration (orbital period as a function of mass ratio) for binaries with MS mass of $M_{\rm MS} = 40 \pm 2.5$ M$_\odot$, regardless of their fate. We show the two-dimensional distributions for each simulated set of this work (Section 3.3.2).

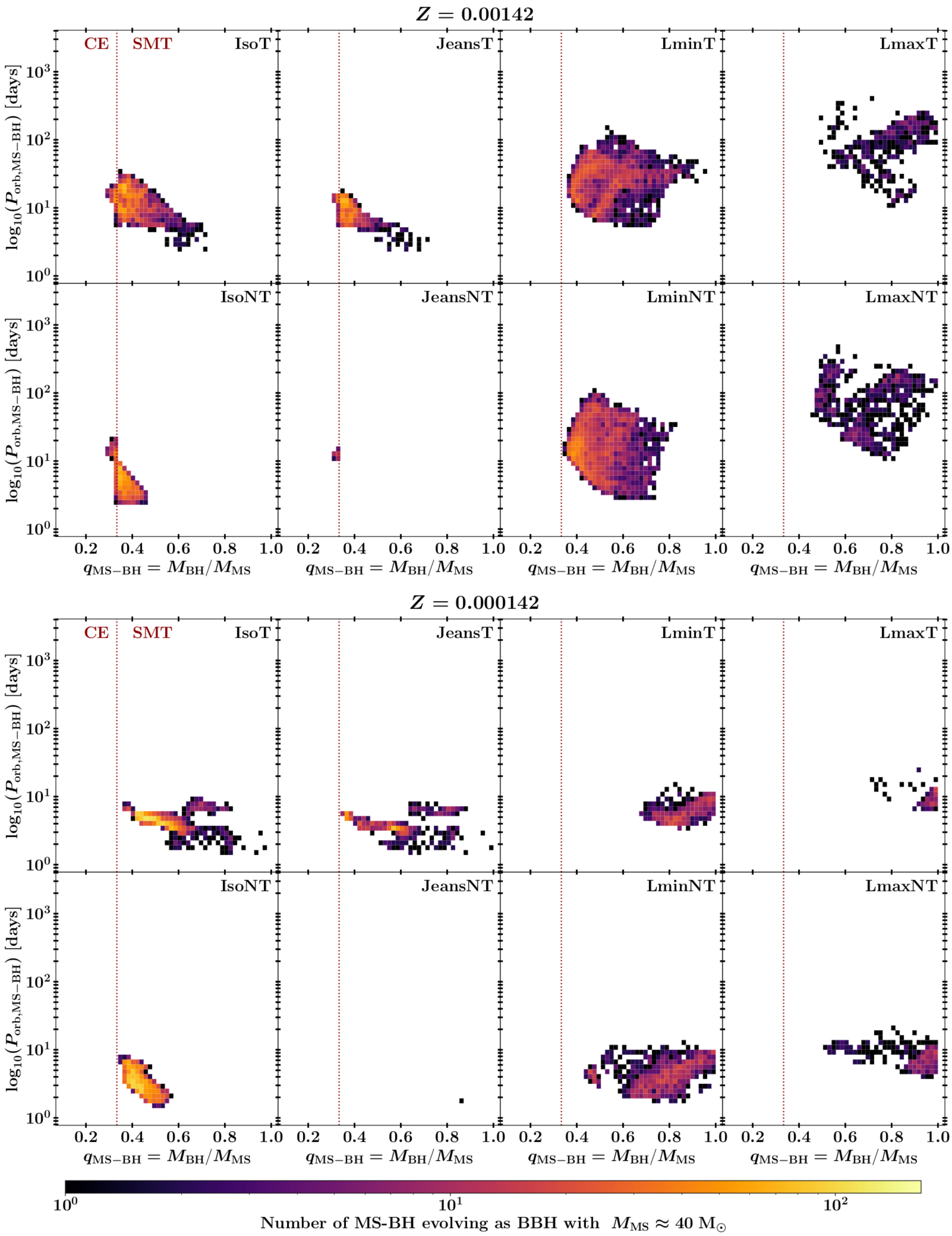

Figure 3.19: As Figure 3.18, but we restrict only to the systems that become BBHs after having a MS-BH with a $M_{\rm MS} \approx 40$ M$_\odot$ star.

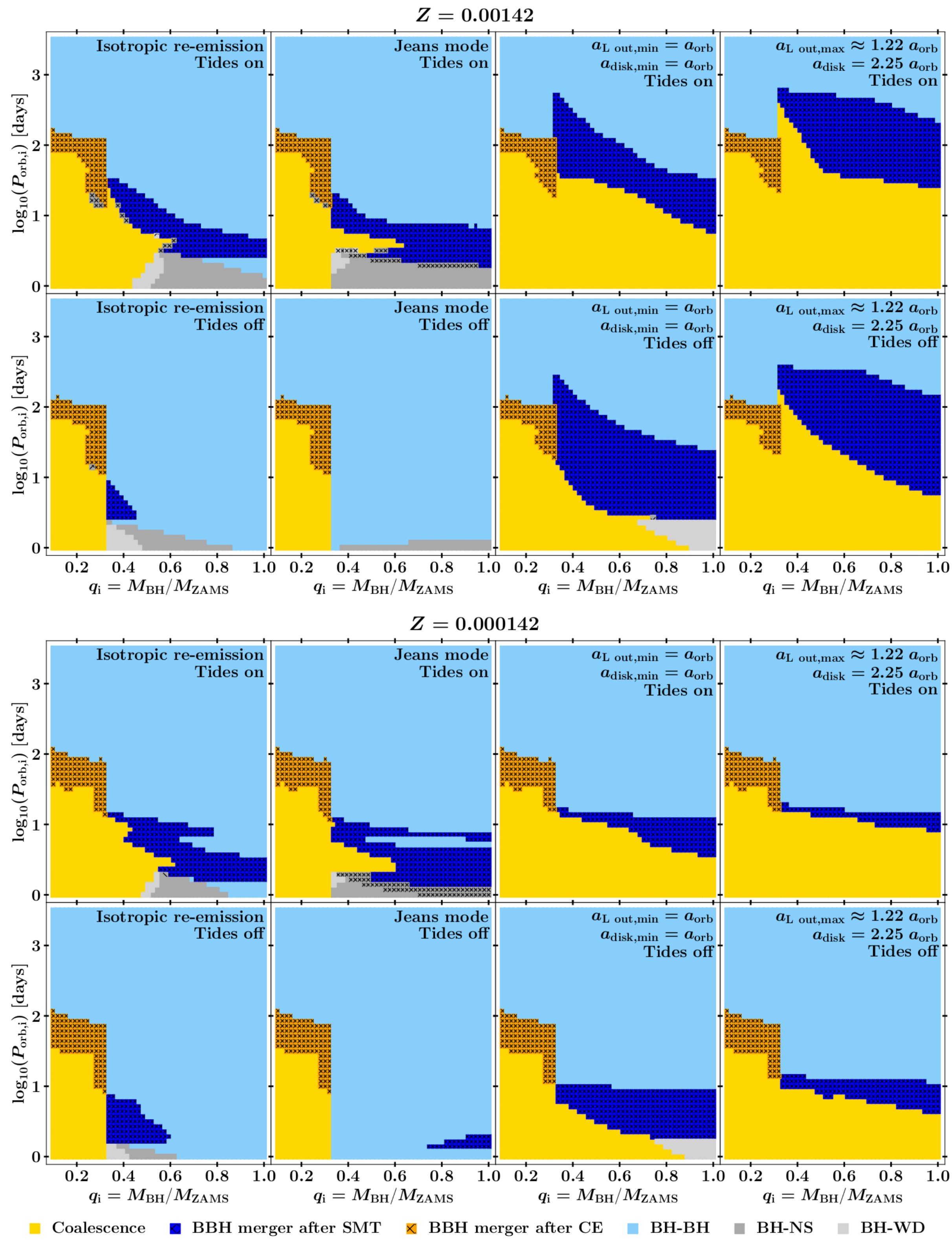

Figure 3.20: ZAMS-BH configurations (orbital period as a function of the mass ratio) for systems with a $M_{\text{ZAMS}} = 40\ \text{M}_{\odot}$ star that is evolved with SEVN under the fiducial assumptions considered in this work (Section 3.3.2), that are similar to the fiducial ones of Gallegos-Garcia et al. 2021.

and the systems will prematurely coalesce rather than form BBHs. Furthermore, assuming the Jeans model and no tidal synchronization the extraction of orbital angular momentum is quenched so much that nearly none of the MS–BH binaries of Figure 3.18 will become a BBH merger (only few will have this fate if tides are active, see Figure 3.19.

ZAMS-BH grids as proxy of MS - BH grids?

Many works in the literature investigated the impact of mass transfer on detailed or population-synthesis simulations (e.g., Marchant et al. 2021; Gallegos-Garcia et al. 2021; Picco et al. 2024; Klencki et al. 2025) starting from grids of ZAMS-BH systems. In order to compare our results with the literature, with `SEVN` we also generated a grid of ZAMS-BH systems (keeping the ZAMS star at $M_{\rm ZAMS} = 40\ \mathrm{M}_{\odot}$) to cover the same orbital configurations reproduced the MS–BH grids of Figure 3.18 and Figure 3.19.

We find that, in a first approximation, the ZAMS-BH grids in Figure 3.20 can reproduce qualitatively the region of MS-BH orbital configurations that will form BBHs via stable or unstable mass transfer. However, we note that considering ZAMS-BH systems broadens significantly the parameter space of MS–BH configurations that could lead to the BBH formation. On the one hand, ZAMS-BH systems allow more wider and symmetric ZAMS–BHs to produce BBHs via SMT channel. On the other hand, we find that the ZAMS-BH configuration predicts a CE formation channel that it is, instead, nearly completely suppressed in the full MS-BH population produced from the ZAMS-ZAMS stage, as shown also by the formation efficiencies in Figure 3.10. Except for few systems in the isotropic re-emission or Jeans model, nearly none of our MS–BHs with MS mass of $M_{\rm MS} = 40 \pm 2.5\ \mathrm{M}_{\odot}$ will form a BBH through the CE channel (Figure 3.19) because none of our binaries will produce a MS-BH in that region of the MS–BH configurations ($q_{\rm MS-BH} < 0.3$ and $P_{\rm MS-BH} \gtrsim 10$ days) in the first place (Figure 3.18). Even if we were to consider the full MS-BH population, without a limit on the MS mass range, in our simulations we find that few or no BBHs will be produced via CE ($q \lesssim 0.3$) if their MS-BH orbital period is larger than $P_{\rm MS-BH} \gtrsim 100$ days, as shown in Figure 3.12.

3.5 Discussion

3.5.1 The role of stellar physics on CE and SMT

CE and SMT in population-synthesis

The latest results of GWTC-4.0 (The LIGO Scientific Collaboration et al. 2025a) show that current theoretical predictions are overestimating the number of merging BBHs effectively observed. It is likely that this is a consequence of the uncertainties in the binary processes, rather than the uncertainties in the star formation rate e.g., Sgalletta et al. 2025. For instance, Gallegos-Garcia et al. 2021 showed that population-synthesis predictions could be very different with respect to predictions from detailed binary simulations. In particular, Gallegos-Garcia et al. 2021 showed that population-synthesis codes could overestimate the number of BBHs produced with the CE channel while simultaneously reduce the number of BBHs produced via SMT, overall estimating the CE contribution to BBH formation up to a factor ≈ 500.

Many works in the literature showed that the approximated approach of population-synthesis to mass transfer stability and efficiency indeed applies somewhat rigid thresholds to describe this phenomenon, and are not able to fully capture the response of the star (e.g., Klencki et al. 2020; Klencki et al. 2021; Klencki et al. 2025). Detailed mass transfer models that can compute the stellar structure while mass transfer processes occur, as the ones explored with the MESA stellar evolution software (Paxton et al. 2019), showed that SMT is an important formation channel for BBHs (e.g., Marchant et al. 2021; Gallegos-Garcia et al. 2021; Picco et al. 2024). These different approaches could determine differences in the predicted BCO populations properties and formation channels. For instance, Gallegos-Garcia et al. 2021 showed that systems becoming BBHs through SMT in detailed simulations are not able to experience the same fate in rapid population-synthesis simulations, reducing the number of BBHs formed via SMT.

Given the importance of the mass transfer after the first BH formation and because of the computational limitations, detailed studies with MESA generally initialize grids with a star and a BH and use them to investigate their possible evolution towards a merging BBH. In many cases (e.g., Marchant et al. 2021; Gallegos-Garcia et al. 2021; Picco et al. 2024), the fiducial initial binary grids initialize the star at the ZAMS. ZAMS-BH systems are not likely to be produced in the isolated evolution scenario, because the two stars should be born together and have the same age at any given time. Therefore, in principle, ZAMS-BH could be not representative of the MS-BH evolution. However, in Section 3.4.7 we show that the evolution from the ZAMS-BH configuration is similar to the evolution from the MS-BH stage. However, even if these grids are indeed representative of the binary evolution after the first BH formation, it is not guaranteed that they are also representative of actual systems that would be produced as intermediate configuration in between the ZAMS-ZAMS and the BBH stage.

Comparison with Gallegos-Garcia et al. 2021

In their work, Gallegos-Garcia et al. 2021 first compared their detailed MESA ZAMS-BH grids with the MS-BH populations produced with the COSMIC population-synthesis code (Breivik et al. 2020) and then used the MS-BH binaries obtained with COSMIC to select the ZAMS-BH binaries representative of the population that will form BBH. With this approach, Gallegos-Garcia et al. 2021 calculated the contribution of the SMT or CE channel to the BBH population ensuring that only the ZAMS-BH representative of the that population were considered. As discussed in Section 3.4.7 and shown in Figure 3.19, we find that SEVN produces a different MS-BH population of BBH progenitors with respect to the one obtained with COSMIC (Figure 2 of Gallegos-Garcia et al. 2021, also reported in Figure 1.7).

In the COSMIC simulations of Gallegos-Garcia et al. 2021, most of the MS-BH becoming BBHs after a CE episode have MS-BH periods larger than $P_{\rm MS-BH} \gtrsim 300$ days and mass ratios $q_{\rm MS-BH} \lesssim 0.3$. Even if also in our SEVN simulations we expect $q_{\rm MS-BH} \lesssim 0.3$ systems to evolve as BBH after a CE, we find that nearly no BBH progenitor has this MS-BH configuration at their same metallicity ($Z = 0.00142$, Figure 3.12). Furthermore, in the COSMIC simulations a negligible portion of 40 $\mathrm{M}_\odot$ donors experience a SMT after the first BH formation. In contrast, many ZAMS-BH systems form BBHs from SMT from that same donor if detailed MESA simulations are considered. With SEVN, we find a scenario in between: our MS donors with BH companions will form BBHs across a wide range of possible orbital configurations (Figure 3.12) and, in particular, 40 $\mathrm{M}_\odot$ donors will experience SMT evolution if their orbital periods and mass ratios are similar to the ones predicted by the detailed simulations of Gallegos-Garcia et al. 2021 (especially if here we consider the isotropic re-emission and Jeans models, as shown in Figure 3.19).

The differences between our population-synthesis simulations and the ones in Gallegos-Garcia et al. 2021 suggest that the comparison illustrated in Gallegos-Garcia et al. 2021, as well as their findings, could be strongly dependent on the assumed physics or code routines. Moreover, the differences could be even larger if we consider that we are taking snapshots of the MS-BH configurations at the BH formation, but a the beginning of the mass transfer the star will have lost some mass and the system will have increased its $q_{\mathrm{MS-BH}} = M_{\mathrm{MS}}/M_{\mathrm{BH}}$ mass ratio, further reducing the contribution of systems in the CE window.

We highlight that we adopted the same set of assumptions of Gallegos-Garcia et al. 2021 for their population-synthesis simulations, with two[12] main differences: (i) we did not force the tidal synchronization at the onset of the Roche lobe overflow and (ii) we adopted a different set of stellar evolution models. Comparing our results with Gallegos-Garcia et al. 2021, we see that the differences persist also when we disable tides, so they are not due to the different treatment of tides during the Roche lobe overflow. We argue that the different results are namely due to the different stellar physics considered.

The `PARSEC` stellar tracks.

In this work, we use the fiducial set of `PARSEC` tracks Costa et al. 2025, initially developed for `SEVN` to explore the evolution of massive stars $M_{\mathrm{ZAMS}} = 2 - 600\ \mathrm{M}_{\odot}$ in a broad range of metallicities $Z = 4 \times 10^{-2} - 10^{-4}$ (Iorio et al. 2023). Other population-synthesis codes, including the `COSMIC` (Breivik et al. 2020) one adopted by Gallegos-Garcia et al. 2021, implement the tracks of Pols et al. 1998, initially developed with the `STARS` stellar evolution code (Eggleton 1971; Pols et al. 1995) to study the evolution of less massive stars $M_{\mathrm{ZAMS}} = 0.5 - 50\ \ \mathrm{M}_{\odot}$, although in a similar range of metallicities $Z = 3 \times 10^{-2} - 10^{-4}$. As discussed in Section 3.1.1 of Iorio et al. 2023 and Section 1.6.2 of this thesis, these two set of stellar tracks are different in the size of the final core masses, size of the convective envelope, time and extent of the radial expansion, with a non-linear dependence on the initial masses and metallicities and a non-linear impact on binary evolution. Therefore, we attribute to these differences in the stellar evolution physics most of the differences between our `SEVN` simulations and the `COSMIC` ones in Gallegos-Garcia et al. 2021, providing some examples in the following sections.

Lifetime of the HG phase and size of the convective envelope.

`COSMIC` (Breivik et al. 2020) implements the standard `BSE` setup for the stellar phases, assuming that core-He burning stars have radiative envelopes, while HG stars develop a deeper convective envelope as they evolve towards the Giant phase (Hurley et al. 2002). In `BSE`, the radial and mass extent of the convective envelope is a function of the HG lifetime and is calculated with the Hurley et al. 2000 fits on the Pols et al. 1998 tracks. The size of the convective envelope influences the strength of tidal forces, through the turnover timescale of the convective cells (Hurley et al. 2002), and the binding energy of the CE, through the λ parameter of the $\alpha - \lambda$ formalism (Webbink 1984; Claeys et al. 2014; Klencki et al. 2021). The radiative or convective nature of the envelope influences

[12] In Gallegos-Garcia et al. 2021, `COSMIC` stars are initialized as rotating, following Hurley et al. 2002. In our `SEVN` simulations we checked that initializing the stars as initially rotating or non-rotating (our fiducial here) does not modify our results.

also the critical mass ratios $q_{\rm crit}$ adopted to discriminate between stable and unstable mass transfer (Ge et al. 2010, 2015, 2020). Moreover, the size of the convective envelope and the possibility to be in a HG phase influence the normalization factor that determines the mass loss rate during a SMT (Equation 3.9).

In SEVN, and in the simulations conducted in this work, the size of the convective envelope and the lifetime of the HG phase are directly interpolated from the PARSEC tables (Iorio et al. 2023). In Figure 3.21 we show that if we were to use Hurley et al. 2000 fits on the PARSEC tracks (thus, ignoring the PARSEC information on the HG lifetime and convective envelope size), we would increase the number of BBHs that can be formed through the CE evolution. If the Hurley et al. 2000 fits are used, nearly every ZAMS-BH with $q < 0.3$ and $P_{\rm ZAMS-BH} \approx 10^2 - 10^3$ days will produce a BBH via CE in place of a wide BH-BH binary. Comparing Figure 3.21 with Figure 3.20, we see that this assumption strongly impacts the CE channel, but has a negligible impact on the other possible evolutionary pathways of ZAMS-BH binaries with a 40 $M_\odot$ ZAMS.

We find that the assumptions on the HG lifetime and size of the convective envelope have an impact on the CE channel that is comparable to (higher than) the assumption on the λ parameter for the CE binding energy (the $q_{\rm crit}$ assumption for mass transfer stability). For instance, in Figure 3.22 we show how our fiducial ZAMS-BH grids (Figure 3.20) would change if we did not assume a fixed $q_{\rm crit} = 0.3$ for all the donors (Belczynski et al. 2008) but we kept the $q_{\rm crit} = 0.3$ threshold only for core-He burning stars, assuming a stable SMT for MS and HG stars and a moving threshold for Giant stars that depends on the extent of the convective envelope (fiducial model "QCRS" in Iorio et al. 2023). This model is based on the BSE standard assumptions but assumes that mass transfer is always stable for stars that did not yet develop a well-defined core. Despite the favourable assumption for mass transfer stability, Figure 3.22 shows that the ZAMS-BH configurations producing a SMT are not modified. Instead, the systems evolving as Giants during the SMT ($q_{\rm ZAMS-BH} \approx 0.2 - 0.3$) in short period binaries ($P_{\rm ZAMS-BH} \lesssim 20$ days) could more easily form a BBH after a CE (in place of a coalescence, at $Z = 0.00142$) or coalesce (in place of a CE evolution, at $Z = 0.000142$). Maintaining this choice of $q_{\rm crit}$, we also considered the impact of a modified version of the λ fits of Claeys et al. 2014: we did not consider the fiducial model adopted so far in this work, that follows Appendix A of Claeys et al. 2014, but we considered a version with a different sensitivity to the fraction of the convective envelope, following the implementation of Claeys et al. 2014 in BSE (for more details, we refer to Appendix A 1.4 of Iorio et al. 2023). This modified version of the λ fits of Claeys et al. 2014 coupled with the "QCRS" $q_{\rm crit}$ prescriptions compose the fiducial setup shown in Iorio et al. 2023. In Figure 3.23 we show that these modifications in the λ binding energy have an effect similar to the adoption of the Hurley et al. 2000 estimates for the HG lifetime and size of the convective envelope, extending the CE evolution to periods up to $P_{\rm ZAMS-BH} \lesssim 1000$ days.

Evolution with the MIST stellar tracks

To further illustrate the impact of stellar physics, we show in Figure 3.24 the evolution of the ZAMS-BH grids at $Z = 0.00142$[13] if we were to interpolate the stellar properties from the MIST stellar models (Choi et al. 2016). We maintained the fiducial setup of this work, but since the MIST tracks did not provide the information on the convective size

[13] At $Z = 0.000142$ the MIST tracks available in SEVN were too sparse, so we did not report here the results of an evolution at that metallicity.

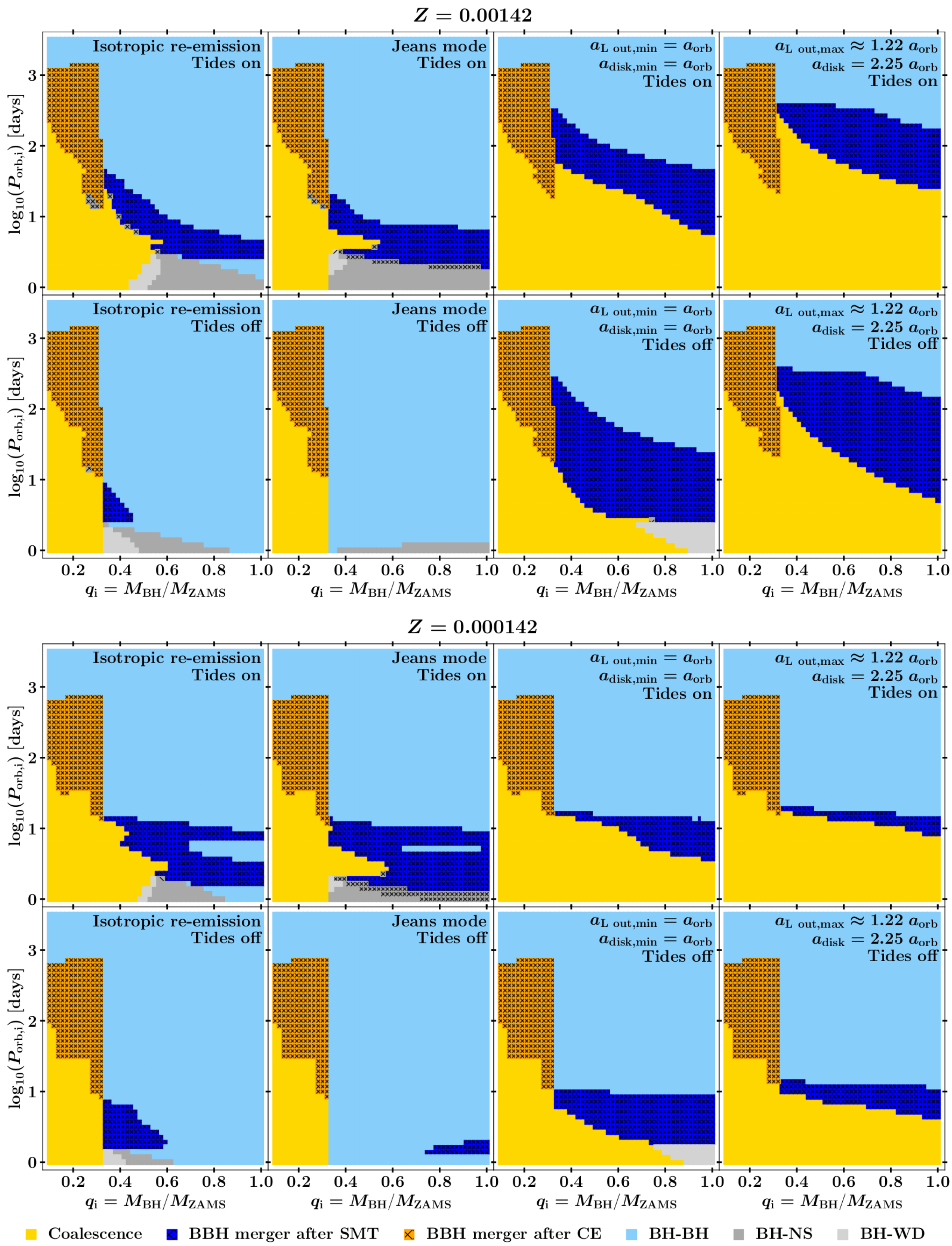

Figure 3.21: As Figure 3.20 (fiducial setup) but we remove the interpolation of the PARSEC convective tables (Iorio et al. 2023). Instead, we adopt the BSE prescriptions to estimate the size of the convective envelope and the duration of the HG time (Hurley et al. 2002).

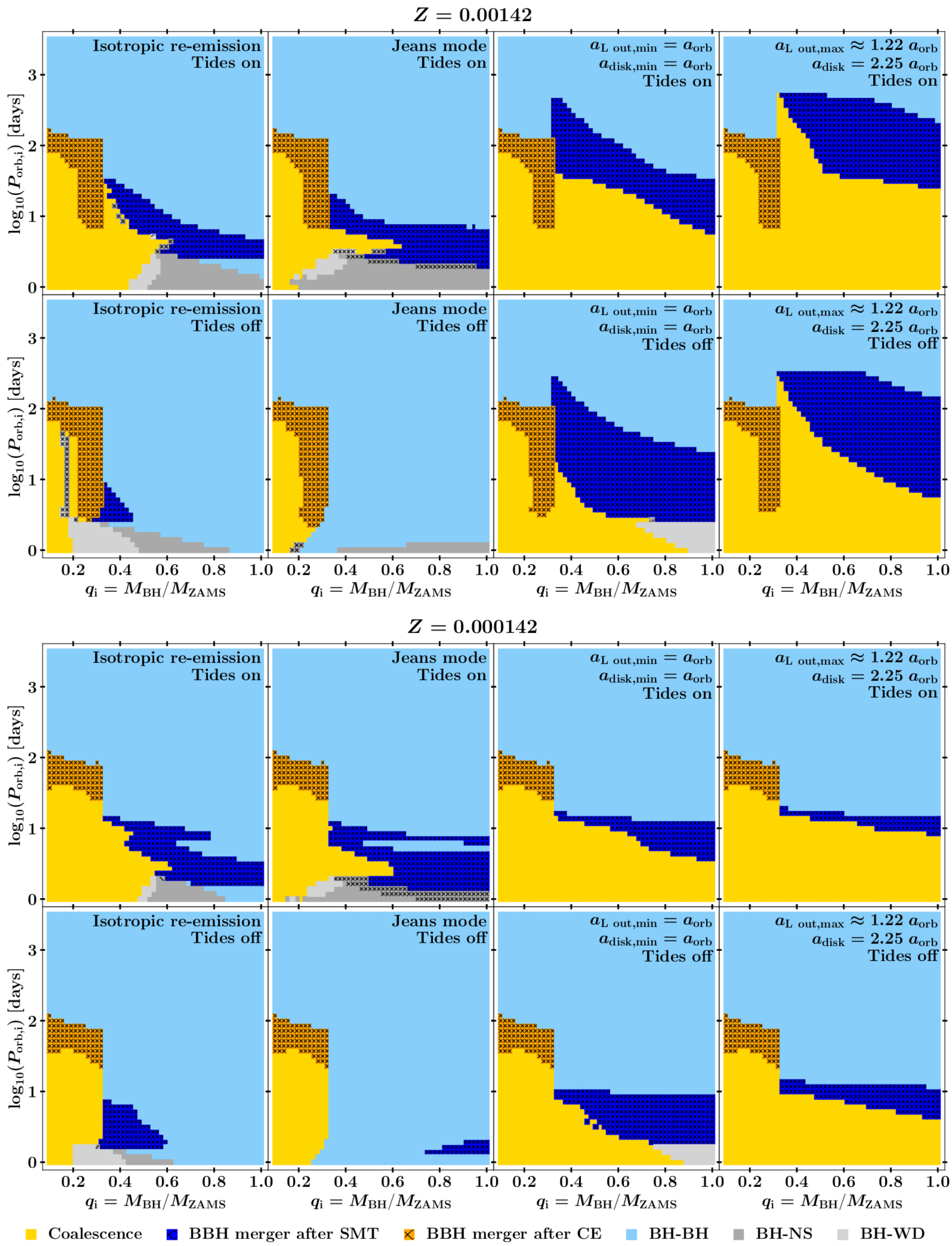

Figure 3.22: As Figure 3.20 (fiducial setup) but we use the fiducial $q_{\rm crit}$ of Iorio et al. 2023 in place of the fiducial $q_{\rm crit}$ of Belczynski et al. 2008 adopted throughout this work.

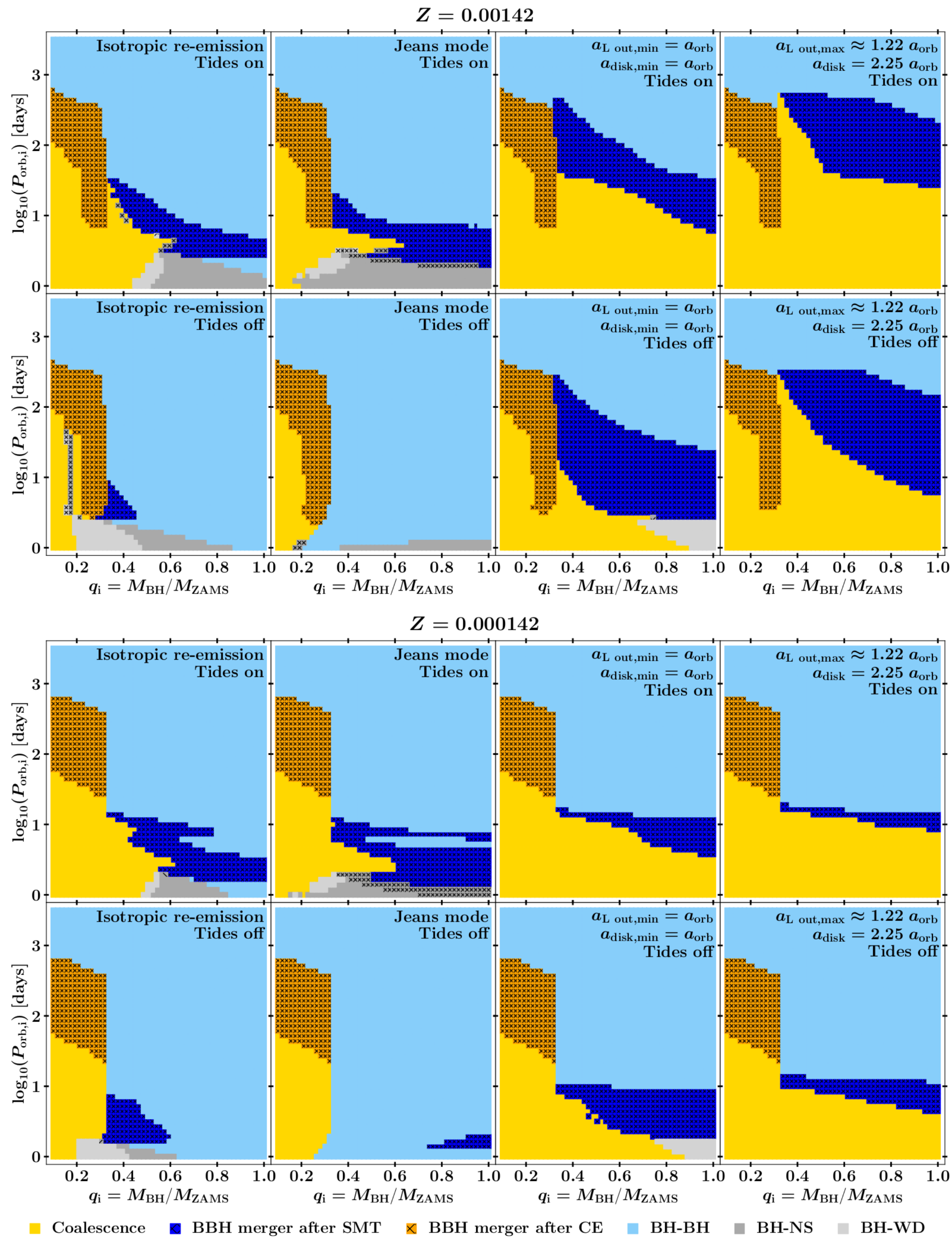

Figure 3.23: As Figure 3.20 (fiducial setup) but we use the fiducial q_{crit} of Iorio et al. 2023 and the λ_{CE} of Claeys et al. 2014 as in BSE, as explained in Iorio et al. 2023, in place of the fiducial q_{crit} of Belczynski et al. 2008 and the full Claeys et al. 2014 prescriptions adopted throughout this work. This new setup is the fiducial one in Iorio et al. 2023.

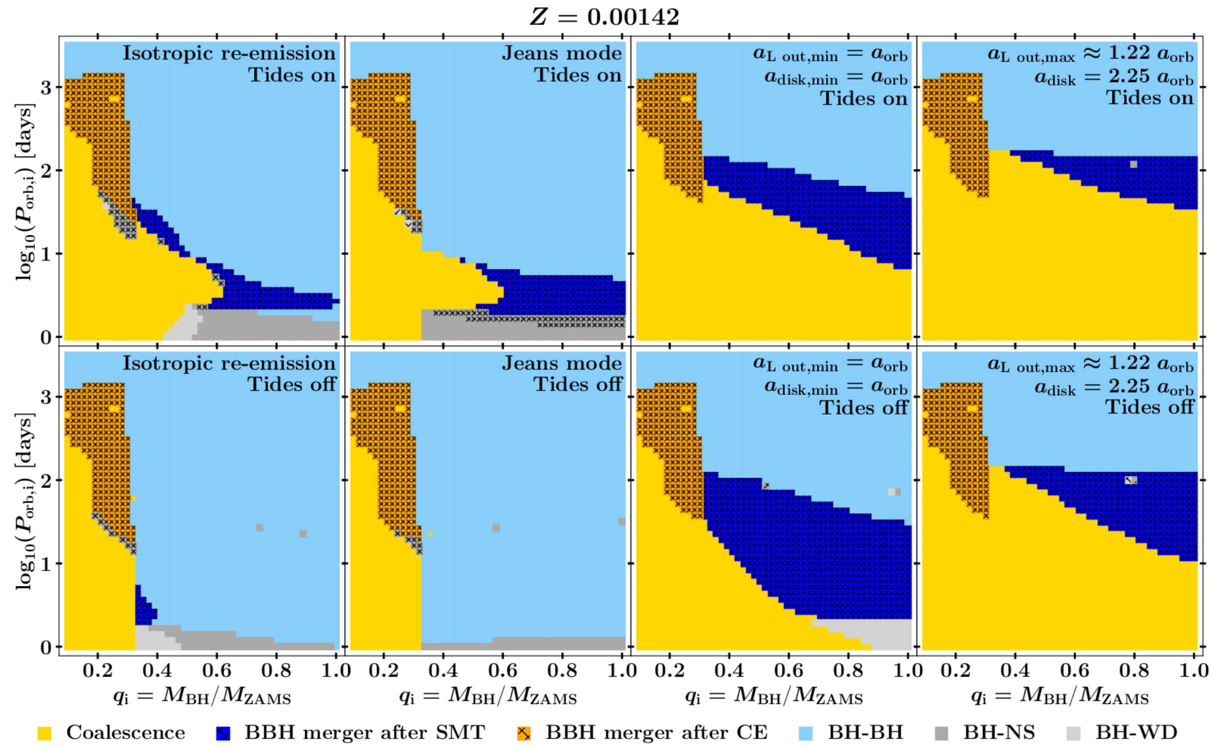

Figure 3.24: As Figure 3.20 (fiducial setup) but we use the `MIST` stellar models (Choi et al. 2016) in place of the `PARSEC` ones (Costa et al. 2025) adopted throughout this work.

of the envelope (thus, on the HG lifetime), we adopted for that the Hurley et al. 2000 fits. In Figure 3.24 we can see that the CE channel for BBH formation extends up to $P_{\rm ZAMS-BH} \lesssim 1500$ days because of the adoption of the Hurley et al. 2000 fits, similarly to what we showed and discussed for Figure 3.21. However, we see that the different stellar radii between the `MIST` and `PARSEC` tracks mark a significant difference in the type of ZAMS-BH systems that can form BBHs after a SMT. `MIST` stars have larger radii than the `PARSEC` ones (see Appendix C of Iorio et al. 2023 for more details on the differences between the `PARSEC` and `MIST` tracks in `SEVN`). In asymmetric binaries ($q_{\rm ZAMS-BH} \lesssim 0.6$), the larger `MIST` radii increase the rate of mass transferred to the companion (and, then, lost by the system), favouring a coalescence rather than the survival of the binary. `MIST` tracks also have longer lifetimes than the `PARSEC` ones, so in wide and more symmetric orbits ($P_{\rm ZAMS-BH} \gtrsim 100$ days and $q_{\rm ZAMS-BH} \gtrsim 0.3$) the mass lost via stellar winds has sufficient time to widen the binary and prevent the onset of an efficient mass transfer interaction.

3.5.2 Role of tides

In mass transfer interactions, the two stars are orbiting so close one to another that tidal forces are expected to circularize and synchronize the orbit (Hut 1981; Hurley et al. 2002). For this reason, many population-synthesis studies assume a circular and synchronized binary at onset of a Roche lobe overflow (e.g., Belczynski et al. 2008; Gallegos-Garcia et al. 2021). In `SEVN` we force tidal circularization but we do not force tidal synchronization at the beginning of a Roche lobe overflow, with important consequences for the evolution of our systems. To illustrate the impact of tides in our simulations (Figure 3.25), we consider

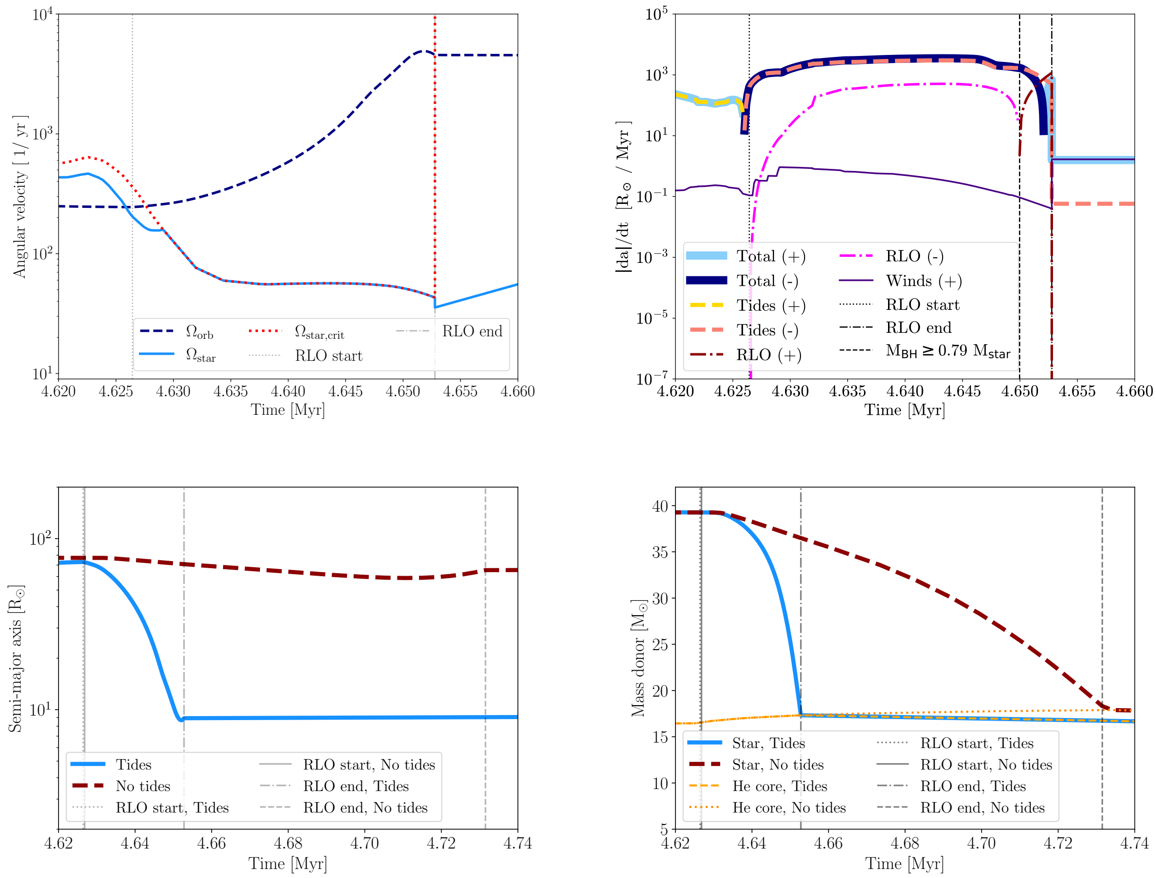

Figure 3.25: Evolution of a ZAMS-BH binary at $Z = 0.000142$, with a donor of $M_{\rm ZAMS} = 40\ {\rm M}_\odot$, BH of $M_{\rm BH} = 20\ {\rm M}_\odot$ and period of $P_{\rm ZAMS-BH} = 10$ days. We show the evolution of the stellar and orbital angular velocity (top left panel), semimajor axis variation (top right), semimajor axis (bottom left) and stellar mass in the case where tides are active or are disabled. For a detailed description of the effects, we refer to Section 3.5.2.

here the evolution of a circular ($e = 0$) ZAMS-BH binary at $Z = 0.000142$, with a donor of $M_{\rm ZAMS} = 40\ {\rm M}_\odot$, mass ratio $q_{\rm ZAMS-BH} = 0.5$ (equivalent to a BH of $M_{\rm BH} = 20\ {\rm M}_\odot$), period of $P_{\rm ZAMS-BH} = 10$ days (equivalent to a semi-major of $a_{\rm ZAMS} = 35\ \ R_\odot$). Considering the fiducial setup of this work and the standard isotropic re-emission case, we expect that tides will produce a BBH after a SMT evolution, while disabling tidal forces will leave the BH-BH binary wide, as shown in Figure 3.20.

As the donor star expands and fill its Roche lobe, the inertia grows and the transferred mass carries away angular momentum (Equation 3.14): overall, the donor slows down. In Figure 3.25 (left panel) we show that, because of this spin-down, the stellar angular velocity could become lower than the orbital angular velocity. Thus, tidal forces act to spin-up the star that lags behind and start to extract angular momentum from the orbit to give it to the star. However, as the orbital angular momentum is transferred, the orbit shrinks and also spins-up: if the star is able to catch up with the orbit, the system synchronizes, otherwise the binary shrinks in a runaway effect and the two orbiting objects collide prematurely, in the so-called "Darwin instability" (Darwin 1880). In our simulations, stars that fill their Roche lobe are already close to a critical rotation and in `SEVN` we assume that they cannot spin supercritical. Therefore, in our simulations tidal synchronization is not achievable and the systems evolve in a Darwin-like runaway effect[14]. As we show in Figure 3.25, tidal forces will indeed drive the evolution of the orbit and will determine a reduction in the orbital separation of about one order of magnitude just in few tenths of Myrs, also peeling off completely the stellar envelope and exposing the helium core: the effect of this type of rapid evolution on the orbital separation and donor mass is similar to a CE. The effect of Darwin instability is generally described in binaries that are conserving their total mass (e.g., Hut 1981), but our mass transferring systems are losing some of the donated mass (Equation 3.11): if they are able to reach a near mass ratio-reversal scenario, the orbit will widen ($q = M_{\rm BH}/M_{\rm star} \gtrsim 0.79$ in the full non-conservative case, see Figure A1 of van Son et al. 2020). In the system examined here, we find that indeed the binary widens when the stellar donor lowers enough its mass to nearly reach the one of the BH ($q = M_{\rm BH}/M_{\rm star} \gtrsim 0.79$): since we are dealing with an Eddington-limited accretion on the BH, its mass remains nearly un-modified during the evolution and the mass transfer is nearly fully non-conservative.

In our simulations, the SMT channel for BBH formation is enhanced by tides because of the onset of Darwin instability and the possibility that the widest systems can avoid the premature coalescence because of the non-conservative nature of the mass transfer. Nevertheless, the tightest systems will still coalesce prematurely because they will not have enough time to reach a near mass-ratio-reversal, as we show in Figure 3.20. We recall here that the duration of the mass transfer is the key parameter that influences also the ability of progenitor stars to completely remove their envelope. The system in Figure 3.25 requires about 8×10^4 more yrs to expose its helium core if tidal forces are not active: if the mass transfer started in the late phase of the stellar evolution, it is possible that the stellar progenitor undergoes a core-collapse supernova event maintaining an hydrogen envelope, explaining the lower incidence of systems that are able to avoid the double pure-Helium stripping in the no-tides case, shown in Figure 3.9. This incomplete envelope stripping could impact the core structure and the amount of H-envelope retained in the supernova progenitors, giving rise to a variety of possible super luminous supernova events ($L \gtrsim 10^{44}$ erg/s) and possibly final BH masses different from the ones predicted by the single stellar evolution cores (Laplace et al. 2020; Laplace et al. 2021, 2025; Schneider et al. 2021, 2023, 2024, 2025; Ercolino et al. 2024, 2025).

3.5.3 Role of metallicity

In this work we considered the evolution at two possible sub-solar metallicities ($Z = 0.00142$ and $Z = 0.000142$) to explore the impact of angular momentum losses on the formation of BBHs. We chose to explore the impact also of metallicity because for lower metallicities we expect the stars to remain more compact, to expand later and to lose less mass via stellar winds (Vink et al. 2011; Laplace et al. 2020; Costa et al. 2025). In Figure 3.26 we show how these physical modifications impact the evolution of binary systems and the formation of BBHs, as explored in this work. Similar to the previous section, we take as an example the evolution of a circular ZAMS-BH binary with donor mass of $M_{\rm ZAMS} = 40\ \rm M_\odot$, mass ratio $q_{\rm ZAMS-BH} = 0.5$ (equivalent to a BH of $M_{\rm BH} = 20\ \rm M_\odot$), and period of $P_{\rm ZAMS-BH} = 3.16$ days (equivalent to a semi-major of $a_{\rm ZAMS} = 35\ \ R_\odot$, so tighter than the binary considered

[14] Currently, in SEVN we calculate the stellar inertia accounting for the full stellar radius instead of the effective stellar radius of the mass bound within the Roche lobe. If we were to use this latter effective radius, the critical rotation would be more difficult to reach and tidal synchronization would be easier to obtain. However, the orbit could still significantly shrink, as we see in the no-tides case.

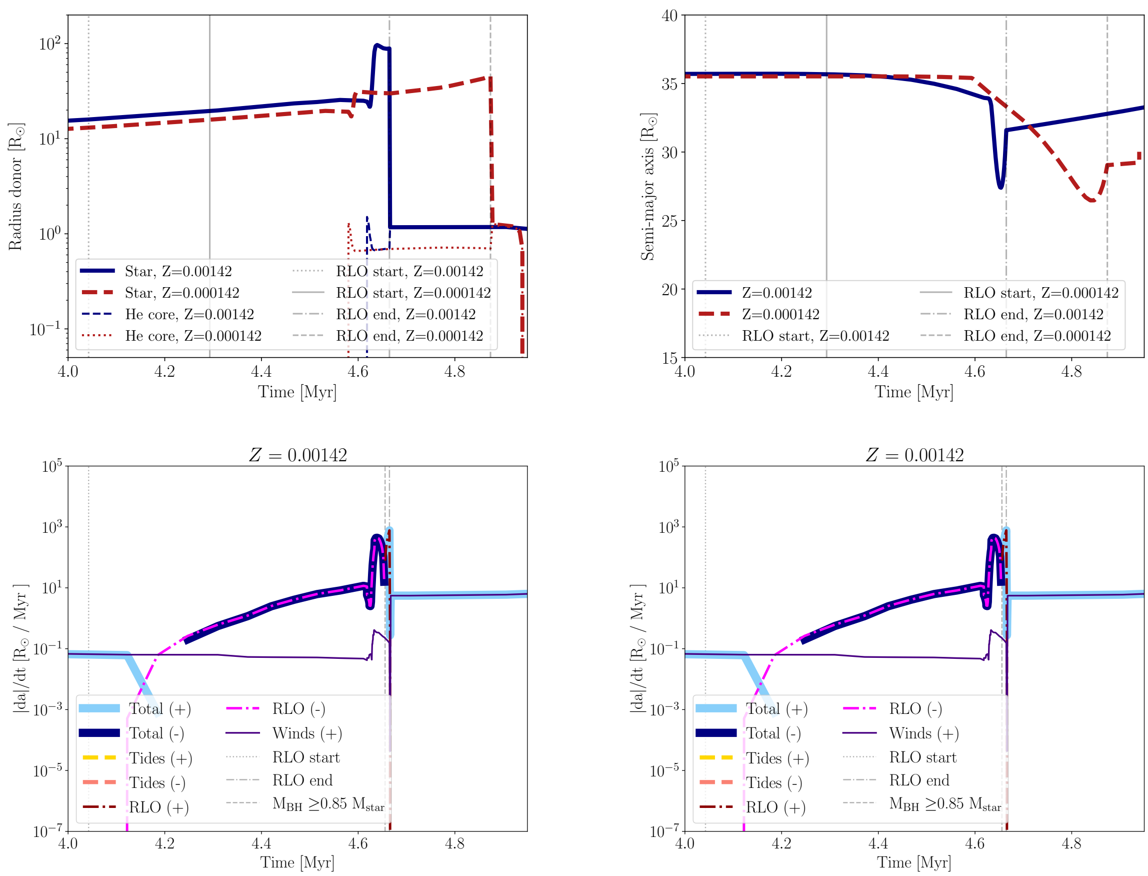

Figure 3.26: Evolution of a ZAMS-BH binary with donor of $M_{\rm ZAMS} = 40$ M$_\odot$, BH of $M_{\rm BH} = 20$ M$_\odot$ and period of $P_{\rm ZAMS-BH} = 3.16$ days and tides disabled. We show the evolution of the stellar radius (top left panel), semimajor axis (top right) at the two metallicities considered in this work. For the $Z = 0.000142$ and $Z = 0.00142$ case we show in the bottom right and left, respectively, the evolution of the variation of the semimajor axis as a result of winds and mass transfer losses. For a detailed description of the effects, we refer to Section 3.5.3.

in Section 3.5.2). Assuming the standard isotropic re-emission model, at $Z = 0.000142$ this binary will become a BBH after a SMT event, while at $Z = 0.00142$ it will remain a wide BH-BH binary, as shown in Figure 3.20.

If we disable the action of tides (as in this example), the evolution of the orbital separation is driven by the amount of angular momentum lost by the system (Equation 3.12 and Equation 3.16). However, the orbit will reduce only when the losses of orbital angular momentum in a Roche lobe overflow will determine a change in the orbital separation that is larger than the one determined by wind mass losses (Equation 3.7 and Equation 3.12). At higher metallicities, wind mass losses are stronger (Vink et al. 2011), so the orbit will widen also at the beginning of the Roche lobe overflow, as shown in Figure 3.26. When the binary starts to lose enough mass to overcome the effect of wind widening, the binary starts to shrink. At $Z = 0.00142$, the donor rapidly expands and transfers a large amount of mass in a short amount of time, since the donor mass loss rate is proportional to the amount of Roche lobe overfilling $\dot{M}_{\rm d} \propto (\log(R)/R_{\rm RL})^3$ (Equation 3.9, as calibrated by Hurley et al. 2002). This expansion enhances the amount of mass that is also not accreted by the companion, thus lost by the system, enhancing the loss of orbital angular momentum (we recall that in our simulations, accretion on BHs is Eddington-limited, so nearly all of the transferred mass is lost in this case). However, the stripping of the hydrogen envelope is so rapid that the orbit cannot shrink as much as in the case of evolution at low metallicity, where the more compact size of the star allow for a prolonged extraction of orbital angular momentum. Therefore, the binary evolved at the lowest metallicity is able to shrink more and produce a BBH able to merge via GW emission within a Hubble time, even if the more compact size of the star delayed the beginning of the mass transfer interaction by few hundreds of Myrs.

3.5.4 Role of supernova model

Pair-instability

Farmer et al. 2019 (hereafter, F19) suggest that population-synthesis studies should determine the BH mass using as proxy the final carbon-oxygen core mass, because binary interactions or evolution close to solar metallicity could partially strip also the helium layer. In the fiducial model adopted in this work - i.e. the Mapelli et al. 2020 fits on Woosley 2017 simulations, hereafter M20 - the helium core is used as proxy for the BH mass. Here, we investigate the sensitivity of our results to the PI model by testing the F19 prescriptions. We find that the choice of the PI model affects mostly the extension of the primary BH mass and the pollution of systems beyond $\gtrsim 45\ \mathrm{M}_{\odot}$, as discussed hereafter.

The Farmer et al. 2019 model The F19 model shifts the beginning of PPI to higher masses with respect to the M20 one, so stars with final carbon-oxygen mass of $38\ \mathrm{M}_{\odot} \leq \mathrm{M}_{\mathrm{CO}} \leq 60\ \mathrm{M}_{\odot}$ undergo PPI, while stars with $M_{\mathrm{CO}} > 60\ \mathrm{M}_{\odot}$ will experience PI (we recall from Section 3.3.2 that the window from M20 assumed here considers PPI for helium cores $32\ \mathrm{M}_{\odot} \leq \mathrm{M}_{\mathrm{He}} \leq 64\ \mathrm{M}_{\odot}$ and PI $M_{\mathrm{He}} > 64\ \mathrm{M}_{\odot}$). In our fiducial `PARSEC` stars evolved in isolation (Iorio et al. 2023; Costa et al. 2025), the shift in the PPI window for F19 allows progenitors with initial masses up to $M_{\mathrm{ZAMS}} \lesssim 80\ \mathrm{M}_{\odot}$ ($M_{\mathrm{ZAMS}} \lesssim 100\ \mathrm{M}_{\odot}$) to form BHs of $M_{\mathrm{BH}} \lesssim 80\ \mathrm{M}_{\odot}$ ($M_{\mathrm{BH}} \lesssim 75\ \mathrm{M}_{\odot}$) at $Z = 0.000142$ ($Z = 0.00142$). In particular, the stars that experience dredge-up during the core-He burning phase at $Z = 0.000142$ can now form an "island" of heavier BHs that extends up to higher masses $M_{\mathrm{BH,max}} \approx 90 - 100\ \mathrm{M}_{\odot}$ (instead of $M_{\mathrm{BH,max}} \approx 90\ \mathrm{M}_{\odot}$), with progenitors of $M_{\mathrm{ZAMS}} \approx 90 - 100\ \mathrm{M}_{\odot}$ (instead of $M_{\mathrm{ZAMS}} \approx 100\ \mathrm{M}_{\odot}$), as shown in Figure 8 of Iorio et al. 2023.

Figure 3.27 shows that the F19 model shifts the distribution of the BH primary masses in bound BH-BH systems towards higher masses with respect to our fiducial M20 results (Figure 3.4), extending the maximum BH mass to $M_{\mathrm{BH,max}} \approx 70\ \mathrm{M}_{\odot}$ (in place of $M_{\mathrm{BH,max}} \approx 55\ \mathrm{M}_{\odot}$) and $M_{\mathrm{BH,max}} \approx 100\ \mathrm{M}_{\odot}$ (in place of $M_{\mathrm{BH,max}} \approx 90\ \mathrm{M}_{\odot}$), at $Z = 0.00142$ and $Z = 0.000142$, respectively.

Similarly to the M20 case, efficient extraction of orbital angular momentum in mass transfer events creates a tail in the primary BH mass spectrum also with the F19 model: BH primaries in BBHs can extend up to $M_{\mathrm{BH,primary,max}} \lesssim 78\ \mathrm{M}_{\odot}$ ($M_{\mathrm{BH,primary,max}} \lesssim 58\ \mathrm{M}_{\odot}$) at $Z = 0.000142$ ($Z = 0.00142$), as shown in Figure 3.28 (to be compared with the fiducial results in Figure 3.2). Assuming the F19 model increases up to $\lesssim 11\%$ the fraction of the BBH population that has a primary BH in the $\gtrsim 45\ \mathrm{M}_{\odot}$ region (or up to $\lesssim 8\%$, if we limit to the $> 46\ \mathrm{M}_{\odot}$ region that cannot be populated by pure-Helium stars) in the most optimistic case ($\gamma = 1.5$, tides active, and $Z = 0.000142$). In Figure 3.29 we show

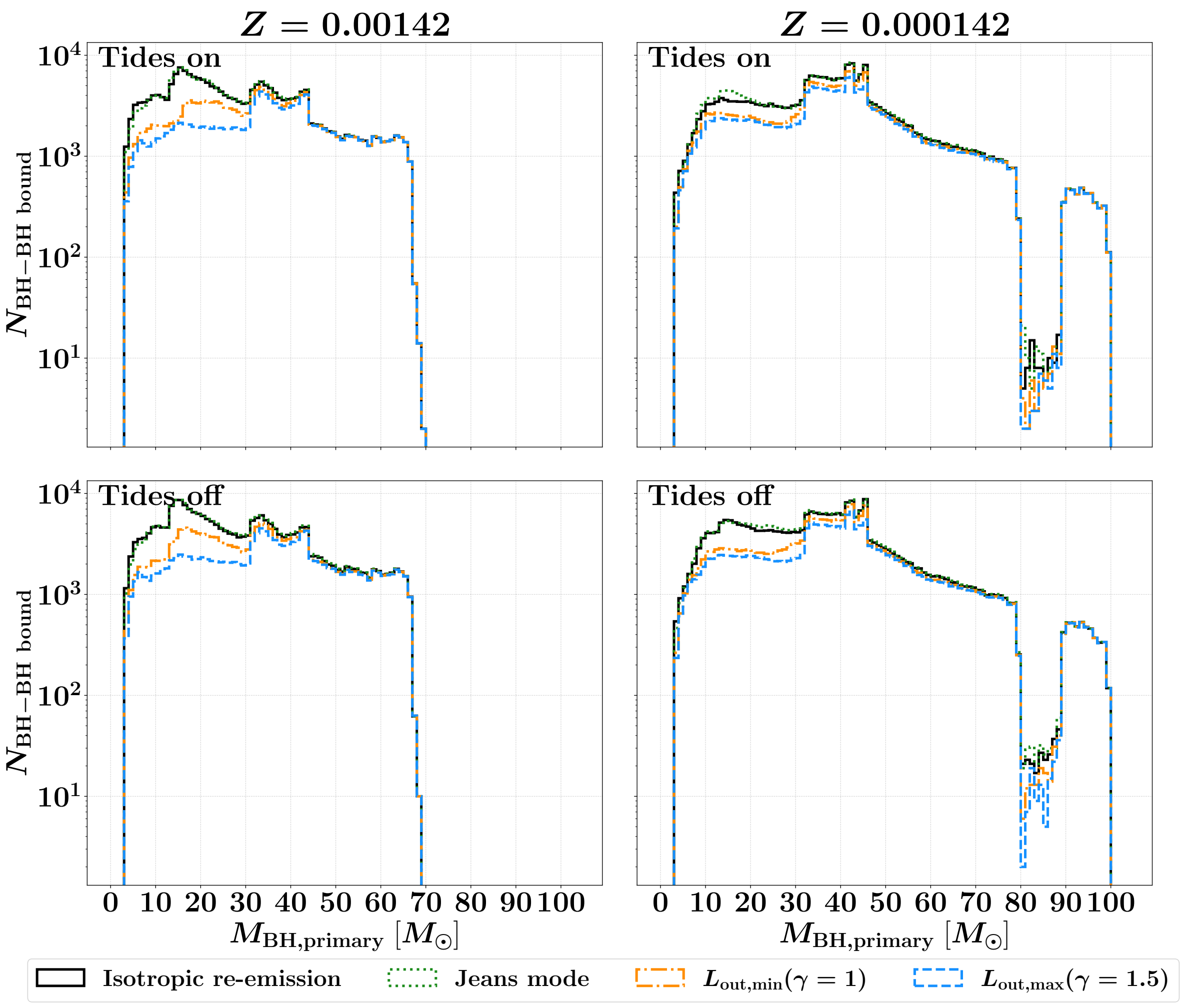

Figure 3.27: Primary BH masses for bound BH-BH binaries obtained with the F19 model under the combinations of metallicity, tides and angular momentum losses considered in this work (Section 3.2). The maximum BH masses are intrinsically higher than the ones found in the M20 fiducial case (Figure 3.4).

that these "additional" heavy BHs, not present with our fiducial M20 model, are indeed produced by the collapse of progenitor stars that were able to avoid the onset of PPI because of the shifted window of the F19 model.

We find that the shift in the PPI window does not change the maximum mass of secondary BHs. Indeed, with the F19 model, we keep retrieving the $M_{\mathrm{BH,max,secondary}} \leq 46\ \mathrm{M}_\odot$ limit due to the action of binary stripping, that either creates a pure-Helium star or it leaves a small hydrogen envelope in the already lighter progenitors, similarly to what was illustrated in Figure 3.8. We highlight that, adopting the `PARSEC` tracks implemented in `SEVN` (Iorio et al. 2023; Costa et al. 2025), both the F19 and the M20 prescriptions predict a maximum BH mass from pure-Helium stars that is precisely 46 $\mathrm{M}_\odot$. Pure-Helium stars are a common evolutionary pathway for secondary BHs (Korb et al. 2025, e.g), so it is mostly because of this limit on the maximum BH from pure-Helium stars, that both PI models retrieve a dearth of secondary BHs above $\gtrsim 45\ \mathrm{M}_\odot$, qualitatively in agreement with the mass distributions inferred from GWTC-4.0 data (The LIGO Scientific Collaboration et al. 2025a; Antonini et al. 2025; Ray & Kalogera 2025; Tong et al. 2025).

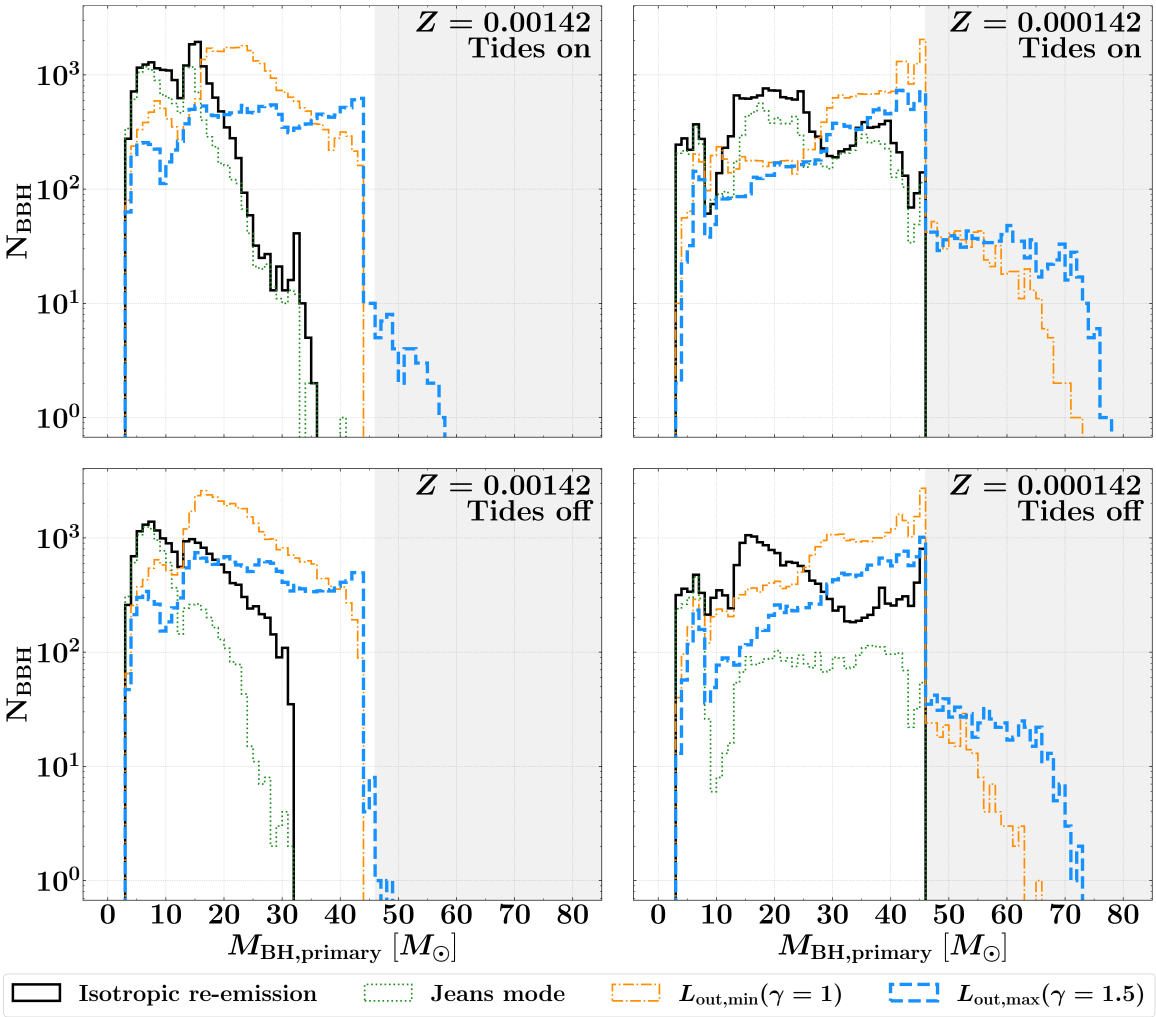

Figure 3.28: Primary BH masses for merging BBHs obtained with the F19 model under the combinations of metallicity, tides and angular momentum losses considered in this work (Section 3.2). The maximum BH masses are higher than the ones found in the M20 fiducial case only for the $\gamma \geq 1$ assumption (Figure 3.2).

A PI gap for BBHs limited by pure-Helium assumptions? Farmer et al. 2019 find that the ≈ 45 M$_\odot$ limit in the BH masses is robust against variations in metallicity, internal mixing and stellar wind mass loss, suggesting that it could be used as an metal-free and redshift-free threshold to discriminate between BHs born from BBHs evolved in the isolated binary evolution scenario or from hierarchical mergers. Even if the location and the existence of such a limit are sensitive to stellar physics uncertainties (e.g., overshooting and $^{12}\mathrm{C}(\alpha,\gamma)^{16}\mathrm{O}$ rate, see Costa et al. 2021 and references therein), the existence of a gap at least in the masses of BHs in BBHs is suggested by the intense binary stripping that they experience in order to become GW sources within a Hubble time, that generally leads to the formation of pure-Helium progenitors (Korb et al. 2025). In addition to this, some works in the literature showed that even under extreme assumptions (such as super-Eddington accretion during a CE), only few (e.g., $\lesssim 2\%$, at $Z = 0.001$) BBHs could indeed form in isolated binaries and contain a BH heavier than ≈ 45 M$_\odot$ (e.g., van Son et al. 2020), unless we consider also metallicities down to $Z = 10^{-5}$ (e.g., Briel et al. 2023). Our results show that even assuming efficient orbital angular momentum losses would still

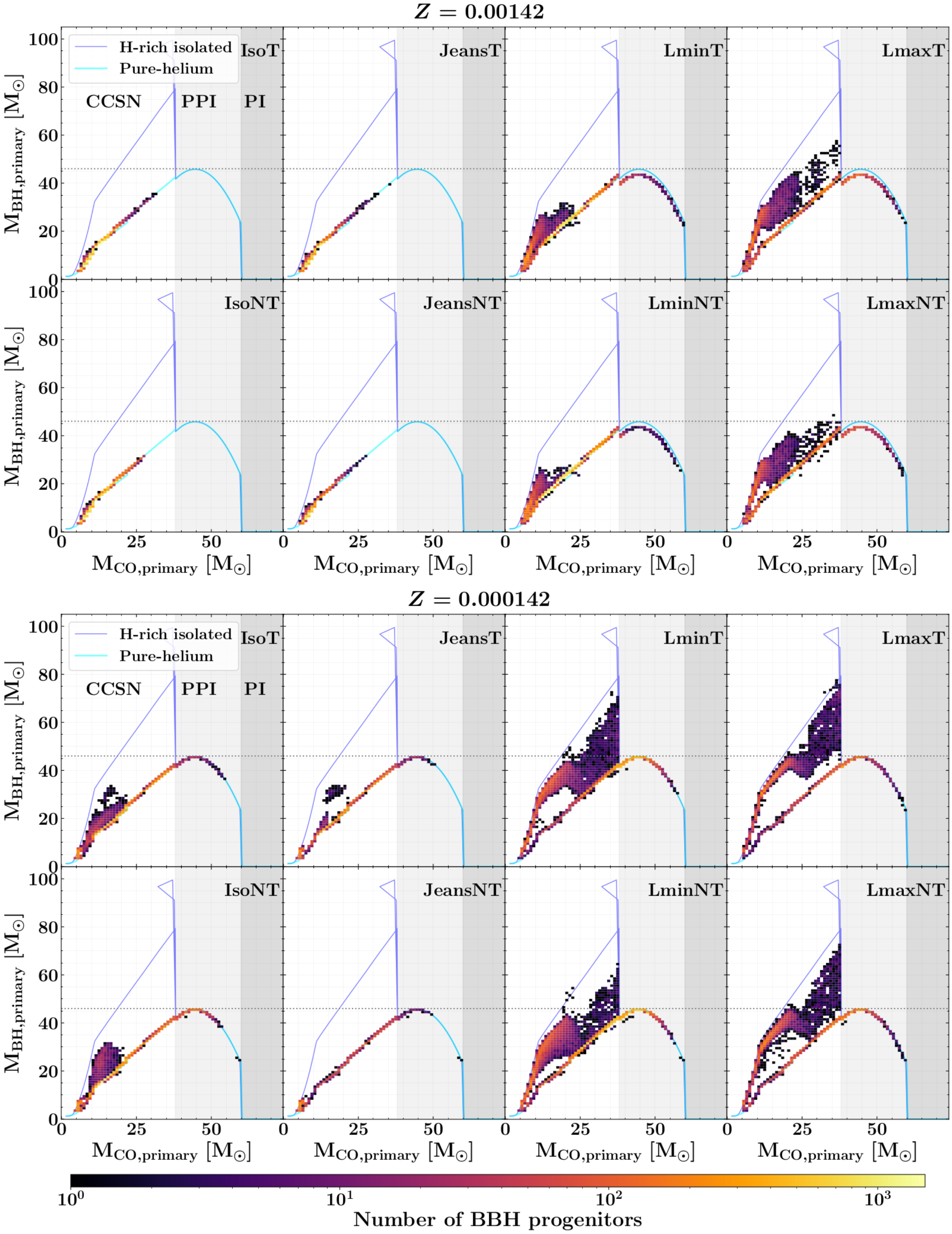

Figure 3.29: BH mass as a function of the CO mass for BH primaries in merging BBHs obtained with the F19 model for all the combinations of angular momentum losses, tidal model and metallicities considered in this work (Section 3.3.2). If we compare with Figure 3.7, we see that the F19 window is shifted to higher masses and this helps with the formation of heavier BH primaries.

produce a negligible pollution in the $\gtrsim 45$ M$_\odot$ region of BH primaries at $Z = 0.00142$ ($\lesssim 1\%$ or even $\lesssim 0.3\%$ of the total BH primary population, assuming the M20 or F19 prescriptions, respectively). However, at lower metallicities ($Z = 0.000142$), we find that this assumption could lead up to $\approx 3 - 11\%$ of BBHs to have a primary above $\gtrsim 45$ M$_\odot$. Moreover, we find that adopting the F19 model pushes the maximum BH primary limit to ≈ 78 M$_\odot$, well-beyond the ≈ 45 M$_\odot$ "standard" limit but also beyond the "extended" limit considered by Farmer et al. (2019) themselves for the 1σ uncertainty in the $^{12}C(\alpha,\gamma)^{16}$ reaction. We find that this pollution is due to stars that did not collapse as pure-Helium, but retained a hydrogen envelope.

We highlight that both the Farmer et al. (2019) and Woosley (2017) results are based on the evolution of bare helium core. In this work, we showed that considering stellar evolution models that have a hydrogen envelope since the ZAMS does impact the final BH mass nearby the PI regime, because dredge-up events could occur, stabilize the core against the PI. This difference allowed us to produce remnants beyond the $\gtrsim 45$ M$_\odot$ limit predicted by pure-Helium stars, polluting the putative primary BH gap of BBHs, especially if efficient orbital angular momentum losses are considered.

3.5.5 Comparison with Iorio et al. 2023

Iorio et al. 2023 adopted the same set of PARSEC tracks used here to explore the impact of many uncertainties (e.g., CE efficiencies, $q_{\rm crit}$ thresholds, core-collapse supernovae, and PI models) on the formation of BBHs. They only considered the isotropic re-emission model for angular momentum loss, so we can use our work on efficient angular momentum losses to extend their results.

None of their explored combinations of parameters was able to populate the BH upper-mass gap, except for one: strong natal kicks, typically associated with the birth of pulsars (Hobbs et al. 2005; Disberg & Mandel 2025). Even if these kicks were probably too strong for typical BHs (Atri et al. 2019), they allowed to produce very eccentric orbits ($e \approx 1$), reducing the time required to merge via GW emission $t_{\rm GW} \propto (1-e)^{-2}$ (Peters 1964). With this assumption, BHs in the upper mass gap were selected randomly from the bound BH-BHs that would have been too wide to merge if it were not for an eccentric orbit. For some of these BBH progenitors, the mass transfer interaction was not sufficient to shrink the orbit to merge within a Hubble time, nor to strip completely the progenitor envelope, allowing form the formation of BHs heavier than the ones allowed by pure-Helium stars. However, Iorio et al. 2023 showed (in their Figure 22) that these kicks are so strong that they destroy more binaries than the other models: their merger rate density is lower by one order of magnitude with respect to the other models explored, resulting even lower than the one of GWTC-4.0 (The LIGO Scientific Collaboration et al. 2025a).

Even if in our simulations we assumed zero natal kick velocities, we can use our results and the ones of Iorio et al. 2023 to show that assumptions on efficient angular momentum loss during stable mass transfer can have a stronger impact on the BH mass spectrum with respect to other parameters usually explored in population-synthesis studies.

3.6 Summary

In this work, we used population-synthesis simulations made with SEVN to investigate how angular momentum loss in binary affect the formation and evolution of BBHs.

We considered four possible models to describe the amount of orbital angular momentum lost during a mass transfer event (parametrizable with a γ parameter, as in Soberman et al. 1997): isotropic re-emission from the accretor, isotropic emission from the donor (Jeans model), outflow from the outer Lagrangian point, or the formation of a circumbinary disk. The latter two models could be described and interpreted through a similar analytical formulation, so for them we explored simultaneously a less efficient ($\gamma = 1$) and more efficient ($\gamma = 1.5$) case of angular momentum loss. In both cases, these models were more efficient ($\gamma \geq 1$) by construction than standard isotropic wind models ($\gamma < 1$) adopted in many population-synthesis studies (e.g., van Son et al. 2020; Broekgaarden et al. 2022; Iorio et al. 2023). In particular, the model for outflows through the outer Lagrangian points was explored as a proxy for the outflows often considered in detailed binary simulations (Marchant et al. 2021; Gallegos-Garcia et al. 2021; Picco et al. 2024; Klencki et al. 2025). Furthermore, in this work we extended the parameter space exploration conducted in Iorio et al. 2023 with `SEVN` to illustrate impact of stellar physics assumptions on the BBH formation, exploiting the fact that `SEVN` can implement the same binary prescriptions of other population-synthesis codes available in the literature (the ones that follow the `BSE` approach, described in Hurley et al. 2002) but interpolates a different set of stellar tracks (the `PARSEC` ones of Costa et al. 2025, in place of the `STARS` ones of Pols et al. 1998).

Our results can be summarized as follows:

- If we assume efficient extraction of orbital angular momentum ($\gamma \geq 1$) we can shift the maximum BH mass in BBHs upward by $\lesssim 10$ $\mathrm{M}_\odot$ in our fiducial scenario. At $Z = 0.000142$, this allows the production of BBHs with primary BHs up to $M_{\mathrm{BH,primary,max}} \approx 45 - 58$ $\mathrm{M}_\odot$, if we assume the fiducial PI prescriptions of Mapelli et al. 2020 on Woosley 2017 models. However, we could produce BH primaries as massive as $M_{\mathrm{BH,primary,max}} \approx 45 - 78$ $\mathrm{M}_\odot$ if we assume the Farmer et al. 2019 PI model. For both PI prescriptions, we find that secondary BHs are always lighter than $M_{\mathrm{BH,secondary,max}} \lesssim 46$ $\mathrm{M}_\odot$. Our results are in qualitative agreement with the cut-off at $\approx 40 - 60$ $\mathrm{M}_\odot$ (model-dependent, see Ray & Kalogera 2025) inferred for the BH mass distribution from GW detections of GWTC-4.0 The LIGO Scientific Collaboration et al. 2025b,a. The existence of a PI gap is predicted by stellar evolution models (Woosley 2017; Farmer et al. 2019), so the main formation scenario suggested for BHs in this mass range is the hierarchical merger (Rodriguez et al. 2019; Antonini et al. 2025; Tong et al. 2025). Nevertheless, our findings suggest that a small fraction ($\lesssim 3 - 11\%$) of the BBH population evolved in the isolated binary evolution scenario could have primaries above $\gtrsim 45$ $\mathrm{M}_\odot$, polluting that region of BH masses more efficiently than other scenarios (e.g., without requiring super-Eddington accretion at $Z0.001$, as explored by van Son et al. 2020, or going down to $Z = 10^{-5}$, as Briel et al. 2023). Moreover, our results show that the $\approx 45 - 50$ $\mathrm{M}_\odot$ limit for BH masses in BBHs is a consequence of complete envelope stripping: the limit can be surpassed assuming efficient angular momentum losses in mass transfer processes and can be influenced by the effects of the H-envelope on the growth of the helium core, such as the occurrence of dredge-ups.

- Assuming efficient angular momentum loss - as in the case of outflows from the outer Lagrangian point or in the case of the formation of a circumbinary disk - the formation of merging BBH does not always require the complete envelope stripping of the progenitors. In these cases, at $Z = 0.000142$ ($Z = 0.00142$) we find that up to

$\lesssim 30\%$ of BBHs could have both progenitors that retain some hydrogen envelope at the pre-supernova stage.

- In the most optimistic case explored in this work (efficient angular momentum extraction $\gamma = 1.5$, tidal synchronization active, and low metallicity $Z = 0.000142$) up to $\approx 60\%$ of primary BH progenitors (that belong to BBHs) can retain a hydrogen envelope at the pre-supernova stage, increasing the BH final mass even by $\approx 15\ \mathrm{M}_\odot$ with respect to core-collapse supernovae from pure-Helium stars. In the BH primaries, the possibility to retain some hydrogen envelope coupled with the lighter helium cores of some $M_\mathrm{ZAMS} \approx 80 - 100\ \mathrm{M}_\odot$ `PARSEC` tracks (as a consequence of dredge-up episodes during the core-He burning phase, see Iorio et al. 2023 and Costa et al. 2025) determines the formation of the BH primaries above the $\gtrsim 45\ \mathrm{M}_\odot$ threshold. In contrast, in our simulations, the $\lesssim 46\ \mathrm{M}_\odot$ limit in the secondary BH masses is due to a collapse of progenitors that were either completely stripped of their envelope or that would have been anyway lighter than that threshold, as their progenitor was generally the lightest star since the beginning ($\approx 88 - 92\%$ of the cases, in each simulated set).

- Assumptions on the angular momentum extraction do not significantly modify the BBH formation efficiencies, that remain compatible with the ones found by Broekgaarden et al. 2022 and Iorio et al. 2023. Therefore, uncertainties due to orbital angular momentum losses have an impact in the formation of BBH that is comparable with other uncertainties in binary evolution and star formation rates. The only exception is constituted by the scenario with the less efficient case of Lagrangian outflows (also equivalent to the formation of an unstable circumbinary disk), that we disfavour because it produces more BBHs than the range found in those works.

- The models for Lagrangian outflows or circumbinary disk formation enhance the creation of a sub-population of asymmetric BBHs ($q_\mathrm{BBH} \lesssim 0.4$) where the secondary progenitor was a light star of $M_\mathrm{ZAMS,secondary} \approx 20 - 30\ \mathrm{M}_\odot$ with a primary companion that was either similar in mass and in a tight orbit ($a_\mathrm{ZAMS} \lesssim 10^3\ \ R_\odot$), or much more massive ($M_\mathrm{ZAMS,primary} \gtrsim 50\ \mathrm{M}_\odot$) and in much wider orbits, up to $\lesssim 5 \times 10^4\ \ R_\odot$.

- Most BBHs ($\approx 40 - 89\%$) have a MS companion at the time of the first BH formation, that will eventually start a mass transfer interaction. By looking at the full MS–BH population of BBH progenitors, we found that the SMT channel is the dominant one for efficient angular momentum extraction ($\approx 55 - 77\%$, although for $Z = 0.000142$ and $\gamma = 1.5$ it occurs only in $\approx 30 - 40\%$ of the BBH progenitors) and is common also in the isotropic models ($\approx 30 - 65\%$ of the cases, except for a $\lesssim 1\%$ contribution from the inefficient Jeans model with tidal synchronization disabled, a setup that in general forms few BBHs). In particular, we find that few or no BBH progenitors have asymmetric ($q_\mathrm{MS-BH} \lesssim 0.3$) and wide ($P_\mathrm{MS-BH} \gtrsim 100$ days) MS-BH systems that would fall in the region where CE evolution is required to produce BBHs, in contrast with other works in the literature (e.g., Gallegos-Garcia et al. 2021).

- We compared the evolution from ZAMS-BH and MS-BH grids of `SEVN`, finding that they have a similar future evolution and could be used reliably as proxy to switch from one configuration to another, as often happens in the literature with detailed binary simulations (e.g., Gallegos-Garcia et al. 2021; Picco et al. 2024; Klencki et al. 2025). However, we found that the MS-BH systems becoming BBHs in `SEVN` have different MS-BH orbital configurations with respect to the ones found by other population-synthesis codes in the literature, such as the `COSMIC` simulations in Gallegos-Garcia et al. 2021. We argue that the differences in the populations are due to the assumptions on the underlying stellar physics (e.g., assuming the tracks of Pols et al. 1998 or Costa et al. 2025), since stellar physics significantly impacts the orbital configurations and the number of systems that experience SMT or CE before the formation of a BBH. Therefore, we highlight that caution should be taken when population-synthesis codes are used to infer population properties from grids of detailed binary models, as the intermediate configurations of BBH progenitors could be very sensitive to the code and physics assumed. Our results suggest that the impact of stellar physics on the final BBH masses and intermediate configurations could be bigger than other assumptions often explored in population-synthesis studies (e.g., mass transfer stability and efficiency or supernova models), and will be further explored in future works.

Chapter 4

Conclusions and outlook

In this thesis, I investigated the formation channels and the properties of the binary compact objects (BCOs) merging via gravitational wave (GW) emission within the lifetime of the Universe. I used the population-synthesis code `SEVN` to explore the impact of model uncertainties on BCO formation. In particular, I characterized the impact of mass transfer physics in the isolated evolutionary scenario and the role of pure-Helium and Wolf-Rayet (WR) stars, as proxy for mass transfer evolution or BCO formation.

In Chapter 2, I demonstrated that WR stars with a compact object companion (WR–CO binaries) represent the dominant evolutionary pathway to BCOs across a wide parameter space. I explored 96 combinations of metallicity, common envelope efficiency, core-collapse supernova (CCSN) prescriptions, and natal kick models, finding that more than $\gtrsim 83\%$ of simulated BCOs evolved as WR–CO phase. At sub-solar metallicity ($Z = 0.00014$), stellar winds are quenched and stars are more compact, so it is possible that $\gtrsim 21\%$ of GW-merging binary black hole (BBHs) progenitors were not able to strip completely, so they could not be visible as WRs with a BH companion. In particular, the WR–CO phase is sensitive to mass transfer and metallicity, which together regulate whether stars are fully stripped to form WR progenitors. At higher metallicity ($Z = 0.02 - 0.00014$), the stripping is more efficient and WR–COs constitute a necessary progenitor configuration for more than $\gtrsim 99\%$ of BCOs, regardless of their final nature (binary black holes, black hole-neutron stars, or binary neutron stars; BBHs, BH-NSs, or BNSs, respectively), progenitor configuration (WR–NSs or WR–BHs), and models assumed (within the combinations explored). I find that CCSNe and natal kicks are important only at solar metallicity $Z \approx 0.02 - 0.014$ and that contribute in the form of "lucky kicks", enhancing the post-supernova eccentricity and reducing the time required to merge via GW emission, otherwise long as a consequence of post-mass transfer circularized orbits. At high metallicity, stellar winds are strong and BCO formation is inefficient. Therefore, the contribution of this chaotic channel becomes relevant because of the low statistics.

Despite their importance, I found that WR–CO binaries are rare and constitute only $\approx 1 - 5\%$ of the initial population. Moreover, only $\approx 5 - 30\%$ of the WR–COs eventually produces BCOs, highlighting once again that BCO formation is rare. However, BCO production is favoured in binaries that exhibit the orbital properties of Cyg X-3, the only WR–CO candidate known in the Milky Way. In particular, if Cyg X-3 hosts a black hole, it is very likely ($\approx 70 - 100\%$) that the binary will evolve into a merging BCO; if it hosts a neutron star, the probability is lower ($< 40 - 60\%$). This makes Cyg X-3 and future observed WR–CO binaries crucial empirical benchmarks to constrain binary-evolution models.

In Chapter 3, I investigated the impact on BBH demography of orbital angular momentum losses in non-conservative mass transfer in circular orbits. I tested four models for angular momentum extraction (isotropic wind emission from the accretor or from the donor, Lagrangian outflows, and circumbinary-disk formation) while also considering the impact of tides and stellar-evolution on the orbital separation and final BH masses, respectively. I found that efficient extraction of the orbital angular momentum extraction (via Lagrangian outflows or via the formation of a circumbinary disk) allows the creation of BBHs with BH primaries up to $\approx 45 - 78$ $M_{\odot}$, depending on the adopted pair-instability prescriptions. Such higher primary BH masses were achieved because efficient angular momentum losses allowed the GW-merger also of binaries with stellar progenitors that were not completely stripped of their envelope. Sometimes the CCSN event occurs still during the mass transfer phase, allowing the collapse of stars with some hydrogen envelope, increasing the final BH mass up to ≈ 15 $M_{\odot}$. This type of evolution produces $\approx 3 - 11\%$ of the BBHs with primary BHs with mass $\gtrsim 45$ $M_{\odot}$. In the standard picture, BBHs evolve from progenitors that were completely stripped and could not fill that region of the BH mass spectrum. Following the simulations presented in this thesis, efficient angular momentum losses in mass transfer evolution can overcome the ≈ 45 $M_{\odot}$ limit for primary BHs but not for secondary BHs. These results indicate that uncertainties in angular momentum loss processes should be further investigated to better interpret the features of the BBH mass spectrum, in particular, to correctly interpret the possible identification of a PI gap from GWTC-4.0 and from future GW detections.

Eventually, I find that the BBH formation efficiencies are comparable to the ones found by other population-synthesis studies that focused on other model uncertainties (e.g., common envelope efficiency, natal kicks, or star formation rate). Moreover, I showed that differences in the underlying stellar models and evolutionary codes can strongly modify BBH progenitor properties and mass distributions, sometimes more than assumptions about mass transfer or supernova physics. These results highlights the key role of stellar physics and underlines the necessity of further investigations of its impact on the BBH demography, along side with the other uncertainties.

The results presented in this thesis show that the demographics of BCOs is determined by an intricate interplay of physical processes, such as stellar winds, mass transfer, orbital angular momentum evolution, and supernova physics. While WR–CO binaries emerge as a key BCO progenitors, evolutionary pathways that consider efficient orbital angular momentum losses may avoid the complete envelope stripping to produce BBHs. Therefore, the role of WR–COs as BCO progenitors and the constraints that we could get on mass transfer models by their observation could depend on the uncertainties on angular momentum losses during mass transfer. Nevertheless, this implies that future observations and characterization of WR–CO systems like Cyg X-3 could be combined with the growing catalogue of GW sources in order to obtain better constraints on mass transfer physics and the other uncertainties affecting the formation of BCO populations. Ultimately, linking detailed stellar physics with GW population studies will be essential to unlock the full potential of GW astronomy.

List of Figures

List of Tables

Bibliography

Aarseth, S. J. 2003, Gravitational N-Body Simulations

Abac, A., Abramo, R., Albanesi, S., et al. 2025, arXiv e-prints, arXiv:2503.12263

Abac, A. G., Abbott, R., Abouelfettouh, I., et al. 2024, ApJ, 970, L34

Abbott, B., Abbott, R., Abbott, T., et al. 2019, Physical Review X, 9, 031040

Abbott, R., Abbott, T., Acernese, F., et al. 2023a, Physical Review X, 13, 041039

Abbott, R., Abbott, T., Acernese, F., et al. 2023b, Physical Review X, 13, 011048

Abbott, R. et al. 2020, Phys. Rev. L., 125, 101102

Addari, F., Marigo, P., Bressan, A., et al. 2024, ApJ, 964, 51

Agrawal, P., Hurley, J., Stevenson, S., Szécsi, D., & Flynn, C. 2020, MNRAS, 497, 4549

Agrawal, P., Szécsi, D., Stevenson, S., Eldridge, J. J., & Hurley, J. 2022, MNRAS, 512, 5717

Antonini, F. & Gieles, M. 2020, Phys. Rev. D, 102, 123016

Antonini, F., Romero-Shaw, I., Callister, T., et al. 2025, arXiv e-prints, arXiv:2509.04637

Arca Sedda, M., Kamlah, A. W. H., Spurzem, R., et al. 2024, MNRAS, 528, 5119

Atri, P., Miller-Jones, J. C. A., Bahramian, A., et al. 2019, MNRAS, 489, 3116

Ballone, A., Costa, G., Mapelli, M., et al. 2023, MNRAS, 519, 5191

Banagiri, S., Thrane, E., & Lasky, P. D. 2025, arXiv e-prints, arXiv:2509.15646

Banerjee, S. 2021, MNRAS, 503, 3371

Banerjee, S. & Olejak, A. 2024, arXiv e-prints, arXiv:2411.15112

Barber, J. & Antonini, F. 2025, MNRAS, 538, 639

Bartzakos, P., Moffat, A., & Niemela, V. 2001, Monthly Notices of the Royal Astronomical Society, 324, 18

Bavera, S. S., Fragos, T., Qin, Y., et al. 2020, Astronomy & Astrophysics, 635, A97

Bavera, S. S., Fragos, T., Zevin, M., et al. 2021, Astronomy & Astrophysics, 647, A153

Bavera, S. S., Fragos, T., Zevin, M., et al. 2021a, A&A, 647, A153

Bavera, S. S., Zevin, M., & Fragos, T. 2021b, Research Notes of the American Astronomical Society, 5, 127

Belczynski, K., Bulik, T., & Fryer, C. L. 2012, arXiv e-prints, arXiv:1208.2422

Belczynski, K., Bulik, T., Fryer, C. L., et al. 2010, ApJ, 714, 1217

Belczynski, K., Bulik, T., Mandel, I., et al. 2013, The Astrophysical Journal, 764, 96

Belczynski, K., Kalogera, V., Rasio, F. A., et al. 2008, ApJS, 174, 223

Belczynski, K., Klencki, J., Fields, C. E., et al. 2020, A&A, 636, A104

Bestenlehner, J. M., Crowther, P. A., Broos, P. S., Pollock, A. M. T., & Townsley, L. K. 2022, MNRAS, 510, 6133

Bethe, H. A. & Brown, G. E. 1998, ApJ, 506, 780

Binder, B. A., Sy, J. M., Eracleous, M., et al. 2021, The Astrophysical Journal, 910, 74

Blaauw, A. 1961, Bull. Astro. Inst. Neth., 15, 265

Blundell, K. M., Bowler, M. G., & Schmidtobreick, L. 2008, ApJ, 678, L47

Boco, L., Mapelli, M., Sander, A. A. C., et al. 2025, arXiv e-prints, arXiv:2507.00137

Boesky, A., Broekgaarden, F. S., & Berger, E. 2024, arXiv e-prints, arXiv:2405.01623

Böhm-Vitense, E. 1958, Zeitschrift für Astrophysik, 46, 108

Bondi, H. & Hoyle, F. 1944, Monthly Notices of the Royal Astronomical Society, 104, 273

Brands, S. A., de Koter, A., Bestenlehner, J. M., et al. 2022, A&A, 663, A36

Breivik, K. 2025, arXiv e-prints, arXiv:2502.03523

Breivik, K., Coughlin, S., Zevin, M., et al. 2020, The Astrophysical Journal, 898, 71

Bressan, A., Chiosi, C., & Bertelli, G. 1981, Astronomy and Astrophysics, vol. 102, no. 1, Sept. 1981, p. 25-30. Consiglio Nazionale delle Ricerche, 102, 25

Bressan, A., Marigo, P., Girardi, L., et al. 2012, MNRAS, 427, 127

Briel, M. M., Stevance, H. F., & Eldridge, J. J. 2023, MNRAS, 520, 5724

Broekgaarden, F. S., Banagiri, S., & Payne, E. 2024, ApJ, 969, 108

Broekgaarden, F. S., Berger, E., Stevenson, S., et al. 2022, MNRAS, 516, 5737

Broekgaarden, F. S., Justham, S., de Mink, S. E., et al. 2019, MNRAS, 490, 5228

Burrows, A. & Vartanyan, D. 2021, Nature, 589, 29

Byrne, C. M., Stanway, E. R., Eldridge, J. J., McSwiney, L., & Townsend, O. T. 2022, MNRAS, 512, 5329

Caffau, E., Ludwig, H.-G., Steffen, M., Freytag, B., & Bonifacio, P. 2011, Solar Physics, 268, 255

Callister, T. A., Haster, C.-J., Ng, K. K. Y., Vitale, S., & Farr, W. M. 2021, ApJ, 922, L5

Cameron, A. G. W. & Mock, M. 1967, Nature, 215, 464

Canal, R., Isern, J., & Labay, J. 1992, ApJ, 398, L49

Castor, J. I., Abbott, D. C., & Klein, R. I. 1975, ApJ, 195, 157

Chandrasekhar, S. 1931, ApJ, 74, 81

Chen, Y., Bressan, A., Girardi, L., et al. 2015, MNRAS, 452, 1068

Cheng, A. Q., Zevin, M., & Vitale, S. 2023, ApJ, 955, 127

Chieffi, A. & Limongi, M. 2013, ApJ, 764, 21

Chieffi, A. & Limongi, M. 2020, ApJ, 890, 43

Choi, J., Dotter, A., Conroy, C., et al. 2016, ApJ, 823, 102

Chruslinska, M., Belczynski, K., Klencki, J., & Benacquista, M. 2018, MNRAS, 474, 2937

Claeys, J. S. W., Pols, O. R., Izzard, R. G., Vink, J., & Verbunt, F. W. M. 2014, A&A, 563, A83

Compas, T., Riley, J., Agrawal, P., et al. 2022, The Journal of Open Source Software, 7, 3838

Costa, G., Ballone, A., Mapelli, M., & Bressan, A. 2022, MNRAS, 516, 1072

Costa, G., Bressan, A., Mapelli, M., et al. 2021, MNRAS, 501, 4514

Costa, G., Chrušlińska, M., Klencki, J., et al. 2024, in Black Holes in the Era of Gravitational-Wave Astronomy, ed. M. Arca Sedda, E. Bortolas, & M. Spera, 1–148

Costa, G., Girardi, L., Bressan, A., et al. 2019, MNRAS, 485, 4641

Costa, G., Mapelli, M., Iorio, G., et al. 2023, MNRAS, 525, 2891

Costa, G., Shepherd, K. G., Bressan, A., et al. 2025, A&A, 694, A193

Crowther, P. A. 2007, Annu. Rev. Astron. Astrophys., 45, 177

Crowther, P. A. 2007, ARA&A, 45, 177

Dall'Amico, M., Mapelli, M., Iorio, G., et al. 2025, A&A, 695, A221

Darwin, G. H. 1880, Philosophical Transactions of the Royal Society of London Series I, 171, 713 de Jager, C., Nieuwenhuijzen, H., & van der Hucht, K. A. 1988, A&AS, 72, 259

de Koter, A., Heap, S. R., & Hubeny, I. 1997, ApJ, 477, 792

de Mink, S. E., Cantiello, M., Langer, N., et al. 2009, A&A, 497, 243

de Mink, S. E. & Mandel, I. 2016, MNRAS, 460, 3545

Delfavero, V., Ford, K. E. S., McKernan, B., et al. 2025, ApJ, 989, 67

Di Carlo, U. N., Giacobbo, N., Mapelli, M., et al. 2019, MNRAS, 487, 2947

Di Carlo, U. N., Mapelli, M., Pasquato, M., et al. 2021, MNRAS, 507, 5132

Di Matteo, T., Springel, V., & Hernquist, L. 2005, Nature, 433, 604

Disberg, P. & Mandel, I. 2025, ApJ, 989, L8

Dominik, M., Belczynski, K., Fryer, C., et al. 2012a, ApJ, 759, 52

Dominik, M., Belczynski, K., Fryer, C., et al. 2012b, ApJ, 759, 52

Eddington, A. S. 1925, The Observatory, 48, 73

Eggenberger, P., Meynet, G., Maeder, A., et al. 2008, ApSS, 316, 43

Eggleton, P. P. 1971, MNRAS, 151, 351

Eggleton, P. P. 1983, ApJ, 268, 368

Ekström, S., Georgy, C., Eggenberger, P., et al. 2012, A&A, 537, A146

Eldridge, J. J., Izzard, R. G., & Tout, C. A. 2008, in Massive Stars as Cosmic Engines, ed. F. Bresolin, P. A. Crowther, & J. Puls, Vol. 250, 179–184

Eldridge, J. J., Stanway, E. R., Xiao, L., et al. 2017, PASA, 34, e058

Ercolino, A., Jin, H., Langer, N., & Dessart, L. 2024, A&A, 685, A58

Ercolino, A., Jin, H., Langer, N., & Dessart, L. 2025, A&A, 696, A103

Ertl, T., Janka, H. T., Woosley, S. E., Sukhbold, T., & Ugliano, M. 2016, Astrophys. J., 818, 124

Esposito, P., Israel, G. L., Milisavljevic, D., et al. 2015, MNRAS, 452, 1112

Event Horizon Telescope Collaboration, Akiyama, K., Alberdi, A., et al. 2019, ApJ, 875, L1

Farmer, R., Renzo, M., de Mink, S. E., Fishbach, M., & Justham, S. 2020, ApJ, 902, L36

Farmer, R., Renzo, M., de Mink, S. E., Marchant, P., & Justham, S. 2019, ApJ, 887, 53

Fernández, R., Quataert, E., Kashiyama, K., & Coughlin, E. R. 2018, MNRAS, 476, 2366

Ferrarese, L. & Merritt, D. 2000, ApJ, 539, L9

Foellmi, C., Moffat, A., & Guerrero, M. 2003a, Monthly Notices of the Royal Astronomical Society, 338, 360

Foellmi, C., Moffat, A., & Guerrero, M. 2003b, Monthly Notices of the Royal Astronomical Society, 338, 1025

Fragos, T., Andrews, J. J., Bavera, S. S., et al. 2023, ApJS, 264, 45

Fryer, C. L., Belczynski, K., Wiktorowicz, G., et al. 2012, ApJ, 749, 91

Gallegos-Garcia, M., Berry, C. P. L., Marchant, P., & Kalogera, V. 2021, ApJ, 922, 110

Gallegos-Garcia, M., Jacquemin-Ide, J., & Kalogera, V. 2024, ApJ, 973, 168

Ge, H., Hjellming, M. S., Webbink, R. F., Chen, X., & Han, Z. 2010, ApJ, 717, 724

Ge, H., Tout, C. A., Chen, X., et al. 2024, ApJ, 975, 254

Ge, H., Webbink, R. F., Chen, X., & Han, Z. 2015, ApJ, 812, 40

Ge, H., Webbink, R. F., Chen, X., & Han, Z. 2020, ApJ, 899, 132

Gerosa, D., Berti, E., O'Shaughnessy, R., et al. 2018, Phys. Rev. D, 98, 084036

Gerosa, D. & Fishbach, M. 2021, Nature Astronomy, 5, 749

Giacobbo, N. & Mapelli, M. 2018, MNRAS, 480, 2011

Giacobbo, N. & Mapelli, M. 2020, ApJ, 891, 141

Giacobbo, N., Mapelli, M., & Spera, M. 2018, MNRAS, 474, 2959

Gilkis, A., Shenar, T., Ramachandran, V., et al. 2021, MNRAS, 503, 1884

Gomez, S. & Grindlay, J. E. 2021, ApJ, 913, 48

Götberg, Y., Drout, M. R., Ji, A. P., et al. 2023, ApJ, 959, 125

Gottlieb, O., Metzger, B. D., Issa, D., et al. 2025, ApJ, 993, L54

Gräfener, G. & Hamann, W. R. 2008, A&A, 482, 945

Gräfener, G., Owocki, S. P., Grassitelli, L., & Langer, N. 2017, A&A, 608, A34

Gräfener, G. & Vink, J. S. 2013, A&A, 560, A6

Greene, J. E., Strader, J., & Ho, L. C. 2020, ARA&A, 58, 257

Häberle, M., Neumayer, N., Seth, A., et al. 2024, Nature, 631, 285

Hainich, R., Rühling, U., Todt, H., et al. 2014, A&A, 565, A27

Hamann, W. R. & Gräfener, G. 2004, A&A, 427, 697

Han, Z., Podsiadlowski, P., & Eggleton, P. P. 1994, MNRAS, 270, 121

Han, Z., Podsiadlowski, P., & Eggleton, P. P. 1995, MNRAS, 272, 800

Heger, A. & Woosley, S. E. 2002, ApJ, 567, 532

Henneco, J., Schneider, F. R. N., & Laplace, E. 2024, A&A, 682, A169

Herwig, F., Bloecker, T., Schoenberner, D., & El Eid, M. 1997, A&A, 324, L81

Higgins, E. R., Sander, A. A. C., Vink, J. S., & Hirschi, R. 2021, MNRAS, 505, 4874

Hillwig, T. C. & Gies, D. R. 2008, ApJ, 676, L37

Hjellming, M. S. & Webbink, R. F. 1987, ApJ, 318, 794

Hobbs, G., Lorimer, D. R., Lyne, A. G., & Kramer, M. 2005, MNRAS, 360, 974

Huang, S.-S. 1963, ApJ, 138, 471

Hurley, J. R., Pols, O. R., & Tout, C. A. 2000, MNRAS, 315, 543

Hurley, J. R., Tout, C. A., & Pols, O. R. 2002, MNRAS, 329, 897

Hut, P. 1981, A&A, 99, 126

Igoshev, A. P. 2020, MNRAS, 494, 3663

Iorio, G., Mapelli, M., Costa, G., et al. 2023, MNRAS, 524, 426

Ivanova, N., Justham, S., Chen, X., et al. 2013, A&A Rev., 21, 59

Izzard, R. G., Preece, H., Jofre, P., et al. 2018, MNRAS, 473, 2984

Izzard, R. G., Tout, C. A., Karakas, A. I., & Pols, O. R. 2004, MNRAS, 350, 407

Janka, H.-T., Hanke, F., Hüdepohl, L., et al. 2012, Progress of Theoretical and Experimental Physics, 2012, 01A309

Jeans, J. H. 1924, MNRAS, 85, 2

Kızıltan, B., Baumgardt, H., & Loeb, A. 2017, Nature, 542, 203

Klencki, J., Nelemans, G., Istrate, A. G., & Chruslinska, M. 2021, Astronomy & Astrophysics, 645, A54

Klencki, J., Nelemans, G., Istrate, A. G., & Pols, O. 2020, A&A, 638, A55

Klencki, J., Podsiadlowski, P., Langer, N., et al. 2025, arXiv e-prints, arXiv:2505.08860

Kolb, U. & Ritter, H. 1990, A&A, 236, 385

Koljonen, K. I. I. & Maccarone, T. J. 2017, MNRAS, 472, 2181

Korb, E., Mapelli, M., Iorio, G., Costa, G., & Dall'Amico, M. 2025, A&A, 695, A199

Kroupa, P. 2001, Monthly Notices of the Royal Astronomical Society, 322, 231

Kruckow, M. U., Tauris, T. M., Langer, N., Kramer, M., & Izzard, R. G. 2018, MNRAS, 481, 1908

Kučinskas, A. 1998, ApSS, 262, 127

Laplace, E., Götberg, Y., De Mink, S., Justham, S., & Farmer, R. 2020, Astronomy & Astrophysics, 637, A6

Laplace, E., Justham, S., Renzo, M., et al. 2021, A&A, 656, A58

Laplace, E., Schneider, F. R. N., & Podsiadlowski, P. 2025, A&A, 695, A71

Laycock, S. G. T., Maccarone, T. J., & Christodoulou, D. M. 2015, MNRAS, 452, L31

Lemasle, B., Hajdu, G., Kovtyukh, V., et al. 2018, A&A, 618, A160

Limongi, M. & Chieffi, A. 2010, in Journal of Physics Conference Series, Vol. 202, Journal of Physics Conference Series, 012002

Limongi, M. & Chieffi, A. 2018, ApJS, 237, 13

Lioutas, G., Bauswein, A., Soultanis, T., et al. 2024, MNRAS, 528, 1906

Maccarone, T. & Knigge, C. 2007, Astronomy and Geophysics, 48, 5.12

Maeder, A. 1987, A&A, 178, 159

Maeder, A. 1992, A&A, 264, 105

Maggiore, M. 2007, Gravitational waves: Volume 1: Theory and experiments (OUP Oxford)

Mahy, L., Sana, H., Shenar, T., et al. 2022, A&A, 664, A159

Maltsev, K., Schneider, F. R. N., Mandel, I., et al. 2025, A&A, 700, A20

Mandel, I. 2016, Monthly Notices of The Royal Astronomical Society, 456, 578

Mandel, I. & Broekgaarden, F. S. 2022, Living Reviews in Relativity, 25, 1

Mandel, I. & de Mink, S. E. 2016, MNRAS, 458, 2634

Mandel, I. & Farmer, A. 2022, Phys. Rep., 955, 1

Mapelli, M. 2021, in Handbook of Gravitational Wave Astronomy, 16

Mapelli, M., Bouffanais, Y., Santoliquido, F., Arca Sedda, M., & Artale, M. C. 2022, MNRAS, 511, 5797

Mapelli, M., Dall'Amico, M., Bouffanais, Y., et al. 2021, MNRAS, 505, 339

Mapelli, M., Spera, M., Montanari, E., et al. 2020, ApJ, 888, 76

Marchant, P. & Bodensteiner, J. 2024, ARA&A, 62, 21

Marchant, P., Pappas, K. M. W., Gallegos-Garcia, M., et al. 2021, A&A, 650, A107

Marigo, P., Cummings, J. D., Curtis, J. L., et al. 2020, Nature Astronomy, 4, 1102

McCollough, M., Corrales, L., & Dunham, M. 2016, The Astrophysical Journal Letters, 830, L36

McKernan, B., Ford, K. E. S., Kocsis, B., Lyra, W., & Winter, L. M. 2014, MNRAS, 441, 900

McKernan, B., Ford, K. E. S., Lyra, W., & Perets, H. B. 2012, MNRAS, 425, 460

Mestichelli, B. 2024

Meynet, G. & Maeder, A. 1997, A&A, 321, 465

Miller, M. C. & Hamilton, D. P. 2002, MNRAS, 330, 232

Miller-Jones, J. C. A., Bahramian, A., Orosz, J. A., et al. 2021, Science, 371, 1046

Moe, M. & Di Stefano, R. 2017, The Astrophysical Journal Supplement Series, 230, 15

Müller, B., Heger, A., Liptai, D., & Cameron, J. B. 2016, MNRAS, 460, 742

Neijssel, C. J., Vigna-Gómez, A., Stevenson, S., et al. 2019, MNRAS, 490, 3740

Nguyen, C. T., Costa, G., Girardi, L., et al. 2022, arXiv e-prints, arXiv:2207.08642

Nguyen, D. D., Seth, A. C., Neumayer, N., et al. 2019, ApJ, 872, 104

Nugis, T. & Lamers, H. J. G. L. M. 2000, A&A, 360, 227

Nugis, T. & Lamers, H. J. G. L. M. 2002, A&A, 389, 162

O'Connor, E. & Ott, C. D. 2011, ApJ, 730, 70

Offner, S. S. R., Moe, M., Kratter, K. M., et al. 2023, in Astronomical Society of the Pacific Conference Series, Vol. 534, Protostars and Planets VII, ed. S. Inutsuka, Y. Aikawa, T. Muto, K. Tomida, & M. Tamura, 275

Olejak, A. & Belczynski, K. 2021, ApJ, 921, L2

Olejak, A., Klencki, J., Xu, X.-T., et al. 2024, A&A, 689, A305

Öpik, E. 1924, Publications of the Tartu Astrofizica Observatory, 25, 1

Oppenheimer, J. R. & Volkoff, G. M. 1939, Physical Review, 55, 374

Orosz, J. A., McClintock, J. E., Narayan, R., et al. 2007, Nature, 449, 872

Orosz, J. A., Steeghs, D., McClintock, J. E., et al. 2009, ApJ, 697, 573

Özel, F. & Freire, P. 2016, ARA&A, 54, 401

Özel, F., Psaltis, D., Narayan, R., & McClintock, J. E. 2010, The Astrophysical Journal, 725, 1918

Paczyński, B. & Ziółkowski, J. 1968, Acta Astronomica, 18, 255

Paiella, L., Ugolini, C., Spera, M., Branchesi, M., & Arca Sedda, M. 2025, arXiv e-prints, arXiv:2509.10609

Papanikolaou, T., Vennin, V., & Langlois, D. 2021, JCAP, 2021, 053

Parkosidis, A., Toonen, S., Dosopoulou, F., & Laplace, E. 2025a, arXiv e-prints, arXiv:2509.05243

Parkosidis, A., Toonen, S., Laplace, E., & Dosopoulou, F. 2025b, arXiv e-prints, arXiv:2511.07190

Pastorelli, G., Marigo, P., Girardi, L., et al. 2020, MNRAS, 498, 3283

Patton, R. A. & Sukhbold, T. 2020, MNRAS, 499, 2803

Paxton, B., Bildsten, L., Dotter, A., et al. 2011, ApJS, 192, 3

Paxton, B., Cantiello, M., Arras, P., et al. 2013, ApJS, 208, 4

Paxton, B., Marchant, P., Schwab, J., et al. 2015, The Astrophysical Journal Supplement Series, 220, 15

Paxton, B., Smolec, R., Schwab, J., et al. 2019, ApJS, 243, 10

Pennington, R. 1985, in Interacting Binary Stars, ed. J. E. Pringle & R. A. Wade, 197–199

Peters, P. C. 1964, Physical Review, 136, B1224

Picco, A., Marchant, P., Sana, H., & Nelemans, G. 2024, A&A, 681, A31

Podsiadlowski, P., Joss, P. C., & Rappaport, S. 1990, A&A, 227, L9

Pols, O. 2008, https://www.astro.ru.nl/~onnop/education/binaries_utrecht_notes/

Pols, O. R. 2011, Lecture notes for a Utrecht University MSc course

Pols, O. R., Schröder, K.-P., Hurley, J. R., Tout, C. A., & Eggleton, P. P. 1998, MNRAS, 298, 525

Pols, O. R., Tout, C. A., Eggleton, P. P., & Han, Z. 1995, MNRAS, 274, 964

Portegies Zwart, S. F. & McMillan, S. L. W. 2002, ApJ, 576, 899

Portegies Zwart, S. F. & Spreeuw, H. N. 1996, A&A, 312, 670

Prialnik, D. 2009, An Introduction to the Theory of Stellar Structure and Evolution

Price, D. J., Wurster, J., Tricco, T. S., et al. 2018, PASA, 35, e031

Qin, Y., Fragos, T., Meynet, G., et al. 2018, Astronomy & Astrophysics, 616, A28

Qin, Y., Hu, R. C., Meynet, G., et al. 2023, arXiv e-prints, arXiv:2301.04918

Qin, Y., Marchant, P., Fragos, T., Meynet, G., & Kalogera, V. 2019, The Astrophysical Journal Letters, 870, L18

Radice, D., Perego, A., Zappa, F., & Bernuzzi, S. 2018, ApJ, 852, L29

Ramachandran, V., Oskinova, L. M., Hamann, W. R., et al. 2022, A&A, 667, A77

Rantala, A., Lahén, N., Naab, T., Escobar, G. J., & Iorio, G. 2025, MNRAS, 543, 2130

Rantala, A., Naab, T., & Lahén, N. 2024, MNRAS, 531, 3770

Rantala, A., Naab, T., Rizzuto, F. P., et al. 2023, MNRAS, 522, 5180

Rastello, S., Iorio, G., Gieles, M., & Wang, L. 2025, arXiv e-prints, arXiv:2509.07067

Rastello, S., Mapelli, M., Di Carlo, U. N., et al. 2020, MNRAS, 497, 1563

Rastello, S., Mapelli, M., Di Carlo, U. N., et al. 2021, MNRAS, 507, 3612

Ray, A. & Kalogera, V. 2025, arXiv e-prints, arXiv:2510.18867

Reimers, D. 1975, in Problems in stellar atmospheres and envelopes., ed. B. Baschek, W. H. Kegel, & G. Traving, 229–256

Renzo, M., Cantiello, M., Metzger, B. D., & Jiang, Y. F. 2020a, ApJ, 904, L13

Renzo, M., Farmer, R., Justham, S., et al. 2020b, A&A, 640, A56

Renzo, M. & Smith, N. 2024, arXiv e-prints, arXiv:2407.16113

Riley, J., Mandel, I., Marchant, P., et al. 2021, MNRAS, 505, 663

Ritter, H. 1988, A&A, 202, 93

Rodriguez, C. L., Zevin, M., Amaro-Seoane, P., et al. 2019, Phys. Rev. D, 100, 043027

Rodriguez, C. L., Zevin, M., Pankow, C., Kalogera, V., & Rasio, F. A. 2016, ApJ, 832, L2

Romero-Shaw, I., Lasky, P. D., Thrane, E., & Calderón Bustillo, J. 2020, ApJ, 903, L5

Röpke, F. K. & De Marco, O. 2023, Living Reviews in Computational Astrophysics, 9, 2

Sabhahit, G. N., Vink, J. S., Higgins, E. R., & Sander, A. A. C. 2022, MNRAS, 514, 3736

Samsing, J. 2018, Phys. Rev. D, 97, 103014

Samsing, J., Bartos, I., D'Orazio, D. J., et al. 2022, Nature, 603, 237

Sana, H., De Mink, S., de Koter, A., et al. 2012, Science, 337, 444

Sander, A. A. C., Hamann, W.-R., Todt, H., et al. 2019, Astronomy & Astrophysics, 621, A92

Sander, A. A. C., Lefever, R. R., Poniatowski, L. G., et al. 2023, A&A, 670, A83

Sander, A. A. C., Vink, J. S., Higgins, E. R., et al. 2022, arXiv e-prints, arXiv:2202.04671

Santoliquido, F., Mapelli, M., Giacobbo, N., Bouffanais, Y., & Artale, M. C. 2021, MNRAS, 502, 4877

Schmitt, A. 2010, Dense Matter in Compact Stars, Vol. 811

Schneider, F. R. N., Laplace, E., & Podsiadlowski, P. 2025, A&A, 700, A253

Schneider, F. R. N., Podsiadlowski, P., & Laplace, E. 2023, ApJ, 950, L9

Schneider, F. R. N., Podsiadlowski, P., & Laplace, E. 2024, A&A, 686, A45

Schneider, F. R. N., Podsiadlowski, P., & Müller, B. 2021, A&A, 645, A5

Schneider, F. R. N., Ramírez-Agudelo, O. H., Tramper, F., et al. 2018, A&A, 618, A73

Schnurr, O., Casoli, J., Chené, A.-N., Moffat, A., & St-Louis, N. 2008, Monthly Notices of the Royal Astronomical Society: Letters, 389, L38

Schootemeijer, A., Shenar, T., Langer, N., et al. 2024, A&A, 689, A157

Schwarzschild, M. 1958, Structure and evolution of the stars.

Sen, K., Xu, X. T., Langer, N., et al. 2021, A&A, 652, A138

Sgalletta, C., Iorio, G., Mapelli, M., et al. 2023, MNRAS, 526, 2210

Sgalletta, C., Mapelli, M., Boco, L., et al. 2025, A&A, 698, A144

Shenar, T. 2024, arXiv e-prints, arXiv:2410.04436

Shenar, T., Gilkis, A., Vink, J. S., Sana, H., & Sander, A. A. C. 2020, A&A, 634, A79

Shenar, T., Sana, H., Crowther, P. A., et al. 2023, A&A, 679, A36

Shenar, T., Sana, H., Mahy, L., et al. 2022, Nature Astronomy, 6, 1085

Shenar, T., Sana, H., Marchant, P., et al. 2021, A&A, 650, A147

Shepherd, K. G., Costa, G., Ugolini, C., et al. 2025, A&A, 701, A126

Sills, A., Adams, T., Davies, M. B., & Bate, M. R. 2002, MNRAS, 332, 49

Simonato, F., Torniamenti, S., Mapelli, M., et al. 2025, A&A, 703, A215

Singh, N., Naik, S., Paul, B., et al. 2002, Astronomy & Astrophysics, 392, 161

Smith, L. F., Shara, M. M., & Moffat, A. F. J. 1996, MNRAS, 281, 163

Soberman, G. E., Phinney, E. S., & van den Heuvel, E. P. J. 1997, A&A, 327, 620

Spera, M. & Mapelli, M. 2017, MNRAS, 470, 4739

Spera, M., Mapelli, M., & Bressan, A. 2015, MNRAS, 451, 4086

Spera, M., Mapelli, M., Giacobbo, N., et al. 2019, MNRAS, 485, 889

Springel, V. 2010, MNRAS, 401, 791

Spurio, M. 2019, arXiv preprint arXiv:1906.03643

Stegmann, J., Olejak, A., & de Mink, S. E. 2025, ApJ, 992, L26

Stone, J. M., Tomida, K., White, C. J., & Felker, K. G. 2020, ApJS, 249, 4

Sukhbold, T., Ertl, T., Woosley, S. E., Brown, J. M., & Janka, H. T. 2016, ApJ, 821, 38

Sukhbold, T., Woosley, S. E., & Heger, A. 2018, ApJ, 860, 93

Suzuki, H. 2024, Progress of Theoretical and Experimental Physics, 2024, 05B101

Tagawa, H., Kocsis, B., Haiman, Z., et al. 2021, ApJ, 908, 194

Tauris, T., Kramer, M., Freire, P., et al. 2017, The Astrophysical Journal, 846, 170

Tauris, T. M. & van den Heuvel, E. P. J. 2006, Formation and evolution of compact stellar X-ray sources, Vol. 39, 623–665

Team Compas, Mandel, I., Riley, J., et al. 2025, ApJS, 280, 43

The LIGO Scientific Collaboration, the Virgo Collaboration, & the KAGRA Collaboration. 2025a, arXiv e-prints, arXiv:2508.18083

The LIGO Scientific Collaboration, The Virgo Collaboration, & the KAGRA Collaboration. 2025b, arXiv e-prints, arXiv:2508.18082

The LIGO Scientific Collaboration, the Virgo Collaboration, the KAGRA Collaboration, et al. 2025c, arXiv e-prints, arXiv:2507.08219

The LIGO Scientific Collaboration, the Virgo Collaboration, the KAGRA Collaboration, et al. 2025d, arXiv e-prints, arXiv:2508.18080

Tolman, R. C. 1939, Physical Review, 55, 364

Tong, H., Fishbach, M., Thrane, E., et al. 2025, arXiv e-prints, arXiv:2509.04151

Toonen, S., Nelemans, G., & Portegies Zwart, S. 2012, A&A, 546, A70

Torniamenti, S., Mapelli, M., Boco, L., et al. 2025, arXiv e-prints, arXiv:2510.12465

Torniamenti, S., Mapelli, M., Périgois, C., et al. 2024, A&A, 688, A148

Vaccaro, M. P., Mapelli, M., Périgois, C., et al. 2024, A&A, 685, A51

van den Heuvel, E. P. J. 1994, in Saas-Fee Advanced Course 22: Interacting Binaries, ed. S. N. Shore, M. Livio, E. P. J. van den Heuvel, H. Nussbaumer, & A. Orr, 263–474

Van Der Hucht, K. A. 2001, New Astronomy Reviews, 45, 135

van Son, L. A. C., De Mink, S. E., Broekgaarden, F. S., et al. 2020, ApJ, 897, 100

van Son, L. A. C., de Mink, S. E., Callister, T., et al. 2022a, ApJ, 931, 17

van Son, L. A. C., de Mink, S. E., Renzo, M., et al. 2022b, ApJ, 940, 184

Veledina, A., Muleri, F., Poutanen, J., et al. 2024, Nature Astronomy, 1

Verbunt, F., Igoshev, A., & Cator, E. 2017, A&A, 608, A57

Vigna-Gómez, A., MacLeod, M., Neijssel, C. J., et al. 2020, Publications of the Astronomical Society of Australia, 37, e038

Vink, J. S. 2015, arXiv preprint arXiv:1510.00227

Vink, J. S., de Koter, A., & Lamers, H. 2001, Astronomy & Astrophysics, 369, 574

Vink, J. S., de Koter, A., & Lamers, H. J. G. L. M. 2000, A&A, 362, 295

Vink, J. S., de Koter, A., & Lamers, H. J. G. L. M. 2001, A&A, 369, 574

Vink, J. S., Muijres, L. E., Anthonisse, B., et al. 2011, A&A, 531, A132

Wang, L., Spurzem, R., Aarseth, S., et al. 2016, MNRAS, 458, 1450

Wang, L., Spurzem, R., Aarseth, S., et al. 2015, MNRAS, 450, 4070

Webbink, R. F. 1984, ApJ, 277, 355

Webbink, R. F. 1985, Stellar evolution and binaries, ed. J. E. Pringle & R. A. Wade, 39

Willcox, R., MacLeod, M., Mandel, I., & Hirai, R. 2023, ApJ, 958, 138

Willcox, R., Schneider, F. R. N., Laplace, E., et al. 2025, arXiv e-prints, arXiv:2508.20787

Wolf, C. J. E. & Rayet, G. 1867, Academie des Sciences Paris Comptes Rendus, 65, 292

Woosley, S. E. 2017, ApJ, 836, 244

Yoon, S.-C., Woosley, S. E., & Langer, N. 2010, ApJ, 725, 940

Zahn, J. P. 1977, A&A, 57, 383

Zdziarski, A. A., Mikolajewska, J., & Belczynski, K. 2013, MNRAS, 429, L104

Zevin, M., Bavera, S. S., Berry, C. P. L., et al. 2021, ApJ, 910, 152